Diss. 2005 -15
December

NUCLEAR STRUCTURE IN THE REGION OF THE DOUBLY-MAGIC ^{100}Sn

A.A. Blazhev

(Dissertation St. Kliment Ohridski University of Sofia)

Gesellschaft für Schwerionenforschung mbH
Planckstraße 1 · D-64291 Darmstadt · Germany
Postfach 11 05 52 · D-64220 Darmstadt · Germany

University of Sofia "St. Kliment Ohridski"
Faculty of Physics

Andrey Atanasov Blazhev

NUCLEAR STRUCTURE IN THE REGION OF THE DOUBLY-MAGIC ^{100}Sn

A thesis submitted for the PhD degree

Scientific code: **01.03.04** (Nuclear Physics)

Scientific supervisors:

Dr. Dimiter Balabanski	Dr. Hubert Grawe
University of Sofia	GSI, Darmstadt
Bulgaria	Germany

Sofia, January 2005

This thesis presents results from scientific work done at the GSI, Darmstadt, Germany and at the Faculty of Physics at University of Sofia, Bulgaria. These results have not been accepted for the award of any other degree or diploma in any university. To the best of the author's knowledge and belief, it contains no material previously published or written by another person, except where due reference is made in the text.

January, 2005 Andrey Blazhev

Acknowledgements

I would like thank my supervisor Dr. Dimiter Balabanski for giving me this opportunity to work and guiding me in the process of becoming a physicist during many years.

I am in particular grateful to my supervisor Dr. Hubert Grawe for his continuous guidance, his invaluable help and his constant encouragement throughout the course of this work.

Special thanks go to Dr. Magdalena Górska, who introduced me to details of the γ-spectroscopy data analysis and helped me in continuing her work on ^{98}Cd.

The sorting and the alignment of the ^{98}Cd data were done under the introduction and cooperation of Dr. Marcin Palacz, to whom I would also like to thank.

Certainly, all the numerous colleagues, who participated in the ^{98}Cd experiment at EUROBALL in Strasbourg, are greatly acknowledged for their work and fellowship.

Dr. Andres Gadea is acknowledged for introducing me to the program TRANS, which was used in the theoretical studies of this thesis to calculate GT-transition strength.

Very important for my work were all my colleagues from the GSI-ISOL group, where I spent most of my time working on the thesis. I thank MSc. Myroslav Kavatsyuk for introducing and helping me to use the ROOT package, as well as the joint work in other subjects. Though the GSI-ISOL has been decomissioned and the last mohicans of the group have just retired, I dearly remember and esteem their impact on my work and life. I appreciate the help, support, the experimental time and everyday company of Prof. Dr. Ernst Roeckl, Dr. Reinhard Kirchner, Dr. Leonid Batist, Dr. Joachim Döring, Dr. Cristina Plettner, Dr. Chiara Mazzocchi, Dr. Ivan Mukha, MSc. Oksana Kavatsyuk, Karlheinz Burkard and Wilfried Hüller. The secretary of the KPII department, Siggi Raiss, was also an important person for many of the administrative and personal needs during my stay at the GSI, Darmstadt.

A special place in my life during my stay at the GSI, Darmstadt, have my friends: MSc. Radomira Lozeva, Dr. Vladimir Arsov, Dr. Orlin Yordanov, Dr. Ivan Kojouharov, Dr. Stepan Yaramishev and Dr. Kalin Gladnishki. I also acknowledge many other people who have helped me and without whom I wouldn't have been

able to proceed with and finish this work, but who are not listed here.

I also thank my parents for raising me up and supporting me in my life and education. I would like to thank especially my wife, Maria, for the constant care for me and for our children, Alexandra and Daniel. I thank my children, for bringing so much joy and sweet troubles in my life. Last, but most, I thank God for helping me to have success in my work, giving me my parents, my friends and colleagues, my supervisors, my family and my children.

Preface

The current work presents studies of the nuclear structure in the region of the doubly magic ^{100}Sn. These studies are based on two experiments and the theoretical interpretation of the experimental results.

The first experiment, which studied the β-decay of ^{100}In, the one proton-hole and one neutron-particle neighbour of ^{100}Sn, was carried out in November 2000, at the GSI-ISOL and the online mass separator. The fusion-evaporation reaction ^{50}Cr(^{58}Ni,$\alpha p3n$)^{100}In was used to produce this nucleus. The recoils were stopped in a thermal ion source. After ionization and extraction from the ion source, the beam delivered by the GSI mass separator was directed to the high-resolution or to the total-absorption set-ups. The $A = 100$ beam was implanted into a tape during 16 s, with the tape being moved at the end of this interval. The high-resolution $\beta\gamma\gamma$ set-up, which was placed around the implantation point, consisted of a plastic scintillator, an EUROBALL cluster, a VEGA superclover and a LEPS detectors. It provided high-resolution γ-spectroscopy data which was analyzed by Dr. C. Plettner. The total-absorption spectrometer consists of a large NaI crystal of 356 mm diameter and 356 mm length and is equipped with ancillary detectors for registering β particles, protons, and X-rays. The low-resolution Total Absorption spectroscopy data was analyzed by Dr. L. Batist. The shell-model calculations used in the interpretation of the decay scheme and the GT-strength distribution are part of this thesis and have been done by the author himself. The comparison of the experimental and theoretical GT-strength distributions favours $I^\pi = 6^+$ for the ground state of the ^{100}In. The hindrance factor for the total GT-strength, which has to be applied with reference to the shell model value, in the case of ^{100}In amounts to $h = 4.1(9)$.

The second experiment was performed to study in-beam the prompt and delayed γ radiation of ^{98}Cd, which is the two proton hole neighbour of ^{100}Sn. The five-day experiment was carried out in April/May 2001 in Strasbourg with the EUROBALL IV multidetector γ-ray array in a configuration with ancillary detectors. The 4π Si-ball EUCLIDES for detecting α particles and protons was mounted around the thin target inside the reaction chamber. The Neutron Wall was used for neutron detection replacing the tapered γ detectors in the front 1π of solid angle. In forward direction, right after the ball, a special delayed spectroscopy set-up was constructed

and installed, consisting of a catcher foil and in close geometry around it, two Cluster and one Clover unshielded detectors. The studied nucleus was produced in the α2n exit channel of the ^{46}Ti+^{58}Ni $\rightarrow$ ^{104}Sn* fusion-evaporation reaction. The technical subject of this work was the gain and offset correction, the calibration, the sorting and the analysis of the data from all different detector systems. The results for ^{98}Cd are the discovery of a new delayed high-energy γ transition assigned to depopulate a core-excited $I^{\pi} = (12^{+})$ state and the determination of new half-lives for the $I^{\pi} = (12^{+})$, (8^{+}) and (6^{+}) levels. From the (8^{+}) half-life a new limit of $\delta e_{\pi} < 0.4e$ for the proton polarization charge is inferred. The experimental results are used together with shell model calculations to make a new improved estimate of 6.46(15)MeV for the ^{100}Sn shell gap.

Outline

Chapter 1 gives a general introduction to the definitions and observables used later in the thesis. Further on, the topic of exotic nuclei is presented. The importance of the region of the doubly-magic ^{100}Sn for the study of the proton-neutron ($\pi\nu$) interaction, proton dripline, Fermi- and GT-decay, particle emission and the astrophysical *rp*-process, together with the experimental status in this region are also discussed. At the end of the chapter, the nuclear reactions, γ spectrometers and ancillary detectors used in the experiments to study the region of ^{100}Sn are briefly mentioned.
Chapter 2 describes the experimental techniques used to produce and study the exotic nuclei in the region of ^{100}Sn. These are the reaction mechanism, the ISOL and the fragment separator technique, the in-beam gamma spectrometry with one of its best examples the EUROBALL IV multidetector γ array. Additional attention is payed to some of the ancillary detector systems used in configuration with EUROBALL IV, like the EUCLIDES 4π Si-ball for light charged particle detection and the 1π Neutron Wall array for detection of evaporated neutrons. The specially constructed delayed gamma spectroscopy set-up used in the ^{98}Cd experiment is also described. At the end of the chapter a general description of the EUROBALL data acquisition and trigger system is given. All these instruments have been used in order to obtain the results of this thesis work.
Chapter 3 describes the analysis of the data from the ^{98}Cd experiment. The extensive work and the procedures performed to align and calibrate in time and energy, and to analyze the data from the multiple detector systems are presented. Some representative energy spectra, used in the analysis, gated with different time and particle conditions are shown. Details on the half-life determination, with the three different methods used, are given.
Chapter 4 presents the experimental results for the studied nuclei. As mentioned in the preface, the experimental results for the decay study of ^{100}In come from my GSI colleagues, but these results are the basis for comparison and the motivation for the theoretical shell model calculations done by the author. The final results of the ^{98}Cd delayed gamma spectroscopy analysis are also presented.
Chapter 5 introduces the Shell Model codes, model spaces, single particle energies, and the sets of residual interactions used in the theoretical interpretation of the two

studied nuclei.
Chapter 6 discusses the spin-parity assignments in the cases of the ^{100}In and ^{98}Cd. The study of the experimental and theoretical ^{100}In GT-decay distribution and the quenching of the observed strength in comparison to theory is presented. A comparison of the ^{98}Cd experimental and the calculated level energies and transition strengths is done, followed by conclusions for the effective core polarization proton charge, the size of the ^{100}Sn shell gap and for the quality of the realistic interaction used in the large-scale shell-model calculation. Besides the description of the experimental data, the theory also gives predictions for other interesting structure features of nuclei in that region. Finally, some consequences for the nuclear structure of the ^{132}Sn region are discussed.
Chapter 7 summarizes the results and the scientific contributions of this work.
Chapter 8 gives an outlook for future experiments, technical developments and structure topics to be studied.

Contents

Chapter 1

Introduction

Atomic nuclei are unique quantal systems, which consist of two species of particles: protons and neutrons. The nuclei are characterized by different sets of experimental observables, e.g. binding energies, nuclear moments, excitation and decay spectra, etc. Nuclear physics is the branch in physics that studies the atomic nucleus. Its main goal is to provide some day a consistent, non-contradicting and universal model that describes the properties of all known nuclei and that predicts the properties of yet unexplored ones. Both theoretical and experimental achievements and a good interplay between them are needed in order for this goal to be achieved. Theory needs input and test data so it relies on the experiment. The experiment itself needs some prediction, not only to better plan and measure the nuclear properties, but also to give an interpretation for many new results.

Nowadays there are some well established approaches to address nuclear properties from theoretical point of view. Most of them have been inspired by some new phenomenon that was experimentally discovered and have been developing influenced by algebraic and numerical limitations. In general there are two main approaches: collective models [Bohr75, Ring80, Slav92, Cast00] and nuclear shell models [deSh63, Brus77, Slav92, Heyd94, Pove01, Graw04].

1.1 Definitions and observables

The main problem of the nuclear structure physics is to define the real Hamiltonian and to solve the Schrödinger equation for the system of interacting protons and neutrons.

$$H\Psi = E\Psi \tag{1.1}$$

The experimental data on nuclear properties of the ground state (g.s.) like the mass, spin-parity, magnetic moments, together with the so called "magic" numbers,

i.e. numbers of protons and/or neutrons at which the number of stable isotopes or isotones is greater, brought the analogy with the atomic shell model. The basic assumption of the nuclear shell model is that to a first approximation each nucleon moves independently in a potential that is generated from the interaction with all the other nucleons in the nucleus. The independent motion of the nucleons in the nucleus is justified by the short range of the nuclear force and the Pauli principle. In the year 1949 Jensen [Jens49] and Göppert-Mayer [Göpp49] have succeeded in merging the assumption of a central potential with the ingenious idea of a spin-orbit force. Then the Hamiltonian is split into kinetic energy term (T) and one-body mean-field potential U. The latter was empirically constructed by adding a strong spin-orbit splitting to a surface corrected harmonic oscillator.

$$H = T + U \quad , with \tag{1.2}$$

$$U(r) = \frac{1}{2}m\omega^2 r^2 + D\vec{l}^2 - C\vec{l}.\vec{s} \quad , \tag{1.3}$$

where

$$\begin{aligned} -\vec{l}.\vec{s} &= -\frac{1}{2}(\vec{j}^2 - \vec{l}^2 - \vec{s}^2) = -\frac{1}{2}\left(j(j+1) - l(l+1) - \frac{3}{4}\right) \\ &= l+1 \quad for \quad j = l - \frac{1}{2} \\ &= -l \quad for \quad j = l + \frac{1}{2} \, , \end{aligned} \tag{1.4}$$

where l is the orbital angular momentum, s is the intrinsic spin, and j is the total spin. The spin-orbit splitting and the approximate positions of single particle levels lower than $1g$ of the nuclear mean field are shown in Fig. 1.1.

Even if the radial quantum number n and the total spin j of two nucleonic states are the same, they could still differ in the projection m of the $\vec{j}$ onto the quantization axis. There are $2j+1$ projections of a $\vec{j}$ state, which in a spherically symmetric potential are degenerate. So every j state forms a *sub-shell* (orbit/orbital) that can be occupied by $2j+1$ protons or $2j+1$ neutrons. As it is shown on Fig. 1.1, the spin-orbit splitting groups some of the sub-shells together, and introduces energy gaps between the groups. A group of sub-shells lying close in energy is referred to as a *major shell*. The figure shows to the right the "magic numbers" (2, 8, 20, 28, 50, 82 and 126), i.e. the particle numbers at which shell closures occur , as deduced by the spherical mean field with spin-orbit term. For some nuclei, both the proton and neutron numbers are magic and one speaks about *doubly-magic* nuclei. They are much more stable and have higher binding energy per nucleon compared to the neighbouring ones. The reproduction of the empirically found "magic" numbers and g.s. properties of many nuclei was the main goal and success of the mean field theory and it served as a trigger for development of the nuclear shell model.

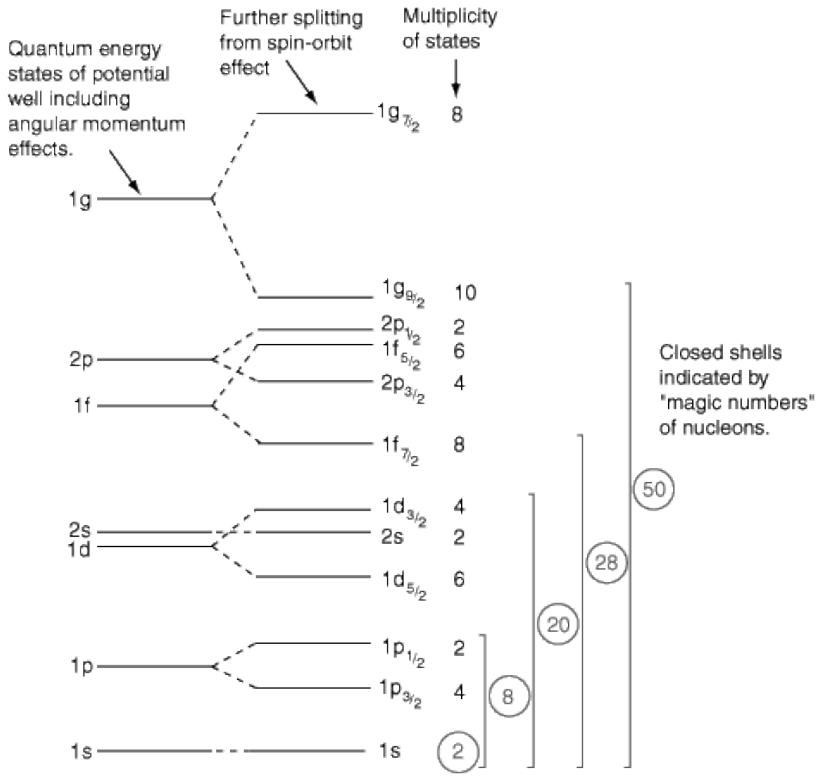

Figure 1.1: The single particle levels of the spherical mean field. To the right the predicted magic numbers. (from [HYPhys]) Note that the definition of the radial quantum number n in the figure is different from the rest of the thesis. Here n counts the node at $r = 0$, whereas the usual convention does not ($1g$ vs. $0g$).

However, in contrast to the atomic shell model with a spatially well defined central Coulomb potential, in the nuclear shell model, the central mean field potential is created by the individual nucleons. The principle idea of nucleons, i.e. equality of the protons and neutrons with respect to the strong force, naturally introduces the *isospin* quantum number t, which is a vector in the isospin space with a length of $1/2$. Like the s quantum number it can only have 2 different projections onto the quantization axis Z. The nuclear physics nomenclature defines that $t_z = -1/2$ for protons and $t_z = 1/2$ neutrons.

Further experimental results have shown that also two-body and three-body forces should be considered. If we limit the interactions between the nucleons in the nucleus to only two-body interaction, we can express the Hamiltonian as the sum of the kinetic (T) and potential (V) energy:

$$H = T + V = \sum_{i=1}^{A} \frac{\vec{p}_i^2}{2m_i} + \sum_{i>k=1}^{A} V_{ik}(\vec{r}_i - \vec{r}_k) \tag{1.5}$$

To bring it back to the solvable case we introduce a one-body nucleon potential U_i and split the Hamiltonian into the independent-particle Hamiltonian H_0 and the residual interaction Hamiltonian H_{res}.

$$\begin{aligned} H &= \left[\sum_{i=1}^{A} \frac{\vec{p}_i^2}{2m_i} + \sum_{i=1}^{A} U_i(\vec{r})\right] + \left[\sum_{i>k=1}^{A} V_{ik}(\vec{r}_i - \vec{r}_k) - \sum_{i=1}^{A} U_i(\vec{r})\right] \\ &= H_0 + H_{res} \end{aligned} \tag{1.6}$$

The solutions of a Schrödinger equation with H_0 are the nucleon single particle energies (SPE) in a central potential. The smaller the H_{res}, the better the multi-nucleon wave-function is represented by the independent-particle wave function. The H_{res} is often represented by a matrix, which elements define the strength of the mutual interactions of the valence nucleons. These matrix elements in a general many-particle configuration can be calculated from two-body matrix elements (TBME) only.

In most of the cases we expect that the separation between a block of orbits and the rest is valid even when the residual interaction is turned on. For a given nucleus the mean field prescribes which orbits are filled (those under the Fermi level) and which are empty (those above the Fermi level). But mostly the states close to the Fermi levels are dictating the nuclear properties. The residual interaction can mix them and produce correlated states. These states naturally form a valence space, where the configuration of the occupying particles will have a dominant effect on the nuclear properties. Therefore, the infinite set of the mean field orbits will be separated in three parts: (i) *Inert core*: the orbits that are forced to always be fully occupied; (ii) *Valence space*: the orbits available to the valence particles, which will partially occupy the orbits according to the mean field and the residual interaction; (iii) *External space*: the remaining orbits that are assumed to be always empty. The set of specific orbits included in the valence space is referred to as *model space*.

In practical applications[Brus77, Graw04] SPE are obtained from an empirical globally adjusted central potential of e.g. the harmonic oscillator [Brus77], the Woods-Saxon [Brus77], folded Yukawa [Möll97] type or can be extracted from the single particle(hole) states in the neighbouring nuclei of a doubly-closed shell nucleus. The TBME of the residual interaction are derived in three ways. *Empirical interactions* can be extracted from experimental data, in the simplest approach from the binding energies of closed shell (CS), $CS \pm 1$ and $CS \pm 2$ nuclei, but giving the SPE and only the diagonal TBME, which means that for more than one orbit, the configuration mixing is neglected. For not too large model spaces one can apply the χ^2-fitting method to determine SPE and TBME (including non-diagonal) from an abundant data set of experimental binding and excitation energies of states. Good examples of empirical interactions can be found in the Refs. [Cohe67, Gros76, Blom85, Brow88a, Richt91, Honm02, Lise04]. A χ^2-fitting procedure is greatly simplified by assuming a *schematic interaction* that can be specified by a few parameters. But the restrictions and symmetries of a given analytic

function introduce deficiencies in the energies (pairing, level density) and electromagnetic (EM) transition rates (configuration mixing) calculated in the shell model application. Some of the schematic interactions are the Yukawa [Heyd94], Gaussian [Heyd94], delta [Heyd94] and surface delta [Arvi66] interactions. Another type of schematic interaction is widely used in mean field calculations employing the HF method, namely the Skyrme [Skyr59, Vaut72] and Gogny forces [Gogn75]. They have been successfully used to calculate gross properties as masses, shapes, radii, level densities and single particle energies, but do not reproduce well the nuclear excited states and transition rates, and therefore are not used in the detailed shell model spectroscopy. *Realistic interactions* are derived from effective nucleon-nucleon potentials, which were fitted to experimental data on nucleon-nucleon scattering. The problem of obtaining a regularized effective interaction in a given valence space was solved in the pioneering work of Brückner [Brüc55] by calculating the G-matrix needed to eliminate the strong repulsive core in the bare nucleon-nucleon potential. The modern developments in this field can give reasonable results [HJen95], when the number of the particles (holes) outside the inert core is relatively small. This method introduces a mass (A) dependence in the extracted TBME, thus requiring a new calculation for every new core nucleus.

Chapter 5 gives further details about the shell-model codes, valence spaces and interactions used for the theoretical calculations performed in order to interpret the experimental results. The interpretation of the Gamow-Teller decay of ^{100}In by employing a large-scale shell model calculation with a realistic interaction is a result from this thesis work (see Sect. 5.2.1).

The observable *energy* is the eigenvalue of the Schrödinger equation. Another result of the solution is the non-observable *wave function*, which can also be used to calculate other observables, such as *spectroscopic factors*, *electromagnetic* and *β-decay transition rates* and *static moments*. The shell model calculations are tuned to reproduce *binding energies and level schemes*, which can be achieved with different interactions and model spaces. Therefore, the corresponding wave functions will generally be different and consequently the observables calculated from them could differ a lot.

From the experimental point of view we have access to observables like γ-ray energy, half-life, time difference, reduced transition strength and multipolarity of an EM transition, spin, parity and static moments of a nuclear state, mass, charge, spin alignment, kinetic energy and momentum of a nucleus, coincidence relations ($\gamma\gamma$, αpnγ, $\beta\gamma$) of the particles emitted and registered in a nuclear reaction or decay process, etc.

Gamma rays are associated with high-energy EM transitions which have nuclear origin. They are usually emitted in the process of nuclear de-excitation. This means that if the nucleus is in an excited state it can emit a γ ray and decay to another nuclear state at lower energy. It is often said that these nuclear states are *connected*

via this γ-ray transition. The energy of the γ ray corresponds to the energy difference of the two excited nuclear states.

The γ-rays interact with matter in three ways. These are *Compton scattering* in which only part of the γ-ray energy is transferred to the matter, and electron-positron *pair production* and *photoeffect* in which the full energy of the γ ray is transferred to the matter. To register the energy and time of the radiation, specialized γ-ray detectors are made. The nature of interaction of the γ-ray radiation with matter explains the detector spectrum. The energy of the full absorption (i.e. photoeffect, pair production or Compton scattering with successive photoeffect of the scattered γ quantum) of the γ ray in the detector volume is called *photopeak* energy and corresponds to the total γ-ray energy. The detector output is an electric signal with a certain amplitude which corresponds to a certain γ-ray energy. Certainly the detector signal can be connected to a timing system and the time of detecting the γ ray could be measured with respect to a reference point in time. The time reference could be given by various sources, like the time signal of a beam pulsing system, or the time signal of another registered γ ray or particle or even the ion that has emitted the γ ray itself. Thus, the *time* of the γ event can be determined and for a number of events a time distribution can be built up.

The uncertainty principle defines the relation of the energy width and the lifetime of a nuclear state:

$$\hbar \sim \Gamma\tau \tag{1.7}$$

So the narrower the state is the longer the lifetime of this state is. In a certain nucleus the state lowest in energy is called the *ground* state and is usually the most stable one. However, there are also some excited states that live long enough to be detected and discriminated from the ground state. These states are called *isomers* or *metastable* states and often are marked by an ^{m} in the isotope notation, like ^{98m}Cd for example. These states are subject to great interest in the nuclear structure studies since they provide valuable information about the in-medium nucleon-nucleon interaction and on the other hand they can be studied in detail. Due to their metastability, it is easier to measure them separately or under a reduced level of contamination. The first property which could be measured is their lifetime. That is done by analyzing the decay of that isomeric state. The lifetime of a single isomeric state is determined when the time distribution of the measured decay radiation (α, β, γ) is fitted with an exponential function to satisfy the radioactivity law, which gives the number of the survived nuclei as a function of time:

$$N = N_0 e^{-t/\tau} \tag{1.8}$$

The half-life $T_{1/2}$ of such state is defined as the time for which $N = N_0/2$. That is $e^{-t/\tau} = 1/2$ or $t/\tau = \ln 2$ and:

$$T_{1/2} = \tau \ln 2 \tag{1.9}$$

Obviously one can talk about the probability of that process to happen, or about the *transition strength*. In the perturbation theory the transition strength is defined by Dirac's "golden rule" [Slav92]:

$$W_{fi} = \frac{2\pi}{\hbar}|\langle f|H_{INT}|i\rangle|^2 g(E_f) \tag{1.10}$$

where $g(E_f)$ is the density of the final states and H_{INT} is the operator of the time dependent interaction between the initial and the final states. For photons we can transform the above equation into [Slav92]:

$$W_{fi}(\lambda, kIm) = \frac{8\pi(I+1)}{\hbar I[(2I+1)!!]^2}\left(\frac{E_\gamma}{\hbar c}\right)^{2I+1}|\langle f|\hat{\boldsymbol{O}}(\lambda, kIm)|i\rangle|^2 \tag{1.11}$$

where $\hat{\boldsymbol{O}}(\lambda, kIm)$ is a generalized multipole transition operator and λ, k, I, m are quantum numbers. Usually the experimental transition strength is a sum over transitions to/from all m states which are degenerate and are resolvable only in experiments with polarized ensembles. Therefore we end up with a following expression for the total transition strength [Slav92]:

$$W_{fi}(\lambda I) = \frac{1}{2I_i+1}\sum_{m_f, m_i, m} W_{fi}(\lambda, kIm) \tag{1.12}$$

It is accepted to write the transition strength as follows [Slav92]:

$$W_{fi}(\lambda, kIm) = \frac{8\pi(I+1)}{\hbar I[(2I+1)!!]^2}\left(\frac{E_\gamma}{\hbar c}\right)^{2I+1} B(\lambda I, I_i \to I_f), \tag{1.13}$$

where

$$B(\lambda I, I_i \to I_f) = \frac{1}{2I_i+1}\sum_{m_f, m_i, m}|\langle f|\hat{\boldsymbol{O}}(\lambda, kIm)|i\rangle|^2 \tag{1.14}$$

is the so called *reduced transition strength*. These $B(\lambda I, I_i \to I_f)$ contain information about the wave functions of the nuclear states. For EM transitions these reduced transition strengths are noted by $B(EL)$ or $B(ML)$, where E stands for electric and M for magnetic transition, and the L is the multipolarity of the transition. Besides the natural units of $B(EL)[e^2 fm^{2L}]$ and $B(ML)[\mu_N^2 fm^{2L-2}]$, very often the so-called Weisskopf units [*W.u.*] are used. They are based on an estimate for the single-proton strength [Weis51, Brus77, Cast00] and defined as:

$$B_{W.u.}(EL) = \frac{1}{4\pi}\left(\frac{3}{L+3}\right)^2 R^{2L}e^2 \quad [e^2(fm)^{2L}] \tag{1.15}$$

and

$$B_{W.u.}(ML) = \frac{10}{\pi}\left(\frac{3}{L+3}\right)^2 R^{2L-2}\mu_N^2 \quad [\mu_N^2(fm)^{2L-2}] \tag{1.16}$$

where $R = 1.2 \cdot A^{-1/3}$ $[fm]$ is the nuclear mean radius, e – the elementary charge and μ_N – the nuclear magneton. These units give a basis for comparison of different transition strengths and a scale to discriminate the single-particle from the collective phenomena. They also give typical transition strengths and may be used to distinguish between E and M transitions for a given L.

Reduced transition strengths can be calculated assuming an EM interaction between the initial and the final states. On the other hand experimentally measured half-lives can be used to extract the reduced transition strengths, and then to compare and adjust the theoretical interaction. Therefore, measuring half-lives is a primary experimental goal.

When one knows the γ-ray transitions that connect some excited states with the ground state, one can build up a *level scheme* of the excited levels and their energies relative to the ground state. There is a special set of excited levels which is called the *yrast* line. This is the set of excited states with the lowest energy for a given spin. The term was initially introduced by Grover in [Grov67]. The *γ-ray multipolarity* is the angular momentum l that this γ-ray carries and this defines the change in spin from the initial to the final state that it connects. The study of the *γ-ray angular distribution* gives information on the γ-ray multipolarity. This is true, but to use it we need to know the spin orientation of the emitting nucleus and in most of the nuclear reactions this spin direction is difficult to be determined. In this respect, a very favorable case is the nuclear fusion-evaporation reaction (for details see Sect. 2.1.1). It has a feature that most of the produced excited nuclei have their spin perpendicular to the axis of the beam direction. This preferential spin orientation of the product nuclei is called *spin alignment*. This means that the γ-ray intensity distribution will be symmetric around the beam axis, but will exhibit the effects of γ-ray multipolarity when looking at the γ-ray intensities at different angles. By taking ratios of intensities at forward (backward) angles to the ones at $\sim 90^\circ$ one can deduce the character and the multipolarity of the γ-ray transition. Thus, by a comprehensive study of the γ-ray properties one could built up a level scheme starting from the ground state and assigning a defined spin and parity to each excited state that is being de-excited by the detected γ-ray. To this end the angular momentum coupling and γ-ray selection rules are exploited. For a given L the parity of the transition, as given by $(-)^L$ for electric (E) and $(-)^{L+1}$ for magnetic (M) transitions, has to be determined. This requires a measurement of the polarization of the emitted γ-ray, which is often replaced by arguing with typical strengths for a given L.

The experimental achievements in the nuclear γ spectroscopy have been quite

considerable so that nowadays the measurement of single γ rays is most often not sufficient for extracting new information on the nuclear properties. Therefore it has become a practice to use many detectors and not only measure γ-ray energies, times and angular distributions, but also $\gamma\gamma$-coincidence relations. The analysis of the data is greatly simplified by the information on $\gamma\gamma$ coincidences. They can help also in cleaning up the spectra from contaminants. In many cases one can use these relations to establish parallel branches in the level scheme of the excited states. The properties of the correlated γ rays can be sorted in various ways to have access to new information. This was the case in the current work when the detection time of γ rays with a certain energy was used as a start and the detection time of γ rays of another energy – as stop. This *time difference* produced a time distribution which is inaccessible to direct measurement, but which was used to estimate the half-life of a nuclear isomeric state (see Sect. 3.4.2).

When the studied nuclei are difficult to produce, *i.e.* with small production cross-sections, even multiple $\gamma\gamma$-coincidence relations are unable to clean the spectra. This is also the case when the nucleus of interest has a relatively small number of excited levels and therefore the γ *multiplicity* (the number of the emitted γ-rays in a single de-excitation cascade) is small. In such cases we need additional detectors to help in some way for discriminating γ rays originating from different nuclei. These detectors are often called *ancillary* or *auxiliary* detectors. They include detectors for light charged particles, detectors for neutrons and detectors for heavy ions (HI). The purpose of these ancillary detectors is to detect the particles that are correlated with the detection of the γ rays. Then by requiring a certain condition for the additionally measured particles one can select only that part of the γ rays that have been in relation with the imposed condition. In fusion-evaporation reactions it is very useful to detect α, protons and neutrons that are emitted in the evaporation phase of the reaction (see Sect. 2.1.1) and build up the correlations of the type αpnγ. In the β- or α-decay studies it is a routine to use correlations of the type $\beta\gamma$ and $\alpha\gamma$, correspondingly. Else, there would be a complete domination of the background for weakly populated reaction channels. The typical usage of the $\gamma\gamma$ or particle-γ coincidences is to set a *gate* on one of them and look at the spectrum of the other. The *gate* is simply a window/range, in the spectrum of one of the coincidence partners, used as a condition for the construction of the spectrum of the other partner. If the distribution of a single observable like the γ-ray energy is represented by a one-dimensional spectrum, then the representation of two observables in coincidence relations is a *coincidence matrix*. For the case of three and more observables in coincidence relation the representation is a coincidence *cube* in the corresponding three and larger dimensional space. Nowadays sorting and analyzing such matrices and cubes is widely used. This is also done in the present work with respect to the experimental data analysis and has been described in Chapter 3.

All these efforts are being done in order to be able to measure even more “exotic”

nuclei. In the last years it has become a fashion to study and talk about all kinds of "exotic" nuclei. There are many possible interpretations of this word and since this is a work that is also on "exotic" nuclei, in the following I will give some details on this topic.

1.2 Exotic nuclei

To understand what is exotic we have to define what is normal. First in the year 1896 the natural radioactivity was discovered by Bequerel. The radioactive material contained heavy elements like Thorium, Uranium, Polonium and Radium which have extremely long half-lives. In year 1902 this phenomenon was described with the radioactivity law by Rutherford and Soddy. Later, by using the natural α-particle beam sources from Polonium α decay and a target of natural Aluminum, I. Curie and P. Joliot studied the first artificially produced radioactive isotope ^{30}P. The *isotope* as defined in the beginning had the same chemical properties of a given element, but different atomic mass. As we would define them now, two nuclei are isotopes when they have equal number of protons and different number of neutrons.

The increasing number of isotopes brought the necessity of systematization which naturally appeared in the form of a table. The so called *table of isotopes* or the *Segré chart* is a chart presenting the nuclei in an XY plane. It has the neutron number N on the horizontal axis and the proton number Z on the vertical axis. Then the nuclei of the different elements and their isotopes are represented by squares each one at the proper number of N and Z.

Figure 1.2 shows this chart in one of its contemporary versions with some additional information. It is assumed, though not exactly known, that Emilio Segré invented the chart around 1935. Quoting from "A Mind Always in Motion: the Autobiography of Emilio Segré", 1993, Univ. of California Press:

> "Tables of natural radioactive isotopes go back to Curie, Rutherford and their colleagues. With the discovery of artificial radioactivity, they became much larger. A first one was drawn up in Rome by our group and by G. Fea. I drew a useful diagram, following Heisenberg, while still in Rome."

A quote from the proceedings of the CSEWG Symposium in 2001 [Hol01U] brings clarity to this issue:

> "A member of Fermis group, Emilio Segre, introduced a scheme for presenting data on all known nuclides in a chart form, where he represented the neutron number, N, in horizontal rows along the left side of the chart and the atomic number, Z, as vertical columns along the bottom

of the chart. A revised edition of Segre's Chart from May 15, 1945 was published with classified data omitted [Segr46]."

In the very first years of the nuclidic chart's introduction one could only see the black squares and the very close neighbours around them. These black squares represent the nuclei that are naturally abundant and are practically stable against any decay. These nuclei were available from the very beginning to be used in reactions and measure their properties.

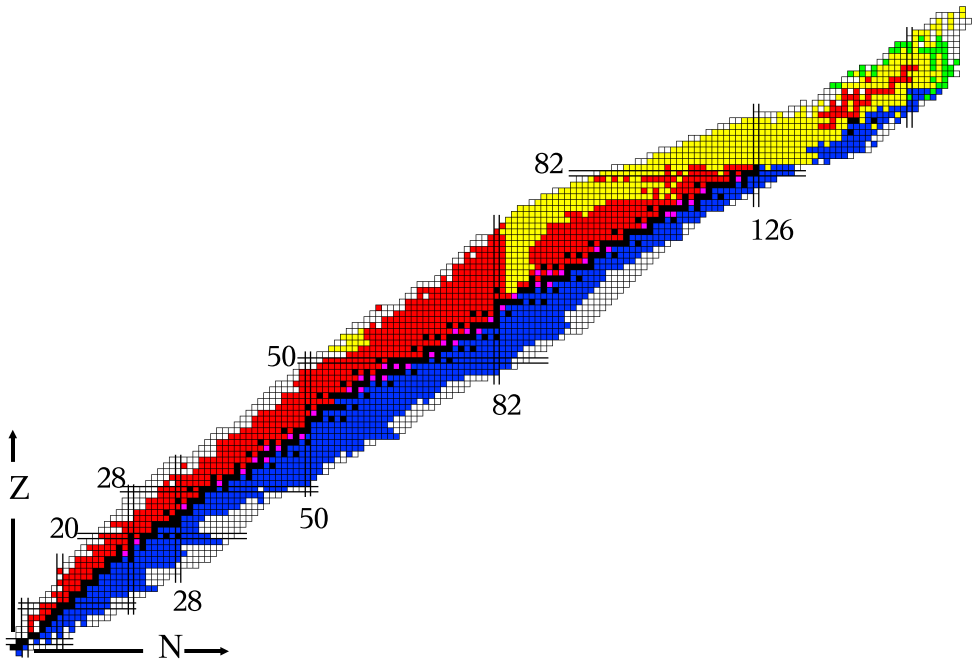

Figure 1.2: The chart of nuclides with some of the magic numbers noted.

The chart of nuclides gives a natural definition not only to the term isotope, but also to the terms *isotone* and *isobar*. The isotopes are nuclei with $Z = const$, that is every horizontal line in this chart defines a set of isotopes. The isotones are nuclei with $N = const$, which corresponds to the nuclei in a single vertical line of the chart. And finally, the isobars are nuclei that have equal mass, that is $A = const$, and since $A = Z + N$ this corresponds to diagonal lines such that the sum of Z and N is constant. The backbone of this chart are the stable nuclei (black squares) which form a kind of line and this line is called the *line of stability*. The other nuclei are subject to decay. It is the β decay, driven by the weak interaction, that determines the position and the form of the stability line. The empirical nuclear mass formula

of Bethe and Weizsäcker [Weiz35, Beth36] could show that if the nuclear mass is plotted as a function of Z, the masses of each set of isobars form a parabola with a minimum around the middle. The nuclei with masses in this minimum are stable against β decay, while the ones on the slopes do decay into the neighbours of smaller mass. The set of all isobaric mass parabolas looks like a valley with rising slopes on both sides. The stable nuclei are located in the valley and the β-unstable ones on the slopes.

Originally nuclei far from the line of β-stability [Pori64] were called exotic. Those nuclei are of a special interest due to their extreme composition of neutrons and protons. They are characterized by an unusual, compared to the stable ones of the same mass for a given region of nuclei, z component of the nuclear isospin defined as $T_z = (N-Z)/2$. The extremeness of isospin depends on the mass of the nucleus and the region of the nuclidic chart. While light nuclei with $N = Z$ are nearly stable, with increasing proton number in the nucleus, the stability line turns to direction of neutron rich nuclei. This is caused by the increasing Coulomb repulsion of protons in the nucleus, that has to be compensated by the strong nuclear force that binds protons and neutrons together. Hence, the heavier the nucleus is, the greater excess of neutrons in the system is needed for the nucleus to be stable. Already with a hundred nucleons and $T_z = 0$, the nucleus ^{100}Sn (*i.e.* $N = Z = 50$) lies on the proton dripline [Haus88, Doba94]. Higher mass nuclei with this value of T_z become unbound with respect to the proton decay. Similarly the T_z for the very neutron rich nuclei will be characterized by much larger value for heavier nuclei then for those of a small mass.

Now it is widely accepted to call a nucleus "exotic" whenever it is at a "limit". That means nuclei with high angular momentum, excitation energy, deformation, extreme Z value and, of course, the discussed case of extreme isospin.

High angular momentum is usually connected to the nuclei that exhibit collective structure, with rotational bands that become yrast at high spin. The spin value record ($\simeq 70\hbar$) in the system belongs definitely to nuclei in the superdeformed phase. In this range of excitation the nuclear shape is very exotic, where the prolate deformation reaches the value of $\beta \simeq 0.5$ (β is a parameter related to the ratio of the two semi-axes of the ellipsoid). Even higher spins and deformation are predicted to exist in the third nuclear potential minimum — the hyperdeformation phase of the nucleus. A superdeformed nucleus, being de-excited by γ rays, loses angular momentum and becomes usually only slightly deformed or almost spherical in the ground state. The nuclei with deformed shapes lie generally in the regions between the closed shell nuclei.

The island of superheavy elements (SHE) is the possibly existing region of nuclei that is supposed to show an evidence of predicted shell closures and doubly-magic nuclei. So far there are many controversial calculations on the highest magic numbers. The experimental data there are still scarce, but there is certainly progress

going on. It is only recently that spherical SHE have become accessible, the known ones lie in the deformed region and therefore give only indirect evidence for spherical shell gaps.

All known or predicted doubly-magic nuclei gain a lot of interest when these nuclei are close to proton or neutron dripline, since for those nuclei the binding energy per nucleon is expected to be larger than for the neighbouring ones. This is called the shell closure effect and is a basic signature of the nuclear shell model.

The aim of these kind of studies is to examine the nucleus in its extreme conditions, where some specific features of the nuclear structure are largely enhanced with respect to the situation when the nucleus is not excited and/or is close to the stability valley. This provides a stringent test and necessary parameters for the nuclear structure models, which often are formulated and parameterized according to information obtained from less exotic nuclei. The doubly closed shell nucleus ^{100}Sn, the nuclei in the region around it and their properties are of great importance for understanding nuclear structure. The following section gives an overview of the specific nuclear-structure phenomena in that region.

1.3 The region of ^{100}Sn

Atomic nuclei near $^{100}_{50}\mathrm{Sn}_{50}$ play a special and important role in the study of exotic nuclei, since they exhibit several exceptionally interesting nuclear-structure phenomena, *i.e.*

- the double shell-closure N=Z=50 with an *ls*-open core giving rise to strong spin-flip $g_{9/2}^{-1}g_{7/2}$ and stretched $\Delta l = 2$ $g_{9/2}^{-1}d_{5/2}$ core-excitations,
- the isospin symmetry (N≅Z), which relates to questions concerning proton-neutron pairing and isospin mixing,
- the neighbourhood of the proton drip-line,
- fast Gamow-Teller (GT) β-decays of the type $\pi g_{9/2} \rightarrow \nu g_{7/2}$ ("southeast" of ^{100}Sn) and/or $\pi g_{9/2} \rightarrow \nu g_{9/2}$ ("southwest" of ^{100}Sn),
- the occurrence of an island of α, proton and maybe even cluster radioactivity,
- the astrophysical *rp*-process is supposed to end in the neighbourhood of ^{100}Sn [Scha98].

The study of these very neutron-deficient isotopes has attracted considerable interest recently, in particular since the doubly closed-shell nucleus ^{100}Sn and some of its neighbouring isotopes have been identified [Schn94, Lewi94]. The present experimental status on decay properties of Z≅N nuclei in the Palladium-to-Tellurium

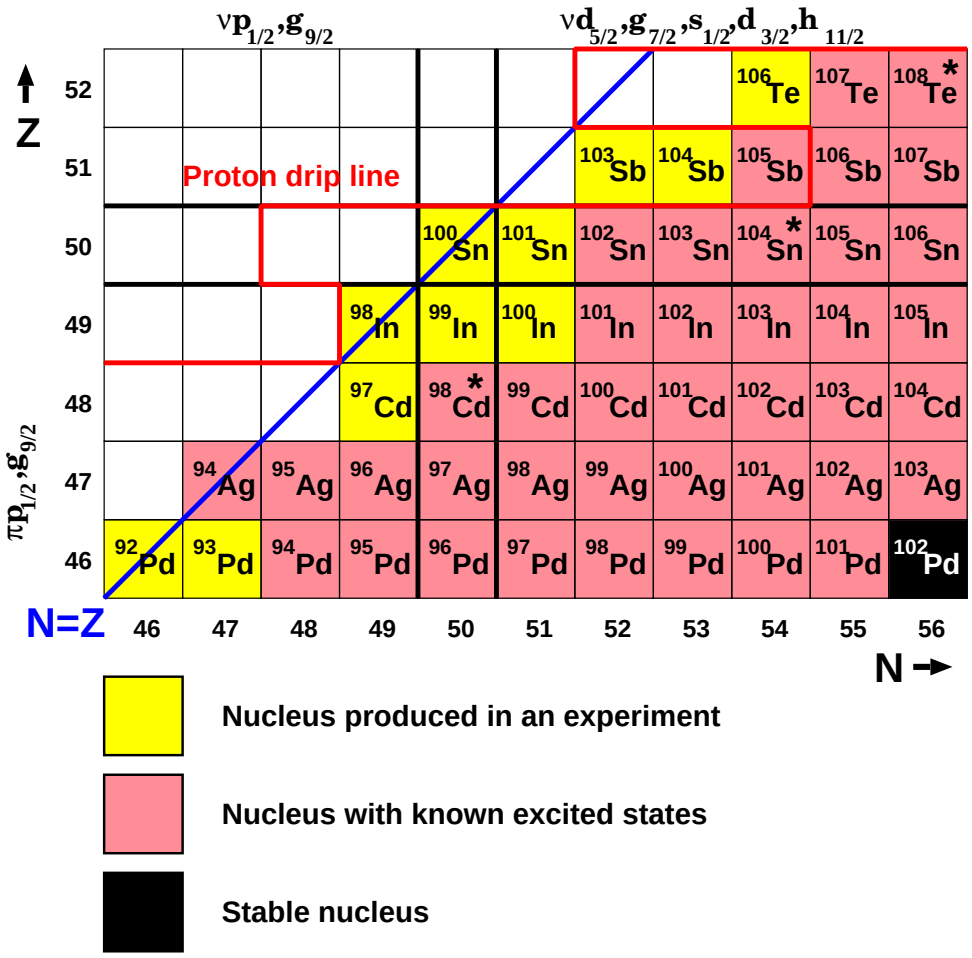

Figure 1.3: Section of the chart of nuclides showing the region around ^{100}Sn and the knowledge status. For some of these nuclei the decay properties were studied and for some in-beam spectroscopy was performed. The stars show some of the most often used compound nuclei to access this region via fusion-evaporation reactions.

region, displayed in Fig. 1.3, is based almost exclusively on measurements performed by using beam-line spectrometers or isotope separator on-line (ISOL).

The experimental progress in this field includes the measurement of the mass of ^{100}Sn and ^{100}In [Char96], the in-beam spectroscopy of ^{99}Cd [Lipo02], ^{102,103}Sn [Lipo96, Fahl01] and ^{98}Cd [Górs97, Grzy98, Blaz04], the β-decay studies of ^{94}Ag [SchK94, LaCo02, Plet04, Mukh04], ^{95}Ag [Doer03], $^{100-104}$In [Plet02, Gier03, Szer95, Szer97, Karn98], ^{101}Sn [Jana95], ^{102,104}Sn [Karn04, Stol01], ^{103,105}Sn [Kava04], and the observation of proton radioactivity for ^{112}Cs [Page94] and for ^{105}Sb [Tigh94], the latter of which is questionable according to the recent investigations [Shib97, Liu04]. Some other experiments performed recently and still being analyzed are the decay

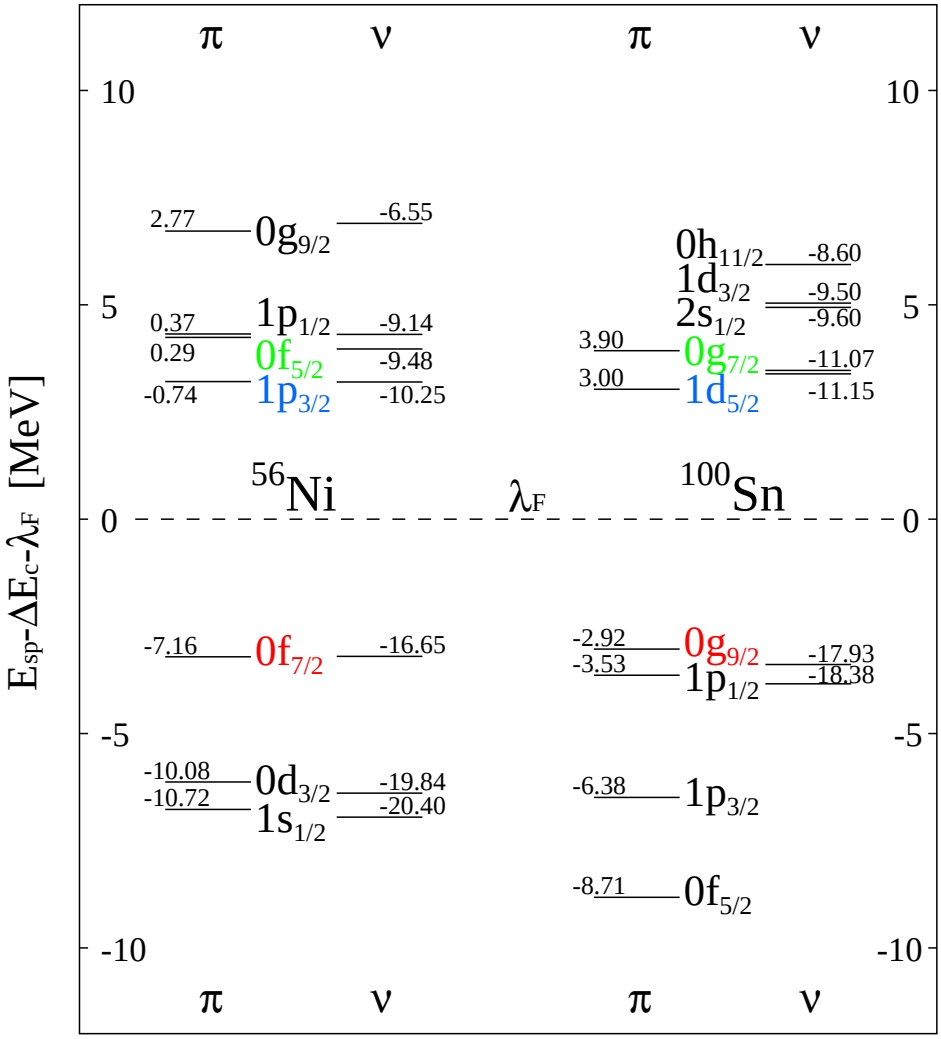

Figure 1.4: Energies of single-particle orbits for the doubly-magic nuclei ^{56}Ni and ^{100}Sn, obtained either from experiments or from "shell-model extrapolation" [Graw01a]. Both nuclei ^{56}Ni and ^{100}Sn are *ls*-open cores. The levels are drawn subtracting the Coulomb repulsion and normalized to the middle of the shell gap. The energies are given in MeV.

study of light Sn and Sb isotopes, including attempts for ^{100}Sn at the GSI-ISOL facility and an in-beam spectroscopy of ^{100}In at the EUROBALL IV multi-detector gamma array.

The proton and neutron orbits relevant to the structure of nuclei in the ^{100}Sn region are given in Fig. 1.4. According to the knowledge [Graw95, Graw01a] prior to this work, the $N = 50$ and $Z = 50$ gaps amount to 6.8 and 5.9 MeV, respectively.

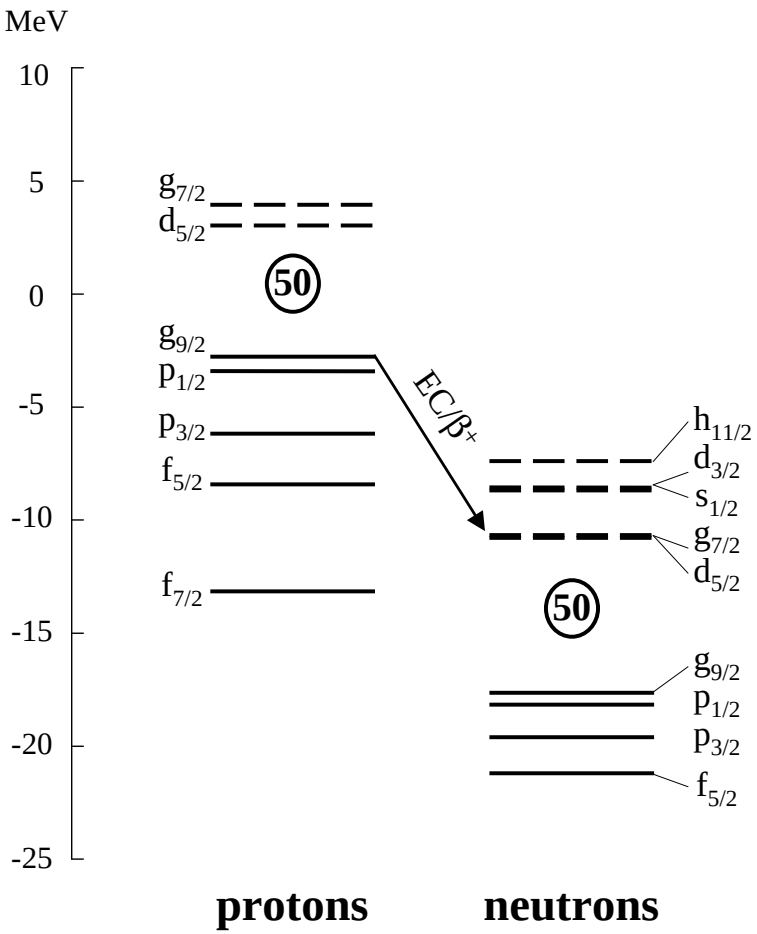

Figure 1.5: The single-particle orbitals that are active in the region of the doubly-magic nucleus ^{100}Sn in their native scale and approximate position. The arrow shows the GT β-transition $\pi g_{9/2} \rightarrow \nu g_{7/2}$ occurring in the ^{100}Sn region.

As a result of this work a new more precise estimate for the $N = 50$ shell gap of 6.46(15) MeV is given [Blaz04]. While filling the $0g_{9/2}$ level with protons, one follows the elements from niobium (Z=41) to tin (Z=50). Neutron orbitals $1d_{5/2}$ and $0g_{7/2}$ are getting occupied when crossing the N=50 line. They are energetically quite close to each other, almost degenerated, according to the present understanding of the nuclear structure in this region [Skou93, Brow94, Graw95, Graw01a].

The unique nuclear structure features of nuclei in the region below ^{100}Sn make β decay interesting, as it is characterized by a fast $\pi g_{9/2} \rightarrow \nu g_{7/2}$ Gamow-Teller (GT) transition (see Fig. 1.5). Within the extreme single-particle shell model, such a transition involves protons in the (partially filled) $g_{9/2}$ orbital, with the corresponding GT partner shell $\nu g_{7/2}$ being completely empty. This model predicts the total GT

strength, summed over the entire Q_{EC} value, ($\Sigma B(GT)$), to be

$$\Sigma B(GT) = \frac{N_{9/2}}{10}(1 - \frac{N_{7/2}}{8})B_0(GT) \tag{1.17}$$

where $N_{9/2}$ denotes the number of protons filling the $g_{9/2}$ orbital, $N_{7/2}$ the corresponding value for the $g_{7/2}$ orbital, and $B_0(GT) = \frac{(2j_>+1)4l}{(2l+1)} = \frac{160}{9} = 17.78$ the $\Sigma B(GT)$ value of ^{100}Sn. However, the $\Sigma B(GT)$ values obtained from experiments are significantly smaller than those from theoretical predictions. This "hindrance" or "quenching" of GT transitions can be expressed as the ratio between the theoretically and experimentally determined GT strengths. In this work, the GT hindrance factor h is used with reference to the extreme single-particle shell model. The h values for the $N = 50$ even-even nuclei ^{96}Pd and ^{98}Cd are 4.6(2) [Ryka85] and 4.1(9) [Ploc92], respectively, according to the experimental B(GT) values deduced from β-decay studies.

In an attempt to explain the observed GT hindrance, Towner [Town85] has taken the contributions from pairing correlations, core polarization and higher-order effects into account. As we will further discuss (see Sect. 6.1), the core-polarization and higher-order effects are both large and together can account for most of the observed hindrance. However, one probably needs correlations between the $0g_{9/2}$ and $0g_{7/2}$ orbitals which go beyond the core-polarization model, such as those incorporated in the recent Monte-Carlo shell-model calculations [Koon97], in order to fully account for the observed hindrance.

The GT strength can be experimentally determined by measuring β-delayed particles and γ rays. The EM radiation is normally measured with high-resolution germanium detectors. However, in the cases of odd-even and odd-odd nuclei with high Q_{EC} values, it is expected that a significant part of the total β-decay strength is distributed over many daughter states at large excitation energy, where the level density is very high. Since the β feeding to individual levels is often very weak, and moreover the γ de-excitation might proceed through several partly parallel cascades, standard high resolution γ-γ spectroscopy is generally insufficient to determine the complete GT-strength distribution due to its limited detection sensitivity.

Alternatively, the β strength can be obtained from total-absorption spectrometry by using 4π detectors. A highly advanced version of a total-absorption spectrometer (TAS) (see Sect. 4.1.3) has been installed at the mass separator on-line to the heavy-ion accelerator UNILAC of GSI [Karn97] for studying the β decay of nuclei around the doubly-magic nucleus ^{100}Sn.

Since the TAS technique is based on recording cascades of β-delayed γ rays, and the energy resolution of NaI detectors is poor compared with germanium detectors, the evaluation of TAS data depends strongly on the knowledge of the response function of the TAS spectrometer for each particular cascade. The information required to obtain the response function concerns excited levels and their de-excitation pat-

tern, which can be determined from high-resolution experiments. Thus, the "double strategy" of combining high- and low-resolution β-delayed γ-decay studies provides a tool to map the GT-strength distribution to high excitation energies in the daughter nucleus.

A major goal of γ-ray spectroscopy along the $N = Z$ line is to study ^{100}Sn, the heaviest self-conjugate doubly magic nucleus which can exist. The single particle energies and residual interactions with respect to the ^{100}Sn core can be deduced directly from properties of excited states of ^{101}Sn(νp), ^{99}In(πh), ^{98}Cd($\pi h - \pi h$), ^{100}In($\pi h - \nu p$) and ^{102}Sn($\nu p - \nu p$) which have one or two nucleons outside the ^{100}Sn core. Spectroscopy of ^{100}Sn, although still a distant goal, would reveal the properties of the core itself.

The main reaction mechanism used to access the region of the ^{100}Sn is the fusion-evaporation reaction. The fusion of two light stable nuclei produces a compound nucleus that is close to $N = Z$ line and is on the proton-rich side of the beta-stability line. Typical heavy ion reactions used in experiments to study this region are ^{46}Ti+^{58}Ni $\rightarrow$ ^{104}Sn*, ^{50}Cr+^{58}Ni $\rightarrow$ ^{108}Te* and ^{40}Ca+^{58}Ni $\rightarrow$ ^{98}Cd*. Certainly, the fragmentation and in-flight separation/identification is the other major technique to produce nuclei from the region of ^{100}Sn. Often this is done by fragmenting ^{124}Xe, ^{112}Sn or ^{106}Cd isotopes.

In-beam γ-ray experiments in the ^{100}Sn region require both high γ-ray detection efficiency and ancillary detectors providing excellent reaction channel selection. Relatively small Ge-detector arrays such as OSIRIS [Lied84] at the Hahn-Meitner Institute in Berlin or NORDBALL [Hers85] at the Niels Bohr Institute in Denmark combined with charged particle detectors and neutron detectors already proved to be very powerful tools for in-beam studies in this region. The further progress into even weaker channels, at the microbarn level and beyond, required the high efficiency of multidetector γ-ray arrays like GASP [Ross93], EUROBALL [Simp97] and Gammasphere [Lee90] combined with an improved exit channel selection.

The most promising way of enhancing exit channel selection from the contemporary point of view appears to be the addition of ancillary detectors to the multidetector gamma array. In the case of EUROBALL these are the NEUTRON WALL array [Skep99], the EUCLIDES array [Farn97], the DIAMANT detector [Sche97], the PYRAMID PPAC array [Gerl98], the SAPhIR detector [Thei98], the Recoil Filter Detector for EUROBALL [Spoh95]. The list of analogous devices for Gammasphere contains the MICROBALL array [Sara96], the Fragment Mass Analyzer (FMA) [Davi89], the Neutron Shell [Sara04], the CHICO detector [Simo00]. Part of this thesis work is the analysis of data from a EUROBALL IV plus Neutron Wall, EUCLIDES and a delayed gamma set-up experiment. Therefore, details of the multidetector spectrometer as well of the used ancillary arrays are given in Sect. 2.4.

Chapter 2

Experimental Techniques

2.1 Nuclear reactions used to access the region of ^{100}Sn

Two reaction mechanisms are used to access the very neutron deficient nuclei in the region of the doubly magic ^{100}Sn. The traditional and most employed one is the fusion-evaporation reaction mechanism. Along with it in the last years the projectile fragmentation has been used in many pioneering experiments.

2.1.1 The fusion-evaporation reaction

In 1936 Niels Bohr came up with the idea that when bombarding a target with a light particle, a *compound nucleus* [Bohr36] in a highly excited state is produced, and it decays purely statistically and independently on the entry channel. When a heavy ion is used, additionally a large angular momentum is transferred to the compound nucleus. A considerable amount of its excitation energy is released by *evaporating* (emitting) particles. Most often these are neutrons, protons and α particles. The process of neutron evaporation brings the nucleus into bound states with energy up to 10 MeV above the yrast line. To remind, the *yrast* line is the set of the excited states with the lowest energy for a given spin. After reaching the yrast line, the de-excitation would follow it by a cascade of γ rays typically ending at the ground state of the nucleus (see Fig. 2.1).

Depending on the impact parameter of the bombarding ion the reaction follows different patterns. At very large values of the impact parameter one observes quasi-elastic scattering. If the impact parameter is small enough, it is possible to transfer considerable energy and momentum to the internal nucleons and observe a *deep-inelastic collision*. At even smaller impact parameters the bombarding and the target nuclei can fuse. Then the whole kinetic energy of the impinging nucleus is

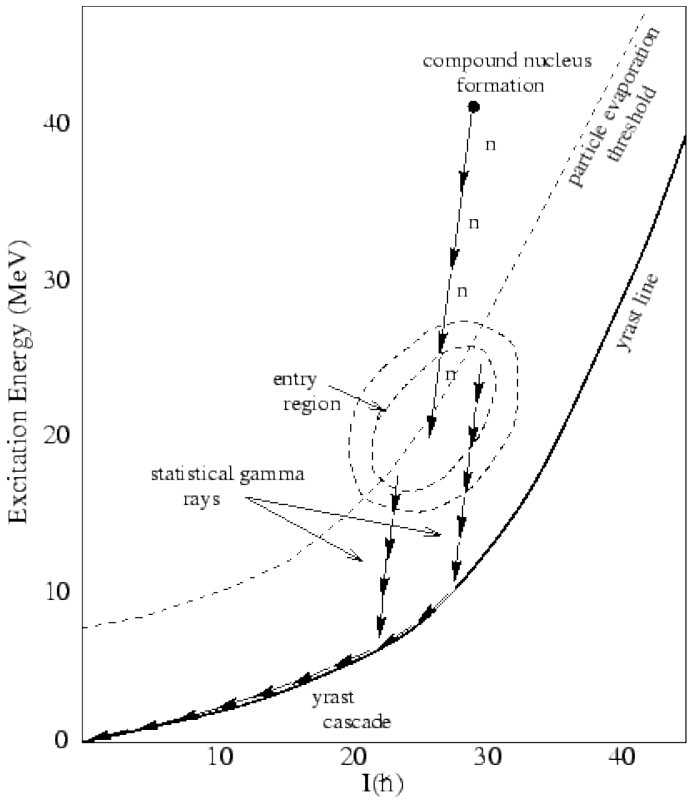

Figure 2.1: A schematic representation of the fusion-evaporation reaction mechanism.

used to introduce high angular momentum and excite the compound system. If the fission barrier of the compound nucleus is small then fission will follow. The population of high angular momentum is much higher in the fusion-evaporation reaction than in all other reactions: deep-inelastic, quasi-elastic and fission. This is what makes fusion-evaporation the preferred reaction to study high-spin nuclear structure. Generally speaking, the heavier the bombarding ion is, the higher the angular momentum of the compound nucleus will be. The angular momentum of the system is limited only by the fission process. Figure 2.2 shows the simulated cross section for producing the compound nucleus ^{104}Sn* with a certain angular momentum in the reaction ^{58}Ni(215MeV) + ^{46}Ti. The simulation was done with the fusion-evaporation Monte-Carlo code PACE4 [Tara03]. This distribution shows clearly that in the reaction used in the ^{98}Cd experiment (part of this work), the residual nuclei are produced with high spins. This spin distribution will be compared with the one resulting in the fragmentation reaction (see Sect. 2.1.2).

The decay of the compound nucleus is described by the statistical nuclear reaction model introduced by Weisskopf and Ericson [Weis52]. This model assumes that the decay of each state is independent on its creation and it follows one of the open

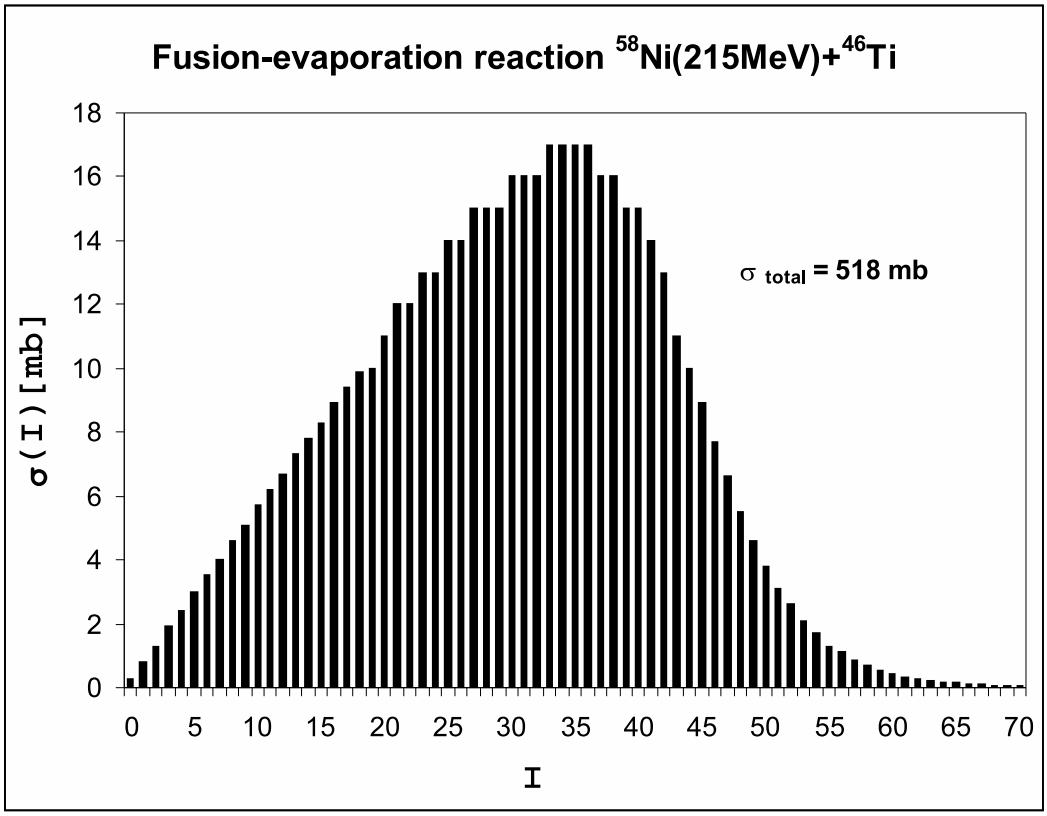

Figure 2.2: The partial cross section as a function of the populated spin in the compound nucleus in the fusion-evaporation reaction ^{58}Ni(215MeV) + ^{46}Ti $\rightarrow$ ^{104}Sn* simulated with the fusion-evaporation Monte-Carlo code PACE4 [Tara03].

decay channels. The decay probability is defined only by the width of the channel. Open channels for the fusion reaction are fission, evaporation of neutrons, protons, α-particles and excitation of giant nuclear resonances. The γ-ray de-excitation proceeds in two steps. The first step is the emission of statistical γ rays which de-excite the nucleus with little change in the angular momentum. And the second step are cascades of γ rays which connect states from the yrast line or parallel to the yrast line. The latter are mainly of $M1$ and $E2$ character and reduce the energy and the angular momentum of the nucleus. Several systematic studies support the idea that the statistical γ rays are not connected to any structure, but only to the temperature of the nucleus, while the yrast-like γ rays at low energies form a distribution that depends the nuclear structure of the specific system [Hill79, Dele78].

It should be pointed out that the main disadvantage at present of the fusion-evaporation method is the impossibility to populate neutron-rich nuclei. So far only stable isotopes were used for the beam and the target. The line of stability

is bending toward the neutron rich isotopes with increasing mass number. The consequence of this is that the compound nucleus is always on the proton rich side of the of the β-stability line. The limiting case is populating nuclei close to the line of β stability. On the other hand when approaching in heavy proton-rich systems nuclei with large fissility parameter (Z^2/A), the fast fission of the compound nucleus becomes the dominating process. Certainly, the usage of radioactive beams would open possibilities for other studies, e.g. spectroscopy of neutron-rich nuclei. The prospects of using radioactive targets, up to now, are very limited and subject to strict safety regulations. Besides the radioactive ion beams, the nuclear fission opens a wide possibility to populate neutron-rich nuclei.

2.1.2 The fragmentation reaction

Another mechanism to produce exotic nuclei is the projectile fragmentation. The reaction mechanism can be understood by a two step model [Rein94]. The first step is the collision phase, which is described as the overlap of the projectile and the target nuclei. In the simple "Abrasion-Ablation" model [Gaim91] the loss of mass of the projectile has a pure geometrical explanation. Since the projectile velocity is higher than the velocity of the nucleons at the Fermi-surface, then the nucleons outside the collision zone will preserve their intrinsic velocities and original direction even after the collision, and thus form an excited prefragment. A realistic description is obtained when looking at the individual nucleon-nucleon collisions in a intranuclear cascade model [Yari79]. In the second stage of the reaction, the de-excitation phase, the prefragment is being de-excited via emission of light particles (p, n, α) and γ rays. Neutrons are the most emitted particles, since they have no Coulomb barrier. This makes the distribution of the produced isotopes to lie on the proton-rich side of the valley of stability. If the projectile energy is considerably higher that the Fermi energy ($\sim$ 40 MeV·A), then the production cross-sections are independent of the beam energy. The isobaric distribution of the produced fragments has a Gaussian shape with a steeper slope on the neutron deficient side. For fragments with small loss of mass ($< 15\%$), the centroid of the isotope distribution lies close to the projectile [Sümm00]. Additionally the position of the distribution depends on the neutron excess of the projectile relative to the β-stability line. Based on this "memory" effect, the production of neutron deficient fragments is easier starting with a neutron deficient projectile.

In an experiment at GANIL a beam of ^{106}Cd at 66.5 MeV·A was fragmented on a ^{nat}Ni target. One of the final fragments that were studied was the nucleus ^{98}Cd. It is produced after the removal of 8 neutrons from the projectile. On the basis of the measured γ rays it was inferred that in this fragmentation the nucleus is populated up to spin $I = 8$. The question whether and with what probability

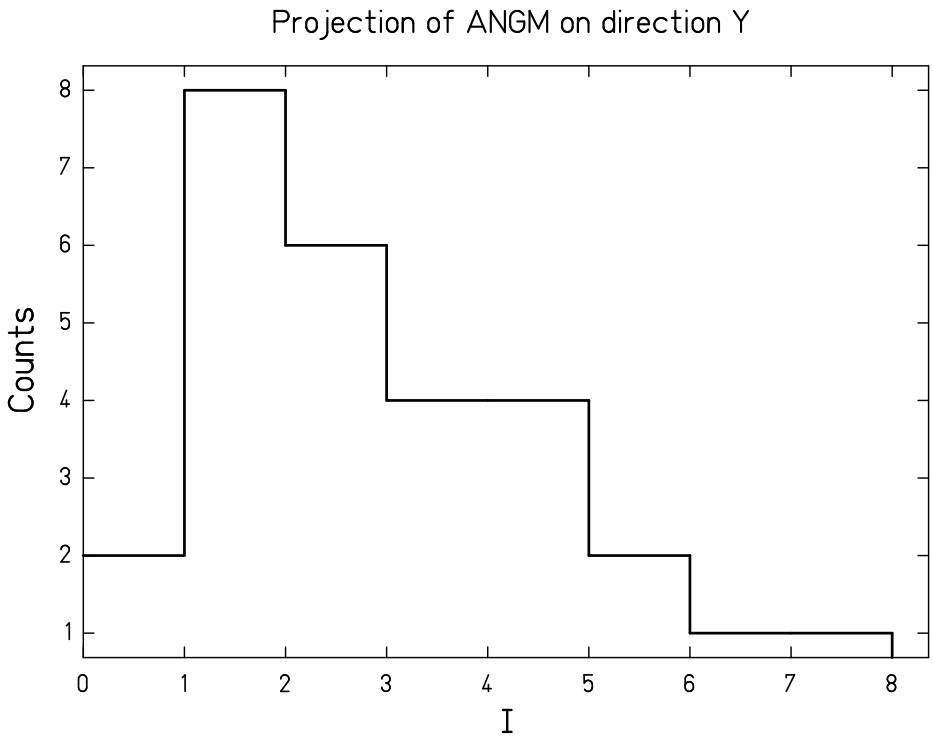

Figure 2.3: The spin distribution of the produced ^{98}Cd nuclei in the fragmentation of ^{106}Cd at 66.5 MeV·A on a ^{nat}Ni target, as simulated [YordPC] by the fragmentation Monte-Carlo code "ABRABLA" [Gaim91].

higher spins are populated in that reaction is a very important one. On my request, in order to better understand the spin population in the specific reaction, Dr. Orlin Yordanov has simulated the above reaction with the Monte Carlo fragmentation code "ABRABLA" [Gaim91]. The code is optimized for higher energies of the incident projectile of about 400 – 1000 MeV·A, which are typically used in experiments at the GSI FRagment Separator (FRS). Therefore, the calculation shown on Fig. 2.3 gives the spin distribution of the produced ^{98}Cd only qualitatively [YordPC]. Even if we know from the experiment that spin $I = 8$ is populated, the shape and the centroid of the spin distribution, shown on Fig. 2.3, tell us that in this fragmentation reaction the population of low spins is preferred and the cross-section for ^{98}Cd nuclei produced with any spin higher than 8 is steeply decreasing. Even if only qualitative this is a very important difference to the case of fusion-evaporation reaction where nuclei with predominantly high spins are produced.

Examples of other fragmentation reactions and the experimental techniques for fragment separation and identification are given in the Sect. 2.3.

2.2 The isotope separator on-line (ISOL) method

2.2.1 Ion source at the GSI-ISOL facility

The isotope separator on-line (ISOL) is an instrument to select specific reaction products out of the bulk of products formed in fusion, fission, or multi-nucleon transfer reactions. A sketch of the ISOL facility at GSI is shown in Fig. 2.4.

The products are stopped in a hot catcher inside the separator ion source, from which they are released via solid-state diffusion and surface desorption. A fraction of the particles is re-ionized to charge-state 1^+, accelerated to typically 55 keV, and separated unambiguously according to atomic number A in a magnetic sector field; in favourable cases an additional separation according to element number Z may be

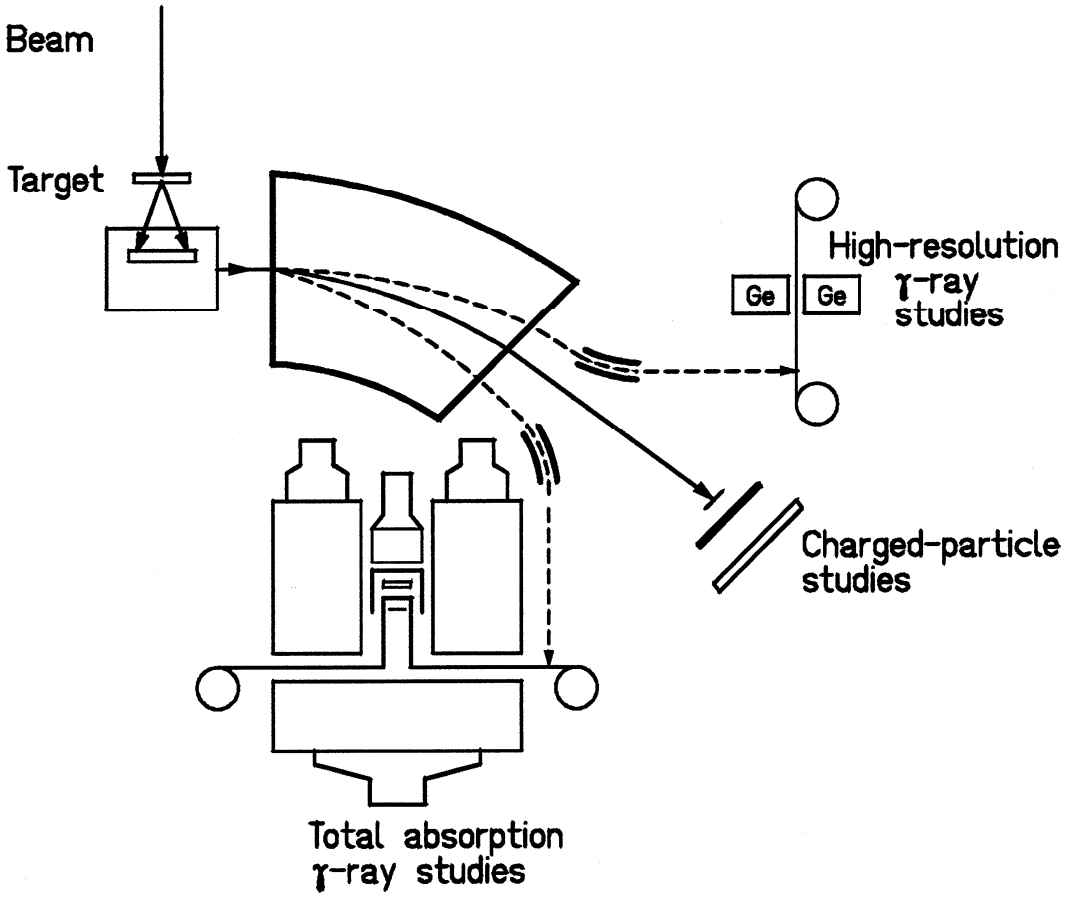

Figure 2.4: Sketch of the ISOL method used at GSI. (from [Hu98b])

reached by catcher/ion-source techniques. Several of these separated beams may be investigated simultaneously: either in the focal-plane chamber or in the three subsequent beamlines. The monoenergetic beams as such may be subject of investigation or, alternatively, the products may be implanted into fixed or moving tape collectors to give thin point-like sources for decay spectroscopy. Various detector set-ups for β-particle, γ-ray, X-ray, conversion-electron, or charged-particle spectroscopy are available to be used either at the irradiation positions or in the counting positions of tape stations. The tape stations as shown on Fig. 2.4 are used for collection the mass-separated beam to measure the activity of interest and after a predefined period of time to quickly remove the point-like source where the activity from the long-lived isobars (usually not interesting for the experiment) starts to dominate. A description of the most recent developments at the ISOL facility at GSI Darmstadt is given in Ref. [Roec03].

There are three main modes of measurement synchronized with the tape station operation. The first one is the so-called *decay* mode. In the decay mode the activity is collected outside the detector, then quickly transported to the measurement position and after the measurement time is over, the active spot of the tape is again quickly transported away, to suppress the unwanted activity. It is very common while measuring the first implanted sample, to continue collection of the second one, so that after the next transport of the system there is a radioactive sample to continue the next measurement cycle. This method is good for half-life determination, but requires enough mass-separated beam intensity to collect a good radioactive sample for each measurement cycle. The second mode of measurement is the *grow-in* mode. This means the activity is measured, while being implanted and so the total activity is growing up to the saturation limit, when the new implanted activity equals to the decayed one. After the predefined measurement time, the sample is removed and a new clean peace of the collection/transport tape is moved to the collection spot. This mode is very good and necessary when the mass-separated beam intensity is low since it utilizes all of it. The half-life measurements, though, could be subject to systematic errors. The third mode of operation combines both above mentioned and is therefore called *grow-in-and-decay*. The measurement starts together with the collection of the source (the grow-in phase), then the collection is stopped and the measurement continued (the decay phase), after the time is over, the cycle is repeated. For all modes the times for collection and measurement can be optimized for the beam intensity, the detector set-up and the expected half-life of the isotope of interest. For example, the total-absorption spectrometer (see Sect. 4.1.3) is operated only in decay mode, and all the cycle optimization should be done for decay mode.

With respect to extraction, acceleration, magnetic deflection, and beam handing as a whole, this facility has essentially remained unchanged since the first on-line experiments performed about thirty years ago till the end of its operation in January 2004. The ion source and the collector/detector arrays, however, have been improved

continuously during this period.

The most important part of any ISOL facility is the target/ion source system, and there is a continuing effort to increase the release efficiency and to improve the chemical selectivity [Kirc96]. An important technique for determining these parameters has been extensively applied at GSI. This method consists in implanting stable-isotope beams from the UNILAC into the catcher positioned inside the ion source and measuring the release-time profile for this isotope [Kirc92].

The Forced Electron Beam Induced Arc Discharge (FEBIAD) ion source [Kirc92] in its normal operation mode is used in cases in which the distribution of fusion-evaporation cross-sections and/or the choice of catcher material guarantees sufficient chemical selectivity. The heaviest $N = Z$ odd-odd nucleus, ^{94}Ag, was identified [SchK94] and studied extensively [LaCo02, Plet04, Mukh04] and the prerequisite for the success of these experiments is the high release ion-source efficiency of 42% even for the short-lived $T_{1/2} = 0.39(4)s$ $I^{\pi} = (21^{+})$ isomer [Mukh04].

In cases where the FEBIAD source in normal or bunching mode [Kirc92] does not result in sufficient chemical purity of the mass-separated beams, the thermal ion source (TIS) [Kirc90] offers an alternative for elements of low ionization potential. This solution was chosen in the experiment to study the β decay of ^{100}In, the heaviest odd-odd, $T_Z = 1$ nucleus with known decay properties [Szer95, Plet02]. The shell-model calculations for the theoretical interpretation of this GT decay are part of this work (see Sects. 5.2 and 6.1 for details). The nucleus of interest ^{100}In was produced via the ^{50}Cr(^{58}Ni,αp3n) reaction. A ^{58}Ni beam of 6.20 A·MeV was delivered by the UNILAC accelerator of GSI Darmstadt. The beam impinged on a 96.9% enriched ^{50}Cr target of 3.5 mg/cm^2 thickness, backed by a molybdenum foil of 2 mg/cm^2 thickness. The reaction recoils were stopped inside a catcher of a thermal ion source. The indium has a lower ionization potential than the anticipated contaminants, silver and cadmium. Therefore, the suppression of the isobaric silver and cadmium contaminants was achieved by choosing an ionization potential that was above the one of the indium, but below that of the silver and cadmium isotopes. After ionization and extraction from the ion source, the mass-separated beam was directed to the high-resolution and to the total-absorption set-ups.

It is worth mentioning that other solutions for reducing the isobaric background in ISOL experiments could be the laser ion source [Mish93] or the extraction from the sources of molecular ions instead of atomic ions, which was described so far. The fluorination ion source [Kirc97] combines high release efficiency with very efficient suppression of cesium and other contaminants. It was applied to separate and identify ^{114}Ba, the heaviest known $T_Z = 2$ nucleus, and to measure the decay properties of this and neighbouring barium isotopes [Gugl95, Jana97]. The most recent and exciting molecular ion technique is the sulphurization [Kirc03], which permitted a powerful on-line chemical separation of tin from isobaric indium, cadmium, silver and palladium isotopes.

2.2.2 Total-absorption spectrometer (TAS)

The total γ-ray absorption technique is a powerful tool for the study of nuclear states with large excitation energies. It is specially useful in the investigation of those nuclei where the spacing between excited levels becomes so small that a statistical description of the nucleus becomes appropriate. Correspondingly, the total-absorption method is adequate for the study of β-decay very far from the β-stability line, where the decay energy windows are large and high-lying states in the daughter nucleus can thus be fed.

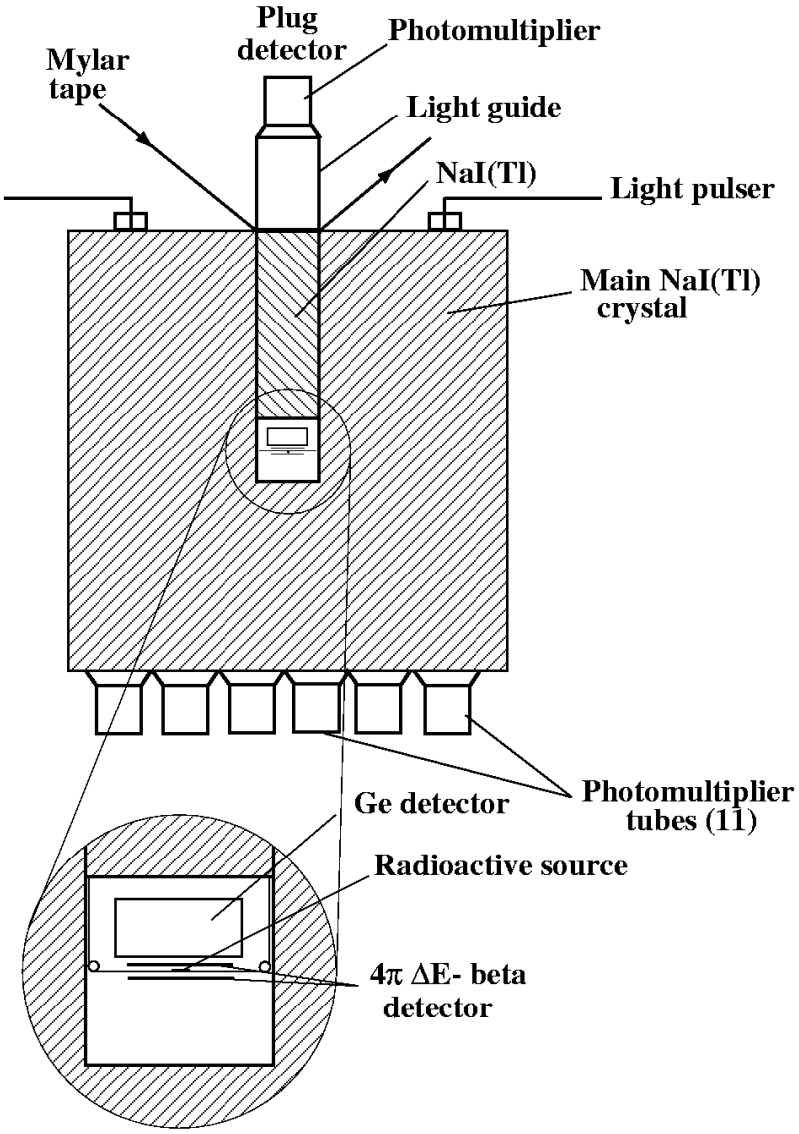

Figure 2.5: A schematic view of the total-absorption spectrometer. (from [Hu98b])

After the shut-down of the SuperHILAC at LBL Berkeley, the total-absorption spectrometer (TAS), constructed there, was moved to the GSI on-line mass separator. A schematic view of the TAS is shown in Fig. 2.5. As it was mentioned before (Sect. 2.2) that TAS allows operation only in decay mode, which means a limitation for short half-lives due to transport times and only ∼50% utilization of the ISOL beam. Altogether these imply a limitation for measurements with low yields.

A special platform was built above the mass separator where the entire set-up was placed. The mass separated beam is deflected by 90° by means of an electrostatic mirror, refocused by electrostatic lenses and implanted on a transportation tape which moves the radioactive sample via differential pumping stages to the measurement point within 0.5 s. At this position the sample is viewed by a ΔE detector for electrons and positrons comprised of two 0.5 mm thick silicon wafers. Above the top wafer a high-purity germanium X-ray detector (10 mm thick) is installed for registering characteristic X-rays following electron capture (EC) decay. Together with the top silicon wafer it can also serve as a β telescope for electrons up to 9 MeV energy. All detectors are contained in the 5.1 cm long and 5.1 cm diameter cavity in the center of large NaI(Tl) crystal. The well is closed off by a 15.2 cm long and 5.1 cm diameter "plug" detector. Further on in the text, the top and bottom Si detectors are often called BOT Si or TOP Si, while the small HpGe X-ray detector is nicknamed GeX. Similarly the TAS spectra which are produced by a condition on some of the other detectors have notations of the type TAS(BOT). For instance, TAS(β^+) is a TAS spectrum with a condition on the positron spectrum registered in TOP and BOT detectors, while TAS(EC) is a TAS spectrum gated on some X-ray transition visible in the GeX spectrum.

The detailed technical description and the performance are reported in Ref. [Karn97]. However, due to the limited (close to, but not 100%) efficiency of the TAS, the determination of the β-feeding distribution from the experimental spectra requires thorough knowledge of the detector response and application of deconvolution procedures [Karn98, Cano99, Gier03]. Partial decay schemes resulting from the high-resolution studies are used as a constraint in the unfolding procedures and thus both techniques, *i.e.*, high-resolution and total-absorption spectroscopy remain complementary.

2.2.3 γ- and β-arrays

Besides total-absorption spectroscopy the γ radiation following some decay can be measured with low efficiency, but high resolution Ge-arrays. The other advantage is that unlike the TAS at GSI these arrays allows for in-(ISOL)beam measurements, i.e. grow-in and grow-in-and-decay measurement modes, which implies optimum utilization of the beam at low yields.

Usually these Ge-arrays are accompanied by a plastic scintillator or silicon de-

tector for measuring the β, p and α particles. In general there were built and used many different set-ups, depending on the experimental needs and detector availability. The biggest Ge-array ever used at the GSI-ISOL is a cube-like array of six EUROBALL Cluster germanium detectors called the CLUSTER CUBE [Hu98a]. It was used to measure very extensively the decay of ^{97}Ag [Hu99], ^{98}Ag [Hu00], and ^{102}In [Gier03]. Another powerful set-up was used in the last ^{94}Ag experiment. There the implantation point was surrounded by a prism-shaped array of silicon (Si) detectors [Mukh03], each 1 mm thick, having a total efficiency for charged-particle detection of 65%, and an array of germanium (Ge) detectors. The Ge array consisted of a Cluster [Eber96], two Super-Clover detectors [Gerl94] and two single Ge crystals, resulting in a total photopeak efficiency of 3.3% for a γ-ray energy of 1.33 MeV. The Si detectors were used for detecting both positrons and β-delayed protons. The segmentation of these detectors represents a considerable improvement with respect to the preceding ^{94}Ag experiment [LaCo02].

In the ^{100}In experiment the high-resolution $\beta\gamma\gamma$ set-up was similar to that used in a previous experiment [SchK00]. The $A = 100$ beam was implanted into a tape during a 16 s interval, with the tape being moved at the end of this interval to suppress long-lived activity. The total number of tape cycles amounted to 18600, which corresponds to 83 hours. The implantation point was surrounded by a plastic scintillator of 70% efficiency used to detect positrons. Gamma-ray detection was achieved by means of a hyperpure germanium detector (HPGe), a cluster of the EUROBALL type [Eber96], a superclover from the VEGA array [Gerl94] complemented by a LEPS detector. Beta-γ and $\beta\gamma\gamma$ coincidence data were taken by using signals from individual germanium (Ge) detectors (single-hit mode) and time-digital converters with time windows of 1μs for the cluster and 400 ns for the other Ge detectors. List mode data were accepted if the events occurred within a coincidence window of 8 μs. Energy and efficiency calibrations for each of the 13 individual Ge detectors together with the gain matching were performed off-line. Standard γ-ray sources of ^{133}Ba and ^{152}Eu were used for this purpose, covering an energy range from 30 keV to 1408 keV. The photopeak γ-detection efficiency amounted to 2.7 % at 1.33 MeV γ-ray energy. By using the aforementioned values for the γ and β efficiencies, the intensity of the mass-separated ^{100}In beam was determined to be approximately 2 atoms/s at an average primary ^{58}Ni beam intensity of 43 particle-nA.

2.3 The fragment separator method

Having in mind the projectile-fragmentation mechanism introduced in the Sect. 2.1.2, the production of ^{100}Sn was tested with a primary beam of the closest neutron deficient stable isotopes, namely ^{124}Xe and ^{112}Sn.

In an experiment at the FRagment Separator (FRS) at the GSI, Darmstadt,

Germany, in 1994, employing projectile fragmentation of ^{124}Xe at 1 GeV·A on a Be target, the doubly-magic ^{100}Sn was for the first time identified and its decay studied [Schn94]. The production cross section for ^{100}Sn was measured to be $\sigma = 11$ pb. Close in time another experiment at GANIL, France, has produced ^{100}Sn via the fragmentation of ^{112}Sn at 63 MeV·A on a ^{nat}Ni target [Lewi94]. The corresponding cross-section for production of ^{100}Sn was given to be $\sigma = 120$ pb.

It is the fragment separator and the detectors put in the flight path, that make it possible to identify the mass and charge of the produced fragments. To illustrate the method, the work of the FRS spectrometer is presented below.

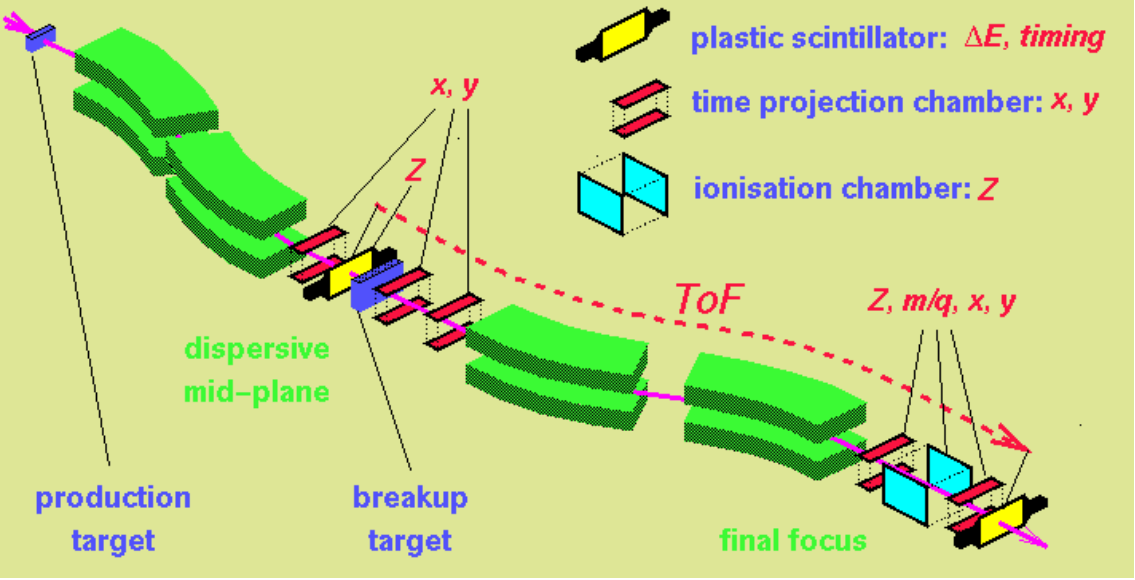

Figure 2.6: The FRagment Separator (FRS) at GSI.

The FRS is a high resolution zero degree spectrometer which could separate in-flight monoisotopic, exotic secondary beams of all elements up to $Z = 92$ effectively by combination of ion-optical devices [Mage94]. It is constructed for the isotope selection of projectile fragments by their momentum-loss and is called also momentum-loss achromat [Geis87].

The FRS facility which is schematically shown in Fig. 2.6 consists of 4 dipole sections arranged symmetrically to a dispersive intermediate focal plane, one set of quadrupoles before and one set after the dipoles to achieve first-order focusing conditions. The ion-optical system can be corrected for second-order aberrations by using sextupole magnets placed in front of and behind each dipole magnet. The required sextupole fields are relatively low, implying that the induced aberrations of third and higher order are minimized. The act of separating an individual isotope is

a combination of two different selection criteria. These selections can be presented as line-cuts in the nuclear chart. The cuts correspond to nuclei, which are deflected to the same positions in the intermediate focal plane and at the exit of the separator, respectively. The separation of fragments is based on the measurement of their magnetic rigidity ($B\rho$: between $4-18$ T.m [Geis87]) in front and behind an energy degrader mounted in the central plane. Thus the selection could be described as follows :

In the first stage, the ions produced by fragmentation at the entrance production target (with a thickness in order of 10% of the projectile range) of the FRS are deflected and roughly separated according to their A/Z ratio or with nearly the same $B\rho$ values by the first two dipoles (see eq. 2.1). Where

$$\frac{A}{Z} = \frac{p}{q} = \beta\gamma\frac{mc}{q} = \frac{B\rho\ e}{\beta\gamma}\frac{1}{cu} \tag{2.1}$$

with the relativistic parameters $\beta = \frac{v}{c}$ and the Lorentz factor $\gamma = \sqrt{\frac{1}{1-\beta^2}}$, the speed of light c, the elementary charge e and the atomic mass unit u. The assumption that the fragments are fully stripped ($q = Z$) could be ensured in the first stage of the FRS.

Even if the velocity distribution of each isotope is narrow, this separation can not select a single isotope, and so a variety of nuclei with $A/Z \sim const$ still reaches the intermediate degrader. The momentum loss in this thick degrader (in order of 50% of the range of the fragments) depends on the parameters (A, Z, v) of the fragments in a different way compared to the magnetic deflection in the first stage. Thus the separation of a single isotope becomes possible.

In the second stage, the shape degrader situated in the middle focal plane slows down the fragments following their residual magnetic rigidity. Then, the ions pass through the other dipoles, which again deflect and separate them according to their charge and A/Z. Dependent on the magnetic rigidity of the ions in the first stage, the profile of the degrader can be chosen in a way that the momentum (energy) dispersion of a selected fragment is compensated by the second dipole section that means the system is achromatic. The identification set up associated with the FRS is in charge of measuring the fragments in position, energy loss and time of flight. Different kinds of detectors are used for this purpose: the x position of each fragment is deduced at each focal plane by using plastic scintillation detectors, whereas the combination of the two scintillator time signals gives the Time Of Flight (TOF) between the two focal planes (S2-S4) [Voss95].The energy loss information is obtained from the ionization chambers called MUSIC (MUltiple-Sampling Ionization Chamber) [Pfue94]. Position (x, y) sensitive Multi Wire (MW) chambers [Stel91] are placed before and behind the MUSIC to measure the position information, which is later used to correct the energy loss of each fragment. These parameters are, in

principle, sufficient to determine completely the mass A and the charge Z of each ion reaching the final focal plane.

This enables to perform spectroscopy at the level of a single ion with the fragment separator method. Finally at the end of the FRS the experimentalists can put an active or a passive catcher and surround it with all the needed detectors for the specific experiment. Some of the exciting experiments are the decay studies in the region of ^{100}Sn [Stol01] and K-isomer spectroscopy at 0.2 ion/s production rate [Podo00].

2.4 EUROBALL multidetector array

EUROBALL is an European project to build and operate a highly efficient and powerful γ-ray spectrometer for nuclear spectroscopy. The countries involved are Denmark, France, Germany, Italy, Sweden and the UK. The story of EUROBALL begins with EUROGAM in the early 90's. EUROGAM was a UK-French collaboration to build an array of γ-ray detectors for nuclear spectroscopy studies. In its first phase (1993), at the Daresbury Laboratory, UK, it consisted of 45 large volume Ge detectors, each surrounded by a BGO suppression shield. In its second phase (1994-96), at the Centre de Recherches Nucleaires in Strasbourg, France, EUROGAM was composed of 30 phase-one-type detectors + 24 clover detectors. EUROGAM then became an European project: EUROBALL, involving 6 countries (Denmark, France, Germany, Italy, Sweden, UK). In its third phase, (1997-98), the array consisted of 30 phase 1-type detectors, 26 clovers and 15 clusters and it was installed at the Laboratori Nazionali di Legnaro, Legnaro, Italy. In November 1998, EUROBALL was moved to IReS Strasbourg and upgraded to include an inner BGO ball.

Euroball IV has ceased its operations in the middle of year 2003. Now the Euroball resources are used in a series of new international projects. These include RISING at GSI, Jurogam at Jyväskylä, and CLARA/PRISMA at Legnaro.

2.4.1 EUROBALL Ge-detector array

The quality of a Ge detector depends on its efficiency, energy resolution and peak-to-total ratio. Throughout the period of the EUROBALL project the size and quality of hyperpure Ge (HPGe) crystals has increased. The drive for bigger and bigger detectors was given by the nuclear structure community because of the need for higher and higher detection efficiency. Today HPGe crystals with relative efficiency of up to 200% are available, but usually the spectrum quality is poor due to Doppler broadening. Ideally, large detectors with high granularity are needed.

The EUROBALL multi-detector γ-ray array is based on two main advances in detector technology. The first is the Compton escape suppressed spectrometry. That is realised by surrounding the main detector by another additional detector with high γ efficiency. The additional detector gives a signal whenever it detects a γ-ray in coincidence with a γ-ray event in the main detector. We assume then that the detected γ-ray has scattered in this detector and has escaped into the surrounding detector. So the γ-ray energy registered in the main detector is incomplete and the event from the main detector is then rejected(supressed). Fig. 2.7 shows a typical γ spectrum from a ^{60}Co source with and without Compton escape suppression.

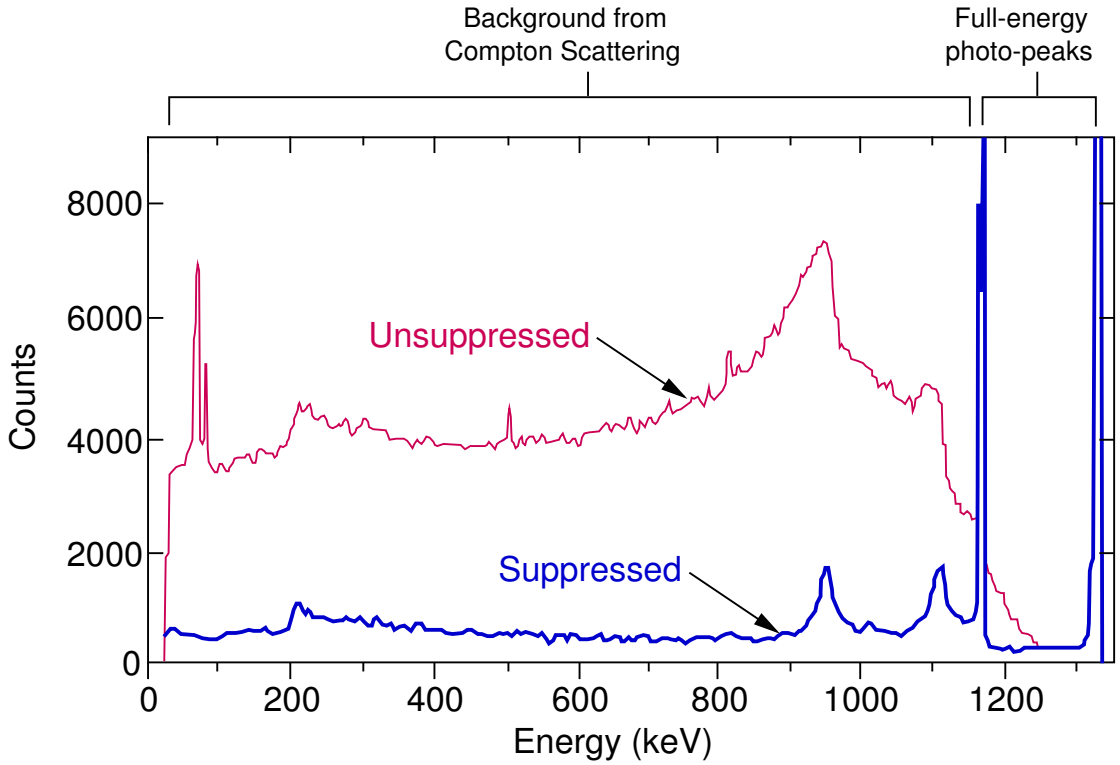

Figure 2.7: Typical gamma spectrum from ^{60}Co source with and without Compton escape suppression.

The spectrum quality can be expressed by the *Peak-to-Total (P/T)* ratio defined as:

$$P/T = \frac{N_{peak}}{N_{tot}} \tag{2.2}$$

where N_{peak} is the full-absorption peak area and N_{tot} is the total spectrum area. In case of two neighbouring peaks (^{60}Co) the definition (2.2) can be used and N_{peak} has

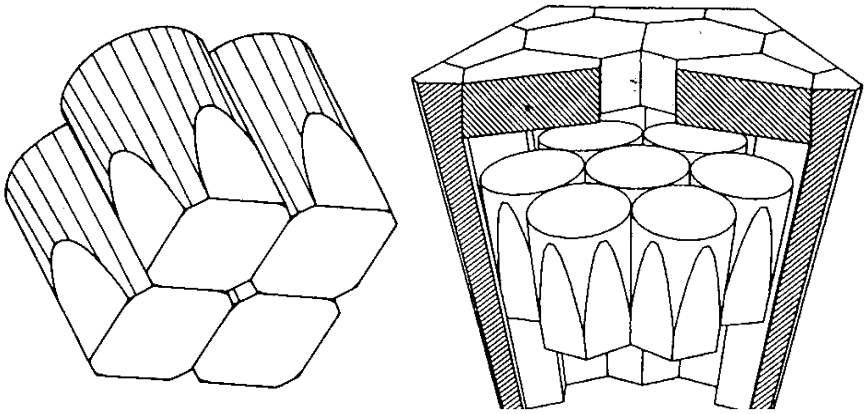

Figure 2.8: The segmentation of the two types of composite detectors developed and used in the EUROBALL project.

to be defined as a sum of the two full-absorption peaks. In case of multiple peaks spectra the (2.2) is incorrectly defined and it is better to use the following form:

$$P/B = \frac{N_{peak}}{N_{bg}} \tag{2.3}$$

where N_{bg} is the background counts on the left peak side. The spectrum quality can be considerably improved by an escape-suppression (anti-Compton) shield surrounding the detector. Nowadays the shields are usually made of bismuth germanate better known as BGO ($Bi_4Ge_3O_{12}$). For ^{60}Co the P/T can increase from $\sim 25\%$ to typically 65% with suppression. This improvement in the P/T is crucial in high fold coincidence spectroscopy since the photopeak-photopeak coincidence probability is proportional to P/T.

The second strength of the EUROBALL multidetector array comes from using composite Ge-detectors. In the EUROBALL project there were developed two types of composite detectors. The first one is the Clover [Eber96] detector, which consists of four independent HpGe crystals packed together like a four-leaf clover. The second one is the Cluster detector, which consists of 7 semi-hexagonal tapered detectors separately encapsulated. Partial sections of both can be seen on Fig. 2.8.

The total photopeak efficiency of a composite detector $(\epsilon_p\omega)_t$ can be written as a sum over all N detector efficiencies $(\epsilon_p\omega)_i$:

$$(\epsilon_p\omega)_t = \sum_{i=1}^{N} (\epsilon_p\omega)_i \tag{2.4}$$

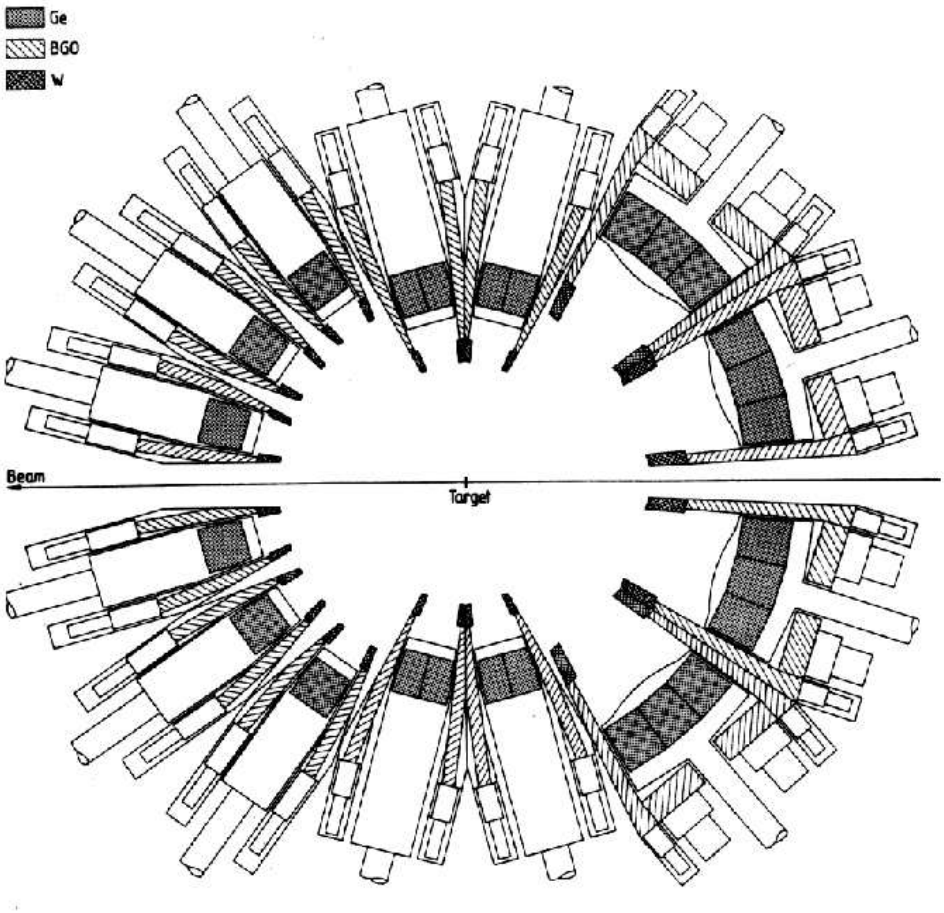

Figure 2.9: Cross section of the EUROBALL multi-detector γ-ray array. On the picture the beam comes from the right side.

It can be increased using the add-back procedure but when it is applied "phantom" peaks could appear in the spectra.

A composite detector with N crystals will have an efficiency which is higher than the efficiency defined in eq.(2.4) if the *add-back* mode is applied. Let us suppose that one γ-ray has Compton-scattered into several crystals of one composite Ge detector, with exception of the last crystal where it is absorbed by photoeffect. Then by an adequate algorithm the initial γ-ray energy could be restored by summing (adding-back) the energies deposited in the hit crystals. Thus, the total composite detector efficiency will be:

$$(\epsilon_p\omega)_t = \sum_{i=1}^{N}(\epsilon_p\omega)_i + \sum_{j=1}^{M}(\epsilon_p\omega)_j \tag{2.5}$$

where $(\epsilon_p\omega)_i$ is the i^{th} crystal efficiency, $(\epsilon_p\omega)_j$ is the photopeak efficiency of two and

more Ge crystals fired simultaneously. N is the number of the single crystals and M is the number of combinations of two and more crystals. Obviously, the total efficiency obtained with eq.(2.5) is higher than the previous one defined by eq.(2.4).

A single crystal has relative efficiency of 20% for clovers and 59% for clusters. The relative efficiencies of these two composite detectors in add-back mode are 123% and 595% respectively.

The EUROBALL IV in its main configuration (see Fig. 2.9) is built-up from 239 individual Ge crystals mounted in 71 Compton escape-suppressed spectrometers. These are 15 composite Cluster detectors placed in the backward quadrant with respect to the beam direction, 26 composite Clover detectors placed in two rings close to 90^o and 30 individual Ge detetors (Tapered) positioned in the front quadrant.

In many cases the γ-coincidences and multiplicity restrictions are not enough to clean up the spectrum and therefore additional *ancillary detectors* are required. Some of them like the Neutron Wall and the EUCLIDES Si-ball array are discussed in the following sections. They are designed to detect specific particles emitted in the decay of the compound nuclei and thus help in the exit channel identification.

2.4.2 Neutron Wall

The EUROBALL Neutron Wall detector array [Skep99] is designed, built and managed by groups from Sweden, Germany, UK, and Poland. It is mounted in the forward hemisphere of EUROBALL, replacing the tapered Ge spectrometers and covering a solid angle of about 1π (see Fig. 2.10). The array consists of 15 pseudo-hexagonal detector units in three rings and a central pentagonal unit. Each hexagonal unit is subdivided into three hermetically separated segments, each viewed by a 130 mm diameter PMT (Philips XP4512PA). This amounts to a total granularity of 50 segments and a total volume of 151 liters. The scintillation liquid used is BC501A. The distance from the focal point to the front face of the detectors is 510 mm.

Neutron-γ discrimination is made by using a combination of the zero-cross-over (ZCO) time signal and the difference in measured time of flight (TOF) of neutrons and γ rays. Neutrons interact in the detectors mainly by elastic scattering with the protons of the scintillation liquid. When the recoiling protons are slowed down in the liquid, they give rise to a larger proportion of the slow component of the scintillation light than the recoiling electrons, which are produced by γ-ray interactions. This gives rise to a difference in the pulse shape of the anode signal, a difference which is observed as a delayed ZCO time signal for neutrons interacting in the detector compared to γ rays. In the Neutron Wall set-up, n-γ discrimination works very well down to an equivalent electron energy of at least 100 keV, which corresponds to a neutron energy of about 0.5 MeV.

The external time reference signal, needed for the TOF measurement, is usually

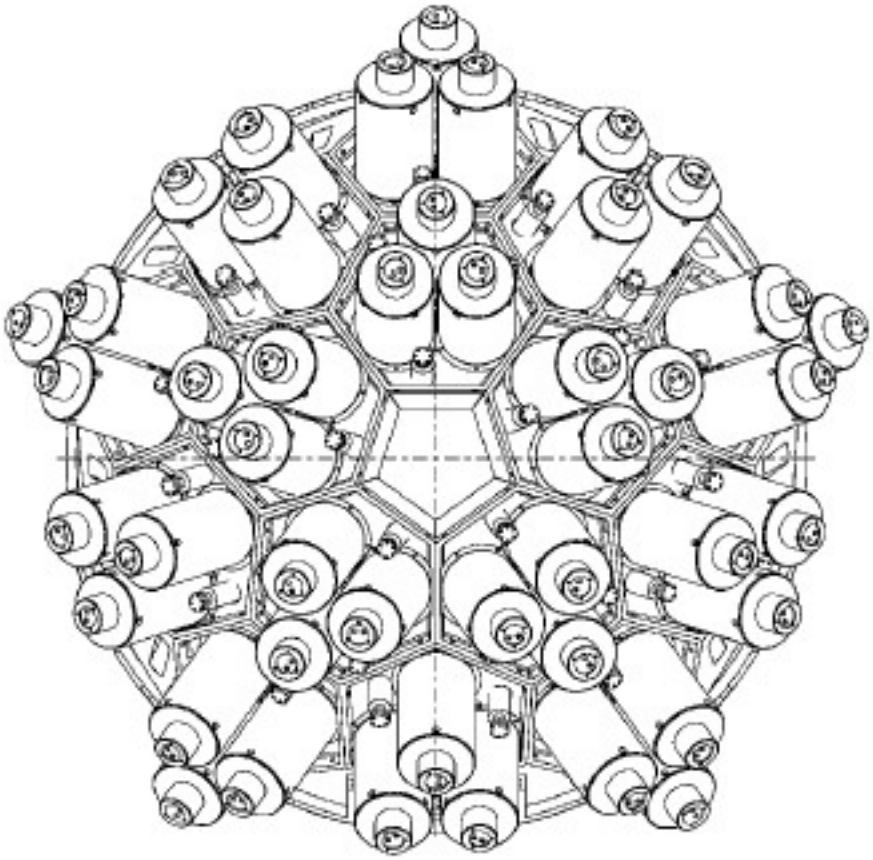

Figure 2.10: The Neutron Wall detector array as viewed from the downstream side of EUROBALL. Here the central pentagonal detector is not included. (from [EBrep])

made as a precisely time aligned OR of all the Neutron Wall constant fraction discriminators (CFD) signals (self-timing mode), or taken from the RF system of a pulsed beam.

The measured total neutron efficiency, i.e. the probability of detecting and identifying one neutron out of one emitted, in coincidence with γ-rays detected by the Ge spectrometers of EUROBALL, is $\sim$25-30% [EBrep] for symmetric reactions with compound nuclei in the A$\sim$100 region. For studies of the most neutron deficient nuclei, reaction channels in which more than one neutron is evaporated are most interesting. The major problem of clearly identifying such reactions, with a closely packed neutron detector array, is the scattering of neutrons. In the Neutron Wall the scattering probability, i.e. the probability that one neutron is detected as two or more neutrons, is about 7% [EBrep].

2.4.3 EUCLIDES

The EUCLIDES array is a charged-particle detector array developed and built within a collaboration of the Institito Nazionale di Fisica Nucleare (INFN) groups in Legnaro, Padova and Firenze, Italy, as well as the University of Liverpool and the Daresbury laboratory, UK. EUCLIDES is composed of 40 ΔE-E Si telescopes 130 μm and 1000 μm thick, correspondingly. The geometry of the array is shown on Fig. 2.11, which is the same as the geometry of the ISIS Si-ball [Farn97]. Figure 2.11 shows also

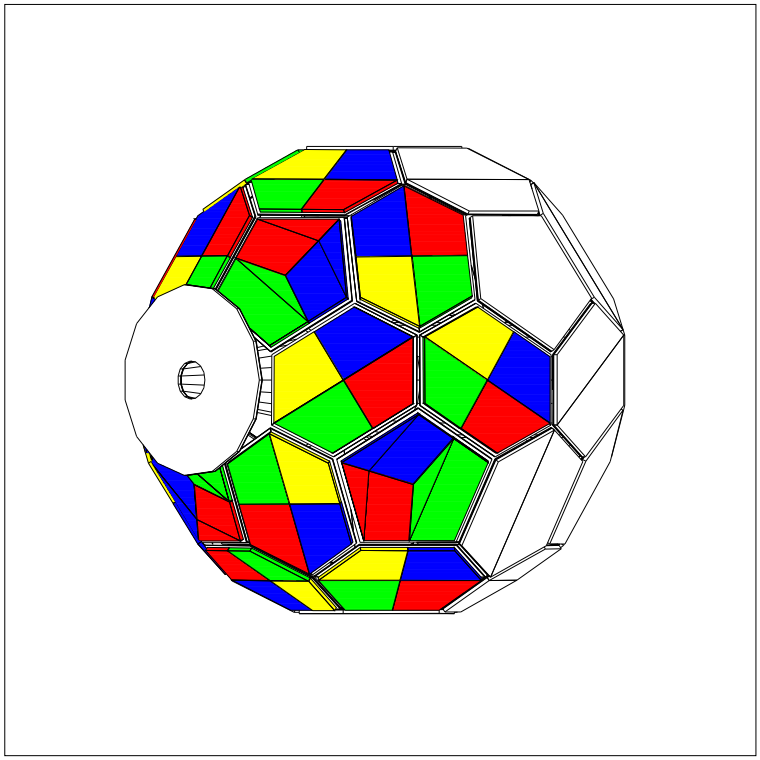

Figure 2.11: Schematic design of the EUCLIDES detector array from the GEANT3 Monte-Carlo simulations.(from [EBrep])

the planned segmentation of the forward 1π, but so far only the five forward elements are electrically segmented in four parts. This was the status of the EUCLIDES at the time of the ^{98}Cd experiment. The ΔE detector is mounted in reversed configuration, enabling charged particle discrimination with pulse shape techniques [Paus95]. The front-end electronics is composed of charge-sensitive preamplifiers and of specially designed single-unit CAMAC modules, called Silicon Shaper Analyser, which provide linear (Gaussian and stretched) and logic (fast timing and crossover timing for pulse shape analysis) outputs. Data are collected through FERA ADCs and TDCs and sent to the EUROBALL data acquisition via the Fera-VXI interface (see Sect. 2.4.5).

The performance of EUCLIDES as a standard ΔE-E array is very satisfactory. The discrimination capability is excellent, since less than 0.01% of the detected particles are misidentified. The detection efficiency depends strongly on the reaction and on the absorbers used to stop the scattered beam ions. Values of ϵ_p ∼60% for protons and ϵ_α ∼40% for α particles can be obtained.

In the ^{98}Cd experiment we had to distinguish between events for which the γ-rays were emitted at the target and at the catcher position, and the charged particle efficiencies of the EUCLIDES array were different in coincidence with γ-rays from the target and those measured around the catcher foil. This difference is a result of the correlation between the evaporated charged particles efficiency and the residues hitting the catcher. The catcher covers the most forward part of the recoil cone. Due to the reaction kinematics this corresponds to preferential forward and backward particle evaporation, where the detection efficiency is reduced by the holes in the EUCLIDES array for the beam entrance and exit, and by the absorption in the detector absorbers. Therefore, the effect is largest when the recoiling nucleus was created after an α-particle evaporation. The efficiencies of the EUCLIDES array based on γ-rays emitted at the target (catcher) (see Sect. 2.4.4) position were 60% (55%) for protons and 40% (15%) for α particles.

The EUCLIDES experimental spectra and the particle identification (discrimination) are shown and discussed in Sects. 3.1 and 3.2.

2.4.4 Delayed γ-spectroscopy set-up

In the ^{98}Cd experiment a pulsed beam of ^{58}Ni served as projectile and as a time reference for the ^{46}Ti(^{58}Ni,α2n)^{98}Cd reaction. The pulse repetition time was Δt= 330 ns. The ^{46}Ti target of 1 mg/cm^2 thickness was made of a material enriched to 86%.
The EUROBALL [Simp97] spectrometer consisting of 26 Clover [Duch99] and 15 Cluster detectors [Eber96] was used in combination with the EUCLIDES [Farn97] Si-ball and the Neutron Wall [Skep99]. In this way the identification of the reaction channel was assured and prompt γ rays emitted directly from the target were measured. Downstream from the thin target, at a distance of 1.19 m, a catcher foil was mounted where the recoiling nuclei were stopped after a flight time of about 100 ns. The whole experimental set-up is schematically shown in Fig. 2.12.

The catcher foil had an inner hole to let the non-interacting beam particles pass through. The outer diameter of the catcher foil was 10 cm and the central hole had a diameter of 1 cm. To know what amount of the residual nuclei of interest would land on the foil, one has to know the realistic angular distribution of the residual nuclei. The angular distribution of residual ^{98}Cd nuclei in the ^{46}Ti(^{58}Ni,α2n)^{98}Cd (^{58}Ni beam at 215 MeV) reaction was estimated before the experiment with the simulation code PACE [Spoh94] to about 40%, which includes reaction kinematics, slowing down and multiple scattering processes in the target. The value of 81.6%

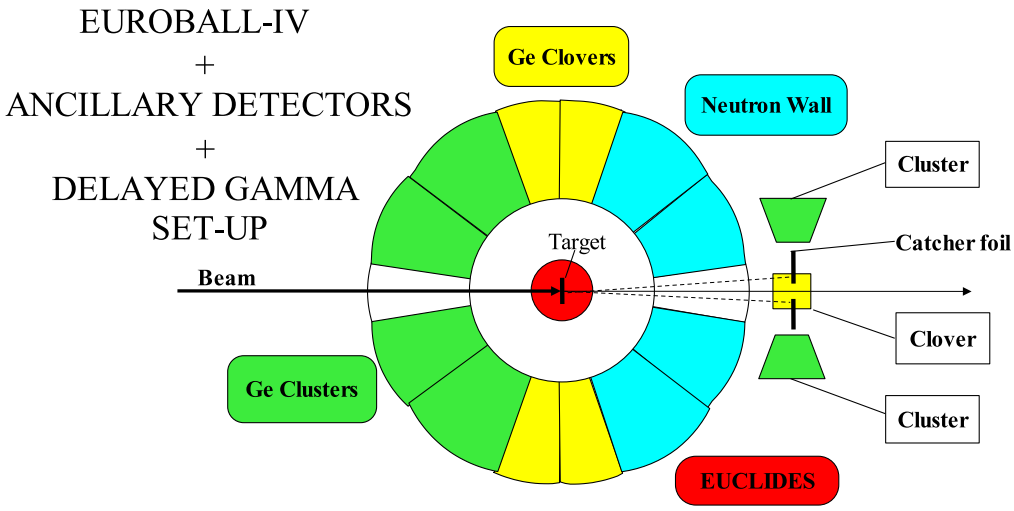

Figure 2.12: Schematic sketch of the ^{98}Cd experimental set-up.

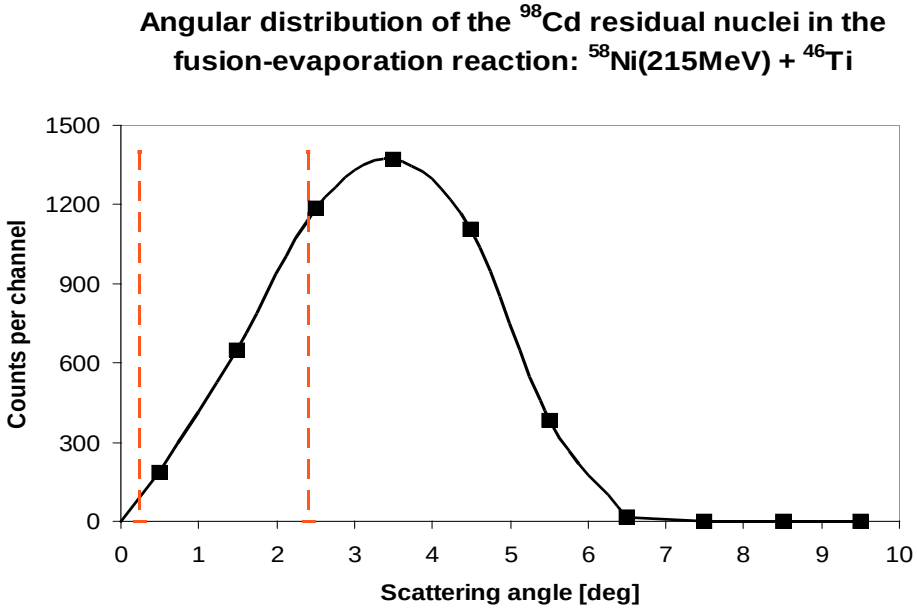

Figure 2.13: A Monte-Carlo simulation for the angular distribution of ^{98}Cd residual nuclei in the ^{46}Ti(^{58}Ni,α2n)^{98}Cd fusion-evaporation reaction, performed by the program PACE4 [Tara03]. The points represent the integral values for the corresponding range of neighbouring integer scattering angles, i.e. $0^\circ - 1^\circ$, $1^\circ - 2^\circ$, etc. The solid line connecting the distribution points was smoothed to resemble simulations with a smaller scattering angle step. The two dashed lines give the angular range covered by the catcher foil in the experiment.

catching efficiency in the previous experiment [Górs97] is about twice larger.

Here I present a new Monte-Carlo simulation (see Fig. 2.13 and figure caption) done recently with the updated code PACE4 [Tara03]. The total number of simulated incident beam particles is 10^6. The dashed lines on Fig. 2.13 mark the angular range covered by the catcher foil in the current experiment, i.e. $0.24° - 2.41°$. To extract the catching efficiency, the simulated distribution points were fitted by a sixth-order polynomial function which for the region $0° - 6°$ excellently reproduced the simulated points. This function was integrated in the angular range covered by the catcher foil in our experiment and the integral divided by the total number of simulated residual nuclei. Thus, the new estimate of the catching efficiency is 26%.

The reduced catching efficiency is due to many limitations among which are: (i) that we could not place the foil together with the delayed-γ set-up closer to the target; (ii) that the diameter of the vacuum tube, i.e. foil, was limited and (iii) the increase of the foil diameter would move the Ge-detectors away thus reducing their gamma efficiency. So under these conditions the set-up was very close to optimum. Unlike the previous experiment [Górs97], the catcher foil was exchanged only once during the five-day experiment, so the built-up long-lived activity brought considerable contamination in the delayed γ spectra (see Sect. 3.3).

Around the catcher an array of two Cluster and one Clover detector was placed. In order to assure high efficiency for γ-rays from decaying isomeric states which lived long enough to survive the flight time between the target and the stopper, the BGO shields were not used and the detectors were placed in a close geometry around the stopper foil. The efficiency of the delayed γ-spectroscopy set-up after applying add-back procedure was 2.8% at 1.3 MeV γ-ray energy. This was estimated relative to the efficiency of the γ-ray spectrometer around the target which had e_γ =6.6% in this configuration, i.e. without the Ge-tapered detectors. For details on the energy and efficiency calibrations as well as the add-back procedure see Sects. 3.2 and 3.3.

A photograph of the partial ready set-up is shown on Fig. 2.14(see the figure caption for details).

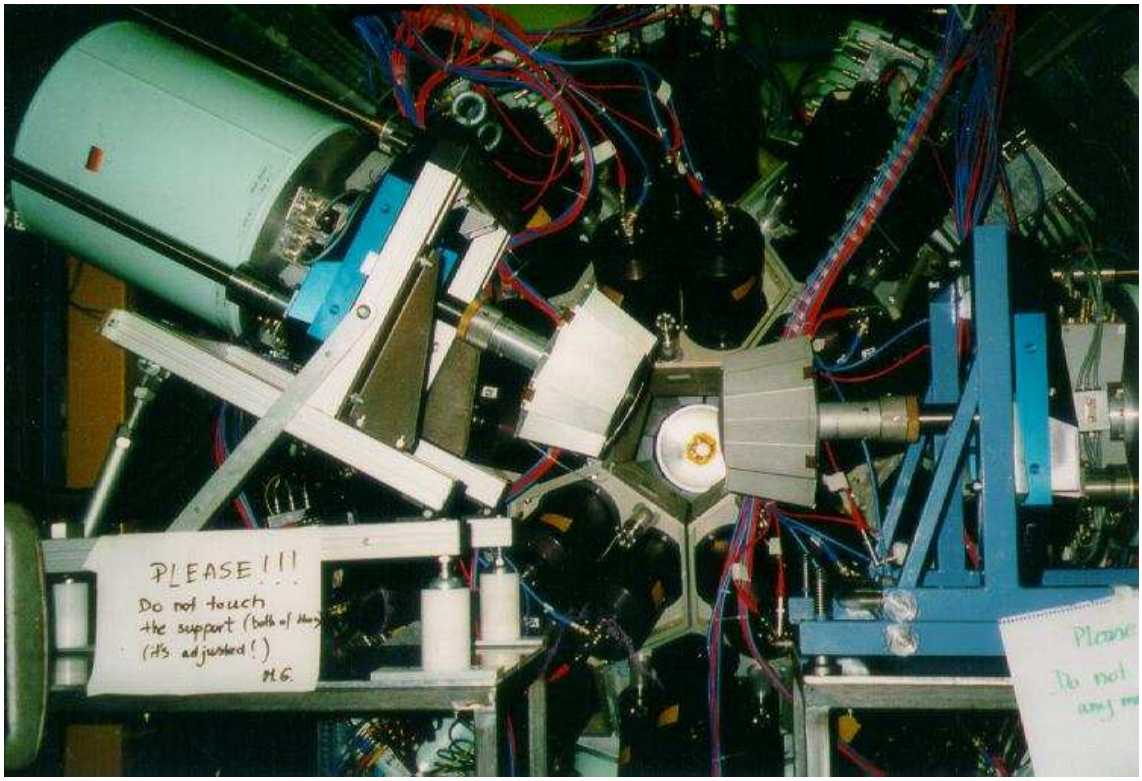

Figure 2.14: A photo of the experimental set-up in a preparatory stage. At the position of the delayed gamma spectroscopy set-up only the two Cluster detectors are mounted. Behind them one can see the Neutron Wall, where in the hole of the missing central pentagon, half of the target chamber is visible. The EUCLIDES array, that would be placed in the target chamber, the downstream beam pipe with the catcher foil inside and the Clover detector, to be put from the bottom of the delayed set-up, are missing at the time of taking the picture.

2.4.5 EUROBALL Data acquisition and trigger system

As described in the numerous documents [EDOC], the EUROBALL electronics system is a modular, open system in which there are specific cards designed for different detector types. These include Cluster detectors, Clover detectors and conventional single crystal tapered Ge detectors. The cards are built in the D-sized VXI standard [VXIs92] which permits the implementation of both analogue and digital electronics in the same chassis. VXI is VME bus with extensions to make it suitable for instrumentation by providing analogue and emitter coupled logic (ECL) power supplies, triggering features and larger board sizes. The selection of VXI was made on 2 grounds: firstly it is the best bus system available, at the time when the project started, for building large spectroscopy systems, and secondly it recycles EUROGAM's considerable investment in VXI cards and systems [McPh92]. EUROGAM's use of VXI has proved that it is a suitable environment for high resolution (13 bit) γ-ray spectroscopy electronics [Laza95a]. Standards have been agreed within the European nuclear structure physics community for the use of the "user defined" VXI features [EDOC] and all EUROBALL VXI electronics adheres to these. The VXI cards: Up to 13 VXI cards can be located in a single VXI crate. Two of these cards are "infrastructure" cards: the Slot 0 controller (Resource Manager) [Cole90] and the crate readout card [EDOC]. The remaining 11 slots are usable for detector electronics although 1 slot in one crate must be allocated to the system's Master Trigger card. The VXI cards used in EUROBALL are:

- Slot 0 controller/Resource Manager
- Clover Detector card (4 Ge channels +1 spare + a BGO shield channel) [Laza95b]
- Cluster Ge card (7 Ge channels + 1 spare) [EDOC]
- Cluster BGO card (18 BGO channels + 1 spare + 1 sum energy channel) [EDOC]
- Master Trigger card
- Crate readout card (STR8080)
- Tapered Ge card (6 channels) [Richa91]
- BGO shield card (6 channels, for use with tapered Ge card) [Boss91]

The EUROBALL system comprises 9 VXI crates for the main escape suppressed Ge detectors plus a crate each for Neutron detector electronics and for Si detector electronics, giving a total of 11 VXI crates handling over 1000 detector output signals. Each VXI crate reads data in parallel and writes it into a buffered crate

readout card where it is stored together with a subevent header, including a 16 bit event number and an end subevent trailer. Data stored in the crate readout card are transferred to the event collector over the DT32 bus [Alex92, EDOC] and stored in VME buffers in the event collector.

Ancillary detectors may be connected in 3 different ways. The preferred route is by designing a VXI card for a particular type of detector. This is done for the Neutron detectors. An alternative is to use FERA ADCs and connect them either via the EUROGAM FERADT32 interface or directly to the event collector buffer memories which can have their DT32 interface module swapped for a FERA interface module. The third method is to use NIM ADCs and the EUROGAM NAM (NIM ADC Module) card. Figure 2.15 shows a typical EUROBALL system configuration. A CAMAC system is shown to illustrate how nonVXI data acquisition equipment can be connected if necessary using the second method from the paragraph above involving a FERA input stage for the event collector buffer memories. Several DT32 bus chains are shown to illustrate the possibility of having single or multiple VXI crate configurations on a DT32 bus. After merging the event is sent to the in-line processing farm and further to the tape server and the histogram processing servers. The EUROBALL system is designed to operate in parallel mode, that is more than one event being processed in parallel. The parallelism operates at the detector level for Cluster and Clover detectors i.e. if any of the detector's crystals detects a γ ray, the whole detector is dead until the processing of that γ ray is complete.

The EUROBALL trigger system was first suggested in the original EUROBALL proposals [Ende90] and later implemented in EUROGAM [Laza92]. The concept of the trigger is that each channel of electronics has some timing and logic, called a local trigger, which is programmed according to the particular experimental set-up. The local trigger's timer is started by the channel's discriminator and two programmable delays are used to test for the presence or absence of the global first and second level trigger pulses known as the fast trigger and the validation. The first level trigger occurs within 1μs of the CFD firing, and the second level trigger within 10μs of the discriminator firing. The global fast trigger and validation trigger pulses are generated by the master trigger module as a result of two programmable user defined logic decisions. Typically only Ge multiplicity is used unless ancillary detectors are attached, which was the case in our ^{98}Cd experiment.

The trigger diagram is shown on Fig. 2.16. A fast trigger was generated when at least one gamma ray (prompt or delayed within about 1800 ns) was registered together with at least one prompt neutron pre-discriminated from γ rays detected in the Neutron Wall by hardware pulse shape analysis. The average trigger rate throughout the experiment was about $3 - 3.5$ kHz. In the off-line processing of the data it became clear that a total number 9.6×10^8 "good" events with detection of prompt/delayed γ rays have been collected during the experiment (see Sect. 3.2).

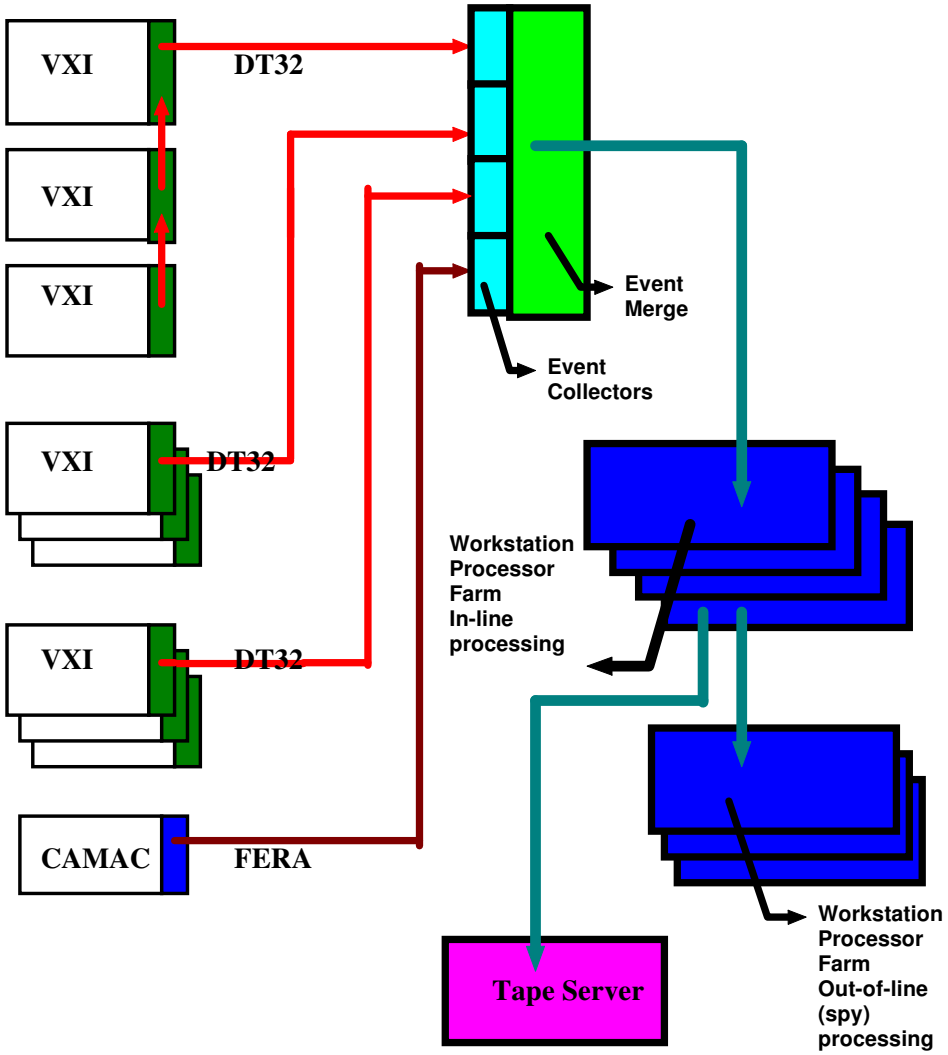

Figure 2.15: A simplified diagram of the EUROBALL data acquisition system (from [EDOC]).

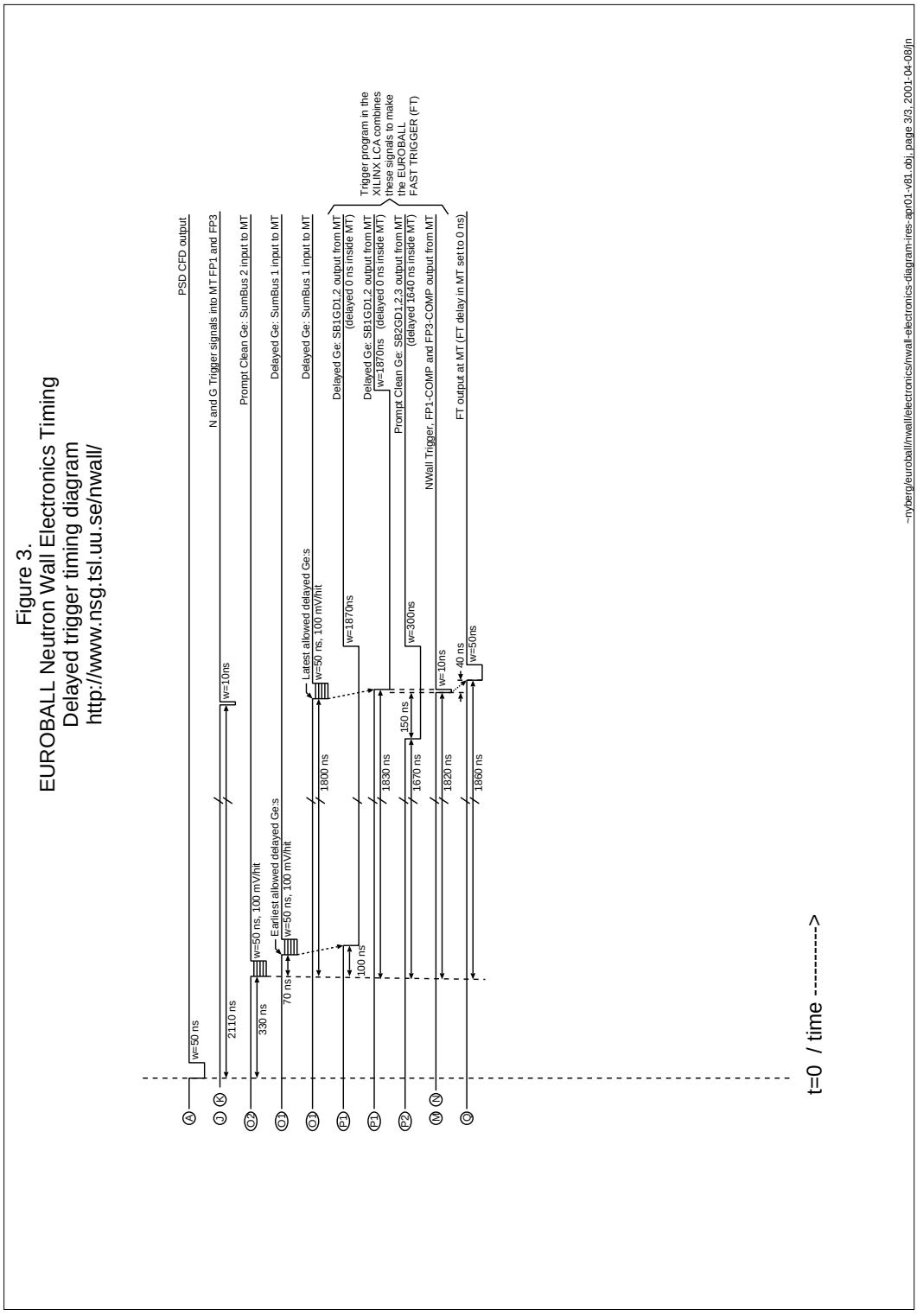

Figure 2.16: A diagram of the delayed trigger timing used in the ^{98}Cd EUROBALL experiment. (from [NWweb])

Chapter 3

Data Analysis

The aim of this chapter is to describe in details the ^{98}Cd EUROBALL experiment data analysis. The complexity of the EUROBALL experimental data is very high, due to the fact that in this experiment one of the most sophisticated EUROBALL set-up configurations was used. It included γ-ray spectrometers, 209 Ge crystals for measuring prompt and 16 for delayed γ rays, 55 charged particle detectors in the EUCLIDES array and 45 neutron detectors from the Neutron Wall array. More than a thousand experimental parameters (see Table 3.1) were registered on tapes, which in five days of experimental time resulted in an extremely large data set. The tapes used to store the online stream of data were of the type DLT-IV with a raw data capacity of 40Gb. The raw data including calibration runs amounted to about 300Gb. This was done to enable a sophisticated off-line processing of the data. The analysis of the data has roughly three stages. The first one is called alignment, the second sorting and the third spectra analysis. The first stage took a very long time and in addition the sorting and analyzing the coincidence relations spectra, matrices and cubes were also time consuming. Therefore, the analysis of the experimental data is still in progress and more results are to be expected. So far the stress was put on the delayed γ-ray spectra and the search of the expected higher lying core-excited isomer in ^{98}Cd, which is part of this thesis and will be presented in the following. The experimental term *run* is used for a period of the experiment between start and stop of the data acquisition system (DAQ). Usually runs differ by some experimental condition and therefore it is useful to mark and separate the data from different runs. In the production runs (i.e. without counting test and calibration runs) a total number of 1.15×10^9 raw events were collected. In the analysis, the program ALIGN [Pala96] and parts of the software packages TSCAN [Jin97U], RADWARE [Radf95] and ROOT [Brun96] were used.

Table 3.1: Parameters stored on tapes in the ^{98}Cd EUROBALL experiment.

parameter	number of detectors
Ge prompt γ low energy ($\leq 4MeV$)	209
Ge prompt γ high energy ($\leq 20MeV$)	209
Ge prompt γ time	209
Ge delayed γ low energy ($\leq 6MeV$)	16
Ge delayed γ high energy ($\leq 20MeV$)	16
Ge delayed γ time	16
Neutron energy	45
Neutron time of flight (TOF)	45
Neutron zero-cross-over (ZCO)	45
EUCLIDES ΔE energy	55
EUCLIDES E energy	55
EUCLIDES ΔE time	55
EUCLIDES E time	55
Trigger pattern	1
RF	1

3.1 Alignment

Each detector is subject to instabilities and shifts in gain and offset. For short measurements this is usually not important as the changes are very small, but for longer measurements it becomes a real problem for sum spectra. These floating and shifts of the peaks in the spectra are summed up and lead to decrease of resolution, and in some cases may even distort the spectrum completely. Therefore, one has to account and correct for these effects for each individual parameter of the detectors.

The parameters collected in the ^{98}Cd EUROBALL experiment are summarized in Table 3.1. This makes a total of 1032 parameters stored on tape. By reducing the resolution of the less important parameters and selecting off-line the "good" events, the size of the *pre-sorted* data was reduced to more than half of the original size. In the pre-sort the stability corrections for all parameters, together with *gain matching* and energy calibration of all Ge detectors were applied. The gain matching is the procedure when the corresponding spectra of different detectors are matched together so that the spectra summing is possible. And certainly one needs not only the total spectrum, but also its calibration, in energy or time, in order to read it properly. The advances in hardware and software have enabled certain optimizations of the data handling. Until recently the only way to store and sort such amounts of data was to use magnetic tapes with high capacity and the correspondingly high-cost tape drives. In the course of this work, the relatively slow and cumbersome tape

sorting was replaced by sorting of the data, which was stored on the local hard disk. This gave a factor of about 10 in the data processing speed compared to the standard tape sorting. Finally it should be mentioned, that together with an optimization of the sorting algorithm the time required to sort the five-day experimental data, for example into 20 different coincidence matrices simultaneously on a standard PC, is now less than an hour. All the file/tape handling was realized by the routines included in the TSCAN [Jin97U] package. The user subroutine containing all the event-by-event processing algorithm, written in the programming language C, is a result of the author's work. It was based on an existing subroutine for previous experiment provided by Dr. Marcin Palacz.

The whole data set was scanned for possible gain and time shifts and matched mostly with the help of the program ALIGN [Pala96, PalaPC]. The full description of the program is given in the above cited scientific reference, but for completeness I will shortly introduce the highly-automatic method of shift and gain correction of arbitrary spectra. This method is based on the calculation and minimization of the sum of differences (χ^2) between the bin contents in one selected spectrum and each of the *test(model) spectra*, i.e. the ones which are used as a sample to align to. The method does not require the presence of any particular shape in the analyzed spectra and as such can be used for the discrete γ-ray spectra as well as for any ancillary detectors spectra. It is sensitive to deviations occurring anywhere in the spectra and not only in certain regions. It is usually applied to align the spectra from one and the same detector since it is supposed to have the same pattern structure, but to some extent it can be also used to match also spectra from different detectors of the same type.

In this method the model spectrum is treated as a tabulated function $m(x)$, where $m(x)$ is equal to the counts in the bin number x(integer), and for x non-integer $m(x)$ is interpolated. Then the problem of finding the required transformation f_a along the x-axis is equivalent to fitting the following function to the data points (x_i, y_i):

$$M(x) = Cm(f_a(x)) \ , \tag{3.1}$$

where C is the normalization factor and a are parameters of the fit. Palacz *et al.* [Pala96] have defined the transformation by the following formula:

$$f_a(x) = a_0 + a_1 x + a_2 x^2 + a_3 x^3 + a_4 \sqrt{x} \ , \tag{3.2}$$

but usually only the a_0 and a_1 coefficients are allowed to vary, while the others are fixed to zero. The reason is that in most applications a linear transformation is enough, but their experience in spectroscopy has suggested that in rare cases other transformations are also required.

The sum of the squares of differences between the values y_i and the values M of

the calculated function is:

$$\chi^2 = \frac{1}{n_{dof}} \sum_{i=i_{low}}^{i_{high}} (y_i - M(x_i))^2 \, w_i \ , \tag{3.3}$$

where the number of degrees of freedom n_{dof} is equal to the number of channels between the lower limit channel i_{low} and the higher limit channel i_{high}, which are set manually to define the alignment range. The standard weights w_i are equal to the inverse of the variance of the number of the counts in a bin [Pala96].

Figure 3.1 shows a typical summary of the χ^2_0, χ^2_{min}, the transformation coefficients, in this case a_0 and a_1 and the bottom plot the ratio of the total counts in the section spectra to the model spectrum. The last plot could often give an idea if the detector is not working or has statistics higher than usual often suggesting a detector malfunction. The alignment procedure has shown that most of the Ge parameters were relatively stable throughout the experiment, except for a few crystals that had technical problems. In addition the ancillary detectors spectra are of crucial importance for the particle-γ coincidences (see Sects. 3.2 and 3.3) and had, therefore, also to be aligned. In the cases of Ge prompt-γ-time, neutron TOF and ZCO, only the a_0 coefficient was varied to preserve internal time calibration since there was no time calibration run. Unfortunately EUCLIDES ΔE and E time spectra were seriously misaligned even in short period spectra and were used without any physical time gate of the detected particles, but gated to exclude the regions of electronic noise. The Ge delayed γ-time spectra, however, contain a peak structure due to the beam pulse repetition frequency (see Sects. 3.2 and 3.4), which allowed for a more precise linear transformation in the alignment.

In this work the model spectrum for each parameter was created by summing the raw data from the last 1/8 of the experiment when the performance of the system proved to be most stable and least affected by shifts. These data were also closest to the energy calibration runs done after the production runs, and thus the energy calibration from the calibration run can be used without any additional transformations. In order to obtain the characteristic spectral shape for each parameter, the model spectra need higher statistics, than the spectra which are to be aligned. The latter were produced splitting the whole data into 82 consecutive sections having roughly the same amount of raw events $\sim 1.4 \times 10^7$. For each of the one thousand parameters a separate spectrum was created for each of the 82 sections. Each parameter section spectrum was compared by the program ALIGN to its model spectrum and then the transformation coefficients yielding best matching, i.e. minimum χ^2, were written in a file. The automation procedure contains inspection of the transformation coefficients as well as the χ^2 before and after the alignment. In any case a visual inspection is also included, especially in cases of transformation quite different from unity. Since the author needed every piece of statistics, a detailed visual analysis of

the trouble cases was performed. After finding all transformation coefficients and deciding in which cases to abandon(skip) the data for specific detectors/sections, all transformation coefficients were gathered into a file and used as an input for the data pre-sort.

The pre-sorted data was then used to sort spectra, coincidence matrices and cubes, which were of interest and were analyzed in the final stage of the procedure (see Sects. 3.3 and 3.4). During the pre-sort, prompt γ-rays were corrected for the Doppler effect, due to the velocity of the emitting nuclei. The analysis of the prompt γ-rays is beyond the scope of this work and is not discussed here.

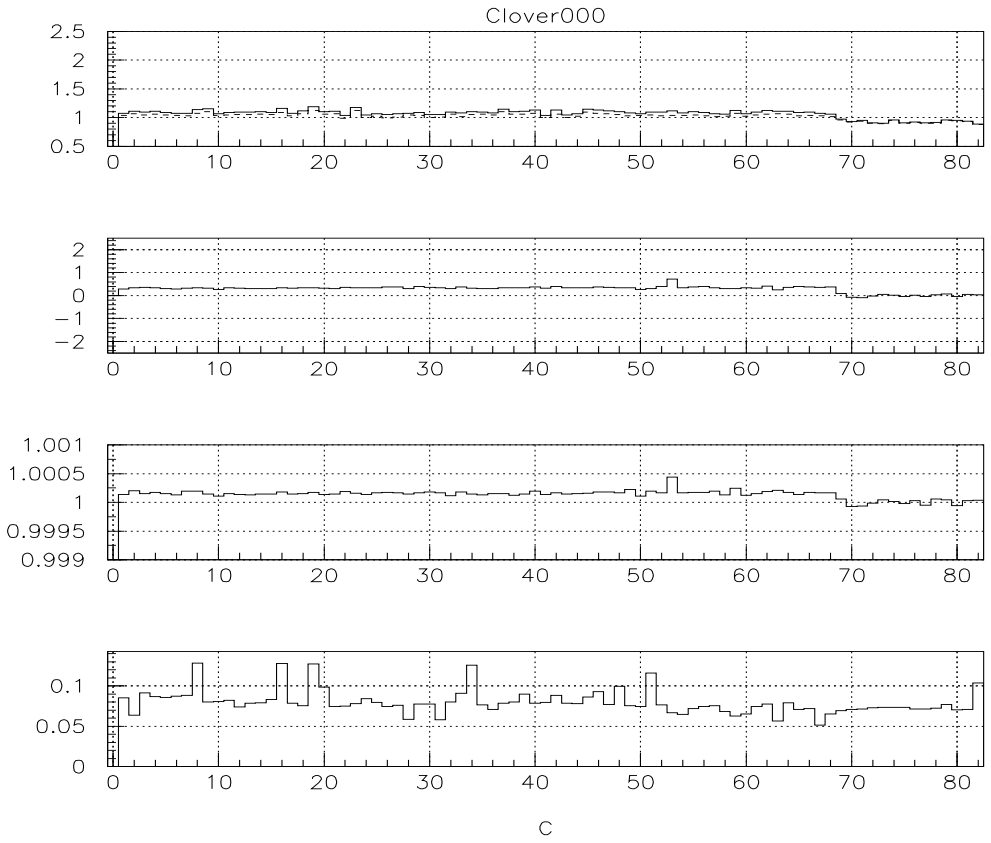

Figure 3.1: A typical summary of the transformation coefficients, output from the ALIGN [Pala96] program, of the energy spectra of Ge-clover detector crystal 000 for the spectra of 82 experiment sections. The top panel shows the χ^2_0 before alignment (solid line), and the χ^2_{min}(dashed line) after alignment as a function of the section number. Similarly, the second and third panels from top, show the transformation coefficients a_0 (in channels) and a_1, respectively. The bottom panel shows the number of counts of the section spectrum normalized to the number of counts of the model spectrum.

3.2 Sorting

The experimental set-up and the structure of the data allowed to sort coincidence spectra between prompt and delayed, prompt-prompt, and delayed-delayed γ rays gated with different particle and time range conditions. The technical realization was the same as in the pre-sort (see Sect. 3.1), only the user subroutine, again in event-by-event mode, was changed in order to satisfy the new goals addressed in the sorting:

- based on the aligned parameter spectra, set one- and two-dimensional gates to establish the particle and γ multiplicity;
- optimize the time range for isomer γ spectroscopy;
- implement when necessary additional processing of the parameters, i.e. like an *add-back* of the Ge γ-ray energy or a procedure to discriminate the true 2n or 3n events against events where neutron scattering has falsely increased the neutron multiplicity;
- sort the relevant data in various coincidence and non-coincidence spectra, symmetric and non-symmetric matrices and cubes for the use of further physics analysis (see Sects. 3.3 and 3.4).

Following the list order, Figs. 3.2 and 3.3 show sample two-dimensional (2D) spectra which are built during the pre-sort in order to visually inspect the spectra and manually set particle 2D gates (*bananas*). The ancillary particle-detectors' spectra of different detectors are not gain matched. In this work, they were used only for particle gating and therefore it was easier to set individual 2D gates for each detector, rather than gain match and calibrate the ancillary detectors. The 2D gate for γ rays on Fig. 3.2 was practically not used and is shown only for completeness. The important message of Fig. 3.2 is that the performance of the Neutron Wall together with the approach of plotting ZCO vs. TOF result in a perfect separation of the neutrons and γ rays registered by the neutron detectors. Figure 3.3 also shows the typical charged particle telescopes approach to plot the ΔE vs. E 2D spectrum. It has a very good separation of the one-proton, two-proton and α-particle events located in different regions, marked by the corresponding 2D gates which were used in the sorting procedure. This easy discrimination is not found, for example, in the corresponding 1D spectrum of the ΔE energy, shown in the inset of Fig. 3.3. The advantage of the 2D over the 1D discrimination is obvious. In case when only one of the ΔE-E telescope detectors is working, i.e. present, 1D gates can still be set to discriminate the light charged particles, although less effectively than on the 2D plot.

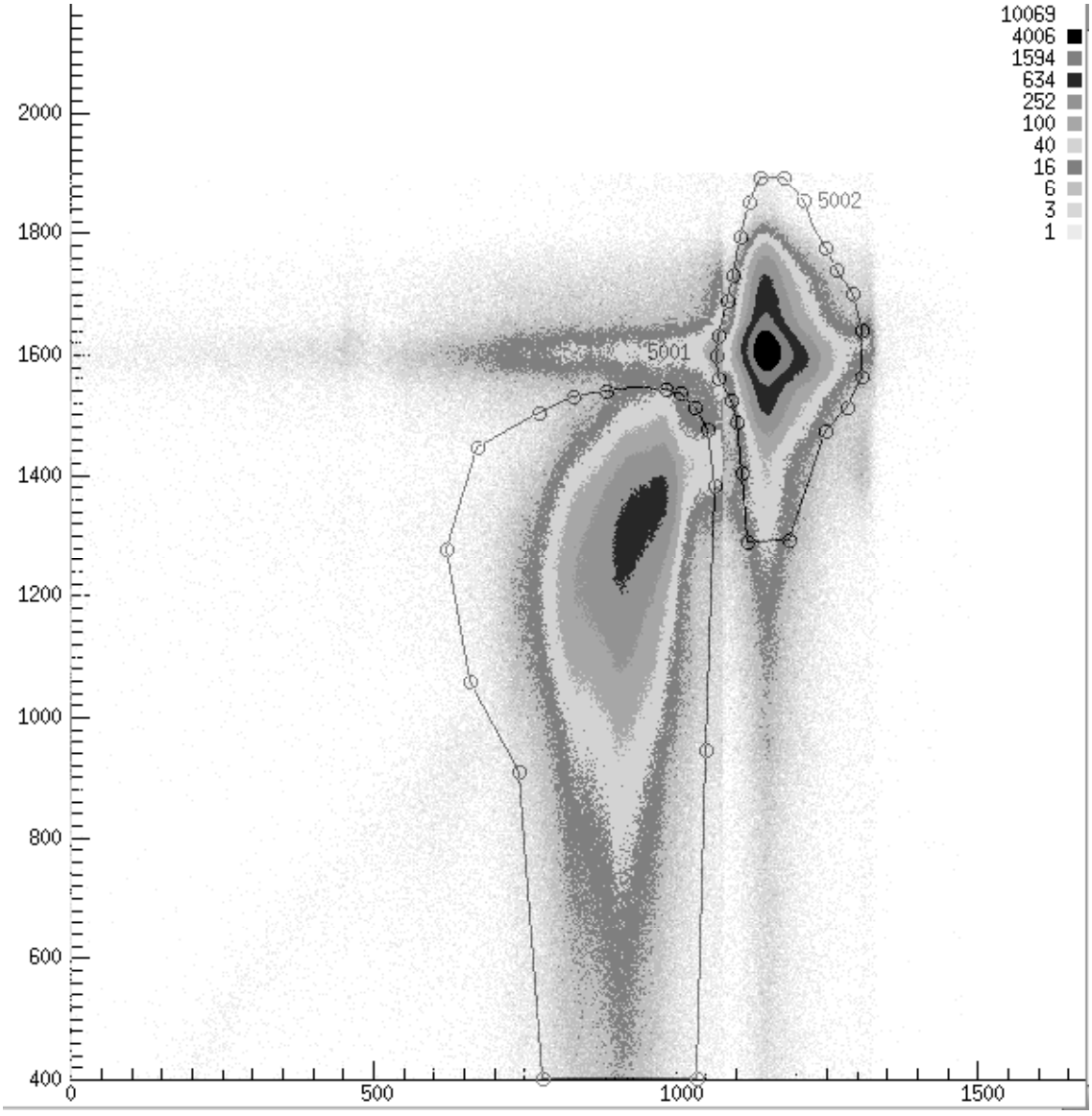

Figure 3.2: A typical Neutron Wall ZCO(abscissa) vs. TOF(ordinate) two-dimensional spectrum showing the perfect n-γ discrimination of this approach, and the corresponding two dimensional gates used in the sorting procedure. The time is running to the left and to the bottom, correspondingly.

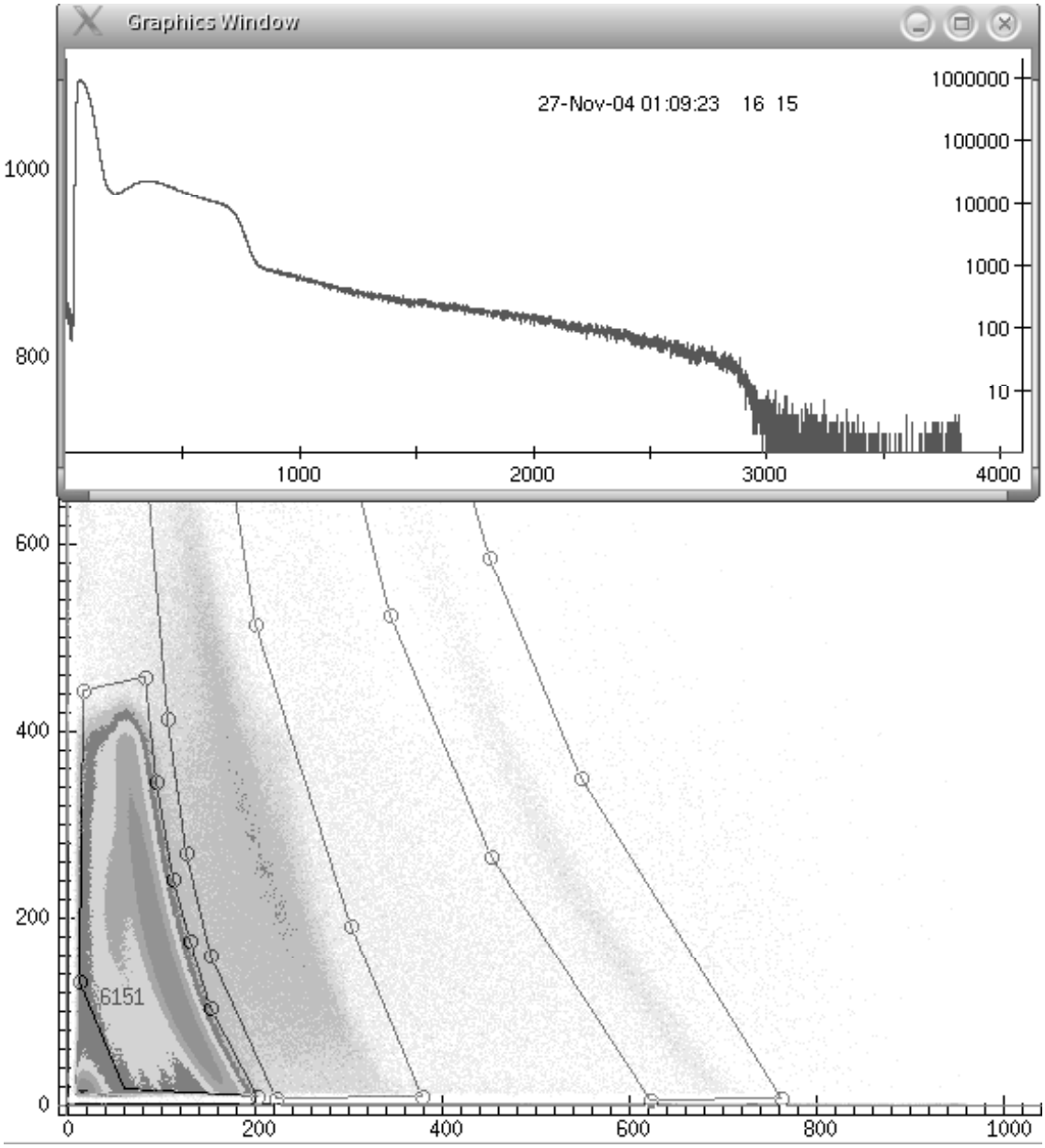

Figure 3.3: A typical EUCLIDES ΔE vs. E two-dimensional spectrum showing the discrimination of the one-proton, two-proton and α-particle events separated in different regions marked by the corresponding two dimensional gates used in the sorting procedure. For comparison in the inset, the one dimensional spectrum of the ΔE energy is shown.

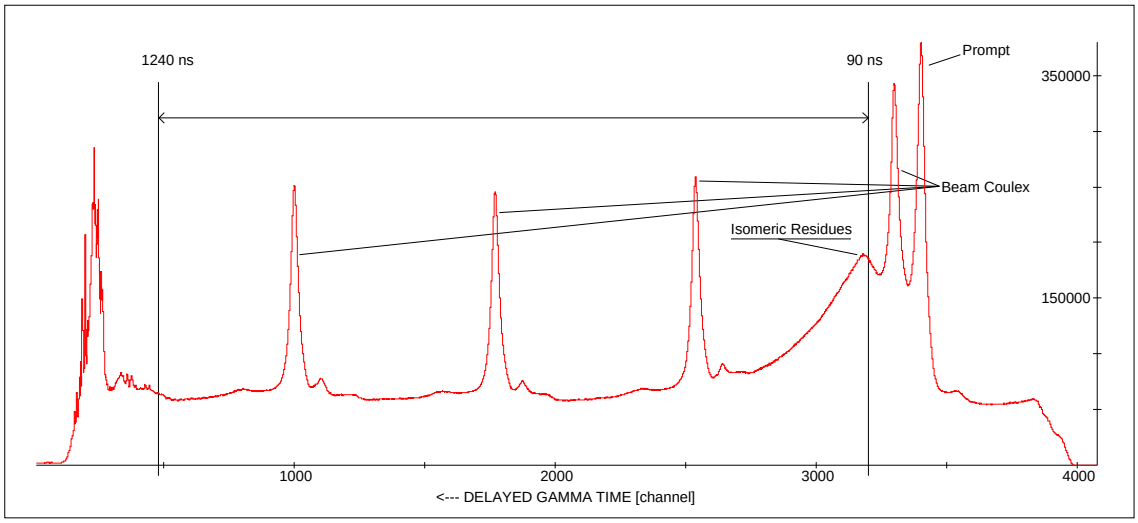

Figure 3.4: The total sum of the delayed γ time spectra. The time increases to the left. Isomer γ spectroscopy for $A \sim 100$ is optimal in the time range $90 - 1240$ ns, which is marked on the plot. The equally spaced comb-structure peaks are result from the Coulomb excitation of the RF-pulsed beam. See text for details and Sect. 3.4.1 for time calibration.

Figure 3.4 shows the sum of the delayed γ time spectra, or as could also be said – the total projection of the delayed γ energy-time matrix onto the time axis. After analysis of the energy-time matrix, and additional inspection of some strongly populated isomers, mainly the 8^+ isomer in ^{100}Cd [Albe92, Górs94] (see Sect. 3.4), the optimum time range (window) for isomer γ spectroscopy could be determined. It is indicated on Fig. 3.4 and ranges from 90 to 1240 ns after arrival of the beam pulse on target. The lower limit is due to the time of flight of the residues, while the upper limit is set to avoid the electronic noise at the end of the time range (see channels on the left on Fig. 3.4). There are 1.9×10^8 delayed γ rays present in the time window optimized for isomer spectroscopy. It should be noted that unfortunately, the larger portion of these γ rays comes from the β-decay of the longer-lived activity built-up on the catcher foil (see Sect. 3.3). An immediate inspection of the time spectrum shows the following. The peak at channel 3400 corresponds to the prompt γ burst detected at the catcher position after a γ-ray flight (target $\rightarrow$ catcher) time of 4ns, and it is used to give the time zero of the event. Therefore, the background found earlier in time, i.e. channels above 3400 on Fig. 3.4, corresponds to β-delayed γ rays, which follow decays with half-lives much longer than the measurement time window and therefore give a flat background time distribution. Now, looking in time after the time zero of the event, i.e. at channels below 3400 on Fig. 3.4, one can see a similar peak close to the prompt γ peak. This second peak corresponds to the γ-rays following the Coulomb excitation (Coulex) of the beam nuclei in the catcher foil.

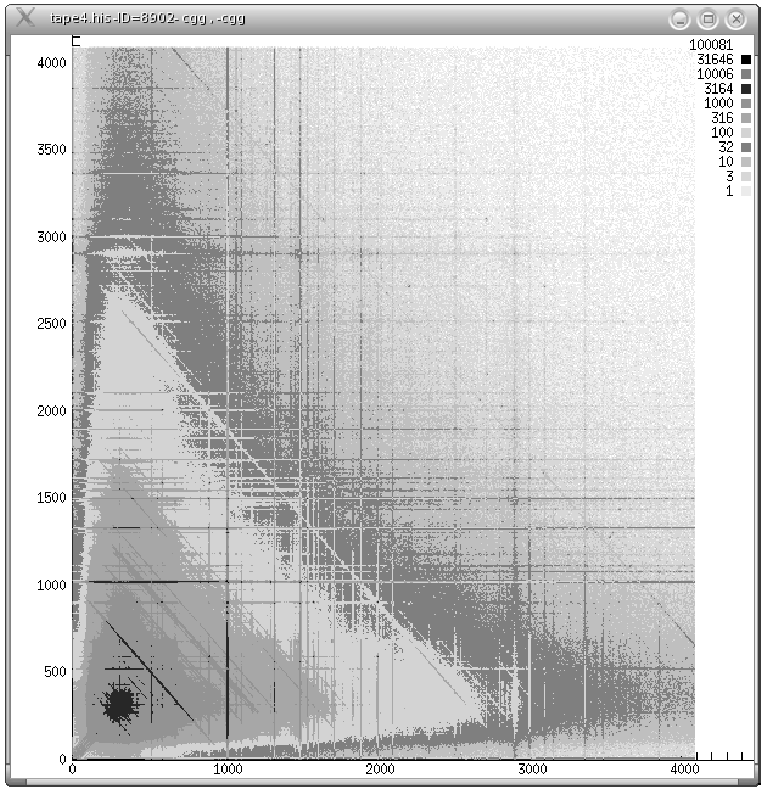

Figure 3.5: The $\gamma\gamma$ coincidence matrix for part of the pre-sorted delayed γ rays. Both axes show energy in channels. The diagonal lines with $x + y = const$ show Compton-scattered γ rays.

Since the beam pulse repetition time is shorter than the measurement window there appears a regular comb-like peak structure. Starting with the first Coulex peak in the time spectrum, one can follow and see several such peak in the channels below 3000 on Fig. 3.4. This structure was used to manually gain-match the time response of the delayed γ spectrometers and to time calibrate the spectrum (see Sect. 3.4).

Finally, the sorting procedure included an add-back for prompt and delayed γ-rays detected in the neighbouring crystals of a composite Ge detector. This procedure has been discussed many times [Hu98a, Wilh96, Lalk03] and applied especially to improve the γ-efficiency for high energies. To illustrate the necessity of add-back in this work, Fig. 3.5 shows the $\gamma\gamma$ (energy) coincidence matrix built for part of the pre-sorted delayed γ rays. The diagonal lines of the type $x + y = const$ show intensive γ rays which have Compton-scattered once and have been detected as two γ rays. Therefore to restore the initial γ-ray energy, an add-back is applied during the event-by-event sorting. This add-back algorithm checks in each event for γ-rays registered in different crystals but one composite detector, and depending on the relative geometrical position of the "fired" crystals decides if the γ-ray energies

detected in the single crystals should be added-back or not.

In order to properly do the add-back one needs to include γ rays from the very beginning of the measurement time window, since the "start" of a Compton-scattered γ ray could be earlier than the isomer spectroscopy optimized time window (see Fig. 3.4). Therefore, during the sort γ rays with channels up to 4000 (see Fig. 3.4) were accepted. This is certainly true for the γ rays that "end" after the isomer spectroscopy window. But the presence of electronic noise at the end of the time range, made it dangerous to include γ rays after the upper limit of the isomer spectroscopy optimized window in the add-back procedure. Thus, in the sorting γ rays with time between channels 4000 and 480 (see Fig. 3.4) were added-back, but for building energy spectra and matrices, the range was reduced to time channels 3200 to 480 (see Fig. 3.4), since the other channels 3200 to 4000 contain irrelevant γ rays, which only contaminate the energy spectra.

3.3 Energy spectra

The energy and efficiency calibrations were performed using standard sources (i.e. ^{56}Co, ^{152}Eu and ^{133}Ba). The energy calibration of the delayed γ-spectroscopy array above 3.5 MeV was analyzed via comparison of extrapolations of first and second order polynomial fits and accounting for the energies of the single escape peaks. The relative efficiency of the downstream array was estimated by joining the calibration points from a ^{152}Eu + ^{133}Ba calibration run, which has its maximum calibration γ peak at 1408 keV (^{152}Eu), and a ^{56}Co calibration run which has a range of 848 keV to 3.5 MeV. The points in the overlapping range $848 - 1408$ keV were used for normalization of one relative efficiency curve to the other. Then all renormalized points were fit together and the resulting relative efficiency, shown on Fig. 3.6, was used in the γ-intensity analysis. Unfortunately, the absolute activity of the sources was unknown. Therefore, the absolute efficiency of the downstream array was estimated relative to the target array (Clusters and Clovers). In a separate measurement the absolute efficiency of the Ge-clusters plus Ge-clovers array was estimated to be 6.6% [DorvPC]. Using this value and knowing the absolute measurement time in the calibration runs at the target and the catcher, I could deduce the absolute efficiency of the delayed γ-spectroscopy set-up to be 2.8%. The specific goal to measure high-energy γ transitions predicted in the range $3.5 - 4.5$ MeV had to be adapted to the standard number of channels for matrices, i.e. 4096x4096 (4k x 4k). That is why Fig. 3.6 presents the energy calibration of 1.4 keV/channel introduced in the sorting of the delayed γ-ray spectra.

As discussed in Sect. 2.4.1, the add-back procedure could produce "phantom" peaks. In the add-back procedure, an intense γ line (E_s) could be added to another one (E_0), most often when both are in a prompt cascade. The intensity of the

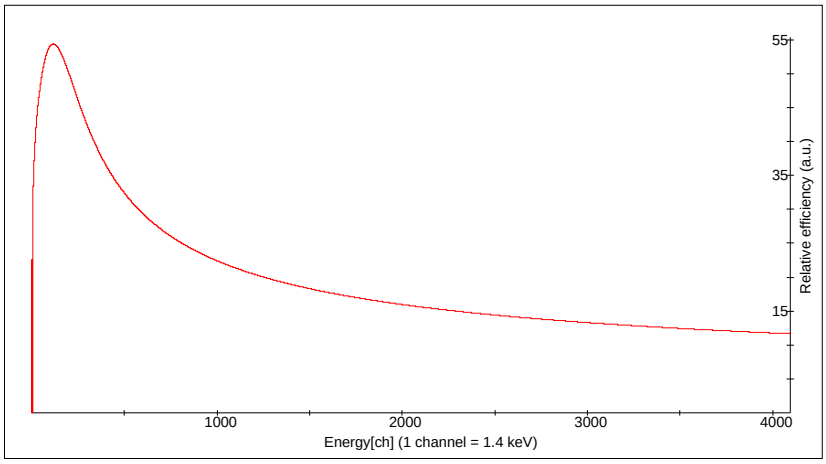

Figure 3.6: Relative efficiency for the sum of all Ge delayed γ detectors after the add-back procedure (see text for details).

"phantom" peak at $E_0 + E_s$ for the current add-back procedure was estimated to be $\sim 1.6\%$ from the intensity of E_0. Thus, to avoid the "phantom" the analysis would have to discard any γ lines with intensities less than 2%. On the other hand, the estimated increase of the γ intensity with add-back compared to the non-add-back spectrum is on average $\sim 16\%$, which shows the positive effect of the add-back on the relative γ efficiency, especially for the high-energy part of the spectrum.

The γ-ray energy spectra were analyzed exclusively with the help of the program GF3, part of the RADWARE package [Radf95]. Figure 3.7 shows several delayed γ-ray spectra. Plot (a) shows "singles" γ rays, i.e. without requirement for coincidence, in the full time range optimized for isomer spectroscopy (see Fig. 3.4). This is actually close to the spectrum produced with the original EUROBALL trigger. The dominating e^+e^- annihilation peak at 511 keV is a strong indication for the presence of β-delayed γ transitions. Plot (b) shows a spectrum produced by gating on the Coulex peak at time channel 1000 (see Fig. 3.4) with subtracted β-decay background. Therefore, the γ peaks seen on plot (b) are exclusively γ-transitions following the Coulomb excitations of the catcher foil material (^{93}Nb) and the ^{58}Ni beam. Plot (c) shows the β-decay background, which is seen by gating on time channels $550 - 850$ (see Fig. 3.4). This type of β-delayed γ transitions originate from the long-lived activity from evaporation residues built-up on the catcher foil. The highest portion of β-decay background comes from residues with the highest fusion-evaporation cross-section and their daughters from β^+/EC-decay chains, i.e. ^{102}In, ^{100,101,102}Cd and ^{100,101,102,103}Ag. Plot (d) shows the γ-energy spectrum created by a gate on time channels $2800 - 3200$ (see Fig. 3.4) with subtracted β-decay background. Since the gated region corresponds to the arrival and decay of the initial isomeric states, the peaks seen on plot (d) do represent the γ decay of populated isomers. It should be

noted that in the high-energy region, i.e. the inset of plot (d), a peak at about 4.2 MeV is clearly visible. Finally, plot (e) of Fig. 3.7 shows an energy spectrum for the full time range optimized for isomer spectroscopy, like plot (a), but this time with a particle gate, i.e. on α, proton and neutron multiplicity, such as that the α2n exit channel of ^{98}Cd is selected with highest statistics (see below). It is again worth noting that the inset of plot (e) contains, even cleaner, the 4.2 MeV high-energy peak. Eventually, this peak was attributed to the γ-transition de-exciting the core-excited isomer in ^{98}Cd.

The "singles" γ-ray spectra with various combinations of coincident particles were used for the identification of the reaction exit channel. The high-energy part of the γ-ray spectra created with different particle conditions is shown in Fig. 3.8. The relative intensity of high-energy γ-transition 4207 keV shows a clear dependency on the particle gate. Inspecting Fig. 3.8 one can draw the following conclusions. First, the absence of the line in the 1p gate and the high efficiency for protons, proves that proton exit channels are excluded. Second, the presence of the 4207 keV in the gates with evaporation of neutrons and α clearly testifies a $x\alpha y$n exit channel. The standard exit-channel analysis involves taking ratios of the γ-peak intensity in different particle gates and then plotting these ratios with their error-bars. The position of the intensity ratio relative to theoretically calculated values is then used to assign the most probable particle exit channel. The method applied here is described in Appendix A and the results are shown on Fig. 4.8 in Sect. 4.2.1.

The fact that the ^{98}Cd exit channel is α2n was used to decide on the optimum particle gate for the ^{98}Cd γ-ray analysis. To exploit the full statistics all possible particle conditions were used for the summed energy and time spectra, namely 0α0p1n, 0α0p2n, 0α0p3n, 1α0p0n, 1α0p1n, 1α0p2n and 1α0p3n (see Fig. 3.8). Since discrimination of the scattered neutrons was not applied, the 3n condition also provides γ-rays correlated with the (1α2n) exit channel. Therefore, the analysis of ^{98}Cd delayed γ rays employed both the optimum particle gate and the optimum isomer-spectroscopy time range. Figure 3.9 shows the x-projection of the $\gamma\gamma$-matrix created with the above particle and time gate. The origin of the marked γ peaks is now easy to determine, looking at the different plots of Fig. 3.7. The rich spectrum, shown on Figure 3.9, testifies the complexity of the delayed γ analysis and the high level of contamination, which in many cases "hides" the low-energy γ transitions of interest. The inset shows the high-energy part with the pronounced high-energy peak at 4207 keV. Since 4207 keV belongs to the ^{98}Cd exit channel (see Fig. 4.8), it is expected that this γ line is in mutual coincidence with the known delayed ^{98}Cd γ-ray transitions [Górs97]. This is shown in Fig. 4.9 (see Sect. 4.2.1). In the actual analysis, however, the order of cross-checking was the reverse one, i.e. initially, the 4207 keV line was discovered to be in mutual coincidence with the known ^{98}Cd γ-ray transitions [Górs97], and only then, the exit channel was determined via particle gates and ratios (see Figs. 3.8 and 4.8).

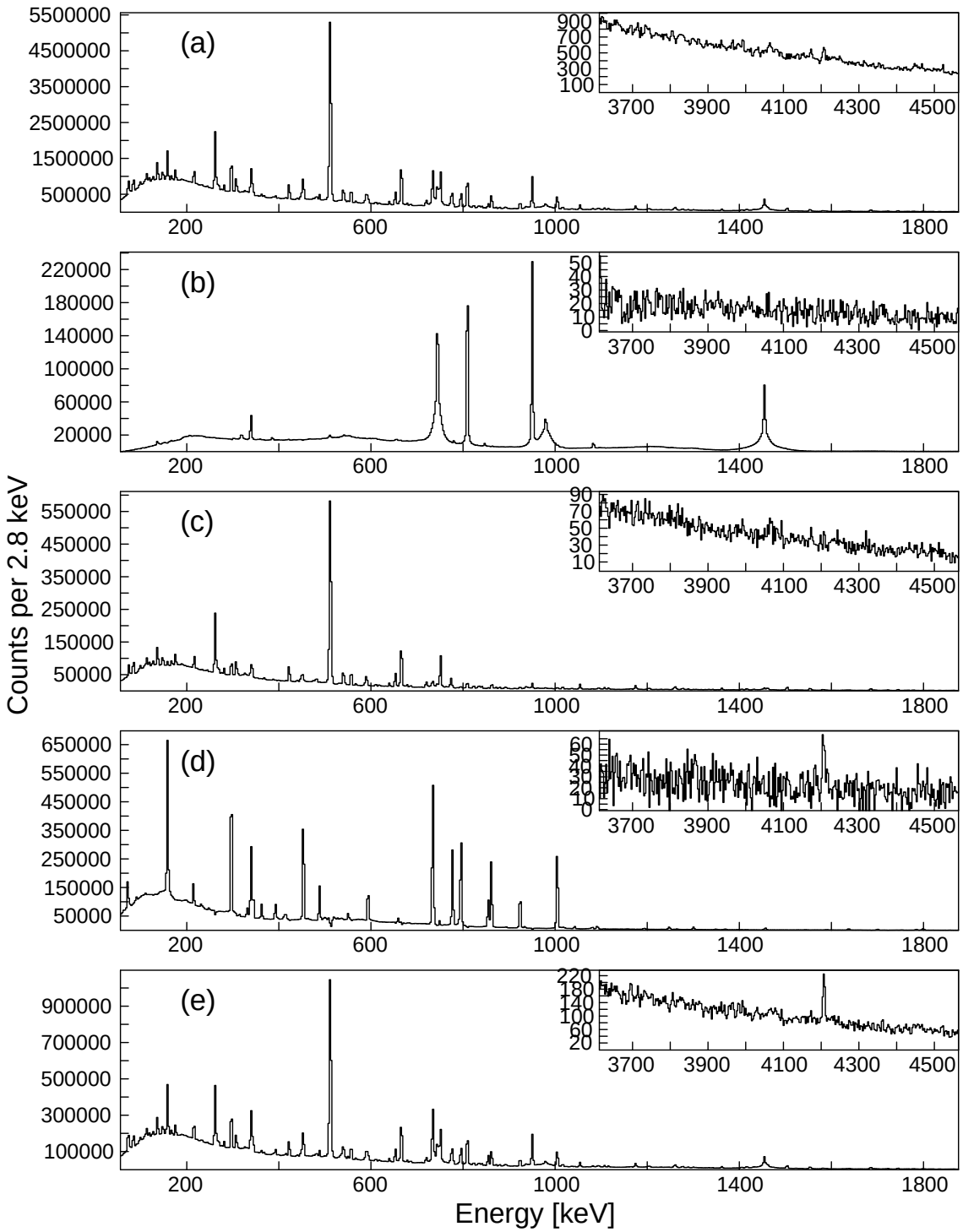

Figure 3.7: The "singles" delayed γ rays, with various gates on time (see Fig. 3.4): (a) – all γ rays for the isomer-spectroscopy optimized range , (b) – gate on the Coulex peak at channel 1000 with subtracted β-decay background, (c) – gate on time channels $550-850$, i.e. mostly β-decay background, (d) – gate on time channels $2800-3200$ with subtracted β-decay background, i.e. mostly isomer γ decay transitions, and (e) – like (a) but with a particle gate optimized for ^{98}Cd exit channel. The insets show the corresponding high-energy part. See text for details.

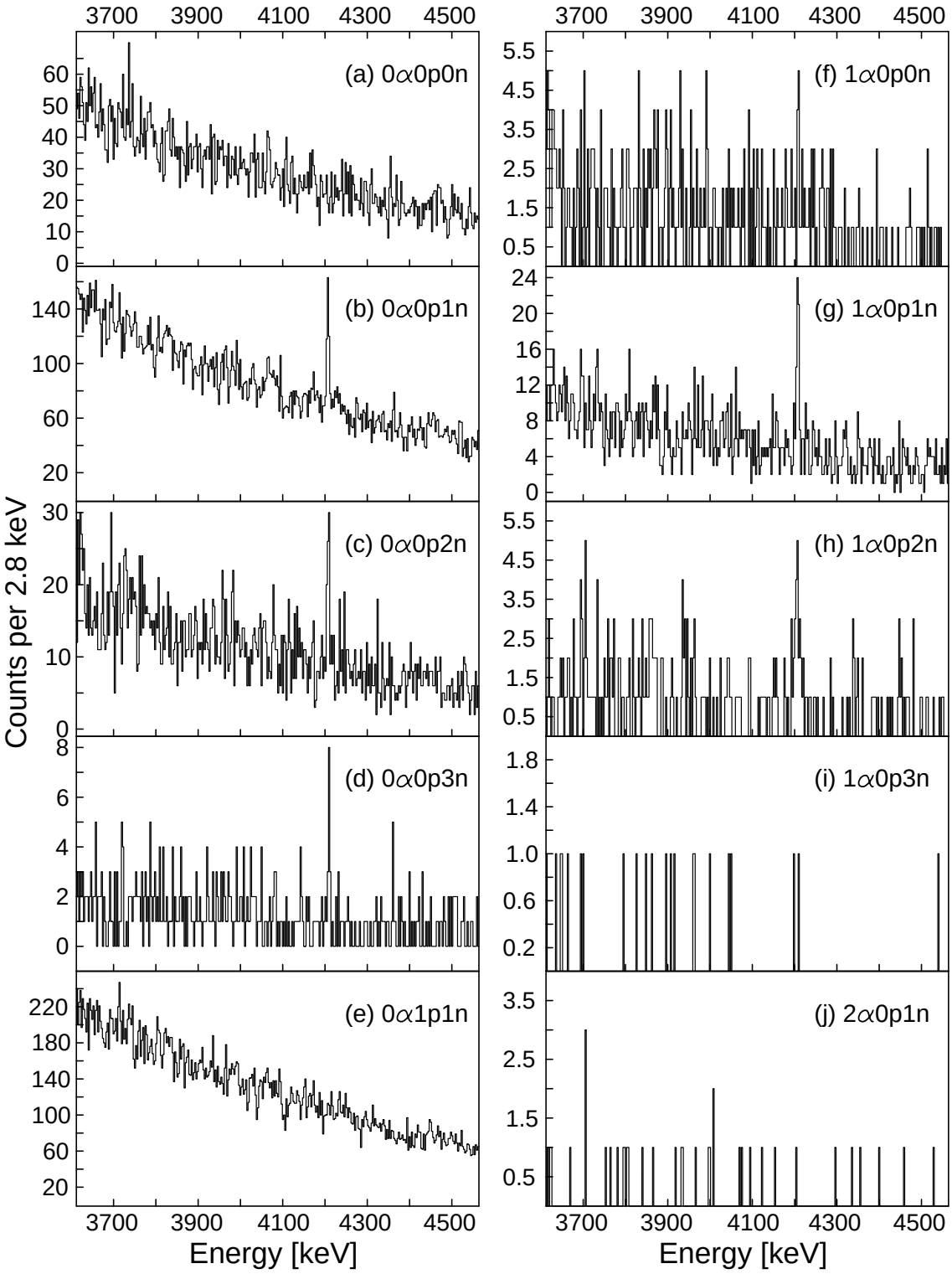

Figure 3.8: High-energy portion of the "singles" γ-ray spectrum gated by various conditions on evaporated particles as follows: (a) $0\alpha0p0n$, (b) $0\alpha0p1n$, (c) $0\alpha0p2n$, (d) $0\alpha0p3n$, (e) $0\alpha1p1n$, (f) $1\alpha0p0n$, (g) $1\alpha0p1n$, (h) $1\alpha0p2n$, (i) $1\alpha0p3n$, (j) $2\alpha0p1n$.

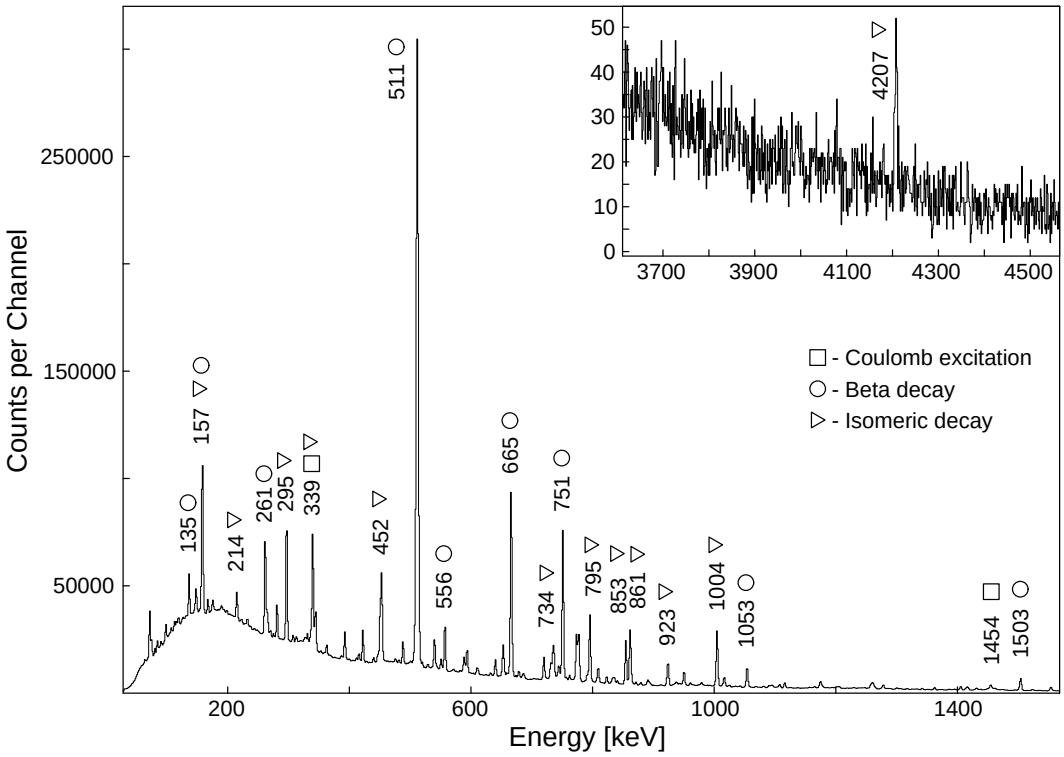

Figure 3.9: The x-projection of the delayed $\gamma\gamma$-coincidence matrix, created with particle gate on 0α0p1n, 0α0p2n, 0α0p3n, 1α0p0n, 1α0p1n, 1α0p2n and 1α0p3n. The legend in the plot shows the origin of the marked γ peaks.

3.4 Time spectra

There are certainly some important prerequisites in order to extract half-life information from time-proportional spectra. The first one is to calibrate the spectral channels into time units. The second is to find the best estimate of the possible background in the time spectrum. Then if possible to subtract it from the gated time distribution, and also take the background into account when applying a decay fit to the distribution. In addition, the type of the decay fit function and the region to which it is applied is also an important issue. Having in mind all of this, one can see how difficult it is to reliably determine a half-life.

These subjects and their concrete application are addressed in the following, where I will concentrate explicitly on the time spectra of the delayed γ spectrometers, since they could give us the information about the measured decay of isomeric states.

3.4.1 Single exponential fit

The first step, as already mentioned, is the time calibration. It was determined on the basis of the peaks generated by the Coulex γ activity of the RF-pulsed beam (see Fig. 3.4). The frequency of the beam was a little bit higher than 3 MHz, so that the distance between two peaks is $\Delta t = 327.12$ ns and taking the average distance of the Coulex peaks in the spectrum, the corresponding time calibration constant is $a_t = 0.42483\ \frac{ns}{ch}$. Other information about the sum time-spectrum is the time resolution of the spectrum, which is influenced by the quality of the alignment and the gain-matching, the internal time resolution of the detectors, the beam pulse length and the half-life of the Coulomb-excitation transitions forming these peaks. The FWHM of a beam Coulex peak in the sum time spectrum is $\simeq 16.14$ ns. Since the half-life of the Coulomb excited levels is in the picosecond range, its contribution should be negligible. Therefore the main effect on the resolution is considered to be the combined effect of the internal time resolution and the beam pulse length. The small differences in the distances between the Coulex peak could be a hint for some problems of the alignment or about non-linearities in the TDC modules, but in this work this effect was not studied.

Since the production rate of ^{98}Cd is very small ($20(10)\mu b$ [Górs97]), one needs a test case to optimize the analysis procedure. Therefore, in order to optimize the background subtraction, the fitting range and the type of the fitting function, the time distribution of the strongly populated 8^+ isomer in ^{100}Cd was studied in detail. The time distribution shown on Figs. 3.10 and 3.11 is a result of a gate on the γ transition of 1004 keV following the γ decay of the ^{100}Cd isomer. The optimized background subtraction results in the disappearance (see Fig. 3.10) of the Coulex-peaks structure. Here, the direction of the time axis is still reversed but beside the sign of the exponent this does not change the conclusions of the study.

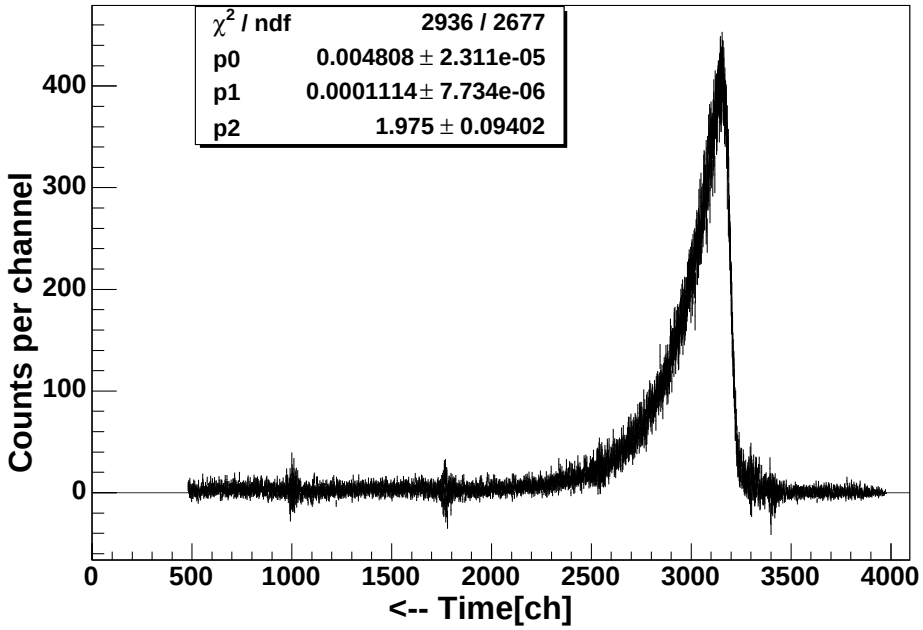

Figure 3.10: Background subtracted time distribution of 1004 keV γ line (^{100}Cd) with error-bars. The fit parameters are given in the inset, while the fit function is discussed in the text. The time increases to the left.

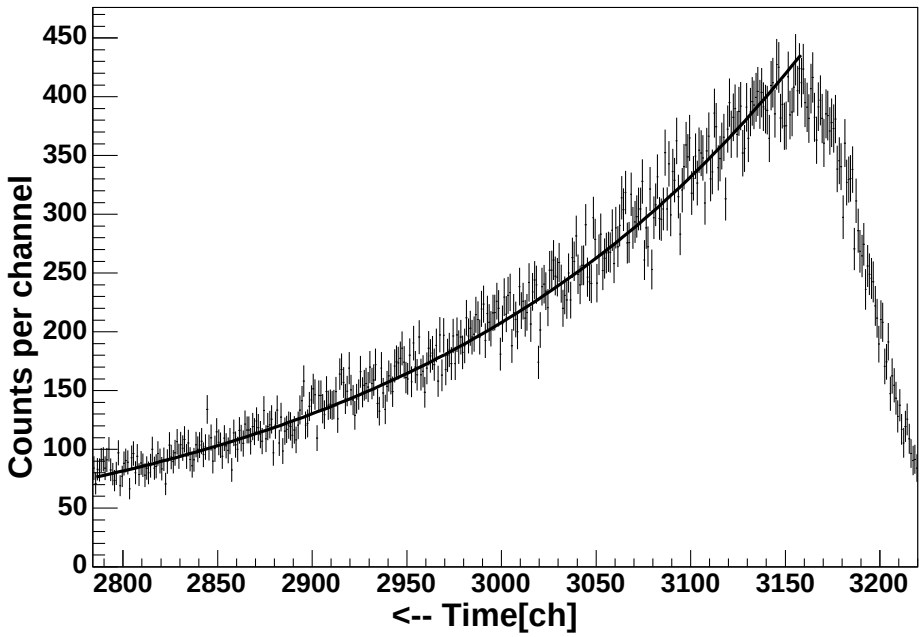

Figure 3.11: This figure is a zoom showing channels $2800-3200$ of the plot from Fig. 3.10. Here, the fit function and the individual channel values with their error-bars are visible. The fit parameters are shown on Fig. 3.10. The time increases to the left.

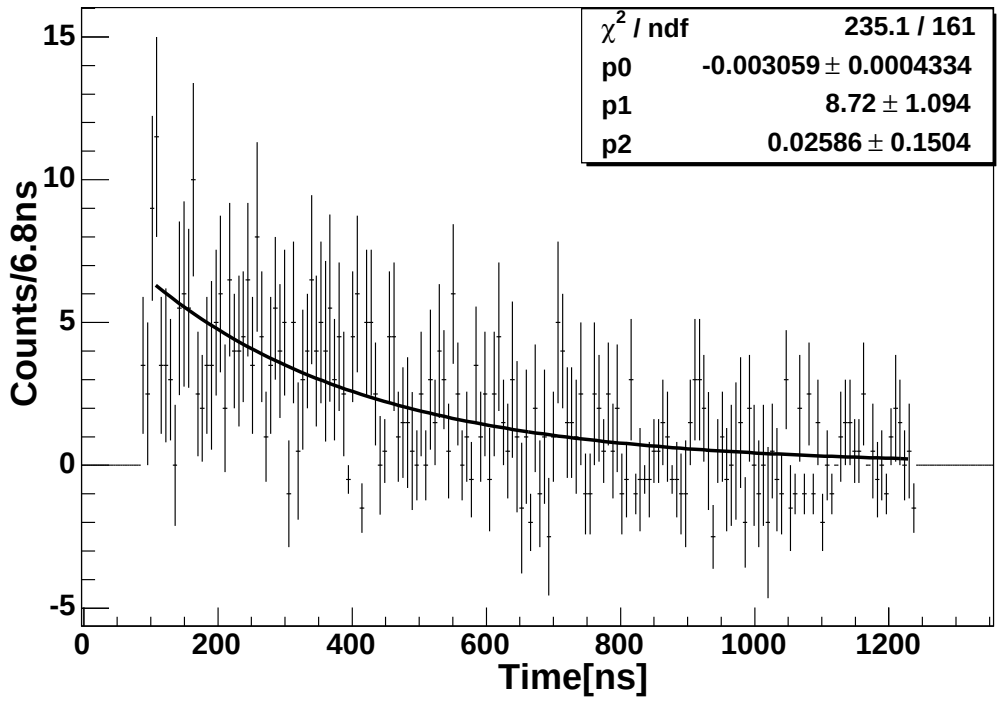

Figure 3.12: The background subtracted time distribution gated on the 4207 keV γ ray. The fit is done by the ROOT package [Brun96]. The fitting method and function are discussed in the text.

Even with the very good background subtraction, the inclusion of a constant background parameter in the function was tested and improved the fit. Thus, the fitting function used for further half-life determination, including the half-life of the core-excited isomer in ^{98}Cd, had finally this form:

$$f(x) = p2 + p1 * e^{p0*x} \ , \tag{3.4}$$

where $p2$ is a parameter for the constant background, $p1$ corresponds to N_0 in the radioactivity law formula (1.8), while $-p0 = 1/\tau$. The result from this fit for the half-life of the 8^+ isomer in ^{100}Cd, with a conservative error estimate, is 61(1) ns, which is in perfect agreement with, and more precise than, the known value of 60(3) ns [Górs94].

An inspection of Fig. 3.11 gives additional information on the beginning of the optimum fitting range, i.e. which points should enter in the fit. For the beginning of the fit this is related to the TOF of the residual nuclei, which in this reaction depends on their mass and velocity distribution due to reaction kinematics. The end of the fitting range was just equal to the end of the time window optimized for isomer spectroscopy (see end of Sect. 3.2). The similarity in mass of ^{98}Cd and ^{100}Cd suggested for the fit of ^{98}Cd to use the fitting range optimized in the case of ^{100}Cd

without further modifications.

The background subtracted time spectrum, in ns, gated on the 4207 keV transition is shown on Fig. 3.12. The fit shown on Fig. 3.12 includes the optimized fitting range $102^* - 1240^*$ ns. It is marked with *, because these numbers are not corrected for the TOF of prompt γ rays, which are used to set the time zero in the delayed γ spectrum. This TOF of prompt γ rays from target to the catcher position is about 4 ns depending on the velocity distribution and therefore the real time of the range is $106 - 1244$ ns. The absolute time does not affect the fit and is mentioned here only for completeness. The formula (3.4) was programmed as a user fitting function in the fitting routine of the ROOT package [Brun96]. For small statistics the maximum-likelihood method gives better results than the χ^2 method. Therefore the maximum-likelihood method included in the ROOT fitting package was used together with the option for fitting non-integer values of x and y, since the time-calibrated background-subtracted spectrum, which was fitted, had non-integer x and y values. Another detail is that some points of the time distribution have negative values, which is due to the background subtraction and the discreteness (discontinuity) of the spectra. Negative values of time distribution, of course, do not have a physical meaning, but have their weight in the fit. The result is presented in Sect. 4.2.2 and discussed 6.2.2.

3.4.2 $\gamma\gamma$ time difference

After the half-life of the higher-lying (12^+) isomer in ^{98}Cd (see Sects. 4.2.3 and 6.2.1) has been determined, one can address the half-life of the lower-lying (8^+) isomer, which so far had two contradicting values 460(160) ns [Górs97] and 190(20) ns [Grzy98] (see Sect. 6.2.2). Therefore this work was important for solving the issue. It is now obvious that the longer value of the experiment employing a fusion-evaporation reaction [Górs97], which populates mostly high-spins (see Sect. 2.1.1), was influenced by the newly discovered higher-lying (12^+) isomer [Blaz04]. On the other hand the value of the experiment employing projectile fragmentation of ^{106}Cd [Grzy98], shown to populate mostly low-spins (see Sect. 2.1.2), was probably little distorted by the (12^+) isomer, and therefore close to the true value.

The $\gamma\gamma(\Delta t)$ method, as its name shows, uses the coincidence of two γ rays and takes the time difference between them to build a time distribution. In other words, the first γ ray is used to give the "start" and the second one to give the "stop" signal for the time distribution. Usually the first γ ray is directly above the isomeric level of interest, while the second one is the one that de-excites the level. One can understand this, for example, by looking at Fig. 4.13 and considering the following scenario. The emission (detection) of 4207 keV γ transition actually gives the time zero of population of the (8^+) isomer. And then the emission (detection) of 147 keV γ transition would mark the decay of the this isomer. Figure 3.13 shows part of the

2D-matrix produced by requiring a $\gamma\gamma$ coincidence where one of the γ rays is the 4207 keV γ ray, and then plotting the energy of the other coincident γ rays versus the time difference relative to the time of the 4207 keV γ ray. The time differences are always calculated by subtracting the time of the 4207 keV line. Therefore the sign of this time difference shows whether the other γ ray was before or after the emission of the 4207 keV γ ray. One can see in Fig. 3.13 the regions and the arrows marking the energy positions of the ^{98}Cd γ-lines known prior to this work [Górs97]. Their time difference distributions are in all cases positive, which clearly fixes the fact that 4207 keV line precedes them, and thus, the only possible placing of the 4207 keV line is on top of the (8^+) state in the known level scheme [Górs97].

Now, looking at the time difference distribution of the 147 keV γ ray (Fig. 3.13), there are several problems. The first one is that statistics are small and the visible intensity of the neighbouring background is comparable with the Δt distribution. Thus, a reliable single-exponent-decay fit for $\gamma(4207)\gamma(147)(\Delta t)$ cannot be performed. One can think of another approach to use this $\gamma(4207)\gamma(147)(\Delta t)$ for extraction of the (8^+) half-life, namely the *centroid-shift method* [Andr82]. Running ahead, this method is also not applicable for $\gamma(4207)\gamma(147)(\Delta t)$ due to low statistics which prevents finding reliably the zero-time line for this low-energy region. Details about this method and terms are given in Sect. 3.4.3. So the solution was to take the Δt distribution of another γ-ray below the (8^+) isomer. This was possible for the $\gamma(4207)\gamma(1395)(\Delta t)$ and $\gamma(4207)\gamma(688)(\Delta t)$. Both are practically background free and the issue of the shifted zero-time is not relevant for their energy ranges (see Fig. 3.13). Both Δt distributions have been fitted independently with the fitting routine of the ROOT package. As in the case of the t(4207) distribution (see Sect. 3.4.1), the maximum-likelihood method was used together with a single exponent fit, this time without a parameter for constant background. Then a result for the half-life was found from the weighted average of both fits. Alternatively, the sum distribution of $\gamma(4207)\gamma(1395)(\Delta t)$ and $\gamma(4207)\gamma(688)(\Delta t)$ was built and a fit, as described above, was performed, which gave the final result of 170^{+60}_{-40} ns value (Fig. 4.11) for half-life of the (8^+) isomer [Blaz04] (see also Sects. 4.2.2 and 6.2.2).

In addition, the small statistics inspired the author to apply another test to the Δt distributions just to inspect better their characteristics. The new statistical test procedure, developed by K.-H. Schmidt [SchKH00] for the analysis of α-decay chains in superheavy elements studies, allows to evaluate whether a set of radioactive-decay data is compatible with the assumption that these data originate from the decay of a single radioactive species. This test is applicable to samples of exponential distributions with two or more events and therefore the resulting $\gamma\gamma(\Delta t)$ distributions with second gate on 1395 keV and 688 keV, shown on Fig. 3.13, were examined with this procedure. The tests proved that both Δt distributions match the criteria to have radioactive-decay origin. This also shows that the background is negligible, otherwise the figure of merit would be outside the limits [SchKH00].

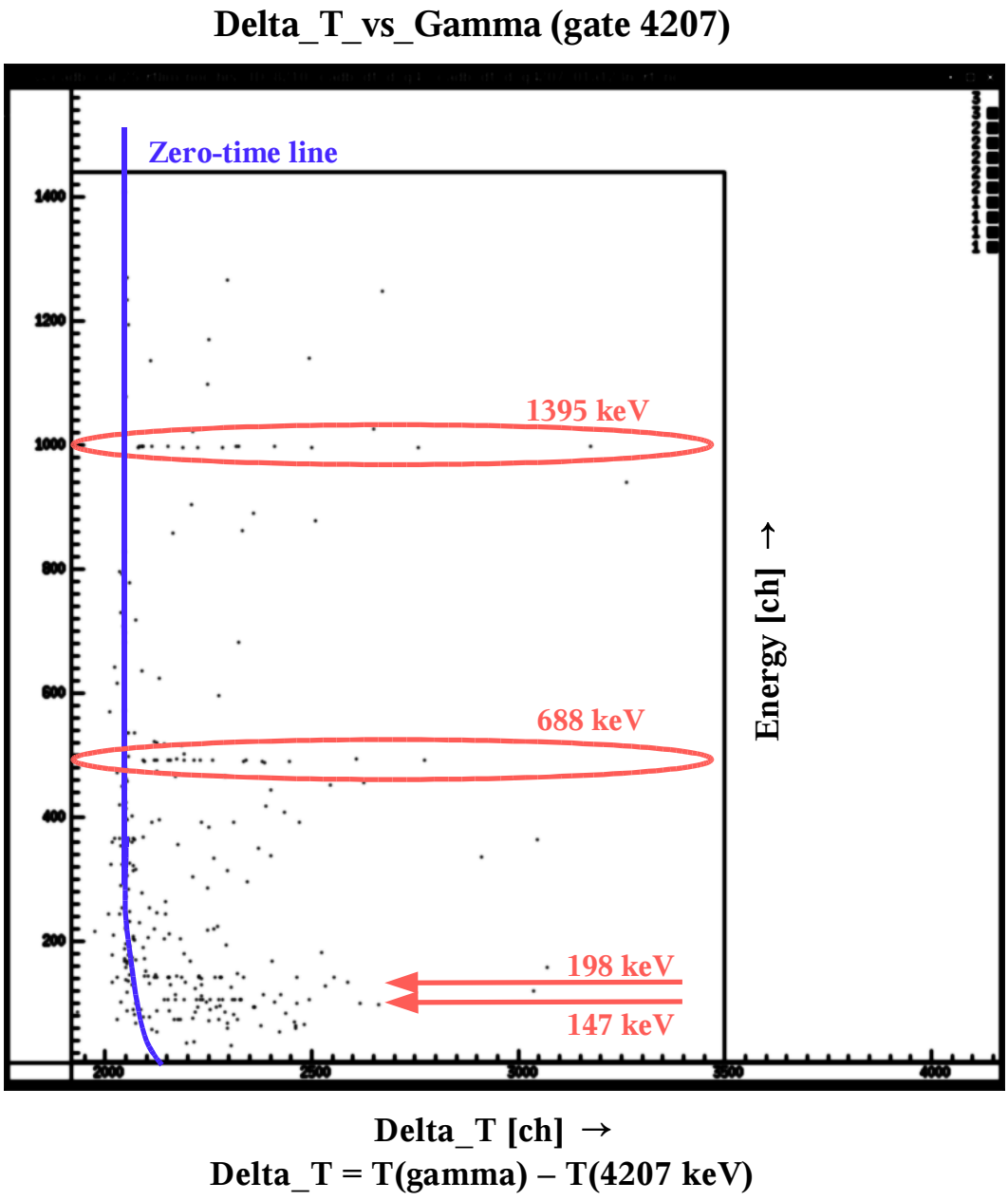

Figure 3.13: A two dimensional plot of part of the coincidence matrix produced by sorting the experimental data, requiring a $\gamma\gamma$ coincidence where at least one of the γ rays belongs to the 4207 keV energy window, and building the time difference of the coincident γ-ray times. The marked regions and arrows show the energy position of the previously known ^{98}Cd γ transitions. Their positive time difference distributions show that they clearly proceed after the 4207 keV transition. The zero-time line is drawn only to guide the eye.

3.4.3 Centroid-shift method

The centroid-shift method was introduced already in the year 1950 by Bay [Bay50, Bay52], who continued and developed the "Statistical theory of delayed-coincidence experiments" [Bay55]. In its simplest form the method uses the fact, that the lifetime of the single-parent decay is equal to the first moment, e.g. the centroid, of the decay time-distribution. Later, the generalized centroid-shift method was introduced by Andrejtscheff *et al.* in Ref. [Andr82]. The authors gave also a specific procedure for the analysis, which is applicable for contemporary, also high-resolution, detector systems. Certainly, the method needs the decay time-distribution and its centroid. But it also requires the precise determination of the beginning or the "zero" of the time axis. Since the γ rays experience "walk" with energy, i.e. the response of the detector timing unit (constant fraction discriminator) is dependent on the energy (i.e. pulse height) with an increasing delay when γ-ray energy is reduced, one has to determine the zero for all the necessary energies. The set of all time-zero or zero-time points for different energies builds the time-zero line. It is known [Andr82], that the Compton-scattered γ rays provide a good estimate (with precision $\sim$0.3 ns [Andr82]) of the time-zero point. The authors point out that the RF-signal of an accelerator, often has worse time definition than the Compton background. The Compton background from both sides of the γ line of interest can be used to determine the time-zero points and then interpolate between them to find the time-zero point for the energy of interest. Once the time "zero" is known, one can find the centroid of the decay time-distribution and take its difference, which would give then the lifetime of the decay.

The power of this method is that it can be applied for half-lives in the range around and even below the time resolution of the detector system. For longer half-lives one can obviously use the slope method, i.e. fitting with an exponential function.

In order to estimate the possible half-life of the (6^+) level in ^{98}Cd [Górs97], one can apply the centroid-shift method. In fact, the above introduction of the method suggests to use it, since the resolution of the delayed γ time-spectra, in this work $\sim$ 16 ns (see Sect. 3.4.1), is of the order of the shell-model predicted half-life for the 6^+ state, i.e. $10 - 20$ ns [Górs97].

To build a time distribution characterizing the decay of the (6^+) state, one has to relate two γ rays – one from above the level, and one from below. The experimental level scheme (Fig. 4.13) and the higher-lying (12^+) and (8^+) isomers imply that one of the transitions is the 147 keV one. As the second γ transition in the analysis, any of the 198, 688 or 1395 keV γ rays could be taken. As for the distribution $\gamma(147)\gamma(1395)(\Delta t)$ it would be difficult to check the time-zero line with other "prompt" transitions, and the $\gamma\Delta t$ matrix would be much dirtier, this work used the reverse distribution $\gamma(1395)\gamma(147)(\Delta t)$ (see Fig. 3.14). It provided a proper

cleanness of the secondary γ-spectrum, as well as enough Compton background in the energy region of 147 keV. Then, the centroids of the background (time-zero) and the background-subtracted "147 keV"-gate were determined. An important check was that the position of the time centroid of the other two γ lines, at 198 and 688 keV, lies on the time-zero line (see Fig. 3.14). The final result is presented on Fig. 4.12 (Sect. 4.2.2) and discussed in Sect. 6.2.2.

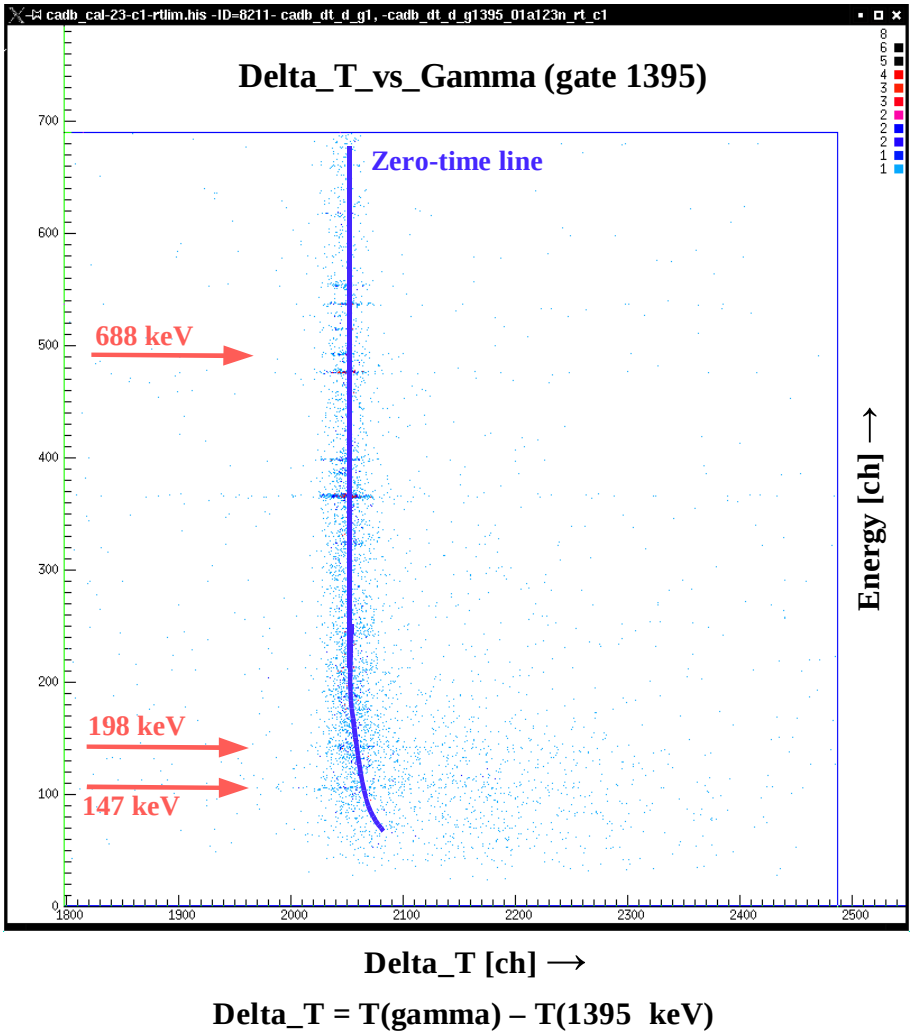

Figure 3.14: A 2D plot of part of the coincidence matrix $\gamma\Delta$t produced by requiring a $\gamma\gamma$ coincidence where at least one of the γ rays belongs to the 1395 keV energy window, and building the time difference of the coincident γ-ray times, similar to Fig. 3.13. The marked regions and arrows show the energy position of previously known ^{98}Cd γ transitions. The zero-time line is drawn only to guide the eye.

Chapter 4

Experimental Results

4.1 Results for ^{100}In

In this section the author presents exclusively experimental results on β-decay of ^{100}In. As already noted the analysis of the high-resolution $\beta\gamma\gamma$ data was done by Dr. C. Plettner, while Dr. L. Batist has analyzed the TAS data. These experimental results are published by Plettner *et al.* in Ref. [Plet02] together with the shell-model calculation results, which are part of this work. Therefore, it is necessary to show not only the theoretical approach (see Sect. 5.2.1), which have been used to assign configurations to states in ^{100}In and ^{100}Cd, and the calculated GT-strength distribution, but also the experimentally observed one. In order to make conclusions about the nuclear structure in this region, a general discussion and comparison between experimental and theoretical results is done in Sect. 6.1.

4.1.1 High-resolution $\beta\gamma$ spectra and β-decay half-life

Figure 4.1 displays the spectrum obtained by summing the single-hit signals from all Ge crystals that were registered in coincidence with positrons [Plet02]. The contributions of room background, which are due to random coincidences, are identified in the spectrum. A sizeable amount of the isobaric contaminant ^{100}Ag, and, therefore, transitions occurring in the daughter ^{100}Pd, are also labelled in the figure. The 451/453 keV doublet, containing γ transitions in ^{100}Pd and ^{100}Cd are only partially resolved. The experimental energies and intensities of β-delayed γ rays of ^{100}In observed in this work, are compiled in Table 4.1 [Plet02].

As described in Ref. [Plet02] the β-decay half-life of ^{100}In was studied by analyzing the β-gated time spectra for each of the three strongest lines 1004, 795 and 297 keV. Their time distributions were fitted with one exponential grow-in curve. The results are listed in the first three lines of Table 4.2. The high-resolution data produced a weighted average for the β-decay half-life ^{100}In g.s. of 5.5(3) s. This

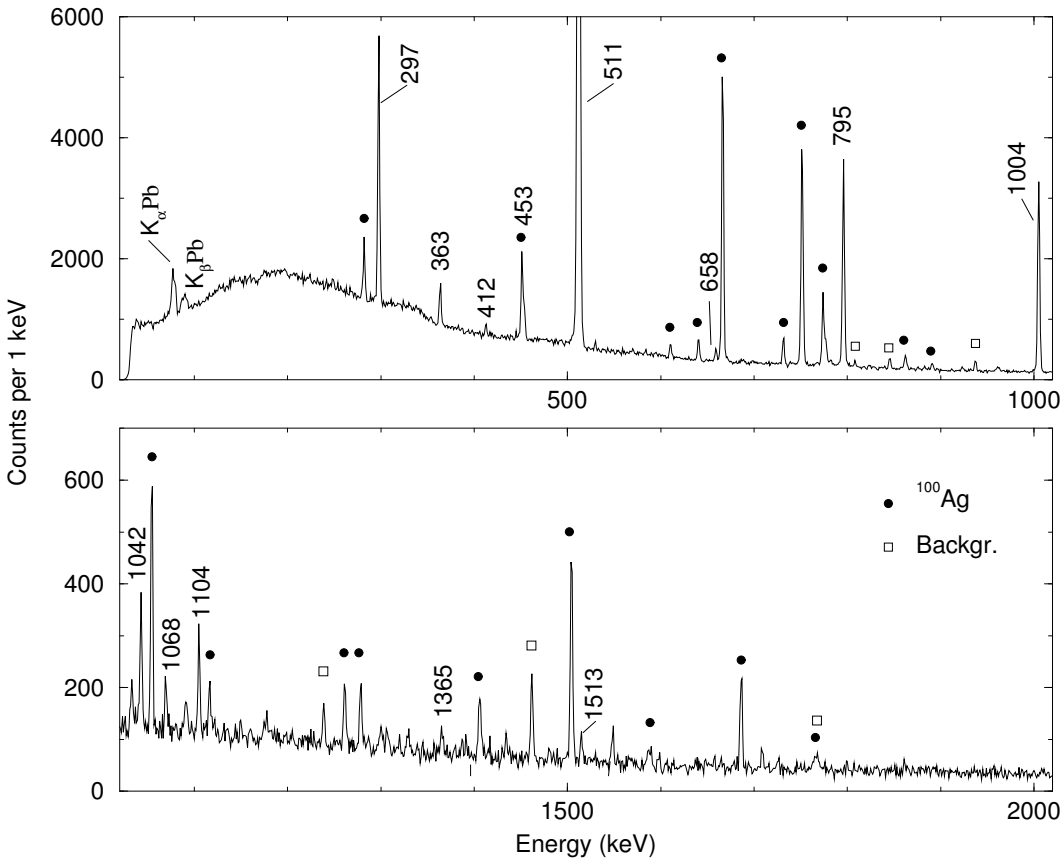

Figure 4.1: Gamma-ray spectrum [Plet02] in coincidence with positrons at mass $A = 100$. The lines labelled with their energy in keV identified as β delayed γ rays of ^{100}In are transitions in ^{100}Cd. The lines marked with symbols are transitions from the isobaric contaminant decay ^{100}Ag $\rightarrow$ ^{100}Pd or from the room background, respectively.

result is in agreement with the value of 6.1(9) s obtained in [Szer95] from the time analysis of the β-delayed proton spectra.

4.1.2 ^{100}In $\rightarrow$^{100}Cd β-decay scheme

Beta-γ-γ coincidence events were recorded on tape and sorted off-line into two-dimensional matrices [Plet02]. The $\gamma\gamma$ coincidences were analyzed [Plet02] in the positron-gated matrix by using the RADWARE package [Radf95].

Examples of β-gated γ-ray spectra (from [Plet02]) in coincidence with the 1004 and 795 keV γ rays are displayed in Fig. 4.2. In the upper panel, strong coincident transitions at 297, 795 keV appear, thus defining the main de-excitation sequence. The weak 453 keV transition de-exciting the 8^+, 2549 keV isomer [Albe92, Górs94], is also seen in the spectrum. This observation is due to the fact that the half-life of

Table 4.1: Level energies (E_x), spin and parity of the initial state (I^π), energy of the de-excitation transition (E_γ), relative intensity (I_γ) of the γ ray normalized to the $2^+ \rightarrow 0^+$ transition, the β-intensities determined from the high-resolution measurement ($I_{\beta\gamma}$), i.e. apparent feeding, and I_β intensities from the analysis of TAS data observed in ^{100}In [Plet02].

E_x (keV)	I^π ($\hbar$)	E_γ (keV)	I_γ (%)	$I_{\beta\gamma}$ (%)	I_β (%)
1004.1(1)	2^+	1004.1(1)	100(5)	5.3(7)	< 1.0
1799.0(1)	4^+	794.9(1)	88(5)	21(8)	< 0.9
2046.0(2)	4^+	1041.9(2)	8.1(5)	5.3(7)	< 0.9
2095.8(1)	6^+	296.8(1)	60(3)	33(3)	< 3.0
2457.7(4)	6^+	362.7(1)	8.9(10)	16(1)	< 1.3
		411.7(3)	2.8(4)		
		658.2(3)	4.2(4)		
2548.6(1)	8^+	452.8(1)	9.4(8)	9.4(8)	< 1.3
3164.3(1)	(6^+)	1068.5(2)	2.9(4)	5.4(6)	< 1.8
		1365.3(5)	2.5(4)		
3199.8(2)	(8^+)	1104.1(2)	6.1(5)	6.1(5)	< 1.8

60(3) ns of this isomeric level is small compared to the coincidence time window of 8 μs (see Sect. 2.2.3). Peaks at 1042 and 412 keV are also visible in the 1004 keV gate, but not in the 795 keV gate (see lower panel of Fig. 4.2). In both gates, weak coincidences at 1068 keV and 1365 keV could be seen, their intensities amounted approximately to 2% and 3% of that of the 1004 keV γ ray (see Table 4.1). Moreover, the 1068 keV transition is in coincidence with the 297 and 795 keV γ rays, while the 1365 keV is observed in coincidence with the latter transition only. Thus, a new ^{100}Cd level at 3164 keV excitation energy has been firmly established. In addition,

Table 4.2: Half-life of ^{100}In determined from the different activities in the high-resolution and the total-absorption measurements[Plet02]. For TAS see also Sect.4.1.3.

Spectrum	Condition	$T_{1/2}$ (s)
γ rays	297 gate	5.4(7)
γ rays	795 gate	4.8(4)
γ rays	1004 gate	6.2(4)
TAS	γ_{TAS} and β^+, $\mathrm{E}_{TAS} \geq 7$ MeV	6.1(2)
TAS	γ_{TAS} and X(Cd), $\mathrm{E}_{TAS} \geq 5$ MeV	5.5(7)
Delayed protons	$\mathrm{E}_p \geq 2$ MeV	6.8(8)
Weighted-average half-life		5.9(2)

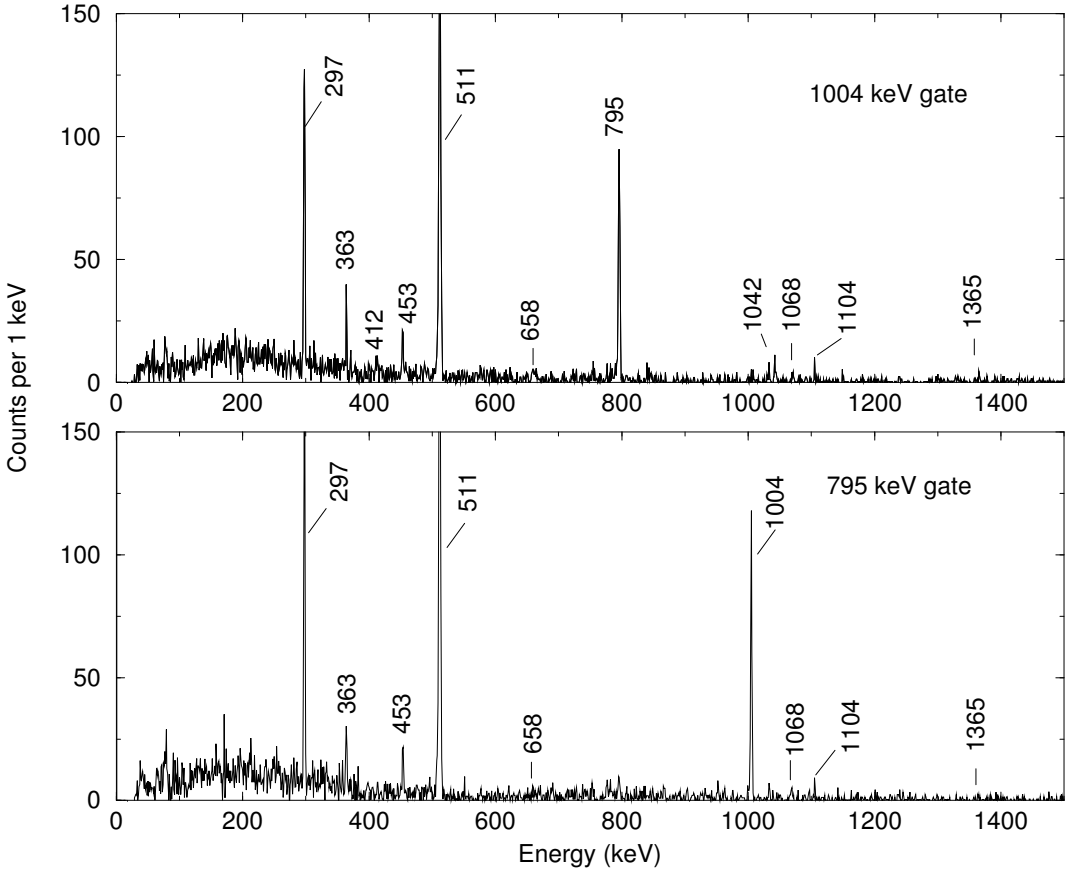

Figure 4.2: Coincidence spectra [Plet02] with gates on the 1004 keV and 795 keV in the $\beta\gamma\gamma$ matrix. Transitions in ^{100}Cd are marked by their energies in keV.

in all 1004, 795 and 297 keV gates a new transition at 1104 keV was observed.

Based on the afore-mentioned β-γ-γ coincidences, the ^{100}In $\rightarrow$ ^{100}Cd decay scheme is constructed and presented in Fig. 4.3. It includes two new non-yrast ^{100}Cd levels and three new γ-rays compared to the data obtained previously in in-beam experiments [Albe92, Górs94, Clar00]. The main E2 sequence de-exciting the 8^+ isomer to the ground state and the yrare 6^+ and 4^+ levels at 2458 keV and 2046 keV and their subsequent decay reported in previous work cited above have also been confirmed by our data. The new level at 3164 keV excitation energy has been introduced on the basis of the coincidence relations discussed above. Its γ decay restricts the spin and parity of the state to $I^\pi = (4-6)^+$. The 1104 keV transition was tentatively placed as de-exciting the new 3200 keV level (see Fig. 4.3). Due to weak and ambiguous coincidence relations between the known transitions and the newly observed 867 and 1513 keV γ-rays, the latter could not be placed in the level scheme.

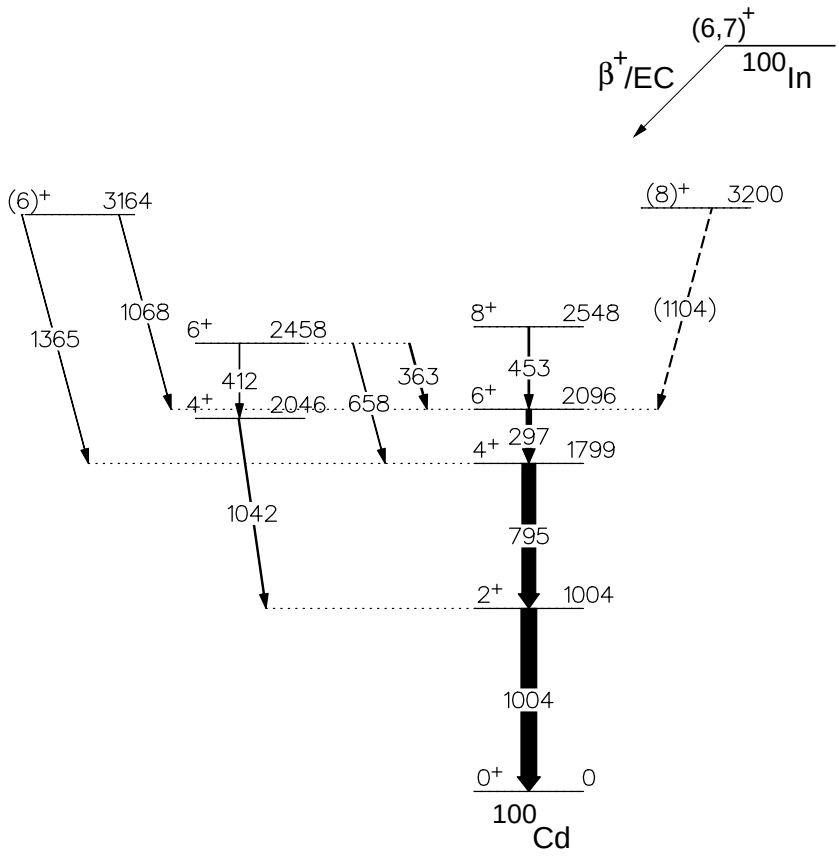

Figure 4.3: ^{100}In $\rightarrow$ ^{100}Cd decay scheme obtained by analyzing $\beta\gamma\gamma$ coincidences [Plet02].

The "apparent feeding" ($I_{\beta\gamma}$), that one may determine by performing the γ-ray intensity balance on the level scheme shown in Fig. 4.3, is related to direct β feeding (I_β) and to unobserved γ feeding following the β decay to higher-lying levels (I_γ^{high}). This is the reason why it is not straightforward to get an insight into the I_β values by inspecting the $I_{\beta\gamma}$ data (Table 4.1) The largest $I_{\beta\gamma}$ intensity was found for the 2096 keV, 6^+ level and amounted to 33(3) %. This observation restricts the spin of the parent ^{100}In state to values of $I^\pi = (5-7)^+$. The β-feeding intensities and spin-parity assignments of the β-decaying ^{100}In state and of ^{100}Cd levels are discussed in Sect. 6.1.

4.1.3 High-efficiency TAS spectra

Despite of the silver yield suppression mode (see Sect. 2.2), the ^{100}Ag activity was dominating in the implanted $A = 100$ samples. A large amount of the isobaric contamination is detrimental for the TAS(β^+) spectrum depicted in the upper panel of Fig. 4.4 where events in the region below 5 MeV are mainly due to the ^{100}Ag and

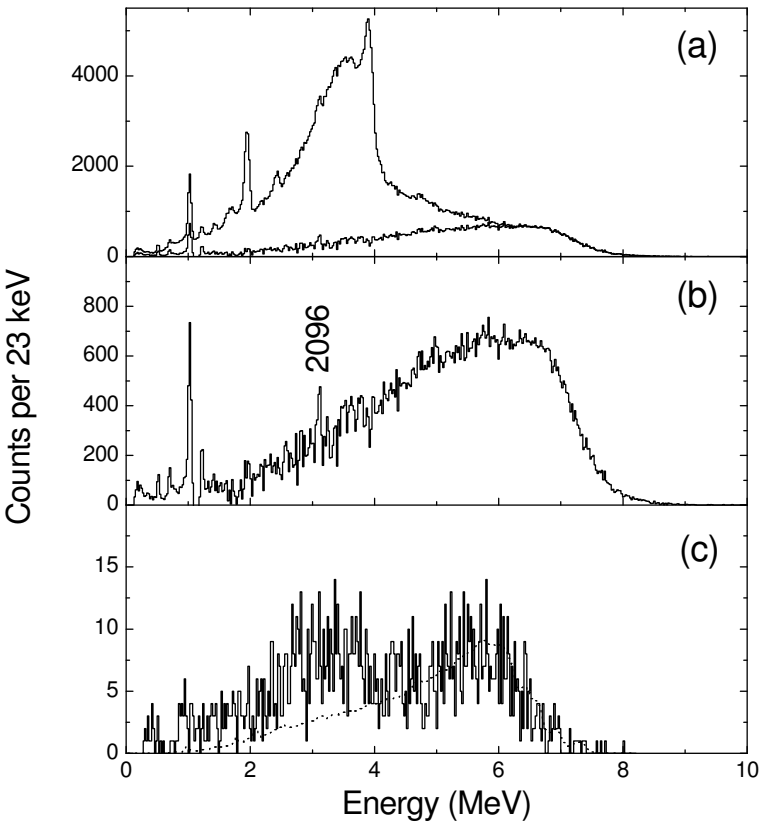

Figure 4.4: TAS spectra obtained in coincidence with positrons registered in the silicon detectors (a) and (b), and Cd X-rays (c). Panel (a) presents TAS(β^+) data with and without contamination subtraction , panel (b) shows the corrected spectrum on an expanded scale. In panel (c) the simulated spectrum is shown as a dashed line. (from [Plet02])

^{100m}Ag decay. In order to purify the ^{100}In TAS(β^+) spectra from isobaric contamination, sources abundant in ^{100}Ag, ^{100m}Ag and ^{100}Cd were prepared and measured in separate experiments.

Properly normalized, the corresponding reference spectra were subtracted from the ones enriched in ^{100}In. A normalization for this procedure was found by demanding complete removal of the peaks corresponding to the X and γ rays from the decay of the isobaric contaminants. The resulting spectrum, shown in the lower panel of Fig. 4.5, contains only Cd X-rays. Because of the contribution from tails of the Pd and Ag X-ray peaks under the Cd peak (see upper panel of Fig. 4.5), such a procedure was applied not only to the X-ray and to the TAS(β^+) spectra, but also to the X-ray gated TAS(EC) spectrum. The TAS(β^+) and TAS(EC) spectra obtained after the subtraction are displayed in Fig. 4.4.

Above an absorbed energy of 7 MeV, contributions of ^{100}Ag, ^{100m}Ag and ^{100}Cd to

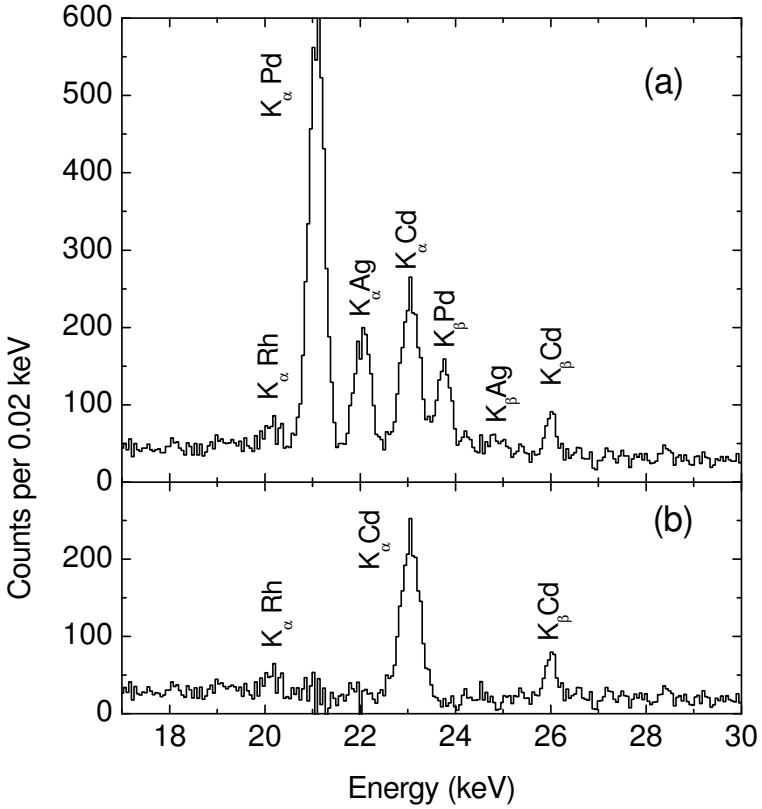

Figure 4.5: X-ray spectrum registered by the small Ge detector inside TAS (a). Peaks assigned to the decays of ^{100}Ag, ^{100}Cd and ^{100}In, i.e. Pd, Ag and Cd X-rays, respectively, are accordingly labelled. After contaminant subtraction, the Cd-X rays corresponding to ^{100}In decay are presented in (b). (from [Plet02])

the TAS(β^+) were measured to be negligible. This is due to the subtraction procedure on one hand, and on the other hand to the different Q_{EC} values for ^{100}In, ^{100}Ag and ^{100}Cd of 10180(370) keV, 7050(80) keV and 3870(60) keV, respectively [Audi97]. This is also borne out by the analysis of the time characteristics of TAS(β^+) events. Events with absorbed energies higher than 7 MeV yielded a half-life of 6.1(2) s (Table 4.2), i.e. comparable to the value of 5.5(3) s obtained from the high-resolution data, whereas the low-energy part of the spectrum yields a much longer half-life. The origin of the latter contribution, the energy dependence of which resembles that of ^{100}Ag, is not fully understood. However, it can be removed from the TAS spectra obtained for $A = 100$ by changing the above-mentioned normalization by about 10%, which is considered to be a reasonable variation within the uncertainty of the normalization procedure.

A similar conclusion with respect to half-lives can be drawn from the TAS(EC) spectrum. A half-life of 5.5(7) s (Table 4.2) was obtained for events with absorbed

energies higher than 5 MeV, whereas the low-energy part, including the pronounced excess of counts in the region below 4 MeV, is characterized by a considerably longer half-life of 14(4) s. In contrast to the TAS(β^+) case, the long-lived excess counts in the TAS(EC) spectrum can *not* be removed by a reasonable renormalization of the isobaric contaminants. Excluding the value of 14 s, the weighted average of the half-life of ^{100}In obtained in this work is 5.9(2) s (Table 4.2). This result is in agreement with, but more accurate than, the previous value of 6.1(9) s [Szer95].

The observation of two time components in the TAS(β^+)and TAS(EC) data might be due to a long-lived isomer in ^{100}In or ^{100}Cd. The fraction of the events which contribute to the longer-lived activity in the TAS(β^+) spectrum is about 35 %. Therefore, this component should have been detected in the high-resolution experiment, provided the β^+ intensity of the decay of such an isomer is not highly fragmented. In contrast to the isomer hypothesis, the time characteristics of the 1004 keV γ-line, determined in the high-resolution measurement, does not yield any evidence for a long-lived component, even though this transition is supposed to collect most of the β^+ intensity from the decays of the ground state and of the possible isomer of ^{100}In. As the shape of the long-lived component in the TAS(β^+) spectrum (see Fig. 4.4 (a)) resembles very closely that of the ^{100}Ag spectrum, it is very likely that, due to a deficiency of the subtraction procedure, the long-lived component represents a remainder of the ^{100}Ag activity. All in all, we refrain from interpreting the low-energy structures of the TAS(β^+) and TAS(EC) spectra and restrict the following discussion to their short-lived high-energy parts.

4.1.4 Beta intensity

The ^{100}Cd levels identified in the high-resolution measurement should be observed as peaks in the net TAS(β^+) spectrum shown in Fig. 4.4(a), shifted by the simultaneously absorbed 1022 keV annihilation radiation, provided that the respective states are directly populated by sizeable β^+ feedings. However, the rather unstructured TAS(β^+) spectrum exhibits only one such peak that can be reliably distinguished from statistical fluctuations. It is observed at an absorbed energy of 3120 keV, and it corresponds to the feeding of the 6^+ level, observed in the high-resolution experiment at 2096 keV (see Fig. 4.3). The value of the TAS β^+ feeding of this level is < 3.0 % while the apparent intensity obtained in the high-resolution part, given for comparison in Table 4.1, amounts to 33(3) %. This discrepancy shows that the intensity balance based on the high-resolution decay scheme gives only a qualitative insight to the β feeding. A second peak corresponding to the 1004 keV level (see Fig. 4.3) with a feeding of 1.0(4) % could be an artefact caused by the strong 936+1022 keV peak from ^{100}Cd decay [Ryka89] in the total spectrum (see Fig. 4.4). For all other ^{100}Cd levels listed in Table 4.1, only upper limits of the β^+ feeding were obtained. The total β^+ feeding to all these levels is $< 12\%$. It is worth

noting that a similar conclusion has been drawn from a TAS study of β^+/EC decay of ^{104}In, where despite of a much better counting statistics, the TAS(β^+) spectrum did not show any pronounced peaks in the low-energy region [Karn01].

The procedure of deriving the β intensities (I_β) from the experimental TAS spectra was described in detail in Refs. [Hu00, Hu99]. The observed TAS(β^+) and TAS(EC) spectra represent convolutions of the response matrix with the respective β^+ and EC intensity distributions. The decay scheme established from the high-resolution experiment was used as a basis for constructing the TAS response matrix. The remaining problem is that the levels established in this way do not comprise all states involved in the $\beta\gamma$ cascades. This is due to the strong fragmentation of the I_β distribution and of the subsequent γ de-excitation, as well as to the low efficiency of the Ge detectors for γ energies higher than 3 MeV. Therefore, we used the statistical level density as obtained from shell-model calculations, which are part of this work (for details see Sects. 5.2.1 and 6.1). In order to extract the I_β distribution, the experimental TAS(β^+) and TAS(EC) spectra were fitted by simulated spectra varying the I_β distribution. The TAS(β^+) spectrum was fitted for absorbed energies up to 10 MeV. Since only the high-energy part of the TAS(EC) data can be reliably assigned to the ^{100}In decay, the fit of this spectrum was restricted to absorbed energies above 5 MeV. The simultaneous fit of the TAS(β^+) and TAS(EC) spectra implies that the Q_{EC} value of ^{100}In is adjusted during the least-squares procedure. Due to the lack of statistics, only a rough estimate of 10.0(5) MeV was obtained for this quantity. A more precise Q_{EC} evaluation is described in Sect. 4.1.5. The simulated TAS(EC) spectrum is shown in Fig. 4.4(c), too.

The partial strength detected by the TAS in γ rays is determined to be $B_{GT,\gamma} = 3.0(9)$. The experimental and the calculated I_β and GT distributions are shown in Figs. 6.2 and 6.3 and discussed in Sect. 6.1.

4.1.5 Beta-delayed proton emission

The low-energy part of the spectrum registered by the bottom (BOT) Si detector without using any selection condition contained a sizeable contribution of events that can not be unambiguously identified as protons (see Fig. 4.6(a)).

In order to clarify this effect, we used the two-dimensional TAS(BOT) spectrum and inspected it for different thresholds of the Si detector. We used the condition $E_{TAS} \leq 1.1$ MeV to create the purified β^+p spectrum shown in Fig. 4.6(b). Figure 4.6(c) shows the spectrum of β-delayed protons that follow EC decay of ^{100}In and populate the ^{99}Ag ground state. In order to select these data, anticoincidence with TAS signals was required. A half-life $T_{1/2}$=6.8(8) s (Table 4.2) was measured for β^+p events with $E_p \geq 2$ MeV.

Figure 4.7 displays the TAS spectrum obtained in coincidence with protons registered in the BOT Si detector under the condition $E_{BOT} \geq 1.5$ MeV. Since the

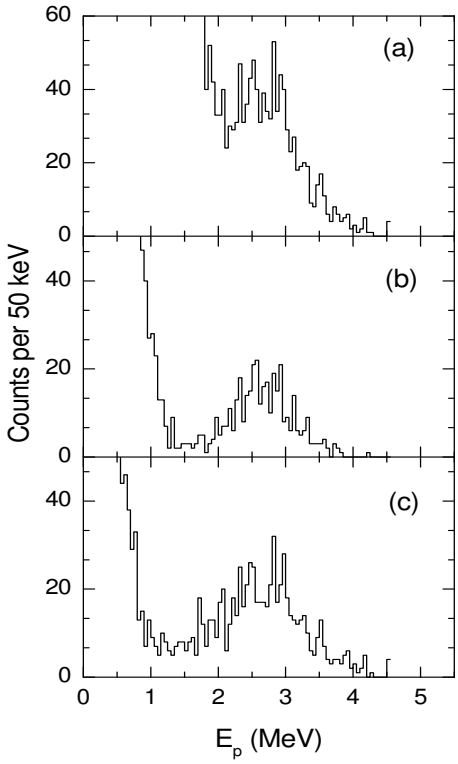

Figure 4.6: Experimental BOT Si proton spectrum feeding ^{99}Ag without TAS selection (a), in coincidence with TAS energies $\leq$ 1.1 MeV (b), and in anticoincidence with TAS (c), i.e. EC delayed protons to ground state. (from [Plet02])

annihilation peak dominates the spectrum, it is evident that the main fraction of the delayed proton intensity goes to the $9/2^+$ ground state of ^{99}Ag. Apart from the annihilation peak, which corresponds to the β^+p emission to the ground state, there are two more peaks which can be unambiguously assigned to known levels in ^{99}Ag. These are the 342 keV, $7/2^+$ level known from β-decay studies [Kals80], and the 916 keV, $13/2^+$ level assigned by in-beam work [Piel88]. As far as the ECp feeding is concerned, this is affected by the uncertainty due to the background of the proton spectrum. This was analyzed in [Szer95], by using a delayed-proton spectrum measured with a ΔE-E technique. The background was found to be 10 % of the total delayed proton intensity in the range of $E_p \geq 1.5$ MeV. Table 4.3 lists the partial intensities of the proton emission to states in ^{99}Ag. The intensity is normalized to 100 βp events. The total branching ratio for β-delayed proton emission following the ^{100}In decay was found to be 1.6(3) %.

By using the energy distribution I_{ECp} of EC-delayed protons, and a total intensity $\sum I_\beta^+$ of β^+p fed to the ^{99}Ag ground state, we estimated the value of $Q_{EC} - S_p$ for the ^{100}In to be 5.25(20) MeV, where S_p is the proton separation energy of ^{100}Cd.

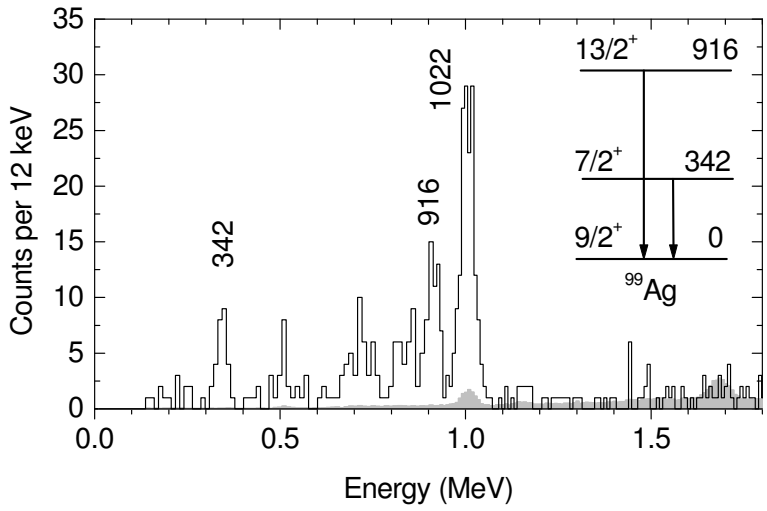

Figure 4.7: TAS spectra in coincidence with protons registered in the Si bottom detector. The estimated background from gating on positrons is shown in the shadowed area. For comparison, the lowest excited states in ^{99}Ag are shown. (from [Plet02])

Table 4.3: Intensities of the β-delayed proton emission to the ^{99}Ag states

^{99}Ag state	$9/2^+$	$7/2^+$	$13/2^+$
$I_{\beta p}^{(\beta^+)}(\%)$	60(6)	2.8(5)	6.2(12)
$I_{\beta p}^{(EC)}(\%)$	31(5)	≤ 1	≤ 2

The $Q_{EC} - S_p$ value was defined to fulfill the condition

$$\sum I_{\beta p} = \sum I_{EC} f_\beta / f_{EC}, \tag{4.1}$$

where f_β and f_{EC} are the statistical Fermi functions for the β^+ and EC transitions, whose ratio is a function of the β-decay energy. We restricted this evaluation to proton energies larger than 2.4 MeV in order to avoid uncertainties due to a small value f_{EC} in the denominator. Using a proton separation energy of 4.83(19) MeV [Audi97] a Q_{EC} value of 10.08(23) MeV was obtained. This result is in agreement with the range of 9.3 MeV $\leq$ Q_{EC} $\leq$ 12.5 MeV, found previously [Szer95], and with a shell-model prediction [John95] of 10.07 MeV (see Sect. 6.1).

By taking the Q_{EC} value of 10.08 MeV (see above) the delayed proton branch results in a partial GT strength $B_{GT,p} = 0.86(15)$. Therefore, the total GT strength is $B_{GT,p} + B_{GT,\gamma} = 3.9(9)$. The experimental I_β and GT distributions are compered to theoretical ones in Figs. 6.2 and 6.3 and discussed in Sect. 6.1.

4.2 Results for ^{98}Cd

In this section the experimental results from the experiment on the delayed spectroscopy of ^{98}Cd are presented. The experimental data analysis (see Chapter 3) is exclusively author's work. In Sect. 6.2, these results are compared to shell-model calculations and discussed.

4.2.1 Gamma-γ and particle-γ coincidences

The four known γ-ray transitions [Górs97] were observed in the delayed spectra and their origin from ^{98}Cd was again confirmed [Blaz04]. However, in the higher energy part of the particle gated spectra a new line at 4207 keV was observed (see Figs. 3.7, 3.8 and 3.9) [Blaz04]. From the arguments presented in Sect. 3.3 and the performed exit-channel identification method as described in Appendix A, it was deduced that the transition occurs in a nucleus produced in an α2n exit channel. Figure 4.8 shows the particle-gated γ-intensity ratios for the exit-channel analysis of the 4207 keV γ transition. The α2n exit channel is easily concluded on the basis of the plots, where the theoretical values (the bars) were calculated (see Appendix A) for the given neutron- and α-efficiencies (see Sects. 2.4.2 and 2.4.3).

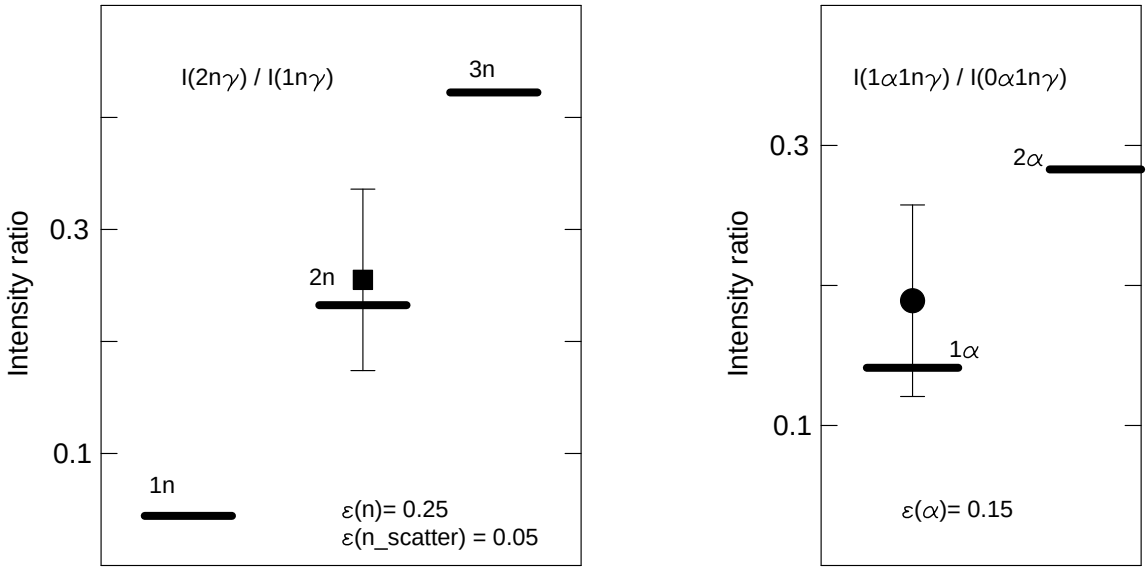

Figure 4.8: Intensity ratios of the high-energy 4207 keV line in coincidence with different particles gates. The segments are the theoretical values. From the left plot the neutron multiplicity and from the right plot the α multiplicity is deduced.

Inspection of the coincidence matrices proves that this high-energy line is in delayed coincidence with the other four transitions belonging to ^{98}Cd, as demonstrated in Fig. 4.9.

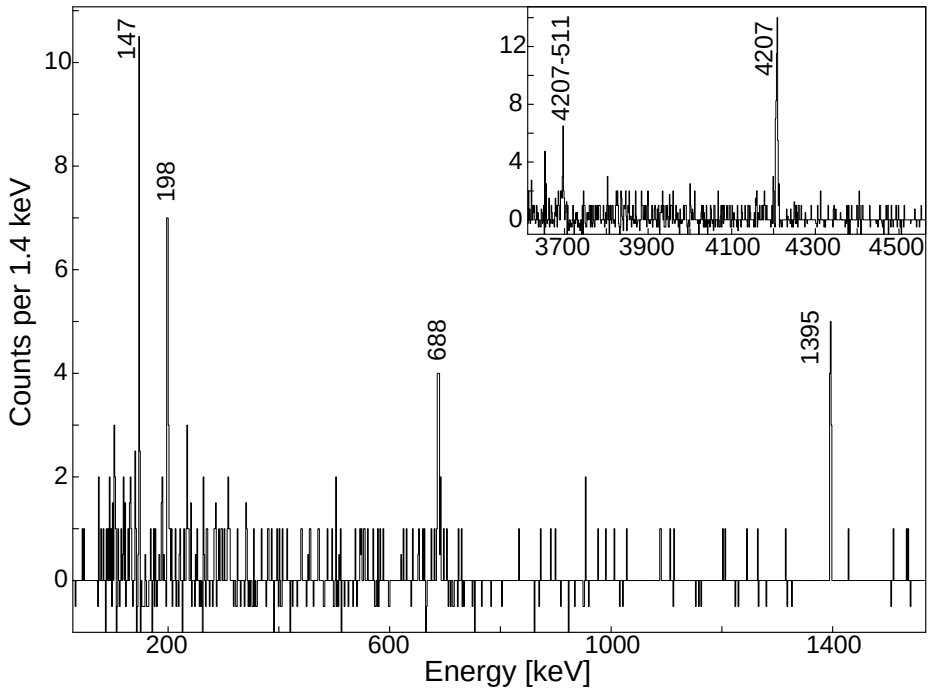

Figure 4.9: Spectrum gated on the 4207 keV line. The inset shows the high-energy part of the cross coincidence spectrum created by the sum of gates on the 147, 198, 688 and 1395 keV lines with particle condition 0α0p1n, 0α0p2n, 0α0p3n, 1α0p0n, 1α0p1n, 1α0p2n and 1α0p3n and with unrestricted coincidence time window.

4.2.2 Time spectra and half-lives

As introduced in Sect. 3.4, three different methods have been employed to determine half-life values and limits for the isomers at 6635 keV, 2428 keV and 2281 keV excitation energy (see Table 4.4 and Fig. 4.13). The background subtraction and the fitting procedure were optimized analyzing the decay of the $I^\pi = 8^+$ isomer in ^{100}Cd (see Sect. 3.4.1), which yielded a half-life value of $T_{1/2} = 61(1)$ ns in good agreement with Ref. [Górs94].

Figure 4.10 shows the background subtracted time-delay spectrum with reference to the beam pulse on target for the new 4207 keV γ ray, which precedes the known $I^\pi = (8^+)$ isomer. The half-life resulting from a single exponential fit is $T_{1/2} = 230\ (^{+40}_{-30})$ ns. This value along with the strong feeding intensity (Table 4.4) explains the long apparent half-life inferred previously in a similar experiment for the $I^\pi = (8^+)$ state [Górs97].

In view of this fact, the similarity of the lifetimes involved and the experimental uncertainties it is not promising to apply the same method to the time distribution of

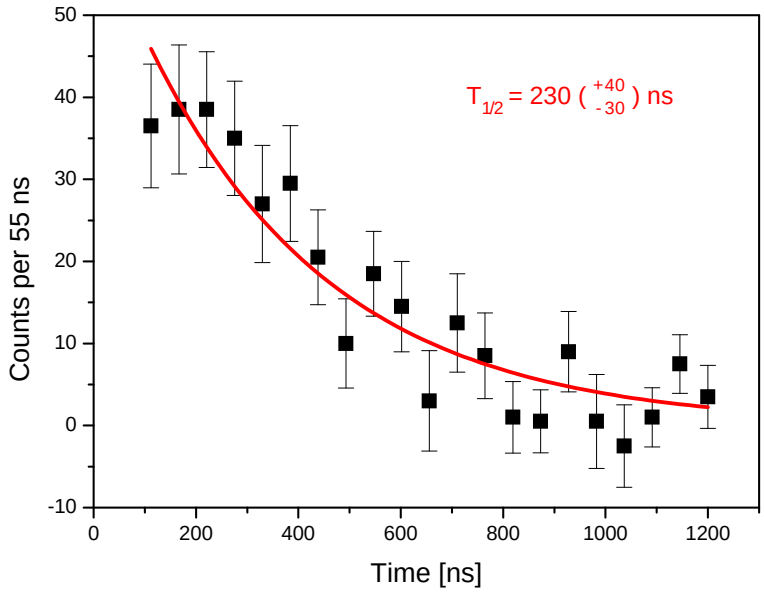

Figure 4.10: Background subtracted time spectrum of the 4207 keV line with particle gates on $0\alpha 0p1n$, $0\alpha 0p2n$, $0\alpha 0p3n$, $1\alpha 0p0n$, $1\alpha 0p1n$, $1\alpha 0p2n$ and $1\alpha 0p3n$. The fit region is $105 - 1240$ ns with reference to the beam pulse on target.

the 1395 keV γ ray to infer the $I^\pi = (8^+)$ half-life from a two exponential component fit. Therefore this lifetime was determined from a $\gamma\gamma(t)$ time distribution with start on the feeding 4207 keV line and stop by the 688 keV and/or 1395 keV γ-rays below the $I^\pi = (8^+)$ isomer. The time spectrum shown in Fig. 4.11 is virtually background free, and from a single exponential fit a half-life $T_{1/2} = 170(^{+60}_{-40})$ ns was determined. The additional delay in the $I^\pi = (6^+)$ state (see below) will enlarge the error bars given above only marginally. Within these error bars the value agrees well with the result from a previous fragmentation experiment [Grzy98].

It has been stated before that from nuclear structure arguments a half-life for the $I^\pi = (6^+)$ state in the $10 - 20$ ns range is expected [Górs97]. This is too short for a $\gamma\gamma(t)$ delay curve analysis, since low-energy γ rays, which are subject to large time walk, are involved. Therefore the centroid shift method [Andr82] was applied in this case. In Fig. 4.12 the centroids of the low-energy 147 keV and 198 keV γ-ray time distributions gated by coincidence with the 1395 keV γ ray are shown. The time-zero line is determined from the time distribution of the Compton background, which is known to provide a good reference [Andr82]. As expected from the decay scheme (Fig. 4.13) the 198 keV line is prompt, while the 147 keV centroid is clearly shifted. A limit on the half-life, $T_{1/2} < 20$ ns, is deduced from this shift at a 2σ confidence level.

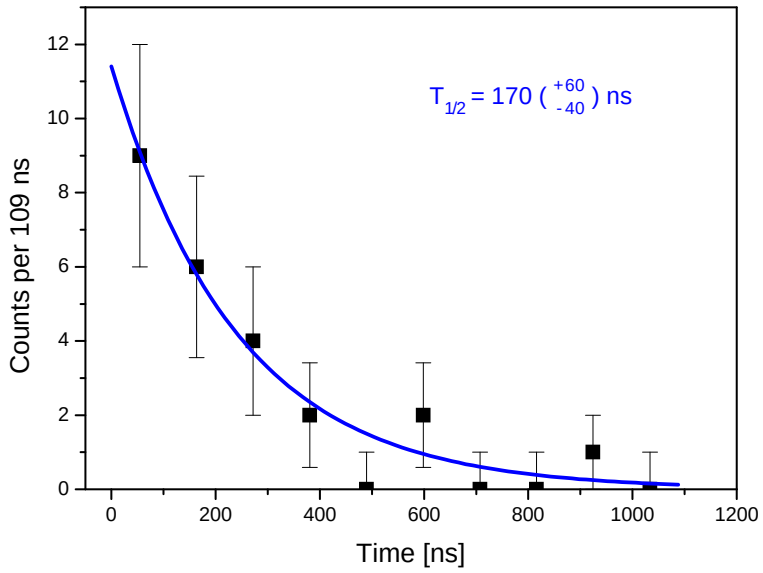

Figure 4.11: Time delay spectrum $\gamma\gamma(\Delta t)$ with start on 4207 keV γ ray and stop on "OR" of 688 and 1395 keV γ rays. (Particle gate on 0α0p1n, 0α0p2n, 0α0p3n, 1α0p0n, 1α0p1n, 1α0p2n and 1α0p3n.)

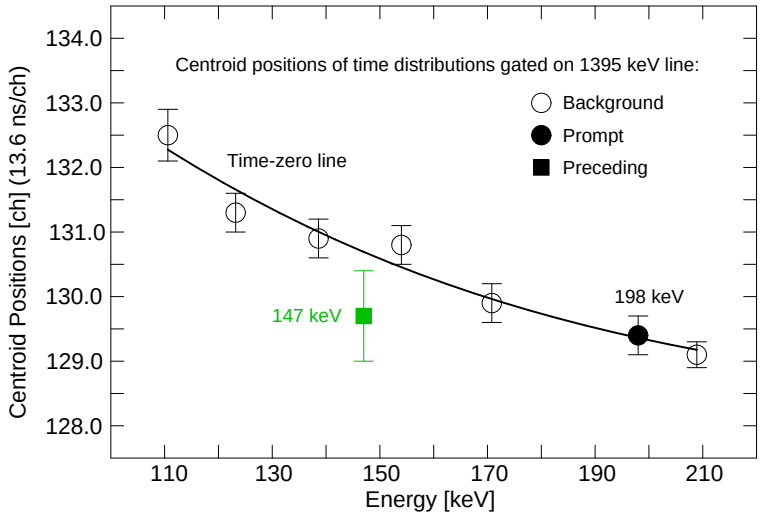

Figure 4.12: Time-zero line of γ ray in coincidence with the 1395 keV line. The reference line is a fit to the centroids of the time distributions for prompt coincidence. The energy dependence reflects the time walk. The centroid shift of the 147 keV line compared to the time-zero line(time of 198 and 1395 keV lines) is a direct measure of the 6^+ state lifetime. (Particle gate on 0α0p1n, 0α0p2n, 0α0p3n, 1α0p0n, 1α0p1n, 1α0p2n and 1α0p3n.)

4.2.3 Level Scheme

Table 4.4 summarizes the γ-ray intensities and the half-lives of the excited levels in ^{98}Cd resulting from this work. Based on the $\gamma\gamma$ and γ-time coincidence relations (Sects. 4.2.1 and 4.2.2), the γ-ray intensities and the half-lives (Table 4.4), the decay scheme shown in Fig. 4.13 is proposed. It consists of one new level, one new γ-ray transition and three new half-lives in comparison to the previously known one [Górs97]. A discussion on the spin-parity assignment of the excited state at 6635 keV and a comparison to the shell-model calculation results are presented in Sect. 6.2.1.

Table 4.4: Level energies, spin-parity assignments, half-lives, γ-ray energies and intensities as deduced from this work.

E_x [keV]	I_i^π	$T_{1/2}$ [ns]	E_γ [keV]	I_γ [%]	I_f^π
1395	(2^+)	-	1394.9(2)	100(15)	0^+
2083	(4^+)	-	687.8(3)	105(15)	(2^+)
2281	(6^+)	<20	198.2(2)	80(15)	(4^+)
2428	(8^+)	$170(^{+60}_{-40})$	147.1(2)	70(15)	(6^+)
6635	(12^+)	$230(^{+40}_{-30})$	4207(2)	50(35)	(8^+)

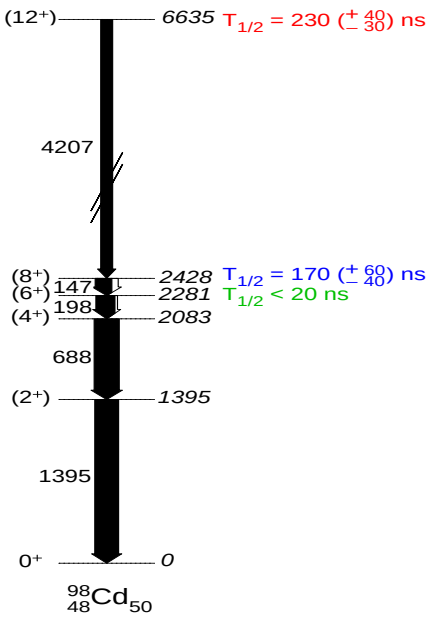

Figure 4.13: Experimental level scheme of ^{98}Cd (this work). The scale is broken between 3 and 6 MeV.

Chapter 5

Shell-Model Calculations

The term "nuclear shell model" has various meanings depending on the context. In the simplest and extreme sense it means the set of single-particle states obtained from a mean field potential as shown in Figs. 1.1, 1.4 and 1.5. In a broader and more general sense it means the multitude of states which can be made by coupling many particle and/or hole single-particle states and accounting for configuration mixing. When referring to *shell-model* (SM) calculation I use the second meaning, except where explicitly stated else.

As introduced in Sect. 1.1, the nuclear shell model is quite a powerful tool to study and explain the nuclear structure in the regions near closed shell or doubly closed shell nuclei. In the case of the ^{100}Sn region this is certainly true and therefore one is naturally driven to use the shell model in theoretical studies of this region.

Certainly most of the nuclear properties will be determined by the order of single particle levels and their occupation. With the exception of the lightest nuclei $A \leq 12$ where "no-core shell model" calculations are possible [Navr98, Barr02], for all the other nuclei one has to choose a model space (see Sect. 1.1) and an *effective* interaction. The effective interaction is acting between the valence orbitals to account effectively for interactions with the non-valence orbitals in the core and the external space beyond the valence space. In the experimental data on ground state and excited states properties the influence from all the other orbitals is naturally present, so when the interaction is derived empirically by fitting to experimental data it is automatically effective. On the other hand the realistic interactions of the G-matrix approach are derived for a specific model space and are calculated to account for the effect of the orbitals outside the model space. So the they are also effective. When using effective interactions one has to pay attention that the operators have to be understood as effective operators. Usually their effective strength is adjusted by replacing the free nucleon coupling constants, i.e. for $E2$ transitions there is an *effective proton/neutron charge* e_π/e_ν where the difference from the free nucleon values $e_\pi = 1\ e$ and $e_\nu = 0\ e$ is denoted by $\delta e_{\pi,\nu}$ and called *proton/neutron polarization*

charge; for $M1$ transitions – *effective g-factors*; and for GT transition – effective g_A/g_V values. Their values are obtained by an overall fit to the experimental values for a given model space.

The drawback of the effective interactions is that they are valid only for the model space they were derived for. This means that for every model space one has to derive and adjust another interaction. So the larger the model space is, the larger the applicability and the more universal the effective interaction is. On the other hand, the pursuit for larger model space including more orbitals is hindered by the increasing dimension of the matrices that have to be diagonalized in order to solve the many-body problem and find the energies and the wave functions of the nuclear excited states. Therefore one has to find a balance between a larger model space that would better describe more properties of interest and on the other hand a small enough model space that would make the calculations possible. If the calculations done in the full basis of a large model space are impossible due to computer limitations there are other ways to proceed. One way of solving this is to truncate the valence space by some restriction: (i) on the number of active orbitals (*vertical truncation*), (ii) the occupation of the valence orbitals (*horizontal truncation*) or (iii) to restrict according to the importance of the configurations [Sina92, Otsu02]. All these, of course, need very good understanding of the interactions and the nuclear structure in the specific region, since the results of some truncations may seriously deviate from the physical sense.

The task of the theory is to find the model spaces that contain the relevant degrees of freedom for a given problem as demanded by the effective interaction. The "safe" valence spaces are those that comprise orbitals between shell closures. There are several typical and well established ones. Here are their notations and characteristics (N_{HO} is the major-shell harmonic oscillator quantum number):

- $p-shell(N_{HO}=1)$, $[0p_{3/2}, 0p_{1/2}]$ — the calculations in this space can describe nuclei with $2 < N, Z < 8$ and use the α-particle as inert core. Since both orbitals have negative parity, only positive(negative) states in even(odd) nuclei can be described;

- $sd-shell(N_{HO}=2)$, $[0d_{5/2}, 1s_{1/2}, 0d_{3/2}]$ — the three orbitals have positive parity and therefore only positive parity states can by calculated for nuclei in the range $8 < N, Z < 20$ and have ^{16}O core;

- $pf-shell(N_{HO}=3)$, $[0f_{7/2}, 1p_{3/2}, 0f_{5/2}, 1p1/2]$ — this space has ^{40}Ca core and naturally would cover nuclei with $20 < N, Z < 40$, but the strong spin orbit splitting brings the $N_{HO}=4$ $0g_{9/2}$ orbital down and for shell model calculations beyond $N, Z = 32$ this intruder orbital has to be included in the model space.

At the same time these valence spaces are not appropriate to study the excitations of the above mentioned doubly-magic nuclei used as inert cores. For excitations of the particles in a closed shell, one has to include in the model space orbitals below and above that shell closure. This is the case for the core-excited states in ^{56}Ni, which core-excited spectrum is described well in the pf-shell model space, since it contains the $0f_{7/2}$ orbital below the $N = Z = 28$ closed shell and the $1p_{3/2}, 0f_{5/2}, 1p1/2$ orbitals above the closed shell.

For heavier nuclei more and more orbitals come into play. So the stress is put on specific regions for which the model spaces and the interactions are optimized. The nuclear structure in the region of ^{100}Sn is the subject of this thesis and therefore a special attention will be given to the model spaces used to describe the nuclear structure in that region. The details are given in the next sections, where shell model studies of two physics cases are presented. The first case is the Gamow-Teller decay $^{100}\text{In} \rightarrow {}^{100}\text{Cd}$ studied by large-scale shell-model calculations (LSSM)(see Sect. 5.2.1) which is part of this thesis, and the second case is a ^{98}Cd core-excitation and transition strength study, which is a contribution to the experimental results for ^{98}Cd (see Sect. 4.2) by my collaborators from Darmstadt (ESM)(see Sect. 5.1) and Strasbourg (LSSM)(see Sect. 5.2.2).

It is widely accepted to do SM calculations with specialized computer codes as RITSCHIL [Zwar85], OXBASH [Brow88b], ANTOINE [Caur89, Caur99a, Caur02], MSHELL [Mizu00], VECSSE [SchA00] and NATHAN [Caur97, Caur99b, Caur02]. More details about the SM codes OXBASH, ANTOINE and NATHAN are given in Sect. 5.2. When the number of basis states becomes very large and especially when diagonalization of the Hamiltonian matrix is performed in the full basis, one speaks about *large scale(basis) shell model* (LSSM/LBSM) calculations. Typically, LSSM calculations are performed with realistic effective interactions.

The next sections use some numbers, the definitions of which are reminded again. As already introduced in Sect. 1.1, l is the orbital angular momentum, s – the intrinsic spin, and $j = l + s$ – the total angular momentum quantum numbers, which for a single independent particle in mean-field coincide with the respective quantum numbers of the occupied orbit (sub-shell). The quantum number noted with capital letters are used for sum quantum numbers in a given multiparticle configuration, where S is the sum of the intrinsic spin quantum numbers, and T (different from the kinetic energy term) is the sum of the individual isospin quantum numbers, *e.g.* the total spin (S) and isospin (T) of the configuration. The quantum number J, similar to I, is the total angular momentum of the configuration. It should be noted that there is a general inconsistency with respect to J and I usage for the total spin. Within the shell model, J is mainly used for general purposes, configurations and intermediate coupling, while in connection with experiment and parity I is used for the total spin of a state.

5.1 The empirical shell model (ESM)

The empirical shell model carries its name because it uses empirical single-particle energies and two-body interaction matrix elements, which as mentioned in Sect. 1.1 are derived from experimental data. It is generally used in a minimum model space, i.e. single j-shell, low-j sub-shells or few-particle configurations. Usually there is no configuration mixing, though there are good examples of ESM in $\pi\nu(0p)$ [Cohe67], $\pi\nu(1s, 0d)$ [Brow88a], $\pi\nu(0f_{7/2})$ [Kuts78], $\pi\nu(1p_{1/2}, 0g_{9/2})$ [Gros76, Blom85] and $\pi\nu(1p, 0f)$ [Richt91, Honm04] model spaces where a free fit of the shell model parameters including the non-diagonal TBME, i.e. the mixing ones, is possible. The latter ESM parameterizations of $\pi\nu(1p, 0f)$ comprising of 195 TBME and 8 SPE represent the current limit of this method.

ESM has successfully been used to interpret experimental data close to doubly-closed shells and even to extrapolate nuclear structure features between adjacent major shells and make configuration assignments in exotic nuclei.

5.1.1 Single particle energies (SPE) and interaction

The single particle energies in this region relative to the ^{100}Sn core have been taken from [Graw01a] and can be read in Fig. 1.4. Thus, the neutron shell gap determined by the SPE is 6.78 MeV. The SPE were extrapolated by a SM analysis in a large enough model space using realistic interactions. The method of extrapolation is described in Refs. [Graw95, Graw01b].

The empirical interaction, used here, is based on the first experimental spectrum of ^{98}Cd by Górska *et. al.* [Górs97]. This nucleus has a filled $N = 50$ shell and for excited states two holes in the $g_{9/2}$ orbital in the $Z = 50$ proton shell. On the basis of good systematics of the $N = 50$ isotones it is assumed that the experimentally observed states are (2^+), (4^+), (6^+) and (8^+) [Górs97], and represent the pure two proton-hole spectrum with the 8^+ being the maximum spin of this $\pi g_{9/2}^{-2}$ configuration. In the ESM approach the experimental level energies have been used to extract the $\pi g_{9/2}^{-2}$ TBME and therefore ESM calculations reproduce exactly the experimental spectrum. The 0^+ g.s. has a mixture of the $g_{9/2}^{-2}$ and $p_{1/2}^{-2}$ configurations. To extract the additional $p_{1/2}$ single particle energy and the $\langle p_{1/2}^2|V|p_{1/2}^2\rangle_{0^+}$ and $\langle g_{9/2}^2|V|p_{1/2}^2\rangle_{0^+}$ diagonal and non-diagonal TBME, information from ^{97}Ag, ^{96}Pd and ^{95}Rh was used, to fit the ^{98}Cd spectrum. This complication has no bearing on the calculation of core-excited states (see below) as the 0^+ state does not enter in this case. As discussed in Ref. [Górs97] and Sect. 6.2, the comparison of the experimentally deduced $B(E2)$ for the (8^+) isomer with the theory suggested the existence of another isomeric state lying above the 8^+. This state was one of the explanations for the measured (8^+) half-life. After having reached the maximum spin of the $\pi g_{9/2}^{-2}$ configuration, the mechanisms of constructing a higher-lying state is to break a neu-

tron pair from below the $N = 50$ shell and promote one neutron above the shell gap into the next major shell. This mechanism is called *core excitation*, since one excites the closed $N = 50$ core. To be able to calculate such excitations with the ESM one had to extend its model space with neutron orbitals below and above the shell gap and extract the residual interaction. So the initial ESM parametrization was "upgraded" [Graw02] and now it includes the pure configurations $\pi g_{9/2}^{-2}$ and $\pi g_{9/2}^{-2}\nu g_{9/2}^{-1}d_{5/2}$ for the proton valence space and the neutron core-excited states, respectively. The $\pi g_{9/2}^{-1}\nu g_{9/2}^{-1}$, $\pi g_{9/2}^{-1}\nu d_{5/2}$ and $\nu g_{9/2}^{-1}d_{5/2}$ interaction energies were taken from ^{90,92}Nb and ^{90}Zr [ENDSF] using the Pandya transformation to convert *pp* into *ph* TBME [deSh63, Cast00, Graw04]. The configuration mixing was neglected. The calculation was done by using the *m-scheme* code OXBASH (see Sect. 5.2). The results from this calculation are shown on Fig. 6.4 and discussed in Sect. 6.2.

5.1.2 Evolution of single particle energies

The shell structure is not fixed for the total Segré chart, but changes with mass A, neutron excess $(N-Z)/A$ and shell occupation. The mass dependence as discussed in textbooks [Bohr98, Cast00] is due to the radial extension of the wave function and characterized in relative increase in binding for high-l orbitals. On the other hand, the neutron excess increase causes a relative upward shift of the high-l orbitals, due to the softening of the Woods-Saxon shape of the neutron potential. This is accompanied by a reduced spin-orbit splitting [Doba94]. These changes depend smoothly and weakly on the parameters A and N/Z, thus requiring extreme variations of their values to noticeably affect the shell structure. A more drastic mechanism to change the shell structure is the monopole shift of selected orbitals. Dufour and Zuker showed [Dufo96] that any effective interaction can be split into two parts:

$$H_{eff} = H_{monopole} + H_{Multipole} \tag{5.1}$$

The $H_{monopole}$ contains all the terms that are affected by a spherical Hartree-Fock variation, and are responsible for the global saturation properties and of the evolution of the spherical single particle field. Generally, for all realistic G-matrix interactions the $H_{Multipole}$ is nearly correct, while $H_{monopole}$ is wrong. Hence, the monopole part of the G-matrices has to be empirically corrected to reproduce the structure of the closed shell (CS) nuclei and CS$\pm$1 nuclei.

Experimentally large monopole shifts are observed in $N = 29$ and $N = 51$ isotones and $Z = 29$ (Cu) and $Z = 51$ (Sb) isotopes for the proton-neutron and the spin-flip pairs of orbitals $(\nu f_{5/2} \leftrightarrow \pi f_{7/2})$, $(\pi f_{5/2} \leftrightarrow \nu g_{9/2})$, $(\nu g_{7/2} \leftrightarrow \pi g_{9/2})$, and $(\pi g_{7/2} \leftrightarrow \nu h_{11/2})$, respectively [Graw03, Graw04]. The origin for these exceptional shifts can be found in the tensor $(\sigma \times \vec{r}) \cdot (\sigma \times \vec{r})(\tau \cdot \tau)$ part of the in-medium NN interaction [Otsu01, Graw04], which generates strong binding between $\pi\nu$ spin-orbit

partners ($\Delta l = 0$, $S = 0$) and ($\Delta j = 2$, $\Delta l = 1$, $S = 0$) $\pi\nu$ pairs of nucleons. Thus, the strongest monopole shift effect can be observed for $S = 0(\uparrow\downarrow)$, $\pi\nu$ ($T = 0$) pairs, plus the criterion of equal radial quantum numbers n, which assures good radial overlap and hence best conditions for the short-range NN interaction. Figure 5.1 shows this monopole shift for the case of ($\nu g_{7/2} \leftrightarrow \pi g_{9/2}$).

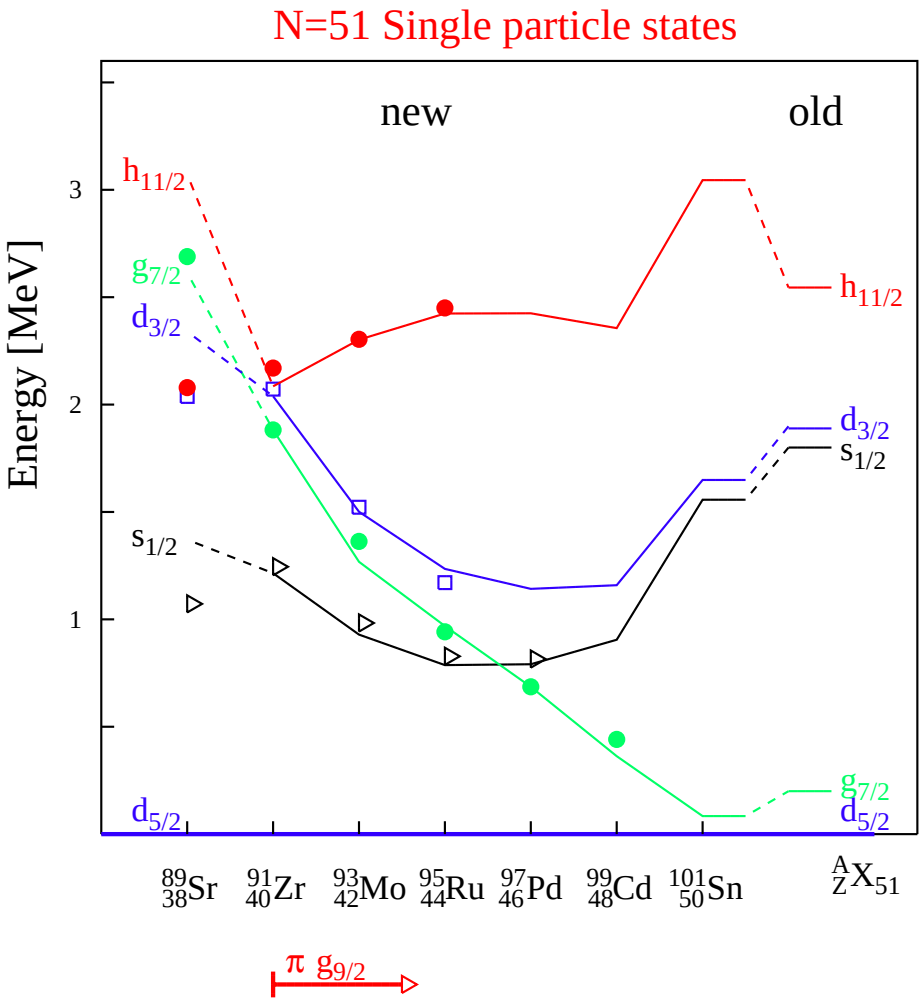

Figure 5.1: The monopole shift in the single-particle states of the $N = 51$ isotones. The filling of the $\pi g_{9/2}$ orbital influences strongest $\nu g_{7/2}$ (see text for details). The experimental energies are marked with symbols, where the open ones indicate not firmly assigned states. The lines are results of shell-model calculations.

5.2 Large-scale shell model (LSSM)

For a given valence space the choice of the basis is only a matter of convenience, but in practical SM calculations there are mainly two possibilities:

- the m-scheme,
- the coupled scheme.

In m-scheme the states of the basis are Slater Determinants (SD) of A particles distributed in k individual orbitals $|nljm\tau\rangle$, each having its own space coordinates $r(k)$. Then the many-body wave-function is constructed as:

$$\Phi_{a_1,a_2,....,a_A}(1,....,A) = det\{\phi_{a_k}(r(k))\} \ , \tag{5.2}$$

which expressed in terms of second quantization looks like:

$$|\Phi_{a_1,a_2,....,a_A}(1,....,A)\rangle = \prod_k a^+_{a_k}|0\rangle \ . \tag{5.3}$$

The advantage of this representation is the simplicity of the calculation of the many-particle matrix elements of H_{eff}, because they reduce to the TBME of H_{eff} in m-scheme with a phase. That means that independently on the size of the matrix, the number of the non-zero matrix elements is relatively limited and the physical states come out of the diagonalization of $\langle\Phi_{a_k}|H_{eff}|\Phi_{a'_k}\rangle$.

Another important advantage is that based on these ideas, the Glasgow group has introduced a very simple computer implementation of the m-scheme [Whit77]. In it, each SD is represented by an integer machine word and each bit of the machine word is associated to a given individual state $|nljm\tau\rangle$. Each bit has a value 1 or 0 depending on whether the state is occupied or empty. The action of the Hamiltonian on such object is very simple, because the creation and annihilation operators are transformed into elementary bit operations. Then, a two-body operator $a^+_i a^+_j a_k a_l$ will search for the word having the bits i, j, k, l in the configuration 0011 and change it to 1100. This generates new words which have to be located on the list of all the words by the bi-section method.

However the drawback of this scheme is that the symmetries of the Hamiltonian are not explicit in this basis and the size of the matrices is therefore maximal: $\sim \binom{d_\pi}{p} \cdot \binom{d_\nu}{n}$, where d_π/d_ν is the degeneracy of the proton/neutron valence space and the p/n is the number of the active protons/neutrons in the corresponding space. The programs OXBASH and ANTOINE, mentioned in this thesis, use the m-scheme approach, and their limitation, as shown, is obviously the computer capabilities to store and handle large amounts of binary data. The ANTOINE program, however, has a superior performance due to optimization of the code with respect to some of the advances in computers, like using large virtual memory, etc.

The J or JT coupled basis, splits the full m-scheme matrix into boxes, whose dimensions are smaller, where J and T are the total spin and total isospin of the configuration, correspondingly. This is especially efficient for $J = 0$ states. The states of n particles in a given j orbital are defined as $|\gamma_i\rangle = |(j_i)^{n_i} v_i J_i x_i\rangle$, where v_i is called seniority and stands for the number of unpaired nucleons in the configuration. Then the k-shell states are obtained by successive angular momentum couplings of the one-shell basic states [Caur99a]: $\left[\left[\left[|\gamma_1\rangle|\gamma_2\rangle\right]^{\Gamma_2}|\gamma_3\rangle\right]^{\Gamma_3}...|\gamma_k\rangle\right]^{\Gamma_k}$. Compared to the simplicity of the m-scheme, the calculation of the non-zero many-body matrix elements is much more complicated and involves products of coefficients of fractional parentage and $9j$-symbols. In the case of J coupling, a strong simplification in the calculation of those matrix elements can be achieved using the quasi-spin formalism [Laws98], which reduces a huge factor of the computing time [Nowa96]. One of the most advanced examples of a coupled scheme code is NATHAN developed by the Strasbourg group.

5.2.1 Calculation of ^{100}In GT β-decay

Figures 1.3, 1.4 and 1.5 in Sect. 1.3 show the orbitals responsible for the nuclear structure in this region and their ordering with respect to the $N = Z = 50$ ^{100}Sn core. The natural model space "south-east" of ^{100}Sn (i.e. $N \geq 50$ and $Z \leq 50$) consists for neutrons of the $1d_{5/2}, 0g_{7/2}, 2s_{1/2}, 1d_{3/2}$ ($N_{HO} = 4$) orbitals complemented by the $N_{HO} = 5$ intruder orbital $0h_{11/2}$, while for protons the pf-shell $N_{HO} = 3$ orbitals are complemented by the $0g_{9/2}$ ($N_{HO} = 4$) orbital. Another issue to consider is if one can find the effective interaction for the chosen model space. In the case of the ^{100}In Gamow-Teller β-decay one certainly needs to include the $\pi 0g_{9/2}$ and the $\nu 0g_{7/2}$ orbitals into the model space. Additionally the neutron $\nu 1d_{5/2}$, which is nearly degenerate with the $\nu 0g_{7/2}$ orbital, and the proton $\pi 1p_{1/2}$, which is very close to the $\pi 0g_{9/2}$ orbital was required. The inclusion of the $0h_{11/2}$ orbital is important for the high-spin configurations, while $\nu 2s_{1/2}, 1d_{3/2}$ have their weight in low-spin configurations.

It was possible to acquire a realistic effective interaction [HJenPC] from the Oslo group. The interaction is derived from a bare nucleon-nucleon potential as described in Ref. [HJen95]. It is derived for the mass region of ^{100}Sn and therefore used in calculations of the closest neighbours without further mass scaling. The model space of the interaction is $\pi 0g_{9/2}, 1p_{1/2}$ and $\nu 0g_{7/2}, 1d_{5/2}, 1d_{3/2}, 2s_{1/2}, 0h_{11/2}$. The TBME are in pp formalism, which means that the calculations are performed relative to the ^{88}Sr core. Therefore besides the TBME one needs the single particle energies relative to ^{88}Sr.

As introduced in Sect. 5.1.2, for this realistic interaction one cannot rely on the SPE resulting in its derivation, but a monopole correction is necessary. As

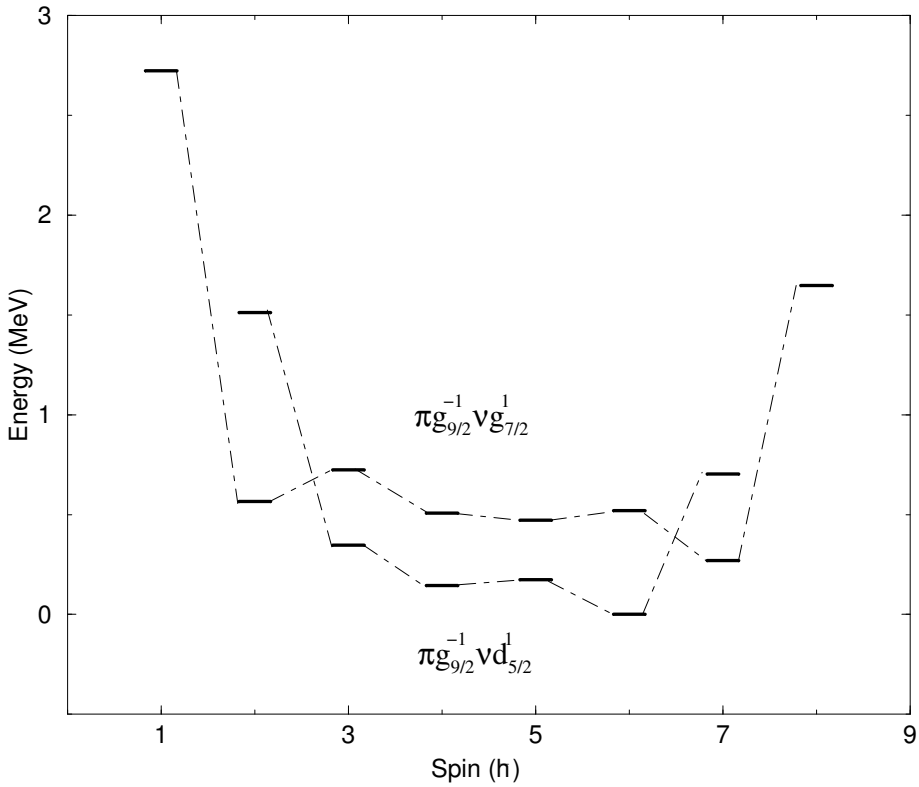

Figure 5.2: Calculated level energies of the $\pi g^{-1}_{9/2} \nu d^{1}_{5/2}$ and $\pi g^{-1}_{9/2} \nu g^{1}_{7/2}$ multiplets of ^{100}In. States belonging to the same multiplet are connected to guide the eye.

a reference I have taken in the calculations the empirical SPE shown in Fig. 1.4 relative to ^{100}Sn [Graw01a], which are: $\pi 0g_{9/2} = -2.92MeV$, $\pi 1p_{1/2} = -3.53MeV$; and $\nu 0g_{7/2} = -11.07MeV$, $\nu 1d_{5/2} = -11.15MeV$, $\nu 1d_{3/2} = -9.50MeV$, $\nu 2s_{1/2} = -9.60MeV$, and $\nu 0h_{11/2} = -8.60MeV$. Then I have adjusted the SPE relative to ^{88}Sr so that the single-particle(-hole) spectrum at the CS$\pm$1 neighbours of ^{100}Sn is reproduced. This procedure fixes the distances between (relative energies of) single particle orbits for the proton and neutron valence spaces. The absolute values were fixed by adjusting the calculated binding energies (B.E.) of the ground states (g.s.) of ^{100}Sn, ^{101}Sn and ^{99}In, so that the B.E. of ^{99}In g.s. minus the B.E. of ^{100}Sn g.s. is equal to the SPE of $\pi 0g_{9/2}$. Similarly, the absolute value for $\nu 1d_{5/2}$ SPE was adjusted from the B.E. difference of ^{100}Sn and its one neutron-particle neighbour ^{101}Sn. The SPE, relative to the ^{88}Sr core as well as all TBME, used in the calculations, are listed in Appendix B.

The calculations were done by the OXBASH shell-model package. The calculations usually start with the program SHELL, which generates a batch command file with all the relevant information needed to complete the calculation. It reads the definition of the single-particle states from data file with extension '.SPS', and

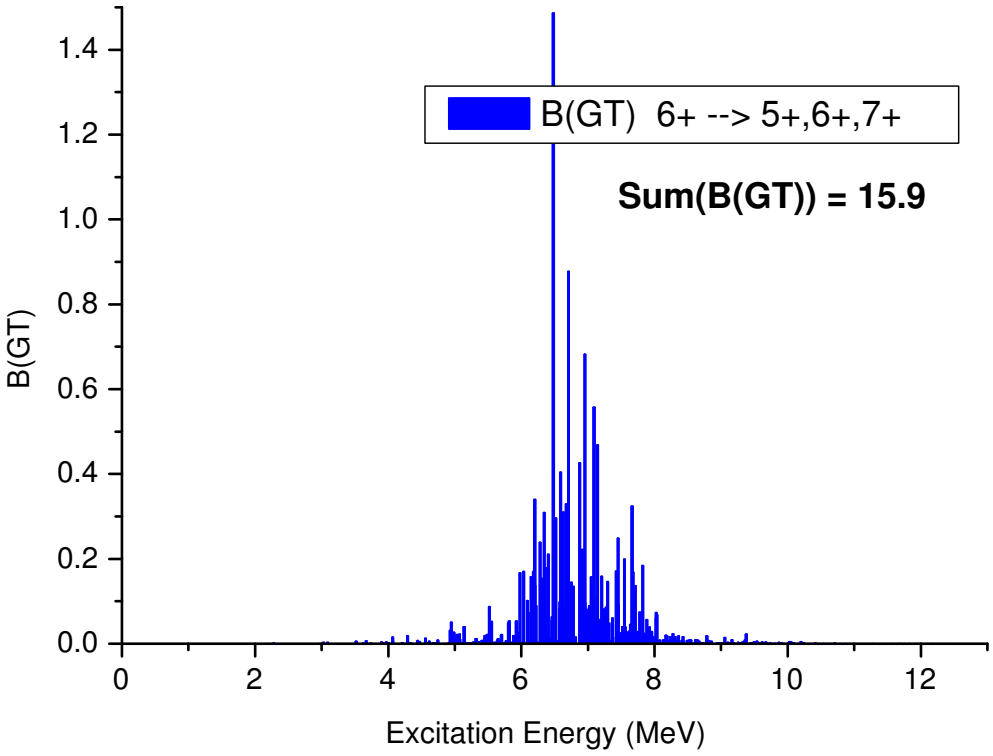

Figure 5.3: The shell model GT-decay strength of the 421 individual transitions from parent 6^+ ground state in ^{100}In to all calculated 5^+, 6^+ and 7^+ states in ^{100}Cd. The sum given in the figure excludes daughter excited stated which lie beyond an excitation energy corresponding to the experimental $Q_{EC} = 10.08$ (see text).

reads the SPE and TBME (see Appendix B), in JT-scheme, from a file with extension '.INT'. Both *isospin* and *proton/neutron* formalisms are possible, but for very large calculations the proton/neutron formalism is the preferred one. Traditionally one calculates the wave functions of the many-body states, finds their energy and builds the predicted level scheme. Additionally one could use the calculated wave functions to calculate one- or two-body transition densities. These could be used further to calculate moments $B(EL)$, $B(ML)$ and $B(GT)$ with the help of the program TRANS, also part of the OXBASH package. For detailed user reference on the OXBASH package read Ref. [Brow88b].

The GT decay of the parent state (6^+ or 7^+) in ^{100}In has the selection rules $\Delta I = \pm 1, 0$ and therefore populates: (i) $6^+ \rightarrow 5^+, 6^+, 7^+$ or (ii) $7^+ \rightarrow 6^+, 7^+, 8^+$ states in the daughter nucleus ^{100}Cd. The g.s. of ^{100}In in the case when the standard empirical SPE energies, as discussed above, are used is 6^+. It is the lowest state from the multiplet $\pi g^{-1}_{9/2} \nu d^1_{5/2}$. The lowest 7^+ state in ^{100}In belongs to the multiplet $\pi g^{-1}_{9/2} \nu g^1_{7/2}$ and is a few hundreds of keV higher in energy. Both multiplets are shown in Fig. 5.2.

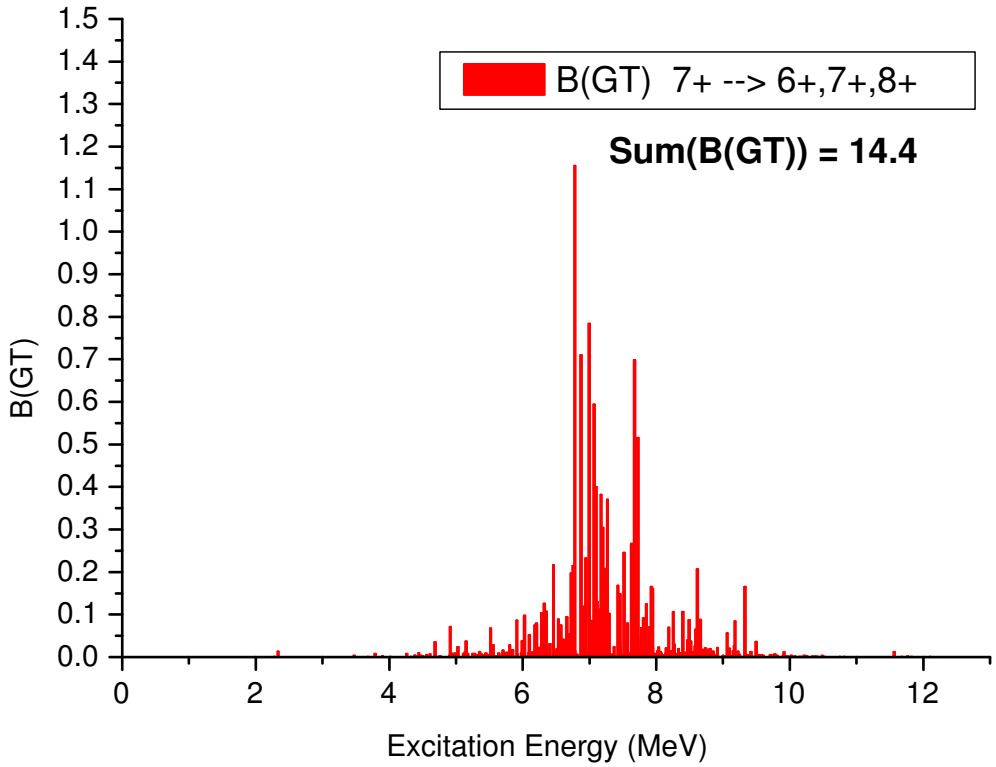

Figure 5.4: The shell model GT-decay strength of the 398 individual transitions from parent 7^+ ground state in ^{100}In to all calculated 6^+, 7^+ and 8^+ states in ^{100}Cd. The sum given in the figure excludes daughter excited stated which lie beyond an excitation energy corresponding to the experimental $Q_{EC} = 10.08$ (see text).

Besides the wave functions of the parent states, I have calculated the spectrum of ^{100}Cd with explicit diagonalization of all states (within this model space) with spins $5^+, 6^+, 7^+$ and 8^+ in order to have their wave functions. The total number of $5^+, 6^+, 7^+$ states is 421, while for $6^+, 7^+, 8^+$ that number is 398 states. All the calculations were done in the full basis of the model space, i.e. without any truncations. Following the OXBASH procedure I have calculated the transitions densities for the transitions $6^+ \rightarrow 5^+, 6^+, 7^+$ and $7^+ \rightarrow 6^+, 7^+, 8^+$. Finally I have extracted the reduced Gamow-Teller strength distributions, which are shown for both cases on Figs. 5.3 and 5.4. The total $B(GT)$ strength, noted on Figs. 5.3 and 5.4, is a sum of the individual transition strengths where the calculated daughter states lie below the experimental Q_{EC} value of 10.08 MeV [Plet02] (see Sect. 4.1). Then to compare with the experimentally extracted β-intensity and GT-strength distributions (see Sect. 6.1.3), the discrete theoretical GT-strength distributions (Figs. 5.3 and 5.4) were folded with Gaussian functions which parameters depend on the experimental response of the Total Absorption Spectrometer. This procedure was done by my col-

league Dr. Leonid Batist who analyzed completely the TAS data (see Sect. 4.1). The resulting spectra folded by the detector response function are plotted on Figs. 6.2 and 6.3 together with the experimental data. They are compared and discussed in Sect. 6.1.

In addition, the multiple calculated $5^+, 6^+, 7^+$ and 8^+ excited states in ^{100}Cd were used for constructing the "statistical" level density, of the states fed in the GT decay, in the TAS unfolding procedure 4.1.3. Finally, the lowest calculated yrast and yrare states in ^{100}Cd, shown in Fig. 6.1, were used to interpret the resolved γ de-excitations following the β decay and spin-parity assignment of some new ^{100}Cd levels (see Sect. 6.1).

5.2.2 Calculation of the ^{98}Cd spectrum

With the availability of large-scale shell model codes such as ANTOINE and NATHAN it has become possible to perform untruncated calculations with monopole corrected interactions in the pf-shell up to ^{60}Zn [Mazz01, CaurPC], which makes an extension to ^{100}Sn including $np-nh$ excitations a new challenge. This was possible and was contributed by our collaborators, Frederic Nowacki and Etienne Caurier, from the Strasbourg-Madrid shell model group.

For calculation of ^{100}Sn core excitations we have chosen the $(gds)(N_{HO}=4)$ model space comprising the $[0g_{9/2}, 1d_{5/2}, 0g_{7/2}, 2s_{1/2}, 1d_{3/2}]$ orbitals above a hypothetical ^{80}Zr core and have used a realistic G-matrix based interaction as described in [HJen95]. At this number of orbitals and valence particles/holes the computer limitations are already strong and only in certain cases calculations in full basis are possible. In all other cases an appropriate truncation is applied. As ^{80}Zr in its ground state is not spherical, single-particle energies were estimated from the global predictions as discussed in Ref. [Dufl99]. Monopole corrections were applied to reproduce the extrapolated single-particle/hole energies of ^{100}Sn [Graw01a] including a shell gap of 6.50 MeV. The higher multipoles were scaled by a factor of 1.15 yielding a consistent description of the core-excited isomers in the region [Plet04]. Effective $E2$ and $E4$ polarization charges of 0.5 e were used to calculate transition rates. The convergence of the shell model with the number of ph excitations t (t is referred to as the truncation level) included in the calculations is shown in Fig. 6.5. This figure compares the theoretical with the experimental results and therefore is shown in the discussion part (see Sect. 6.2). Running ahead I point out that at a truncation level of $t=4$ a near-convergence has been reached for all observables and therefore time consuming calculations with $t>4$ were not performed. The results from this SM calculation are further on referred to as GDS. The calculated levels are compared to the experimental ones in Fig. 6.4 and discussed in Sect. 6.2.

Chapter 6

Discussion

Beta decay and in-beam investigations following fusion-evaporation reactions provide the adequate tools for exploring the structure of nuclei near the double shell closure at $N = Z = 50$. The main topics of interest which characterize this mass region are single-particle energies and shell gaps as determined by the nuclear mean field, residual interaction – specifically in the proton-neutron channel – and the Gamow-Teller strength of the $\pi g_{9/2} \rightarrow \nu g_{7/2}$ transition.

6.1 The nucleus ^{100}In

^{100}In, representing the $\pi\nu$ particle-hole (ph) configuration with respect to the doubly magic nucleus ^{100}Sn, is the closest-lying neighbor to this core nucleus which is accessible to detailed $\beta\gamma\gamma$ spectroscopy while still having a simple ph shell-model structure. The ph multiplets $[\pi g_{9/2}^{-1}\nu d_{5/2}]_{2-7}$ and $[\pi g_{9/2}^{-1}\nu g_{7/2}]_{1-8}$ provide the leading configurations which determine the ground-state spin of ^{100}In. Values of 6^+ and 7^+, respectively, are expected to become the lowest-lying members of these multiplets (see Fig. 5.2). It is decisive for the verification of the $\pi\nu$ residual interaction to experimentally determine the spin of the ground state of ^{100}In.

The following sections discuss in the light of the LSSM calculations (Sect. 5.2.1): (i) the experimental level scheme of the daughter nucleus ^{100}Cd; (ii) the experimental I_β and GT distributions; and address (iii) the spin-parity and configuration assignments to the ^{100}In ground state.

6.1.1 ^{100}Cd low-lying states

Figure 6.1 shows the experimental low-lying states of ^{100}Cd and the lowest positive parity states of spins $2^+ - 8^+$ from the LSSM calculation. The first excited state I^π=2^+ is very close to the experimental value. It has a mixed configuration, where the valence neutrons occupy mainly the $1d_{5/2}$ orbital (47 %), while about 20 %

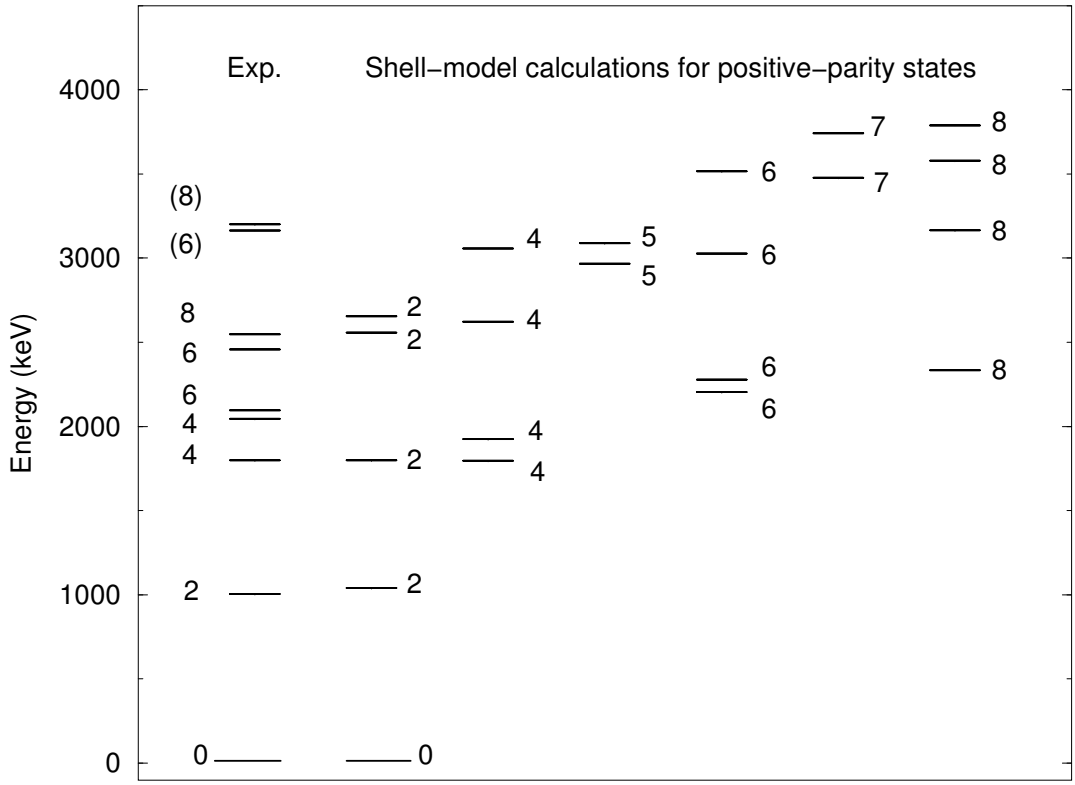

Figure 6.1: Comparison of experimental ^{100}Cd level energies with shell-model predictions. In the first column the experimental energy levels are presented. The other columns comprise yrast and yrare groups of theoretical states ordered according to their spin and energy.

amplitude comes from the $0g_{7/2}$ orbital. For all the shell-model states presented in Fig. 6.1, the proton contribution to the wave function is largely dominated by two holes in $g_{9/2}$ and two particles in the $p_{1/2}$ orbitals, and the other configurations with different occupancies playing no significant role. The 4_1^+ state, correctly predicted in energy, has the same dominant structure as the 2^+ state. The same is true for the 6_1^+ state as well. The 4_2^+ wave function is more fragmented since the dominant configuration is identical with that of 4_1^+, but significant contributions originate from neutrons either in $d^1_{5/2}d^1_{3/2}$ or in $g^1_{7/2}d^1_{5/2}$ orbitals, respectively. This is the lowest state where the pair of valence neutrons is broken and the seniority is different from zero; the next state of this character is 6_2^+. The different wave functions of the 4_1^+ and 4_2^+ states result in a lower mixing between them and leads to their closeness in spacing, which is in agreement with the experiment. A more dramatic effect is observed for the first two 6^+ states, since their wave functions have no major overlap, and thus the energetic spacing is calculated to be 78 keV only. In the experiment, this spacing is much larger, which may point out that the real wave functions have a slightly

different structure than predicted. The calculated 8^+_1 state, predominantly of $\pi g^{-2}_{9/2}$ character, lies somewhat lower than in experiment. The configuration assignments agree also with previous shell-model calculations for ^{100}Cd [Albe92], performed in the same model space but using a set of two-body matrix elements derived from the Sussex and Yale codes [Skou77].

The newly assigned experimental level at 3164 keV, with a tentative spin and parity assignment of 6^+, is very close to the calculated 6^+_3 state. The wave-function is dominated by a 62 % $\nu[g^0_{7/2}d^2_{5/2}]$ configuration. This is well supported by the experimentally observed decay mode of this level, which feeds the 6^+_1 and 4^+_1 levels, see Fig. 4.3. The spin and parity assignment for the newly identified ^{100}Cd state at 3200 keV was inferred from a comparison with the shell-model calculations. The structure of the 8^+_2 state is interpreted as having one neutron pair broken and distributed in the $g_{7/2}d_{5/2}$ orbitals.

All in all, the LSSM calculations (see Sect. 5.2.1) employing a realistic interaction performed as part of this thesis work, give a good description of the low-lying levels of ^{100}Cd.

6.1.2 Beta feeding I_β and GT distribution

Figure 6.2 (a) shows the experimental I_β distribution. The main part of the I_β distribution is characterized by a resonance occurring at excitation energies above 4 MeV, peaking at 6.4 MeV and having a FWHM value of 1 MeV. As the statistical uncertainties of the TAS data are very large for excitation-energies below 5.5 MeV, the corresponding I_β are not reliable. The theoretical results are displayed in panels (b) and (c) of Fig. 6.2. Under the assumption that the ground-state spin of ^{100}In is 6^+ (b), the theoretical I_β distribution shows almost no direct feeding (less than 1%) for the 6^+ 2096 keV level, which is close to the experimental finding, as observed in Fig. 4.4 (b). The centroid position of the resonance is reproduced in the calculations, but not its width. In the calculation assuming that the ground-state spin is 7^+ (panel (c)), a considerable feeding of the 8^+ level is predicted, which is in contradiction with the experimental TAS value (see Table 4.3). The tail of the resonance towards lower energies resembles the experimental one.

The experimental GT distribution as calculated from the I_β distribution by standard procedures [Hu99], making use of the Q_{EC} value of 10.08(23) MeV adopted in Sect. 4.1.5, and using the ^{100}In half-life of 5.9(2) s (see Table 4.2 and Sect. 4.1.3), is shown in Fig. 6.3(a). The centroid of the GT resonance is located at an excitation energy of 6.4 MeV and has a width of approximately 1 MeV. The partial strength detected by the TAS in γ rays is determined to be $B_{GT,g} = 3.0(9)$ [Plet02]. The B_{GT} is given in units of $g^2_A/4\pi$. The uncertainty includes that of the I_β distribution of 0.60, and that of the Q_{EC} value originating from the proton separation value (S_p) of 0.70. Since the latter has the dominating contribution it ought to be measured

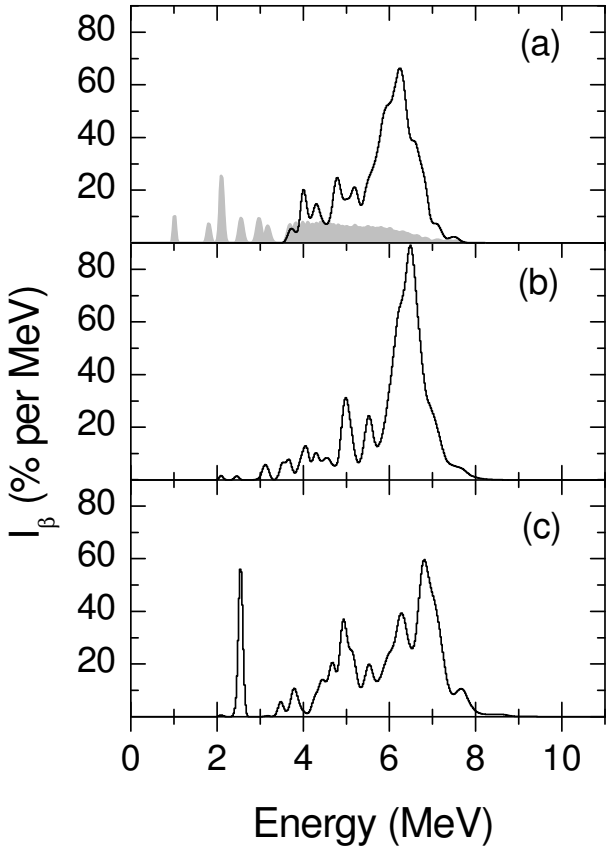

Figure 6.2: Experimental (a) β-intensity distribution, and theoretical predictions from the shell-model, under hypotheses of a 6^+ (b) and 7^+ (c) assignment for the ground state of ^{100}In. The experimental uncertainties are indicated as a shadowed area in panel (a). The calculations have been folded with a Gaussian function having a width equal to the experimental TAS resolution. (from [Plet02])

with higher precision. Similarly, the delayed proton branch results in a partial GT strength of $B_{GT,p}$=0.86(15) [Plet02]. The $B_{GT,p}$ uncertainty originates from the βp counting statistics and the half-life determination, and contains a minor contribution from the $Q_{EC} - S_p$ value. Thus, the experimentally determined total GT strength is $B_{GT,\gamma} + B_{GT,p} = 3.9(9)$ [Plet02].

Total GT strengths of 15.9 and 14.4 are calculated for spins of 6^+ and 7^+, respectively. In the approach of Ref. [Karn01] total GT strengths of 15.9 and 15.8 were calculated for spins of 6^+ and 7^+, respectively, whereas 3.9(9) was determined experimentally [Plet02](see also Sect. 6.1.2). This translates into hindrance factor values of $h = 4.1(9)$ for 6^+ and of 3.7(9) for 7^+. These values should be compared to the experimental values of 3.8(7) for ^{98}Cd [Brow94] and to that of 4.3(6) measured for ^{97}Ag [Hu99]. The theoretical hindrance factor of ^{100}Sn is 3.0 [Hu99]. Thus,

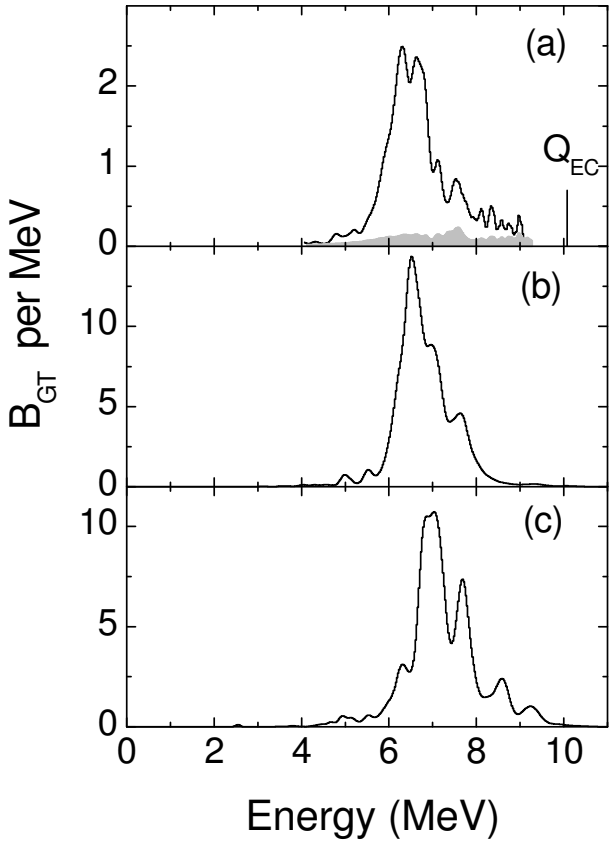

Figure 6.3: Experimental B_{GT} distribution (a) compared to theoretical distributions calculated in LSSM calculations for parent spin assumption 6^+ (b) and 7^+ (c). The experimental uncertainties are indicated as a shadowed area in panel (a). Above 6.3 MeV energy proton contributions can be seen in panel (a).(from [Plet02])

within the large experimental uncertainties, the ^{100}In β decay exhausts the strength of the GT resonance predicted for ^{100}Sn.

In the light of the shell-model results the reasons for the smooth TAS spectrum, the weak feeding of low-lying states and the large β feeding of the GT resonance are threefold.

(i) The low-lying ^{100}Cd states of $2qp$ character $\nu d_{5/2}g_{7/2}$ and $\nu g^2_{7/2}$, can be fed by the unpaired $\pi g_{9/2}$ only, whereas the remaining $(\pi g_{9/2})^8_{0^+}$ decay to the GT resonance of $4qp$ states at high excitation energy. As far as β intensities are concerned, the high suppression of the reduced transition rates is largely compensated by the decay-energy selectivity of the f_{b^+} phase-space factor.

(ii) The wave functions of the $I^\pi = 6^+$ to 8^+ ^{100}Cd daughter states as discussed in Sect. 6.1.1 have little overlap with those of the $4qp$ states. As the two possible parent configurations $(\pi g^{-1}_{9/2}\nu d_{5/2})_{6^+}$ and $(\pi g^{-1}_{9/2}\nu g_{7/2})_{7^+}$ are rather pure the $I^\pi = 6^+$

to 8^+ ^{100}Cd levels cannot be strongly fed in GT decay.

(iii) The dominating $4qp$ GT-resonance configurations $(\pi g_{9/2})^8_{I_\pi}(\nu d_{5/2}g_{7/2})_{I_\nu}$ and $(\pi g_{9/2})^8_{I_\pi}(\nu g_{7/2})^2_{I_\nu}$ under the assumption of $I^\pi = 6^+$ or 7^+, respectively, for the ground state of ^{100}In, are connected to the $2qp$ states by strong $M1$ transitions. This can be concluded from the largely different magnetic moments of the $2qp$ and $4qp$ states [Albe92].

6.1.3 Spin-parity of the ^{100}In ground state

Besides the direct result from the LSSM calculation of the ^{100}In spectrum (this work) predicting that the 6^+ is lowest in energy, there are several other ways of inspecting the data that could help to infer the spin and parity of the ^{100}In ground state.

Firstly, the relative β-delayed proton emission feeding levels of different spins is a quantity sensitive to the spin of the decaying nucleus. Hence an analysis of experimentally measured feeding may provide information about the ground state spin and parity of ^{100}In. On the basis of the statistical approach discussed in Ref. [Horn72], we calculated the relative intensities of the EC-delayed proton emission to ^{99}Ag states, assuming spin and parity values of 6^+ or 7^+ for the ^{100}In ground-state. Table 6.1 presents the experimental and the calculated proton intensities.

Secondly, one may compare the experimental β-intensity and GT distribution with the theoretical calculations as already started in Sect. 6.1.2. The experimental GT distribution Fig. 6.3 (a) is compared to shell-model predictions in Figs. 6.3 (b,c). The calculated distributions are normalized to a total strength calculated with a free-nucleon GT operator. The position and width of the experimental resonance are reproduced very well in the case of the calculation assuming 6^+ for ^{100}In g.s. The small upward shift in position can be attributed to the neglect of excitations of the ^{100}Sn core. It has been pointed out earlier [Hu99] that a small renormalization of the proton-neutron interaction strength can account for this shift.

Table 6.1: Comparison of calculated and experimental ECp intensities for the lowest-lying $9/2^+$ $7/2^+$ and $13/2^+$ ^{99}Ag states.

^{100}In	^{99}Ag states		
ground state	$9/2^+$	$7/2^+$	$13/2^+$
5^+	720	120	22
6^+	610	51	50
7^+	320	28	70
8^+	180	4.4	76
EXP	570(60)	27(5)	62(12)

Finally we should admit, that the presented experimental data do not permit us to draw any firm conclusion with respect to the ground-state spin of ^{100}In. The LSSM calculations described in Sect. 5.2.1 were used to make predictions concerning the $\pi g_{9/2}^{-1}\nu d_{5/2}^{1}$ and $\pi g_{9/2}^{-1}\nu g_{7/2}^{1}$ multiplet energies in ^{100}In, as displayed in Fig. 5.2. It is observed that the calculation favors a ground-state spin of 6. The 7^+ state, originating from the $\pi g_{9/2}^{-1}\nu g_{7/2}^{1}$ multiplet, is located at an excitation energy of 250 keV. Both states have rather pure wave functions with 94% and 70% in the leading configurations for $I^\pi = 6^+$ and 7^+, respectively. The assignment of 6^+ is supported also by the EC-delayed proton analysis and favoured by the I_β and GT-strength distribution analysis. The systematics of the neighbouring In isotopes also support the 6^+ being the ^{100}In g.s. The latest results for ^{102}In [Karn04] and ^{104}In [Sewe95] show that the closest even light In isotopes also have 6^+ ground states.

6.2 The nucleus ^{98}Cd

The nucleus ^{100}Sn has been used as an inert core in numerous shell-model calculations (see [Graw01a] for a recent review) and derivations of realistic interactions [Sina92, HJen95, Andr96]. From the striking similarity of its single-particle structure to ^{56}Ni [Graw01a], one major shell below, it can be inferred, however, that its ground state contains a similar percentage of multiple *ph* excitations as ^{56}Ni [Otsu98, Nowa02]. On the other hand, particle-hole shell-model calculations in minimum model spaces using empirical interactions were performed for $N \leq 50$ nuclei to account for core-excited states [Muto84] and Gamow-Teller β decay [John01, Bati03]. These two extreme approaches are used to enlighten the experimental data on core-excited states and electromagnetic transition rates in ^{98}Cd.

6.2.1 Level energies and shell gap

The decay scheme shown on Fig. 4.13 in Sect. 4.2 is plotted again on Fig. 6.4, this time in full scale and together with the ^{98}Cd ESM (Sect. 5.1.1) and LSSM (Sect. 5.2.2) calculations.

The SM calculations (see Fig. 6.4) and the following considerations imply that the high-energy γ ray is the primary $E4$ isomeric transition. An odd-parity assignment is discarded on the following grounds: (i) Excitations to the $h_{11/2}$ orbit are expected to be at least 2.5 MeV above those to the $d_{5/2}$ and $g_{7/2}$ orbitals [Graw01a]; (ii) the coupling of a possible low-lying $I^\pi = 3^-$ state in ^{100}Sn [Górs98a] to the 8^+ isomer would decay back by a non-isomeric high-energy $E3$ transition. On the other hand the $E1$ transition of a 12^+ state to such an 11^- state would be highly configuration hindered due to particle- and l-forbiddance. Alternatives for the spin-parity assignment to the new isomer and its γ decay require the existence of a non-observed

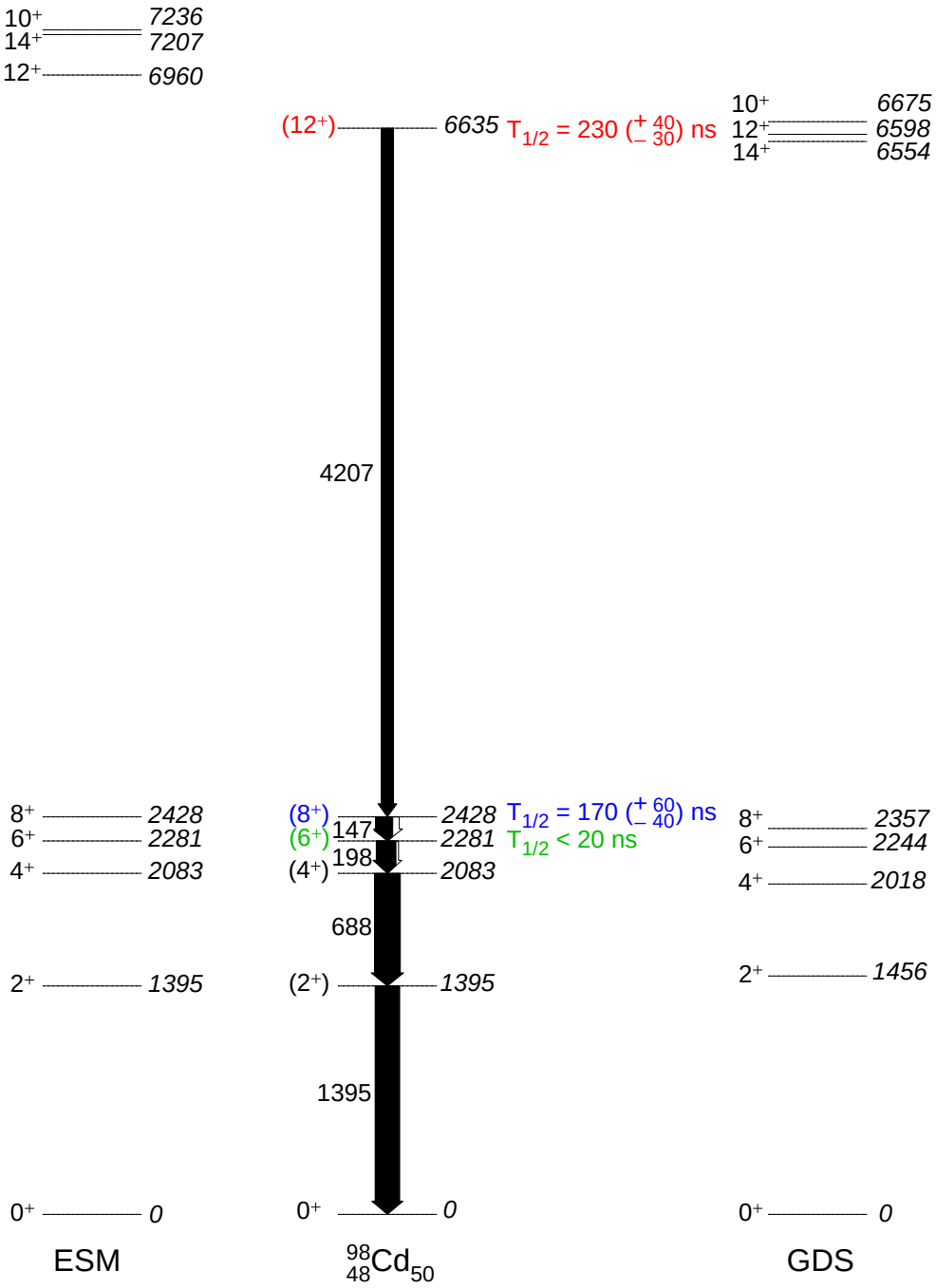

Figure 6.4: Experimental level scheme of ^{98}Cd in comparison to empirical shell model results in the pure configuration $\pi g_{9/2}^{-2}\nu g_{9/2}^{-1}d_{5/2}$ (ESM) and in the full $\pi\nu(gds)$ model space at truncation level $t = 4$ (GDS).

highly converted primary $E2$ transition. The close structural analogy between ^{100}Sn and ^{56}Ni [Graw02, Graw99] would suggest a $12^+ \rightarrow 10^+ \rightarrow 8^+$ sequence as inferred from the analogous $10^+ \rightarrow 8^+ \rightarrow 6^+$ cascade in ^{54}Fe with an $E2/E4$ branching ratio of 54 : 1 [ENDSF, Rafa83]. From the present spectra (Figs. 3.8, 3.9 and 4.9) the branching of a second high-energy γ-ray within $\pm$100 keV of the 4207 keV transition can be restricted to be < 10 %. The dominance of the $E2$ branch in ^{54}Fe after proper scaling with mass A (radius dependence of EL operator), transition energies (E_γ^{2L+1}) and internal conversion reduces to less than 1 : 1 in ^{98}Cd assuming an 80 keV lower observational limit for the $E2$ transition. Based on the assumption of an unchanged relative reduced $E4$ and $E2$ strength between ^{56}Ni and ^{100}Sn, this is at variance with the experimental observation of one dominating transition. Therefore the hypothetical 10^+ would lie either less than 80 keV below the 12^+ state, or above, leaving an $E4$ assignment for the observed 4207 keV transition. A second alternative consistent with the observed γ decay, a $14^+ \rightarrow 12^+ \rightarrow 8^+$ sequence, is unique for ^{100}Sn and has no counterpart in ^{54}Fe. Due to the near-degeneracy of the $d_{5/2}$ and $g_{7/2}$ neutron orbits [Graw01a] the $I^\pi = 14^+$ state of configuration $\pi(g_{9/2})_{8^+}\nu g_{9/2}^{-1} g_{7/2}$ can come very close to the $I^\pi = 12^+$ state involving the $d_{5/2}$ orbital. The corresponding 12^+ state in ^{54}Fe cannot be isomeric as the $\nu p_{3/2} - f_{5/2}$ splitting is 1.03 MeV in ^{56}Ni [Graw01a]. In conclusion $E4$ character was inferred for the 4207 keV primary γ ray originating from an $I^\pi = (12^+)$ state. From the present data, however, the existence of a 10^+ and/or 14^+ state close below and/or above the $I^\pi = (12^+)$ isomer cannot be excluded.

In Fig. 6.4 the experimental decay scheme of the $I^\pi = (12^+)$ and (8^+) isomers is compared to the results of the LSSM calculation at $t = 4$ (GDS) and the empirical ESM approach. The two-proton hole valence levels of predominant (68 %) $\pi g_{9/2}^{-2}$, $I^\pi = 0^+ - 8^+$, which serve in the ESM approach as input, are excellently accounted for by the GDS calculation.

The excitation energy of the core excited I^π=12^+ isomer is determined by the ^{100}Sn neutron shell gap, which in the GDS calculation is adopted to be identical to the proton gap as can be inferred from a comparison to ^{56}Ni [Graw02], and by the interaction energy in the leading configurations $\pi g_{9/2}^{-2}\nu g_{9/2}^{-1}(d_{5/2},g_{7/2})$. The latter is dominated by the strongly binding $\pi \mathrm{g}_{9/2}^{-2}$ $\nu g_{9/2}^{-1}$ interaction energy, which is approximately equal to the $\pi g_{9/2}^{-2}$ pairing energy (see e.g. [Graw99]). Therefore the excitation energy of the isomer is a direct measure of the ^{100}Sn shell gap. This is corroborated by the analogous situation in ^{56}Ni, namely the I^π=10^+ isomer in ^{54}Fe at $E_x = 6527$ keV [Rafa83] as compared to an average 6.410 MeV shell gap for protons and neutrons [Graw99]. In the present shell-model approaches shell gaps of 6.50 MeV (GDS) and 6.78 MeV (ESM) were adopted. From a comparison to the experimental core-excitation energy as documented in the $12^+ \rightarrow 8^+$ transition energy values of 6.47 MeV (GDS) and 6.46 MeV (ESM) are inferred to match theory

and experiment. Therefore an average value of 6.46(15) MeV is adopted for the shell gap with the error stemming from systematic model and interaction dependent uncertainties including a contribution by an unobserved low-energy γ-ray transition (see Sects. 4.2.3 and 6.2.2). The value is in good agreement with previously quoted values and uncertainties [Graw95, Lipo02] but much less affected by systematic ambiguities.

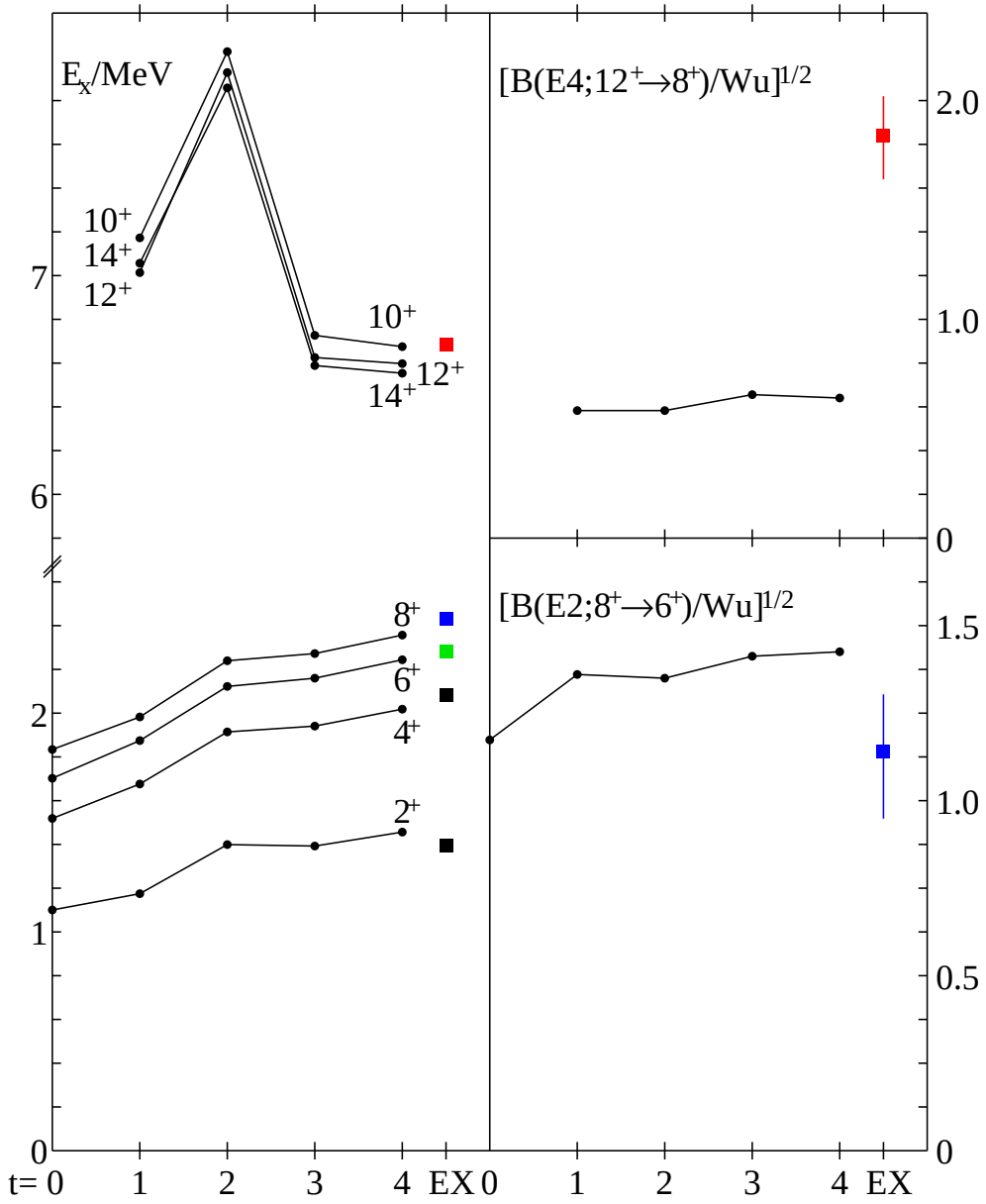

Figure 6.5: Convergence of selected observables with truncation level t in the GDS calculation. Note the broken energy scale between 2 and 6 MeV.

Table 6.2: Experimental and shell model $E2$ and $E4$ strengths in Weisskopf units (for $E2$: 1 W.u. = 26.84 e^2fm^4 and for $E4$: 1 W.u. = 12830 e^2fm^8). Polarization charges of 0.5 e were used for the $E2$ and $E4$ operator, respectively.

$I_i^\pi \rightarrow I_f^\pi$	E_γ [keV]	σL	GDS [W.u.]	EXP [W.u.]
$6^+ \rightarrow 4^+$	198	E2	5.14	>3
$8^+ \rightarrow 6^+$	147	E2	2.03	1.3(4)
				1.1(2)[1]
$12^+ \rightarrow 8^+$	4207	E4	0.41	3.4(7)
$14^+ \rightarrow 12^+$	<80	E2	0.20	>4.9[2]
$12^+ \rightarrow 10^+$	<80	E2	0.69	>4.9[3]
$10^+ \rightarrow 8^+$	-	E2	0.013	-

[1] From ref. [Grzy98]

[2] Estimate in case of the alternative decay sequence $14^+ \rightarrow 12^+ \rightarrow 8^+$

[3] Estimate in case of the alternative decay sequence $12^+ \rightarrow 10^+ \rightarrow 8^+$

The level sequence in the GDS calculation suggests the existence of an $I^\pi = 14^+$ $E6$ yrast trap, which is stable in its position for $t > 1$ (Fig. 6.5). Inspection of the wave functions reveal a leading configuration $\pi g_{9/2}^{-2} \nu g_{9/2}^{-1} g_{7/2}$ for this state in contrast to the $\pi g_{9/2}^{-2} \nu g_{9/2}^{-1} d_{5/2}$ configuration for the $I^\pi = 12^+$ state. This explains the deviating sequence in the ESM estimate, which excludes the $\nu g_{7/2}$ orbit. On the other hand the results for ^{101}Sn for all levels of truncation reproduce the extrapolated $\nu d_{5/2} - g_{7/2}$ splitting, which is inferred from the experimental ^{103}Sn single-particle states [Gros76, Clar00]. The existence of an $I^\pi = 14^+$ yrast trap cannot be excluded by the evidence from the present experiment. An $E6$ γ-ray branch would not compete with β-decay and, moreover, due to the long half-life ($0.1 - 1$ s) would exceed the maximum observational time range limit of 1.2 μs covered in the present experiment. A possible $12^+ \rightarrow 14^+$ branch would escape observation due to high internal conversion and the weak $E2$ transition strength (see Sect. 6.2.2).

6.2.2 Electromagnetic transitions

In Table 6.2 $E2$ and $E4$ transition strengths as calculated in the GDS approach at $t = 4$ are listed and compared to experiment. For the high-spin isomer besides the most likely 12^+ assignment and $E4$ isomerism the options of highly-converted $E2$ transitions $12^+ \rightarrow 10^+$ respective $14^+ \rightarrow 12^+$ are listed with lower limits based on the observational limit of $E_\gamma > 80$ keV. In spite of the large experimental uncertainties in the present work it seems that the GDS calculation with standard polarization charges 0.5 e overestimates the $8^+ \rightarrow 6^+$ $E2$ strength. This is even more apparent in

comparison to a previous measurement of much higher statistical precision [Grzy98], which in view of the present work may, however, be subject to systematic errors due to the unknown feeding by the core-excited isomer. Therefore, from the present work an upper limit $\delta e_\pi < 0.4\ e$ for the proton polarization charge is inferred. The $B(E2)$ value quoted in Ref. [Grzy98] would correspond to the more stringent limit of $\delta e_\pi < 0.2\ e$. The neutron contributions were corrected for by assuming the LSSM values with $e_\nu = 0.5\ e$. This has to be compared to the $I^\pi = 6^+$ isomer in the nucleus ^{102}Sn, with two neutrons outside the ^{100}Sn core. An $E2$ transition strength has been measured to be $B(E2; 6^+ \rightarrow 4^+) = 116^{+70}_{-30}$ e^{2}fm^4 [Lipo98], from which with the GDS value 85 e^{2}fm^4 at truncation level $t = 4$ a neutron polarization charge $\delta e_\nu = 0.6(1)\ e$ is deduced. This supersedes the value of Ref. [Graw02] (SDG) which was obtained at $t = 3$. These effective charges are in remarkable agreement with core polarization calculations, that predict a large isovector effect [Enge00, Corr00]. On the other hand the simple formula quoted in Ref. [Hama01] with reduced isovector strength, yielding $\delta e_\pi = 0.33\ e$ and $\delta e_\nu = 0.65\ e$, accounts for the experimental values. The $E2$ core polarization is made up from two contributions, a high-energy part due to $\Delta N = 2$ ph-excitations to the next harmonic oscillator (HO) shell with the same parity, i.e. the giant quadrupole resonance (GQR), and a soft part due to ph excitations within the valence HO shell, which can be calculated in the LSSM approach. Therefore, assuming convergence of the LSSM calculations, the extracted experimental limits and values reflect the GQR tail contribution to the effective charge and can be directly compared to the quoted theoretical predictions [Enge00, Corr00, Hama01].

Very often effective charges are routinely extracted by assuming minimum model space valence configurations. These normally much larger empirical polarization charges contain the soft ph excitations and are very much dependent on the purity of the assumed valence configuration. On the theory side these values should be compared to RPA results based on Skyrme Hartree-Fock calculations [Hama97]. The LSSM results on $E2$ strengths open an interesting insight into the microscopic nature of ph excitations and empirical effective charges. In a single-j shell ESM approach all $E2$ matrix elements are proportional to each other. For the $\pi g_{9/2}^{-2}$ configuration in ^{98}Cd this results e.g. in the relation $B(E2; 8 \rightarrow 6) : B(E2; 6 \rightarrow 4) : Q^2(8) = 1 : 2.50 : 38.3$, where Q is the spectroscopic quadrupole moment. The LSSM results preserve these ratios at all levels of truncation within $\sim$1 %. This supports the idea of valence nucleons "dressed" by ph excitations and the concept of an effective charge. Whether this holds for more than three valence particles/holes in the shell, when seniority mixing is possible, remains an open question.

Another interesting result can be inferred from the comparison of the $t = 0$ and $t = 4$ $B(E2; I_{max} \rightarrow I_{max} - 2)$ values for the proton and neutron valence nuclei ^{98}Cd ($I_{max} = 8$) and ^{102}Sn ($I_{max} = 6$), commonly believed to have rather pure configurations outside the ^{100}Sn closed shells [Górs97, Lipo98], which in the LSSM

calculations are well converged at $t = 4$. The apparent empirical polarization charges as extracted from the theoretical $B(E2)$ values are $\delta e_\pi = 0.86\ e$ and $\delta e_\nu = 1.70\ e$. The large isovector effect is due to the empirical fact that valence protons (neutrons) are mainly polarized by neutron (proton) core excitation as can be inferred from inspection of the corresponding wave functions. The experimental values for the empirical effective polarization charge as deduced from the present work and Ref. [Lipo98], assuming pure proton hole and neutron particle valence configurations, are $\delta e_\pi = 0.45(^{+20}_{-25})\ e$ and $\delta e_\nu = 2.0(^{+5}_{-3})\ e$, respectively.

Shell-model predictions of $E4$ transition rates are hampered by the fact that little is known about the effective operator, i.e. the polarization charges. The GDS calculation underestimates the enhanced experimental value at least by a factor 6, if $E2$ charges are used (Table 6.2). Though full convergence may not have been reached at $t = 4$ in this case (Fig. 6.5), one can hardly expect more than a factor of two increase. Increase of the polarization charges within reasonable limits may account for another factor of two, which is still a factor of $1.5 - 2.0$ smaller than the experimental value. The aforementioned analogous $E4$ strength in ^{54}Fe $B(E4; 10^+ \rightarrow 6^+) = 0.79(8)$ W.u. [ENDSF] is calculated to be 0.83 W.u. using the KB3 interaction [CaurPC] and 1.81 Wu with FPD6 [Richt91]. Both values are found to be converged at $t = 6$. It is well known though that in the (p, f) shell $E4$ strengths are strongly interaction dependent [Caur02], and thus provide a sensitive test ground.

The alternative $E2$ scenarios for the core-excited isomerism as discussed and discarded in Sect. 6.2.1 are clearly at variance with the shell model results as they underestimate the lower experimental limits by a great margin (Table 6.2) against the trend observed for the $8^+ \rightarrow 6^+$ transition.

6.3 Nuclear structure of ^{100}Sn: consequences for ^{132}Sn

This work also contributes to the understanding of nuclear matter synthesis in astrophysics network calculations. The abundance of stable elements is often shown on graphs together with the theoretical predictions of models including all kinds of astrophysical scenarios, like proton-, neutron-capture, rapid- or slow-capture process, α-, β-decay and fission. The simulated element abundances have so far failed to reproduce (explain) the abundance of elements in several mass regions. One of them is the region of $A < 130$. According to the theory, the *rapid neutron-capture process* or the so called r-process taking place on the neutron-rich side is responsible for producing these elements. Though it may seem that this work, dedicated to nuclear structure of the proton-rich side (^{100}Sn), has nothing to do with the neutron-rich side (^{132}Sn), this is not true. There are some very important consequences for the

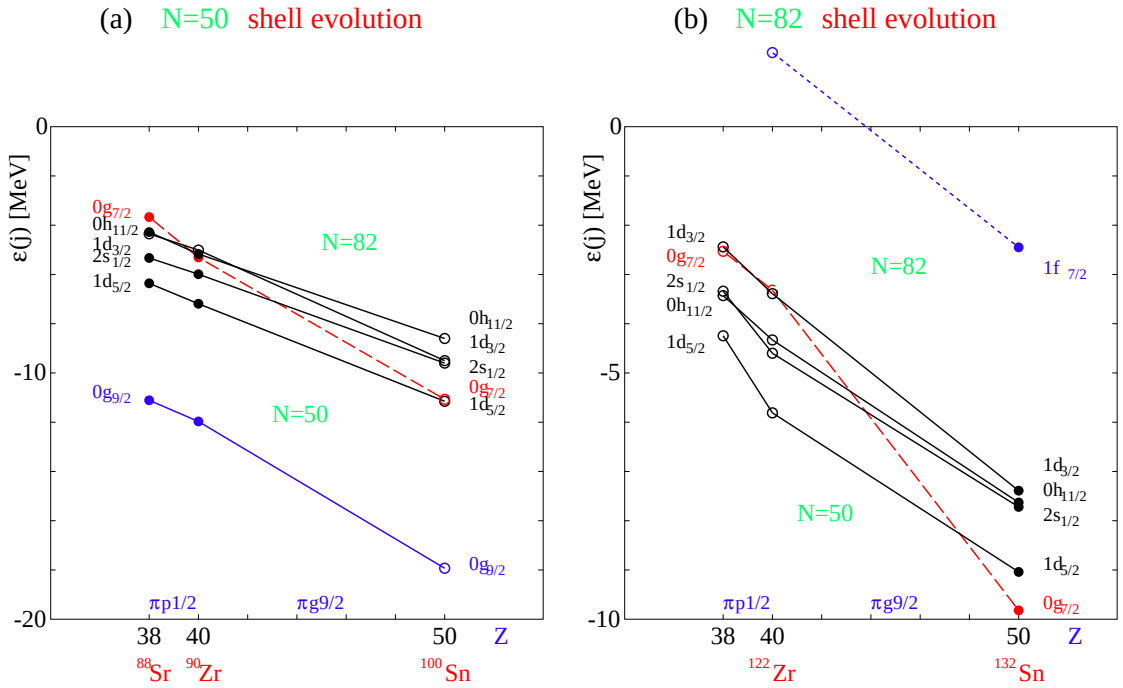

Figure 6.6: Evolution of single neutron particle at $N = 50$ (a) and hole at $N = 82$ (b) energies for $Z = 38, 40 \rightarrow 50$. Measured and extrapolated values are indicated by filled and open circles, correspondingly. (from [Graw04a])

structure of neutron-rich nuclei which can be concluded from the present work.

The most important consequence for the region of ^{132}Sn is drawn from the strong monopole shift of some pairs of j orbitals (see Sect. 5.1.2 and Refs. [deSh63, Caur94, Graw04]). Grawe showed in [Graw04, Graw04a] that SPE at a closed shell (CS) and the next lower closed shell (CS') are related by

$$\epsilon_j^{CS} = \epsilon_j^{CS'} + \sum_{j'} (2j' + 1 - \delta_{jj'}) V_{jj'}^m \tag{6.1}$$

where j, j' specify in short notation radial, orbital angular momentum, spin and isospin quantum numbers of the nucleons and the sum runs over all orbitals in the major shell. The term $V_{jj'}^m$ is the monopole part of the residual interaction for the specific multiplet, and the Kronecker symbol takes care of the Pauli principle for identical nucleons.

Using the monopole shift observed on the proton rich-side as shown on Fig. 6.6 (a) Grawe has extrapolated the monopole effect for specific multiplets on the neutron-rich side (Fig. 6.6 (b)) [Graw04a]. As shown on Fig. 5.1 and repeated in Fig. 6.6 (a) the evolution of neutron orbitals and especially of $\nu g_{7/2}$ is determined by the filling of $\pi g_{9/2}$. Figure 6.6 (b) shows the evolution of the neutron single hole energies at

the $N = 82$ shell gap around ^{132}Sn. Starting with experimental points at ^{132}Sn, an extrapolation towards ^{122}Zr is made [Graw04a]. The slopes generated by the SPE driving interactions $\pi g_{9/2}\nu j$ on plot (b) are the same as for plot (a) [HJenPC], except for an $A^{-1/3}$ scaling. The application of this symmetry gives further nuclear structure characteristics of the exotic neutron rich region. As seen on Fig. 6.6 (b) the shell gap at $N = 82$ remains at ^{122}Zr.

Figure 6.6 (b) has an interesting consequence for the r-process. From the astrophysical point of view the GT transition $\nu g_{7/2} \rightarrow \pi g_{9/2}$ is very important. When we add neutrons during the r-process and approach the region of ^{122}Zr, the GT decay is delayed until $\nu g_{7/2}$ starts to be filled with neutrons about $10 - 12$ neutrons below $N = 82$ [Graw04a]. The delayed decay means that the β-decay half-lives are increased in the region of $N < 82$ ($Z \sim 40$), which helps for catching another neutron before β decaying and getting closer to $N = 82$. On the other hand, the filled $\nu g_{7/2}$ around $N \sim 82$ at the Fermi surface and the empty $\pi g_{9/2}$ ($Z \sim 40$) resulting also in the large effective decay energy, accelerate the GT decay, which decreases the β-decay half-lives and nuclei decay before catching another neutron. It should be noted that the half-life scales with the decay energy as E_{β}^{-5}. In this way the abundance of elements with $A \sim 120$ is increased. Then the r-process "climbs up" the table of isotopes to nuclei with higher Z approaching $Z = 50$, i.e. ^{132}Sn. This means that the $\pi g_{9/2}$ orbital is being filled, which again slows down the GT decay. On the other hand at ^{132}Sn ($N = 82$), the neutron capture is hindered by the neutron shell gap, thus overcompensating the slow GT decay and again producing an increase in the element abundance intensity, this time due to another effect.

These qualitative considerations do not include the full set of the r-process parameters, but compared to the standard r-process simulation with the order of j orbitals fixed, they represent an important step. Thus, the standard theoretical approach enriched by the monopole shift of the $\nu g_{7/2}$ is able to give an explanation to the abundance intensities in $A < 130$ masses [Graw04a].

In Fig. 6.7 the ph transformation is shown for the $\pi g_{9/2}\nu d_{5/2}$ pp multiplet in ^{92}Nb towards the ph nucleus ^{96}Nb . The excellent agreement with the experimental ^{96}Nb levels proves the doubly-magic features of both ^{90,96}Zr at $Z = 40$, $N = 50$ and $N = 56$, respectively. Actually this is the method for the extraction of TBME for the "upgraded" ESM of the ^{98}Cd discussed in Sect. 5.1.1. Note that in this configuration the levels in ^{100}In (ph) and ^{104}In (hh) should be identical to ^{96}Nb (ph) and ^{92}Nb ($pp \equiv hh$), respectively. This is not observed in experiment as the neutron $d_{5/2}$ orbit, energetically isolated at $Z = 40$, is highly distorted by the almost degenerate $g_{7/2}$ at $Z = 50$ (see Figs. 1.4, 5.1 and 6.6 (a)).

In the region of ^{132}Sn, $N = 82$ and the neutron orbitals $1d_{5/2}$, $0g_{7/2}$, $2s_{1/2}$, $1d_{3/2}$ and $0h_{11/2}$, which are empty at ^{100}Sn, are now fully occupied. By analogy with the example from Fig. 6.7 one can understand that the one-neutron hole spectrum of $N = 81$ isotones, should exhibit strong correlation with the one-neutron particle

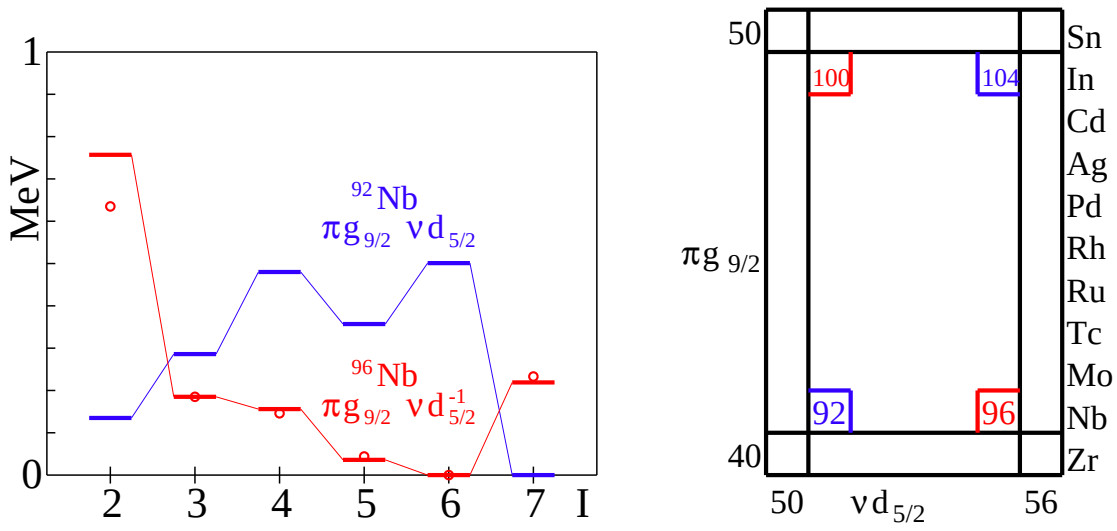

Figure 6.7: Particle-hole conjugated spectra for ^{92,96}Nb $\pi g_{9/2}\nu d_{5/2}$. (from [Graw04])

spectrum of $N = 51$ isotones. Thus, transforming the one-neutron particle spectra ($N = 51$) of nuclei in direction $Z = 40 \rightarrow 50$ (i.e. ^{91}Zr $\rightarrow$ ^{101}Sn), one can obtain the one-neutron hole spectra ($N = 81$) in the reverse direction of $Z = 50 \rightarrow 40$ (i.e. ^{131}Sn $\rightarrow$ ^{121}Zr) which are really very exotic nuclei and are up to now experimentally unreachable. One should only take care, of course, to know which are the relevant multiplets together with their residual interaction, which can be inferred either from studies close to stability or the proton-rich side. To have an insight on the valence orbitals in the region below ^{132}Sn one can, again, use Fig. 6.6 (b).

Chapter 7

Summary

The main scientific contributions of this thesis work are the following:

1. Shell-model calculation of the ^{100}In $\rightarrow$ ^{100}Cd GT β-decay, using ^{88}Sr as a core and empirically tuned realistic effective interaction, yields good agreement with the experimental energies. The LSSM calculation for ^{100}In is used for comparison of the B(GT) strength distribution and for a conclusion about the GT-strength hindrance factor. On the basis of the calculated distribution, the assignment $I^{\pi} = (6^{+})$ of the ground state of the parent nucleus ^{100}In is favoured.

2. In the experimental study of delayed γ rays of ^{98}Cd, a core-excited spin-gap isomer is identified and tentatively assigned as an $I^{\pi} = (12^{+})$ state. Utilizing three different methods, half-lives are determined for the levels: $I^{\pi} = (12^{+})$ $T_{1/2} = 230(^{+40}_{-30})$ ns, $I^{\pi} = (8^{+})$ $T_{1/2} = 170(^{+60}_{-40})$ ns and $I^{\pi} = (6^{+})$ $T_{1/2} < 20$ ns.

3. The estimated half-lives of levels in ^{98}Cd are discussed within the framework of empirical and large-scale shell-model calculations. The LSSM calculation for ^{98}Cd of the Strasbourg group including up to $4p4h$ excitations of the ^{100}Sn core is found to excellently account for the experimental observations. The comparison of the experimental and theoretical $B(E2, 8^{+} \rightarrow 6^{+})$ yields conclusion for the proton polarization charge $\delta e_{\pi} < 0.4e$ in the region of ^{100}Sn.

4. The ^{100}Sn shell gap is inferred from a comparison of the experimental and shell-model excitation energy of the $I^{\pi} = (12^{+})$ isomer. The estimate of the ^{100}Sn shell gap gives a value of 6.46(15) MeV.

5. These results gave the possibility to test and adjust the realistic interaction for the *gds* model space. And as a consequence of this, the optimized calculations yield predictions for a 14^{+} isomer in ^{98}Cd and a 6^{+} isomer in ^{100}Sn.

Chapter 8

Outlook: Future experiments and technical development

As direct consequences of this work, there are several ideas and challenges for future experiments.

First, and probably the easiest to measure with the existing facilities and detector arrays, is to verify the predicted $I^\pi = 14^+$ $E6$ isomer in ^{98}Cd. The $E6$ γ transition, should have much longer partial half-life than the more probable β-, βp, or even p-decay. One should anticipate the population of high-spin states in the daughter nuclei. These states are most often known already from in-beam measurements and thus the presence of their γ cascades would be easy to check. For example, the GT-decay of the $I^\pi = 14^+$ in ^{98}Cd should populate states of minimum spin $I^\pi = 13^+$ in ^{98}Ag, which are well known [Cede98]. One has to provide the high-spin populated ^{98}Cd species under low-contamination background, and have an efficient β-$\gamma\gamma$ measurement. This is actually what is already done in many β-decay experiments with fusion-evaporation production and ISOL separation of the residues. However, it is not excluded that the high-spin state could be populated in a fragmentation of a more distant primary or secondary nucleus and then in-flight tracked, separated, implanted and measured precisely.

Second, and probably most interesting, is to discover the possible $I^\pi = 6^+$ $E2$ isomer in ^{100}Sn. Certainly, this is a task for an in-beam delayed γ-spectroscopy experiment. Since the stable target/beam fusion-evaporation reactions in combination with contemporary detector arrays are unable to address this issue, some development is required. From the reaction point of view, most promising for the nearest future are the fragmentation reaction facilities like GSI-FRS, GANIL-LISE3 and the corresponding implantation detection set-ups, which are also under development. The culmination of the fragmentation research is planned for international facilities like the future GSI Super-FRS, combined with many-orders improved beam intensity of the future SIS100/300 within the FAIR project. According to the de-

sign report and the letters of intent, this would extent the experimentally accessible nuclei in both directions from the β-stability line. Thus, not only the study of currently exotic cases would be possible, but an access to the entire *rp*-process path, as well as most of the *r*-process synthesis path nuclei would be available. Here, one can see the connection with the ^{100}In GT-decay studies, which are part of the systematic study of the GT-decay in the whole chart of nuclides, with an ultimate goal of precisely modelling the capture/decay rates during synthesis processes and understanding the current abundances of the elements.

Besides the accelerator and fragment separator developments, one should mention the current projects about the future of the ISOL technique. Here projects like EURISOL and RIA have great plans for high-intense radioactive secondary beams, which could give the practical application of unstable beam fusion-evaporation reaction techniques. So far, facilities like CERN-ISOLDE with the post-accelerator REX, in Switzerland, and the TRIUMF-ISAAC facility in Canada, continue their developments for experiments using radioactive beams and post-accelerating them to energies above the Coulomb barrier.

There are even ideas to merge the alternative techniques of stopping and extraction in ISOL and the in-flight fragment separation. The nuclei, produced and separated in-flight in a magnetic spectrometer are easily trackable, but have high momentum-spread and lower intensities than in the case of ISOL techniques. The proposed stopping of the fragmentation residues in a gas-cell and the additional extraction and post-acceleration of the species could thus have the advantages of both major techniques. The properties and operation of the gas-cells are subject to extended studies and developments, since many future facilities include the gas-cell option in their design.

Finally, the experiment is dependent not only on the possibility and the production intensity of the studied nuclei, but to an equal degree to the detectors measuring the experimental observables. It is worth mentioning that the γ-spectroscopy communities, on both sides of the Atlantic, are planning and starting the next generation multi-detector γ-ray arrays. The respective projects in Europe and the US are named AGATA and GRETA. The major step is that the Compton escape-suppressed spectrometers are substituted by highly-segmented position-sensitive detectors building a nearly complete 4π shell around the target. The main idea is to measure all the γ-rays and their scattering sub-events and applying a complete *γ-ray tracking* to restore the energy and interaction point of the original γ rays. These arrays would be extremely versatile allowing to work in the regimes of high count rate, high multiplicity and high γ-efficiency. The γ-ray tracking method is the result of a consequent advancement of the present-day add-back method which was used in the analysis of this thesis work.

These future accelerator facilities and detector arrays, their performance and possibilities to study the nuclear structure, are really spectacular. The whole nuclear

physics is facing exciting times, when both the experience of the years and the enthusiasm of the youth, as well as theory and experiment, should work closely together for the benefit of all.

Appendices

Appendix A

Fold analysis of evaporated particles for exit channel identification

Fusion-evaporation reactions provide a possibility to study the nuclear structure at high-spin and high-excitation energy. In the case of the proton rich nuclei the emission of charged particles is not negligible and it is highly desirable to measure the multiplicity of the emitted particles to identify unknown exit channels. Particle detection probability distributions and exact detector efficiencies are needed for designing ancillary detectors and for prediction of experimental results for different multiplicity exit channels. Both types of problems could be addressed by following fold analysis of evaporated particles.

There is a general article on the formalism of multiplicity measurements in Ref. [Werf78], but the current fold analysis is based on the modified multiplicity distribution formula of Ref. [Albe88]:

$$P_{N_p}(M) = \binom{N}{p} \sum_{n=1}^{p} (-)^{n+p} \binom{p}{n} [1 - (N-n)\Omega\varepsilon]^M \times [1 - f(N-n)(\Omega\varepsilon)^*]^M \quad \text{(A.1)}$$

It gives the probability for an array of N identical detectors to register p (fold) of M (particle multiplicity) emitted particles of one kind. Each of the detectors has efficiency $\Omega\varepsilon$ primary radiation. There is also a scattered radiation efficiency $(\Omega\varepsilon)^*$, which is used only for neutrons. For charged particles it is equal to zero, as charged particles fully stop in the volume of the detector they hit. Ω denotes the fraction of 4π taken by a single detector, ε is intrinsic efficiency and f is the average scattering factor weighted with the secondary efficiency $(\Omega\varepsilon)^*$, which according to

equation(A.1) is the relevant number to judge the scattering probability of an array. Required conditions for the application of the method are as follows:

- Independence of the efficiency on the reaction exit channel. That is, the efficiencies should be independent from the excitation energy of the compound nucleus and the number and kind of evaporated particles.

- Independent particle detection. That is, particles of all kinds, should be detected independently, which is not true for protons and α-particles. Nevertheless, the above theoretical approach, when applied to experimental data, is accurate enough for definite determination of the reaction exit channel.

- All detectors of the array should have identical efficiency and see the same portion of evaporated particles. This is generally not true, as due to the center of mass motion the particles have pronounced forward peaked angular distribution in the lab system. To overcome this, one can use parameters like $N_{effective}$ and $(\Omega\varepsilon)_{effective}$, and fit them to satisfy the experimental data.

For low multiplicity events, N does not affect the multiplicity resolution considerably if N is larger than M [Mura85]. That is, the probability P_{N_p} has very small dependence on N (for M-small and $N > M$). For example, the number of the evaporated neutrons in reactions near the proton drip line, as in the ^{100}Sn region, is small and the above is satisfied.

Of course, there are different efficiencies for protons, α and neutrons, e.g. $(\Omega\varepsilon)_\alpha$, $(\Omega\varepsilon)_p$, $(\Omega\varepsilon)_n$. The different efficiencies are then determined from the intensity ratios of the γ transitions in known reaction exit channels. Therefore ratios are taken for intensities with different gate condition. For example: I(1n1p$\gamma\gamma$)/I(0n1p$\gamma\gamma$) for neutrons, and I(1n2p$\gamma\gamma$)/I(1n1p$\gamma\gamma$) or I(1α3p$\gamma\gamma$)/I(0α3p$\gamma\gamma$) for protons and α particles respectively.
One can easily see from the equation(A.1) that ratios of the kind I(p$\gamma\gamma$)/I($\gamma\gamma$) in the case of M_p=1 are equal to $(N\Omega\varepsilon)_p$, which is actually the total efficiency of the proton detectors. The same is true for α particles and neutrons.

Detectors are never 100% effective. That is why, in each spectrum gated with x detected neutrons, all nuclei produced in exit channels with at least x evaporated neutrons will be present. Similarly for charged particle gated spectra, with a required fold of a given particle, there are always present nuclei produced in exit channels where more particles were evaporated, but some were not detected. There are two possible approaches to determine multiplicity. One way is to take ratios for gamma spectra gated with x+ (x and more) particles. The other approach is to take ratios for γ-rays detected in coincidence with exactly x particles. Thus, I(1nγ)/I(0nγ) could mean that both intensities are for (x and more) neutrons, or exactly x neutrons. It is only a matter of choice, which one is used, because they

both give the multiplicity information, but one should be careful to be consistent in the theoretical and experimental ratios, that are compared.

A first application is to calculate the multiplicity distribution, when M, N, $(\Omega\varepsilon)$ and $(\Omega\varepsilon)^*$ are known. Then theoretical values for the ratios, compared to the experimental ratios, are used for exit channel identification. One calculates the ratio of the intensities that correspond to a given gamma line in coincidence with different number and kind of particles. Then one compares it to the theoretical ratio and identifies the particle multiplicity. When it is done for all kinds of evaporated particles, one identifies n, p and α multiplicities and thus selects to which nucleus (exit channel) belongs the γ-peak.

The second application is to deduce the real or effective $(N\Omega\varepsilon)_{n,p,\alpha}$ from experimental ratios which belong to well known exit channels. This can be done by applying numerical methods for calculation of the equation (A.1) and fitting procedures for the $(N\Omega\varepsilon)$ and $(N\Omega\varepsilon)^*$ parameters. In fact, this is often the way of determining the efficiencies of the ancillary detector arrays, which are used then to calculate the theoretical values and identify the exit channels of unknown γ-ray lines.

Appendix B

Single particle energies and two-body matrix elements (TBME) used in the LSSM calculations of ^{100}In GT decay

SPE and TBME file SR88MHJ.INT

This is the file SR88MHJ.INT used in the OXBASH calculations, which sets the SPE and the TBME in this model space in proton-neutron formalism. The first line and any subsequent line starting with "!" are not read by the program, and used for comments. There is a list of the orbitals included in the model space. Each orbital is given an index number. The second line starts with a dummy number, which could be e.g. the total number of TBME, followed by the SPE relative to the ^{88}Sr core for all the orbitals included in the model space. Then comes a list of the matrix elements in the form K1, K2, K3, K4, J, T, V where Ki is the orbital index number. The TBME [HJenPC] at the end of each line are given in MeV. The input is always read in "free" format.

```
!  1)P1g9/2 2)P2p1/2 3)N1g7/2 4)N2d5/2 5)N2d3/2 6)N3s1/2 7)N1h11/2
0  -1.934, -2.684, -2.802, -5.820, -3.935, -4.717, -3.884
 1  1  1  1   0  1   -1.79370
 1  1  1  1   2  1   -0.76120
 1  1  1  1   4  1   -0.23920
 1  1  1  1   6  1   -0.00810
 1  1  1  1   8  1    0.20190
 1  1  2  2   0  1    0.90990
 1  1  2  2   0  0    0.90990
 1  2  1  2   4  1    0.20430
```

```
1  2  1  2   5  1   -0.25850
1  3  1  3   1  1   -2.46060
1  3  1  3   1  0   -2.46060
1  3  1  3   2  1   -1.65150
1  3  1  3   2  0   -1.65150
1  3  1  3   3  1   -0.66140
1  3  1  3   3  0   -0.66140
1  3  1  3   4  1   -0.81080
1  3  1  3   4  0   -0.81080
1  3  1  3   5  1   -0.24680
1  3  1  3   5  0   -0.24680
1  3  1  3   6  1   -0.66080
1  3  1  3   6  0   -0.66080
1  3  1  3   7  1   -0.01390
1  3  1  3   7  0   -0.01390
1  3  1  3   8  1   -1.20370
1  3  1  3   8  0   -1.20370
1  3  1  4   2  1   -0.53030
1  3  1  4   2  0   -0.53030
1  3  1  4   3  1    0.08620
1  3  1  4   3  0    0.08620
1  3  1  4   4  1   -0.12760
1  3  1  4   4  0   -0.12760
1  3  1  4   5  1    0.11900
1  3  1  4   5  0    0.11900
1  3  1  4   6  1   -0.06200
1  3  1  4   6  0   -0.06200
1  3  1  4   7  1    0.18580
1  3  1  4   7  0    0.18580
1  3  1  5   3  1   -0.34980
1  3  1  5   3  0   -0.34980
1  3  1  5   4  1   -0.41660
1  3  1  5   4  0   -0.41660
1  3  1  5   5  1   -0.15310
1  3  1  5   5  0   -0.15310
1  3  1  5   6  1   -0.43290
1  3  1  5   6  0   -0.43290
1  3  1  6   4  1   -0.20950
1  3  1  6   4  0   -0.20950
1  3  1  6   5  1    0.08840
1  3  1  6   5  0    0.08840
```

```
1  3  2  7   5  1    0.28430
1  3  2  7   5  0    0.28430
1  3  2  7   6  1   -0.24390
1  3  2  7   6  0   -0.24390
1  4  1  4   2  1   -0.81840
1  4  1  4   2  0   -0.81840
1  4  1  4   3  1   -0.28270
1  4  1  4   3  0   -0.28270
1  4  1  4   4  1   -0.11560
1  4  1  4   4  0   -0.11560
1  4  1  4   5  1   -0.25960
1  4  1  4   5  0   -0.25960
1  4  1  4   6  1   -0.02830
1  4  1  4   6  0   -0.02830
1  4  1  4   7  1   -0.79090
1  4  1  4   7  0   -0.79090
1  4  1  5   3  1    0.56700
1  4  1  5   3  0    0.56700
1  4  1  5   4  1   -0.16020
1  4  1  5   4  0   -0.16020
1  4  1  5   5  1    0.28840
1  4  1  5   5  0    0.28840
1  4  1  5   6  1   -0.19480
1  4  1  5   6  0   -0.19480
1  4  1  6   4  1   -0.29020
1  4  1  6   4  0   -0.29020
1  4  1  6   5  1   -0.44410
1  4  1  6   5  0   -0.44410
1  4  2  7   5  1   -0.41920
1  4  2  7   5  0   -0.41920
1  4  2  7   6  1    0.08190
1  4  2  7   6  0    0.08190
1  5  1  5   3  1   -0.94290
1  5  1  5   3  0   -0.94290
1  5  1  5   4  1   -0.36670
1  5  1  5   4  0   -0.36670
1  5  1  5   5  1   -0.10730
1  5  1  5   5  0   -0.10730
1  5  1  5   6  1   -0.55490
1  5  1  5   6  0   -0.55490
1  5  1  6   4  1   -0.35220
```

```
1  5  1  6   4  0   -0.35220
1  5  1  6   5  1    0.33690
1  5  1  6   5  0    0.33690
1  5  2  7   5  1    0.32470
1  5  2  7   5  0    0.32470
1  5  2  7   6  1   -0.14170
1  5  2  7   6  0   -0.14170
1  6  1  6   4  1   -0.25000
1  6  1  6   4  0   -0.25000
1  6  1  6   5  1   -0.44490
1  6  1  6   5  0   -0.44490
1  6  2  7   5  1   -0.45570
1  6  2  7   5  0   -0.45570
1  7  1  7   1  1   -1.01310
1  7  1  7   1  0   -1.01310
1  7  1  7   2  1   -0.69820
1  7  1  7   2  0   -0.69820
1  7  1  7   3  1   -0.26240
1  7  1  7   3  0   -0.26240
1  7  1  7   4  1   -0.23240
1  7  1  7   4  0   -0.23240
1  7  1  7   5  1   -0.08700
1  7  1  7   5  0   -0.08700
1  7  1  7   6  1   -0.22440
1  7  1  7   6  0   -0.22440
1  7  1  7   7  1   -0.04740
1  7  1  7   7  0   -0.04740
1  7  1  7   8  1   -0.66200
1  7  1  7   8  0   -0.66200
1  7  1  7   9  1    0.04700
1  7  1  7   9  0    0.04700
1  7  1  7  10  1   -0.95000
1  7  1  7  10  0   -0.95000
1  7  2  3   3  1    0.28080
1  7  2  3   3  0    0.28080
1  7  2  3   4  1   -0.13350
1  7  2  3   4  0   -0.13350
1  7  2  4   2  1    0.33220
1  7  2  4   2  0    0.33220
1  7  2  4   3  1   -0.21920
1  7  2  4   3  0   -0.21920
```

```
1  7  2  5   1  1    0.25320
1  7  2  5   1  0    0.25320
1  7  2  5   2  1   -0.20390
1  7  2  5   2  0   -0.20390
1  7  2  6   1  1   -0.39930
1  7  2  6   1  0   -0.39930
2  2  2  2   0  1   -0.34340
2  3  2  3   3  1   -0.28120
2  3  2  3   3  0   -0.28120
2  3  2  3   4  1   -0.51490
2  3  2  3   4  0   -0.51490
2  3  2  4   3  1   -0.05020
2  3  2  4   3  0   -0.05020
2  4  2  4   2  1   -0.94130
2  4  2  4   2  0   -0.94130
2  4  2  4   3  1   -0.72540
2  4  2  4   3  0   -0.72540
2  4  2  5   2  1   -0.16700
2  4  2  5   2  0   -0.16700
2  6  2  6   0  1   -0.70210
2  6  2  6   0  0   -0.70210
2  6  2  6   1  1   -0.64060
2  6  2  6   1  0   -0.64060
2  5  2  6   1  0   -0.10660
2  5  2  6   1  1   -0.10660
2  5  2  5   1  1   -0.18760
2  5  2  5   1  0   -0.18760
2  5  2  5   2  1   -0.68050
2  5  2  5   2  0   -0.68050
2  7  1  3   5  1    0.28430
2  7  1  3   5  0    0.28430
2  7  1  3   6  1   -0.24390
2  7  1  3   6  0   -0.24390
2  7  1  4   5  1   -0.41920
2  7  1  4   5  0   -0.41920
2  7  1  4   6  1    0.08190
2  7  1  4   6  0    0.08190
2  7  1  5   5  1    0.32470
2  7  1  5   5  0    0.32470
2  7  1  5   6  1   -0.14170
2  7  1  5   6  0   -0.14170
```

```
2  7  1  6   5  1   -0.45570
2  7  1  6   5  0   -0.45570
2  7  2  7   5  1   -0.59220
2  7  2  7   5  0   -0.59220
2  7  2  7   6  1   -0.36350
2  7  2  7   6  0   -0.36350
3  3  3  3   0  1   -1.51650
3  3  3  3   2  1   -0.36250
3  3  3  3   4  1    0.00370
3  3  3  3   6  1    0.26250
3  3  3  4   2  1   -0.02710
3  3  3  4   4  1    0.13090
3  3  3  4   6  1    0.14760
3  3  3  5   2  1   -0.34670
3  3  3  5   4  1   -0.10610
3  3  3  6   4  1    0.10490
3  3  4  4   0  1   -0.64730
3  3  4  4   2  1   -0.09480
3  3  4  4   4  1   -0.09110
3  3  4  5   2  1   -0.13700
3  3  4  5   4  1   -0.16570
3  3  4  6   2  1   -0.21150
3  3  5  5   0  1   -0.50900
3  3  5  5   2  1   -0.09550
3  3  5  6   2  1    0.12320
3  3  6  6   0  1   -0.30670
3  3  7  7   0  1    1.50470
3  3  7  7   2  1    0.19340
3  3  7  7   4  1    0.13900
3  3  7  7   6  1    0.12280
3  4  3  3   2  1   -0.02710
3  4  3  3   4  1    0.13090
3  4  3  3   6  1    0.14760
3  4  3  4   1  1   -0.31430
3  4  3  4   2  1   -0.03930
3  4  3  4   3  1    0.03580
3  4  3  4   4  1    0.01030
3  4  3  4   5  1    0.10420
3  4  3  4   6  1   -0.40230
3  4  3  5   2  1    0.27280
3  4  3  5   3  1    0.00040
```

```
3  4  3  5   4  1    0.21270
3  4  3  5   5  1   -0.08700
3  4  3  6   3  1   -0.12530
3  4  3  6   4  1   -0.26550
3  4  4  4   2  1    0.07220
3  4  4  4   4  1    0.07360
3  4  4  5   1  1   -0.02400
3  4  4  5   2  1    0.06410
3  4  4  5   3  1    0.00390
3  4  4  5   4  1    0.12380
3  4  4  6   2  1    0.09260
3  4  4  6   3  1   -0.02710
3  4  5  5   2  1    0.04470
3  4  5  6   1  1   -0.04710
3  4  5  6   2  1   -0.04390
3  4  7  7   2  1   -0.28720
3  4  7  7   4  1   -0.15380
3  4  7  7   6  1   -0.26490
3  5  3  3   2  1   -0.34670
3  5  3  3   4  1   -0.10610
3  5  3  4   2  1    0.27280
3  5  3  4   3  1    0.00040
3  5  3  4   4  1    0.21270
3  5  3  4   5  1   -0.08700
3  5  3  5   2  1   -0.52450
3  5  3  5   3  1    0.04180
3  5  3  5   4  1    0.04170
3  5  3  5   5  1   -0.01090
3  5  3  6   3  1   -0.10220
3  5  3  6   4  1    0.24480
3  5  4  4   2  1   -0.17230
3  5  4  4   4  1   -0.05020
3  5  4  5   2  1   -0.21770
3  5  4  5   3  1   -0.04760
3  5  4  5   4  1   -0.15940
3  5  4  6   2  1   -0.22940
3  5  4  6   3  1   -0.04380
3  5  5  5   2  1   -0.20970
3  5  5  6   2  1    0.22960
3  5  7  7   2  1    0.45670
3  5  7  7   4  1    0.14470
```

```
3  6  3  3   4  1    0.10490
3  6  3  4   3  1   -0.12530
3  6  3  4   4  1   -0.26550
3  6  3  5   3  1   -0.10220
3  6  3  5   4  1    0.24480
3  6  3  6   3  1    0.00370
3  6  3  6   4  1   -0.14980
3  6  4  4   4  1    0.07630
3  6  4  5   3  1    0.01700
3  6  4  5   4  1    0.19330
3  6  4  6   3  1    0.04060
3  6  7  7   4  1   -0.22310
3  7  3  7   2  1   -0.62420
3  7  3  7   3  1   -0.29270
3  7  3  7   4  1    0.03280
3  7  3  7   5  1   -0.08320
3  7  3  7   6  1    0.02150
3  7  3  7   7  1   -0.17010
3  7  3  7   8  1    0.10140
3  7  3  7   9  1    0.05820
3  7  4  7   3  1    0.18180
3  7  4  7   4  1    0.10120
3  7  4  7   5  1    0.04030
3  7  4  7   6  1    0.07950
3  7  4  7   7  1    0.14370
3  7  4  7   8  1    0.07790
3  7  5  7   4  1   -0.07590
3  7  5  7   5  1   -0.15710
3  7  5  7   6  1   -0.00540
3  7  5  7   7  1   -0.23510
3  7  6  7   5  1    0.08730
3  7  6  7   6  1    0.04790
4  4  3  4   2  1    0.07220
4  4  3  4   4  1    0.07360
4  4  3  5   2  1   -0.17230
4  4  3  5   4  1   -0.05020
4  4  3  6   4  1    0.07630
4  4  4  4   0  1   -0.81330
4  4  4  4   2  1   -0.26840
4  4  4  4   4  1   -0.03450
4  4  4  5   2  1   -0.12510
```

```
4  4  4  5   4  1   -0.32820
4  4  4  6   2  1   -0.27760
4  4  5  5   0  1   -1.12280
4  4  5  5   2  1   -0.22460
4  4  5  6   2  1    0.23820
4  4  6  6   0  1   -0.40370
4  4  7  7   0  1    0.98760
4  4  7  7   2  1    0.37940
4  4  7  7   4  1    0.19170
4  5  3  3   2  1   -0.13700
4  5  3  3   4  1   -0.16570
4  5  3  4   1  1   -0.02400
4  5  3  4   2  1    0.06410
4  5  3  4   3  1    0.00390
4  5  3  4   4  1    0.12380
4  5  3  5   2  1   -0.21770
4  5  3  5   3  1   -0.04760
4  5  3  5   4  1   -0.15940
4  5  3  6   3  1    0.01700
4  5  3  6   4  1    0.19330
4  5  4  4   2  1   -0.12510
4  5  4  4   4  1   -0.32820
4  5  4  5   1  1    0.00680
4  5  4  5   2  1   -0.05260
4  5  4  5   3  1    0.06000
4  5  4  5   4  1   -0.51170
4  5  4  6   2  1   -0.13720
4  5  4  6   3  1   -0.05570
4  5  5  5   2  1   -0.26150
4  5  5  6   1  1   -0.03140
4  5  5  6   2  1    0.25260
4  5  7  7   2  1    0.00980
4  5  7  7   4  1    0.22000
4  6  3  3   2  1   -0.21150
4  6  3  4   2  1    0.09260
4  6  3  4   3  1   -0.02710
4  6  3  5   2  1   -0.22940
4  6  3  5   3  1   -0.04380
4  6  3  6   3  1    0.04060
4  6  4  4   2  1   -0.27760
4  6  4  5   2  1   -0.13720
```

```
4  6  4  5   3  1   -0.05570
4  6  4  6   2  1   -0.38770
4  6  4  6   3  1   -0.01400
4  6  5  5   2  1   -0.25960
4  6  5  6   2  1    0.47590
4  6  7  7   2  1    0.26610
4  7  3  7   3  1    0.18180
4  7  3  7   4  1    0.10120
4  7  3  7   5  1    0.04030
4  7  3  7   6  1    0.07950
4  7  3  7   7  1    0.14370
4  7  4  7   3  1   -0.71260
4  7  4  7   4  1   -0.06770
4  7  4  7   5  1   -0.21850
4  7  4  7   6  1    0.08990
4  7  4  7   7  1   -0.04110
4  7  4  7   8  1    0.15690
4  7  5  7   4  1   -0.15140
4  7  5  7   5  1    0.15890
4  7  5  7   6  1    0.01600
4  7  5  7   7  1    0.30430
4  7  6  7   5  1   -0.30980
4  7  6  7   6  1   -0.08580
5  5  3  3   0  1   -0.50900
5  5  3  3   2  1   -0.09550
5  5  3  4   2  1    0.04470
5  5  3  5   2  1   -0.20970
5  5  4  5   2  1   -0.26150
5  5  4  6   2  1   -0.25960
5  5  5  5   0  1   -0.46620
5  5  5  5   2  1    0.00830
5  5  5  6   2  1    0.16410
5  5  6  6   0  1   -0.38920
5  5  7  7   0  1    0.68790
5  5  7  7   2  1    0.09360
5  6  3  3   2  1    0.12320
5  6  3  4   1  1   -0.04710
5  6  3  4   2  1   -0.04390
5  6  3  5   2  1    0.22960
5  6  4  4   2  1    0.23820
5  6  4  5   1  1   -0.03140
```

```
5  6  4  5   2  1    0.25260
5  6  4  6   2  1    0.47590
5  6  5  5   2  1    0.16410
5  6  5  6   1  1    0.04630
5  6  5  6   2  1   -0.19910
5  6  7  7   2  1   -0.26860
5  7  3  7   4  1   -0.07590
5  7  3  7   5  1   -0.15710
5  7  3  7   6  1   -0.00540
5  7  3  7   7  1   -0.23510
5  7  4  7   4  1   -0.15140
5  7  4  7   5  1    0.15890
5  7  4  7   6  1    0.01600
5  7  4  7   7  1    0.30430
5  7  5  7   4  1   -0.14880
5  7  5  7   5  1   -0.04850
5  7  5  7   6  1    0.10040
5  7  5  7   7  1   -0.39820
5  7  6  7   5  1    0.25090
5  7  6  7   6  1   -0.02660
6  6  6  6   0  1   -0.70300
6  6  7  7   0  1    0.47610
6  7  3  7   5  1    0.08730
6  7  3  7   6  1    0.04790
6  7  4  7   5  1   -0.30980
6  7  4  7   6  1   -0.08580
6  7  5  7   5  1    0.25090
6  7  5  7   6  1   -0.02660
6  7  6  7   5  1   -0.25520
6  7  6  7   6  1    0.06660
7  7  3  4   2  1   -0.28720
7  7  3  4   4  1   -0.15380
7  7  3  4   6  1   -0.26490
7  7  3  5   2  1    0.45670
7  7  3  5   4  1    0.14470
7  7  3  6   4  1   -0.22310
7  7  4  5   2  1    0.00980
7  7  4  5   4  1    0.22000
7  7  4  6   2  1    0.26610
7  7  5  6   2  1   -0.26860
7  7  7  7   0  1   -1.24350
```

```
 7  7  7  7   2  1   -0.70340
 7  7  7  7   4  1   -0.26650
 7  7  7  7   6  1   -0.12150
 7  7  7  7   8  1   -0.03060
 7  7  7  7  10  1    0.15140
```

M-scheme file SR88MHJ.SPS

The next file needed for the OXBASH calculations is SR88MHJ.SPS. In it, the m-scheme of this model space is defined (in this case in proton-neutron formalism). The numbers in the first line have the following meaning: 44 = number of m states, 7 = number of j orbitals, 10 = number of m states in first orbit, 2 = number of m states in second orbit and so on until after 12, then 2 = number of major shells (always 2 in $\pi\nu$ formalism), 2 = number of j orbits in first major shell, 5 = number of j orbits in second major shell, 88 = A of core, and 38 = Z of core. The second line defines the j-orbits names in A9 format. The following lines have the format: dummy and n, l, 2*J, 2*J_z, 2*T_z values.

```
  44   7 10  2  8  6   4  2 12  2  2  5  88  38
P1g9/2 P2p1/2 N1g7/2 N2d5/2 N2d3/2 N3s1/2 N1h11/2
   1   1   4   9  -9   -1
   2   1   4   9  -7   -1
   3   1   4   9  -5   -1
   4   1   4   9  -3   -1
   5   1   4   9  -1   -1
   6   1   4   9   1   -1
   7   1   4   9   3   -1
   8   1   4   9   5   -1
   9   1   4   9   7   -1
  10   1   4   9   9   -1
  11   2   1   1  -1   -1
  12   2   1   1   1   -1
   1   1   4   7  -7    1
   2   1   4   7  -5    1
   3   1   4   7  -3    1
   4   1   4   7  -1    1
   5   1   4   7   1    1
   6   1   4   7   3    1
   7   1   4   7   5    1
   8   1   4   7   7    1
   9   2   2   5  -5    1
  10   2   2   5  -3    1
```

```
11   2   2   5  -1    1
12   2   2   5   1    1
13   2   2   5   3    1
14   2   2   5   5    1
15   2   2   3  -3    1
16   2   2   3  -1    1
17   2   2   3   1    1
18   2   2   3   3    1
19   3   0   1  -1    1
20   3   0   1   1    1
21   1   5  11 -11    1
22   1   5  11  -9    1
23   1   5  11  -7    1
24   1   5  11  -5    1
25   1   5  11  -3    1
26   1   5  11  -1    1
27   1   5  11   1    1
28   1   5  11   3    1
29   1   5  11   5    1
30   1   5  11   7    1
31   1   5  11   9    1
32   1   5  11  11    1
```

Publications

Publications related to this thesis

1. **Proceedings of the XXI International Workshop on Nuclear Theory, Rila Mountains, Bulgaria, June 10-15 2002, ed. V. Nikolaev, Heron Press, Sofia, p.300-305 (2002), ISBN 954-580-125-5**
   A. Blazhev, C. Plettner, L. Batist, J. Doring, H. Grawe, M. Górska, M. Gierlik, Z. Janas, M. Karny, R. Kirchner, C. Mazzocchi, I. Mukha, E. Roeckl, and R. Schwengner
   "Gamow-Teller Decay of ^{100}In"

2. **Physical Review C 66, 044319 (2002)**
   C. Plettner, L. Batist, J. Döring, A. Blazhev, H. Grawe, V. Belleguic, C.R. Bingham, R. Borcea, M. Gierlik, M. Górska, N. Harrington, Z. Janas, M. Karny, R. Kirchner, C. Mazzocchi, P. Munro, E. Roeckl, K. Schmidt, and R. Schwengner
   "β-decay of ^{100}In"

3. **Physical Review C 69, 064304 (2004)**
   A. Blazhev, M. Górska, H. Grawe, J. Nyberg, M. Palacz, E. Caurier, O. Dorvaux, A. Gadea, F. Nowacki, C. Andreoiu, G. de Angelis, D. Balabanski, Ch. Beck, B. Cederwall, D. Curien, J. Döring, J. Ekman, C. Fahlander, K. Lagergren, J. Ljungvall, M. Moszyński, L.-O. Norlin, C. Plettner, D. Rudolph, D. Sohler, K. M. Spohr, O. Thelen, M. Weiszflog, M. Wisell, M. Wolińska, and W. Wolski
   "Observation of a core-excited $E4$ isomer in ^{98}Cd"

4. **Acta Physica Polonica B34, 2439 (2003)**
   C. Plettner, J. Döring, L. Batist, I. Mukha, A. Blazhev, H. Grawe, R. Kirchner, C. Mazzocchi, E. Roeckl, Z. Janas, M. Karny, M. La Commara, C. Hoffman, S. Tabor, M. Wiedeking
   "Beta Decay of Exotic Nuclei Close to ^{100}Sn: ^{94}Ag and ^{100}In"

5. **Proceedings of the XXXI International Workshop on Gross Properties of Nuclei and Nuclear Excitations, Hirschegg, Austria, January 12 - 18, 2003, eds. H. Feldmeier, J. Knoll, W. Nörenberg, J. Wambach, GSI, Darmstadt (2003) pp. 136-141, ISSN 0720-8715; http://theory.gsi.de/hirschegg/2003/Proceedings/**
C. Plettner, J. Döring, L. Batist, I. Mukha, A. Blazhev, H. Grawe, R. Kirchner, C. Mazzocchi, E. Roeckl, Z. Janas, M. Karny, M. La Commara, C. Hoffman, S. Tabor, M. Wiedeking
"New data on β decay of exotic nuclei close to ^{100}Sn: ^{94}Ag and ^{100}In"

6. **AIP Conference Proceedings 704, 176 (2004)**
Z. Janas, L. Batist, A. Blazhev, W. Brüchle, J. Döring, M. Gierlik, M. Górska, H. Grawe, T. Faestermann, S. Harissopulos, A. Jungclaus, M. Karny, M. Kavatsyuk, O. Kavatsyuk, R. Kirchner, M. La Commara, C. Mazzocchi, I. Mukha, C. Plettner, A. Płochocki, E. Roeckl, M. Romoli, M. Schädel, R. Schwengner and J. Żylicz
"Recent results from β-decay studies in the ^{100}Sn region"

7. **Proceedings of the 8^{th} Int. Spring Seminar on Nuclear Physics, "Key Topics in Nuclear Structure", Paestum, Italy, 2004, ed. A. Covello, World scientific, Singapore (2005), (in print)**
M. Górska, A. Blazhev, H. Grawe, Döring, C. Plettner, J. Nyberg, M. Palacz, E. Caurier, D. Curien, O. Dorvaux, F. Nowacki, A. Gadea, G. de Angelis, C. Fahlander, D. Rudolph
"Structure of the ^{100}Sn region based on a core-excited $E4$ isomer in ^{98}Cd"

8. **European Physical Journal A Direct (in print), Proceedings of The Fourth International Conference on Exotic Nuclei and Atomic Masses, September 12-16, 2004 , Pine Mountain, Georgia, USA**
H. Grawe, A. Blazhev, M. Górska, I. Mukha, C. Plettner, E. Roeckl, F. Nowacki, R. Grzywacz and M. Sawicka
"Shell Structure from ^{100}Sn to ^{78}Ni: Implications for Nuclear Astrophysics"

9. **Balkan Physics Letters (accepted), Proceedings of the IV Int. Balkan School on Nuclear Physics, September 22-29, 2004, Bodrum, Turkey**
   A. Blazhev, M. Górska, H. Grawe, J. Nyberg, M. Palacz, E. Caurier, O. Dorvaux, A. Gadea, F. Nowacki, C. Andreoiu, G. de Angelis, D. Balabanski, Ch. Beck, B. Cederwall, D. Curien, J. Döring, J. Ekman, C. Fahlander, K. Lagergren, J. Ljungvall, M. Moszyński, L.-O. Norlin, C. Plettner, D. Rudolph, D. Sohler, K. M. Spohr, O. Thelen, M. Weiszflog, M. Wisell, M. Wolińska, and W. Wolski
   "Delayed spectroscopy of ^{98}Cd"

Other publications

1. **Nucl. Instr. and Meth. in Phys. Res. B 204, 53 (2003)**
   E. Roeckl, A. Blazhev, K. Burkard, J. Döring, H. Grawe, W. Hüller, R. Kirchner, C. Mazzocchi, I. Mukha, C. Plettner
   "Recent Developments at the ISOL Facility of GSI Darmstadt"

2. **Proceedings of the Third International Conference on Fission and Neutron-Rich Nuclei, November 3-9, 2002, Sanibel Island, Florida, USA, World Scientific, Singapore (2003), p. 22**
   M. Hellström, M.N. Mineva, A. Blazhev, H.J. Boardman, J. Ekman, K. Gladnishki, H. Grawe, J. Gerl, R. Page, Z. Podolyák, D. Rudolph for the GSI-FRS-Isomer collaboration
   "Isomer spectroscopy of in-flight fission fragments near ^{132}Sn at the GSI fragment separator"

3. **Proceedings of the XXXI International Workshop on Gross Properties of Nuclei and Nuclear Excitations, Hirschegg, Austria, January 12 - 18, 2003, eds. H. Feldmeier, J. Knoll, W. Nörenberg, J. Wambach, GSI, Darmstadt (2003) pp. 72-77, ISSN 0720-8715; http://theory.gsi.de/hirschegg/2003/Proceedings/**
   M. Hellström, M.N. Mineva, A. Blazhev, H.J. Boardman, J. Ekman, J. Gerl, K. Gladnishki, H. Grawe, R. Page, Z. Podolyák, D. Rudolph for the GSI-FRS-Isomer collaboration
   "Probing neutron-rich In and Cd nuclei with isomer spectroscopy"

4. **AIP Conference Proceedings 681, 209 (2003); Proceedings of the International Symposium on Proton-Emitting Nuclei (PROCON2003) February 12-15, Padova, Italy,**
I. Mukha, C. Plettner, J. Döring, L. Batist, A. Blazhev, H. Grawe, C. Hoffman, Z. Janas, R. Kirchner, M. La Commara, C. Mazzocchi, E. Roeckl, S.L. Tabor, M. Wiedeking
"Beta-delayed proton decay of a high-spin isomer of ^{94}Ag"

5. **Physical Review C 69, 015502 (2004)**
B. Blank, G. Savard, J. Döring, A. Blazhev, G. Canchel, M. Chartier, D. Henderson, Z. Janas, R. Kirchner, I. Mukha, E. Roeckl, K. Schmidt, J. Żylicz
"High-precision measurement of the half-life of ^{62}Ga"

6. **Physical Review C 69, 024320 (2004)**
S. Al-Garni, P.H. Regan, P.M. Walker, E. Roeckl, R. Kirchner, F.R. Xu, L. Batist, A. Blazhev, R. Borcea, D.M. Cullen, J. Döring, H.M. El-Masri, J. Garces Narro, H. Grawe, M. La Commara, C. Mazzocchi, L. Mukha, C.J. Pearson, C. Plettner, K. Schmidt, W.D. Schmidt-Ott, Y. Shimbara, C. Wheldon, R. Wood, S.C. Wooding
"Evidence for a High Spin β-decaying Isomer in ^{177}Lu"

7. **Nuclear Physics A 733, 20 (2004)**
C. Plettner, H. Grawe, I. Mukha, J. Döring, F. Nowacki, L. Batist, A. Blazhev, C.R. Hoffmann, Z. Janas, R. Kirchner, M. La Commara, C. Mazzocchi, E. Roeckl, R. Schwengner, S. Tabor, M. Wiedeking
"On the β-decaying (21^+) Spin Gap Isomer in ^{94}Ag"

8. **Physical Review C 70, 044311 (2004)**
I. Mukha, L. Batist, E. Roeckl, H. Grawe, J. Döring, A. Blazhev, S. Dean, C. Hoffman, Z. Janas, R. Kirchner, M. La Commara, C. Mazzocchi, C. Plettner, S.L. Tabor and M. Wiedeking
"β-delayed proton decay of a high-spin isomer of ^{94}Ag"

9. **Nuclear Physics A 746 , 66 (2004), Proceedings of the Sixth International Conference on Radioactive Nuclear Beams (RNB6), Argonne, USA**
   I. Mukha, L. Batist, F. Becker, A. Blazhev, d, A. Brüchle, J. Döring, M. Górska, H. Grawe, T. Faestermann, C. Hoffman, Z. Janas, A. Jungclaus, M. Karny, M. Kavatsyuk, O. Kavatsyuk, R. Kirchner, M. La Commara, C. Mazzocchi, C. Plettner, A. Plochocki, E. Roeckl, M. Romoli, M. Schädel, R. Schwengner, S.L. Tabor, M. Wiedeking and GSI-ISOL Collaboration
   "Studies of β-delayed proton decays of $N \simeq Z$ nuclei around ^{100}Sn at the GSI-ISOL facility"

10. **Acta Physica Polonica B (accepted), Proceedings of the XXXIX Zakopane School of Physics, August 31 - September 5, 2004, Zakopane, Poland**
    R. Lozeva, S. Mandal, J. Gerl, M. Górska, J. Grębosz, I. Kojouharov, J. Adamczewski, A. Banu, F. Becker, T. Beck, P. Bednarczyk, A. Blazhev, P. Doornenbal, H. Geissel, M. Hellström, M. Kavatsyuk, O. Kavatsyuk, N. Kurz, M. Mutterer, S. Muralithar, G. Münzenberg, W. Prokopowicz, N. Saito, T. Saitoh, H. Schaffner, K. Sümmerer, H. Weick, M. Winkler, C. Wheldon and H.-J. Wollersheim
    " Calorimeter Telescope for identification of relativistic Heavy Ion reaction channels"

11. **European Physical Journal A Direct (in print), Proceedings of The Fourth International Conference on Exotic Nuclei and Atomic Masses, September 12-16, 2004 , Pine Mountain, Georgia, USA**
    M. Karny, Z. Janas, A. Płochocki, J. Żylicz, L. Batist, A. Banu, F. Becker, A. Blazhev, W. Brüchle, J. Döring, T. Faestermann, M. Górska, H. Grawe, A. Jungclaus, M. Kavatsyuk, O. Kavatsyuk, R. Kirchner, M. La Commara, S. Mandal, C. Mazzocchi, K. Miernik, I. Mukha, S. Muralithar, C. Plettner, E. Roeckl, M. Romoli, K. Rykaczewski, M. Schädel, K. Schmidt and R. Schwengner
    "Beta Decay Studies near ^{100}Sn"

12. **European Physical Journal A Direct (in print), Proceedings of The Fourth International Conference on Exotic Nuclei and Atomic Masses, September 12-16, 2004 , Pine Mountain, Georgia, USA**
M. Kavatsyuk, O. Kavatsyuk, L. Batist, A. Banu, F. Becker, A. Blazhev, W. Brüchle, K. Burkard, J. Döring, T. Faestermann, M. Górska, H. Grawe, Z. Janas, A. Jungclaus, M. Karny, R. Kirchner, M. La Commara, S. Mandal, C. Mazzocchi, I. Mukha, S. Muralithar, C. Plettner, A. Płochocki, E. Roeckl, M. Romoli, M. Schädel, R. Schwengner and J. Żylicz
" Beta decay spectroscopy of $^{103,105}Sn$"

13. **European Physical Journal A Direct (in print), Proceedings of The Fourth International Conference on Exotic Nuclei and Atomic Masses, September 12-16, 2004 , Pine Mountain, Georgia, USA**
I. Mukha, E. Roeckl, H. Grawe, J. Döring, L. Batist, A. Blazhev, C. R. Hoffmann, Z. Janas, R. Kirchner, M. La Commara, S. Dean, C. Mazzocchi, C. Plettner, S. L. Tabor, and M. Wiedeking
"Study of the (21^+) isomer in ^{94}Ag"

14. **European Physical Journal A 23, 197 (2005)**
Z. Janas, C. Mazzocchi, L. Batist, A. Blazhev, M. Górska, M. Kavatsyuk, O. Kavatsyuk, R. Kirchner, A. Korgul, M. La Commara, K. Miernik, I. Mukha, A. Płochocki, E. Roeckl, and K. Schmidt
"Measurements of ^{110}Xe and ^{106}Te decay half-lives"

15. **Physical Review C (submitted)**
Z. Liu, P.J. Woods, K. Schmidt, H. Mahmud, P.S.L. Munro, A. Blazhev, J. Döring, H. Grawe, M. Hellström, R. Kirchner, Z.K. Li, C. Mazzocchi, I. Mukha, C. Plettner, E. Roeckl and M. La Commara
"Reinvestigation of direct proton decay of ^{105}Sb"

Bibliography

[Albe88] D. Alber, H. Grawe, H. Haas and B. Spellmeyer, Nucl. Instrum. Methods Phys. Res. A **263**, 401 (1988).

[Albe92] D. Alber *et al.*, Z. Phys. A 344, 1 (1992).

[Alex92] J. Alexander *et al.*, IEEE Trans. on Nucl. Sci. 39, 892 (1992).

[Andr82] W. Andrejtscheff *et al.*, Nucl. Instrum. Methods **204**, 123 (1982).

[Andr96] F. Andreozzi *et al.*, Phys. Rev. C **54**, 1636 (1996).

[Arvi66] S. Arvieu and S.A. Moszkowski, Phys. Rev. **145**, 830 (1966)

[Audi97] G. Audi, O. Bersillon, J. Blachot and A.H. Wapstra, Nucl. Phys. **A624**, 1 (1997).

[Barr02] B.R. Barrett, P. Navratil and J.P. Vary, Nucl. Phys. **A704**, 254c (2002).

[Bati03] L. Batist *et al.*, Nucl. Phys. **A720**, 222 (2003).

[Bay50] Z. Bay, Phys. Rev. **77**, 419 (1950).

[Bay52] Z. Bay, Phys. Rev. **87**, 194 (1952).

[Bay55] Z. Bay, V.P. Henri and H. Kanner, Phys. Rev. **100**, 1197 (1955).

[Beth36] H. A. Bethe and R. F. Bacher, Rev. Mod. Phys. **8**, 82 (1936).

[Blaz02] A. Blazhev *et al.*, Proceedings of the XXI International Workshop on Nuclear Theory, Rila Mountains, Bulgaria, June 10-15 2002, ed. V. Nikolaev, Heron Press, Sofia, p. 300-305 (2002), ISBN 954-580-125-5.

[Blaz04] A. Blazhev *et al.*, Phys. Rev. C **69**, 64304 (2004).

[Blom85] J. Blomqvist and L. Rydström, Phys. Scripta **31**, 31 (1985).

[Bohr36] N. Bohr, Nature 137,344 (1936).

[Bohr75] A. Bohr and B.R. Mottelson, "Nuclear Structure" Vol II, W.A. Benjamin Inc., 1975.

[Bohr98] A. Bohr and B.R. Mottelson, "Nuclear Structure", World Scientific, Singapore, 1998.

[Boss91] G. Bosson *et al.*, Conf. record of the IEEENSS, 879 (1991).

[Brow88a] B.A. Brown and B.H. Wildenthal, Ann. Rev. Part. Sci. **38**, 29 (1988).

[Brow88b] B.A. Brown, A. Etchegoyen and W.D.M. Rae, The computer code OXBASH, MSU-NSCL report, 524 (1988);
also *ftp://ftp.nscl.msu.edu/pub/oxbash/.*

[Brow94] B.A. Brown and K. Rykaczewski, Phys. Rev. C **50**, 2270(R) (1994).

[Brüc55] K.A. Brückner, Phys. Rev. **97**, 1353 (1953).

[Brun96] R. Brun and F. Rademakers, "ROOT - An Object Oriented Data Analysis Framework", Proceedings AIHENP'96 Workshop, Lausanne, Sep. 1996, Nucl. Instrum. Methods Phys. Res. A **389**, 81 (1997);
also *http://root.cern.ch/.*

[Brus77] P.J. Brussaard and P.W.M. Glaudemans, "Shell Model Applications in Nuclear Spectroscopy", North-Holland, Amsterdam, 1977.

[Burk76] K. Burkard, W. Dumanski, R. Kirchner, O. Klepper, and E. Roeckl, Nucl. Instrum. Methods **139**, 275 (1976).

[Burk97] K. Burkard, *et al.*, Nucl. Instrum. Methods Phys. Res. B **126**, 12 (1997).

[Cano99] D. Cano-Ott *et al.*, Nuc. Instrum. Methods Phys. Res. A **430**, 333 (1999).

[Cast00] R.F. Casten, "Nuclear Structure from a Simple Perspective" 2^{nd} ed., Oxford University Press, 2000.

[Caur89] E. Caurier, code ANTOINE, Strasbourg 1989;
also *http://sbgat194.in2p3.fr/~theory/antoine/main.html*

[Caur94] E. Caurier *et al.*, Phys. Rev. C **50**, 225 (1994).

[Caur97] E. Caurier and F. Nowacki, code NATHAN, Strasbourg 1997.

[Caur99a] E. Caurier and F. Nowacki, Acta Phys. Pol. B **30**, 705 (1999).

[Caur99b] E. Caurier *et al.*, Phys. Rev. C **59**, 2033 (1999).

[Caur02] E. Caurier and G. Martínez-Pinedo, Nucl. Phys. **A704**, 60c (2002).

[CaurPC] E. Caurier, private communication.

[Cede98] J. Cederkäll *et al.*, Eur. Phys. J. A **1**, 7 (1998).

[Char96] M. Chartier *et al.*, Phys. Rev. Lett. **77**, 2400 (1996).

[Clar00] R.M. Clark *et al.*, Phys. Rev. C **61**, 044311 (2000).

[Cohe67] B. Cohen and D. Kurath, Nucl. Phys. **A101**, 1 (1967).

[Cole90] P.J. Coleman-Smith and Ch.Ender, Conf. record of the IEEENSS, 368 (1990).

[Corr00] L. Coraggio *et al.*, J. Phys. G **26**, 1697 (2000).

[Davi89] C. N. Davids and D. Larson, Nucl. Instrum. Methods Phys. Res. B **40/41**, 1224 (1989).
C. N. Davids *et al.*, Nucl. Instrum. Methods Phys. Res. B **70**, 358 (1992).

[Dele78] M. A. Deleplanque *et al.*, Phys. Rev. Lett. **40**, 629 (1978).

[deSh63] A. de Shalit and I. Talmi, "Nuclear Shell Theory", Academic Press, New York, 1963.

[Doba94] J. Dobaczewski, I. Hamamoto, W. Nazarewicz, and J.A. Sheikh , Phys. Rev. Lett. **72**, 981 (1994).

[Doer03] J. Döring *et al.*, Phys. Rev. C **68**, 034306 (2003).

[DorvPC] O. Dorvaux, Private communication.

[Duch99] G. Duchêne *et al.*, Nucl. Instrum. Methods Phys. Res. A **432**, 90 (1999).

[Dufl99] J. Duflo and A.P. Zuker, Phys. Rev. C **59**, 2347 (1999).

[Dufo96] M. Dufour and A.P. Zuker, Phys. Rev. C **54**, 1641 (1996).

[Eber96] J. Eberth *et al.*, Nucl. Instrum. Methods Phys. Res. A **369**, 135 (1996).

[EBrep] Scientific and Technical Activity Report 1997-2003 "Achievements with the EUROBALL spectrometer", eds. W. Korten and S. Lunardi, (2003); *http://eballwww.in2p3.fr/EB/final/*

[EDOC] *http://nnsa.dl.ac.uk/Euroball/documents/.*

[Ende90] Ch.Ender *et al.*, IEEE Trans. Nucl. Sci. **37**, 326 (1990).

[ENDSF] Evaluated Nuclear Data Structure File, *http://www.nndc.bnl.gov/nndc/ensdf/.*

[Enge00] T. Engeland *et al.*, Phys. Rev. C **61**, 021302(R) (2000).

[Fahl01] C. Fahlander *et al.*, Phys. Rev. C **63**, 021307(R) (2001).

[Farn97] E. Farnea *et al.*, Nucl. Instrum. Methods Phys. Res. A **400**, 87 (1997).

[Gaim91] J.-J. Gaimard and K.-H. Schmidt, Nucl. Phys. **A531**, 709 (1991).

[Geis87] H. Geissel *et al.*, Projectile FRagment Separator Proposal, (1987).

[Geis92] H. Geissel *et al.*, Nucl. Instrum. Methods Phys. Res. B **70**, 286 (1992).

[Gerl94] J. Gerl, Conf on Physics from Large γ-Ray Detector Arrays, Berkeley, LBL 35687, UC413, p.159 (1994).

[Gerl98] J. Gerl, in "Ancillary Detectors and Devices for Euroball", ed. H. Grawe, (1998).

[Gier03] M. Gierlik *et al.*, Nucl. Phys. **A724**, 313 (2003).

[Gogn75] D. Gogny, Nucl. Phys. **A237**, 399 (1975)

[Göpp49] M. Göppert-Mayer, Phys. Rev. **75**, 1969 (1949)

[Górs94] M. Górska *et al.*, Z. Phys. A **350**, 181 (1994).

[Górs97] M. Górska *et al.*, Phys. Rev. Lett. **79**, 2415 (1997).

[Górs98a] M. Górska *et al.*, Phys. Rev. C **58**, 108 (1998).

[Górs98b] M. Górska, PhD Thesis, Warsaw University (1998).

[Graw95] H. Grawe *et al.*, Physica Scripta **T56**, 71 (1995).

[Graw99] H. Grawe *et al.*, Proc. NS98, AIP Conf. Proc. No. **481**, 177 (1999).

[Graw01a] H. Grawe and M. Lewitowicz, Nucl. Phys. **A693**, 116 (2001).

[Graw01b] H. Grawe *et al.*, Tours Symposium on Nuclear Physics IV, AIP Conf. Proc. **561**, 287 (2001).

[Graw02] H. Grawe *et al.*, Nucl. Phys. **A704**, 211c (2002).

[Graw03] H. Grawe, Acta Phys. Pol. B **34**, 2267 (2003).

[Graw04] H. Grawe, "Shell Model from a Practitioner's Point of View", Springer Lecture Notes in Physics **651**, 33 (2004).

[Graw04a] H. Grawe *et al.*, Eur. Phys. J. A Direct (in print), Proceedings of The Fourth International Conference on Exotic Nuclei and Atomic Masses, September 12-16, 2004 , Pine Mountain, Georgia, USA.

[Gros76] R. Gross and A. Frenkel, Nucl. Phys. **A267**, 85 (1976).

[Grov67] J.R. Grover, Phys. Rev. **157**, 832 (1967).

[Grzy98] R. Grzywacz, Proc. ENAM 98, AIP Conf. Proc. **455**, 257 (1998).

[Gugl95] A. Guglielmetti *et al.*, Phys. Rev. C **56**, 2912 (1997).

[Hama97] I. Hamamoto and H. Sagawa, Phys. Lett. **394B**, 1 (1997).

[Hama01] I. Hamamoto, Int. Symp. "Nuclear Structure Physics", Göttingen 2001, eds. R. Casten *et al.*, World Scientific, Singapore 2001, p. 31.

[Haus88] P.E. Haustien, At. Data Nucl. Data tables **39**, 185 (1988).

[Hers85] B. Herskind *et al.*, Nucl. Phys. **A447**, 353c (1985).

[Heyd94] K. Heyde, "The Nuclear Shell Model", Springer Verlag, Berlin, 1994.

[Hill79] D. L. Hillis *et al.*, Nucl. Phys. **A325**, 216 (1979).

[HJen95] M. Hjorth-Jensen, T.T.S. Kuo and E. Osnes, Phys. Rep. **261**, 125 (1995).

[HJenPC] M. Hjorth-Jensen, Private communication.

[Hol01U] N. E. Holden, in Brookhaven National Laboratory Formal Report 52675, p.3, "A CSEWG Retrospective", CSEWG Simposium, NNDC, BNL, Brookhaven, USA, November 5, 2001

[Honm02] M. Honma *et al.*, Nucl. Phys. **A704**, 134c (2002).

[Honm04] M. Honma *et al.*, Phys. Rev. C **69**, 034335 (2004).

[Horn72] P. Hornshoj, K. Wilsky, P.G. Hansen, B. Jonson and O.B. Nielsen, Nucl. Phys. **A187**, 609 (1972).

[Hu98a] Z. Hu, R. Collatz, H. Grawe, and E. Roeckl, Nucl. Instrum. Methods Phys. Res. A **419**, 121 (1998).

[Hu98b] Z. Hu, Ph.D. Thesis, Universität Mainz, (1998).

[Hu99] Z. Hu *et al.*, Phys. Rev. C **60**, 024315 (1999).

[Hu00] Z. Hu *et al.*, Phys. Rev. C **62**, 064315 (2000).

[HYPhys] The HyperPhysics Web Project, Nuclear Structure Concepts: *http://hyperphysics.phy-astr.gsu.edu/hbase/nuclear/nucstructcon.html*

[Jana95] Z. Janas *et al.*, Physica Scripta **T56**, 262 (1995).

[Jana97] Z. Janas *et al.*, Nucl. Phys. **A627**, 119 (1997).

[Jens49] O. Haxel, J.H.D. Jensen, H.E. Suess, Phys. Rev. **75**, 1766 (1949)

[Jin97U] H.-Q. Jin, TSCAN package v2.8 (ORNL/UTK 1997), Unpublished; also *http://www-highspin.phys.utk.edu/~hjin/download.html*.

[John95] I.P. Johnstone and L.D. Skouras, J. Phys. G **21**, L63 (1995).

[John01] I.P. Johnstone and L.D. Skouras, Eur. Phys. J. A **11**, 125 (2001).

[Kals80] A.W.B. Kalshoven *et al.*, Nucl. Phys. **A337**, 120 (1980).

[Karn97] M. Karny *et al.*, Nucl. Instrum. Methods Phys. Res. B **126**, 411 (1997).

[Karn98] M. Karny *et al.*, Nucl. Phys. **A640**, 3 (1998).

[Karn01] M. Karny *et al.*, Nucl. Phys. **A690**, 367 (2001).

[Karn04] M. Karny *et al.*, GSI Annual Report 2002, p.3
M. Karny *et al.*, Eur. Phys. J. A Direct (in print), *"Beta Decay Studies near* ^{100}*Sn"*, in Proceedings of The Fourth International Conference on Exotic Nuclei and Atomic Masses, September 12-16, 2004 , Pine Mountain, Georgia, USA.

[Kava04] M. Kavatsyuk *et al.*, Eur. Phys. J. A Direct (in print), *"Beta decay spectroscopy of* ^{103,105}*Sn"*, in Proceedings of The Fourth International Conference on Exotic Nuclei and Atomic Masses, September 12-16, 2004 , Pine Mountain, Georgia, USA.

[Kirc90] R. Kirchner, Nucl. Instrum. Methods Phys. Res. A **292**, 203 (1990).

[Kirc92] R. Kirchner, K. burkard, W. Hüller, and O. Klepper, Nucl. Instrum. Methods Phys. Res. B **70**, 56 (1992); Nucl. Instrum. Methods Phys. Res. B **70**, 186 (1992).

[Kirc96] R. Kirchner, Rev. Sci. Instrum. **67**, 928 (1996).

[Kirc97] R. Kirchner, Nucl. Instrum. Methods Phys. Res. B **126**, 135 (1997);

[Kirc03] R. Kirchner, Nucl. Instrum. Methods Phys. Res. B **204**, 179 (2003).

[Koon97] S.E. Koonin, D.J. Dean and K. Langanke, Phys. Rep. **278**, 1 (1997).

[Kuts78] W. Kutschera, B.A. Brown and K. Ogawa, Riv. Nuovo Cim. **1**, No. 12 (1978).

[LaCo02] M. La Commara *et al.*, Nucl. Phys. **A708**, 167 (2002).

[Lalk03] S. Lalkovski, PhD thesis, University of Sofia, (2003);
S. Lalkovski, A. Minkova, S. Ilieva, Sofia University, Annuaire de l'Université de Sofia "St. Kliment Ohridski", Faculté de Physique, v.96, p.19 (2003)

[Laws98] R.D. Lawson and M.H. Macfarlane, Nucl. Phys. **A634**, 41 (1998).

[Laza92] I. Lazarus *et al.*, "The EUROGAM Trigger System" IEEE Transaction on Nuclear Science 39, 1352 (1992).

[Laza95a] I. Lazarus and P.J. Coleman-Smith, IEEE Trans. Nucl. Sci. **42**, 891 (1995).

[Laza95b] I. Lazarus *et al.*, IEEE Trans. Nucl. Sci. **42**, 2288 (1995).

[Lee90] I. Y. Lee, Nucl. Phys. **A520**, 641c (1990).

[Lewi94] M. Lewitowicz *et al.*, Phys. Lett. **332B**, 20 (1994).

[Lied84] R. Lieder *et al.*, Nucl. Instrum. Methods **220**, 363 (1984).

[Lipo96] M. Lipoglavšek *et al.*, Phys. Rev. Lett. **76**, 888 (1996).

[Lipo98] M. Lipoglavšek *et al.*, Phys. Lett. **440B**, 246 (1998).

[Lipo02] M. Lipoglavšek *et al.*, Phys. Rev. C **66**, 011302(R)(2002).

[Lise04] A. F. Lisetskiy, B. A. Brown, M. Horoi, and H. Grawe, Phys. Rev. C **70**, 044314 (2004).

[Liu04] Z. Liu *et al.*, *"Reinvestigation of direct proton decay of* ^{105}*Sb"*, submitted to Phys. Rev. C.

[Mage94] A. Magel *et al.*, Nucl. Instrum. Methods Phys. Res. B **94**, 548 (1994).

[Mazz01] C. Mazzocchi *et al.*, Eur. Phys. J. A **12**, 269 (2001).

[McPh92] G.M.McPherson *et al.*, IEEE Trans. Nucl. Sci. **39**, 886 (1992).

[Mish93] V.I. Mishin et al., Nucl. Instrum. Methods Phys. Res. B **73**, 550 (1993).

[Mizu00] T. Mizusaki, RIKEN Acc. Progr. Report **33**, 14 (2000).

[Möll97] P. Möller, J.R. Nix, K.-L. Kratz, At. Data Nucl. Data Tab. **66**, 131 (1997).

[Mukh03] I. Mukha *et al.*., AIP Conf. Proc. **681**, 209 (2003).

[Mukh04] I. Mukha *et al.*, Phys. Rev. C **70**, 044311 (2004).

[Mura85] T. Murakami, J. Kasagi, H. Harada and T. Inamura, Nucl. Instrum. Methods Phys. Res. A **241**, 172 (1985).

[Muto84] K. Muto *et al.*, Phys. Lett. **135B**, 349 (1984).

[Navr98] P. Navratil and B.R. Barrett, Phys. Rev. C **57**, 3119 (1998).

[NWweb] *http://www.nsg.tsl.uu.se/nwall*

[Nowa96] F. Nowacki, PhD thesis, Strasbourg 1996.

[Nowa02] F. Nowacki, Nucl. Phys. **A704**, 223c (2002).

[Otsu98] T. Otsuka *et al.*, Phys. Rev. Lett. **81**, 1588 (1998).

[Otsu01] T. Otsuka *et al.*, Phys. Rev. Lett. **87**, 082502 (2001).

[Otsu02] T. Otsuka *et al.*, Nucl. Phys. **A704**, 21c (2002).

[Page94] R. D. Page *et al.*, Phys. Rev. Lett. **72**, 1798 (1994).

[Pala96] M. Palacz *et al.*, Nucl. Instrum. Methods Phys. Res. A **383**, 473 (1996).

[PalaPC] M. Palacz, Private comminication.

[Paus95] G. Pausch*et al.*, Nucl. Instrum. Methods Phys. Res. A **365**, 176 (1995).

[Pfue94] M. Pfuetzner *et al.*, Nucl. Instrum. Methods Phys. Res. B **86**, 213 (1994).

[Piel88] W.F. Piel *et al.*, Phys. Rev. C **37**, 1067 (1988).

[Plet02] C. Plettner *et al.*, Phys. Rev C **66**, 044319 (2002).

[Plet04] C. Plettner *et al.*, Nucl. Phys. **A733**, 20 (2004).

[Ploc92] A. Płochocki *et al.*, Z. Phys. A **342**, 43 (1992).

[Podo00] Zs. Podolyak *et al.*, Phys. Lett. **491B**, 225 (2000).

[Pori64] N.T. Porile and L.B. Church, Phys. Rev. **133**, 310 (1964).

[Pove01] A. Poves and F. Nowacki, "The Nuclear Shell Model", Springer Lecture Notes in Physics **581**, 70 (2001).

[Radf95] D.C. Radford, Nucl. Instrum. Methods Phys. Res. A **361**, 297 (1995); also *http://radware.phy.ornl.gov/*.

[Rafa83] M.H. Rafailovich *et al.*, Phys. Rev. C **27**, 602 (1983).

[Rein94] J. Reinhold, Ph.D. thesis, TU München, (1994).

[Richa91] A. Richard *et al.*, Conf. record of the IEEENSS, 873 (1991).

[Richt91] W.A. Richter *et al.*, Nucl. Phys. **A523**, 325 (1991).

[Ring80] P. Ring and P. Schuck, "The Nuclear Many-Body Problem" Springer, New York, (1980).

[Roec96] E. Roeckl, in Proc. Int. Nuclear Physics Conf. 1995 (INPC'95) (World Scientific, Singapore, 1996), p. 526.

[Roec03] E. Roeckl *et al.*, Nucl. Instrum. Methods Phys. Res. B **204**, 53 (2003).

[Ross93] C. Rossi-Alvarez, Nuclear Physics News, vol. **3**, nr. 3 (1993).

[Ryka85] K. Rykaczewski *et al.*, Z. Phys. A **322**, 263 (1985).

[Ryka89] K. Rykaczewski *et al.*, Z. Phys. A **332**, 176 (1989).

[Sara96] D.G. Sarantites *et al.*, Nucl. Instrum. Methods Phys. Res. A **381**, 418 (1996).

[Sara04] D.G. Sarantites *et al.*,Nucl. Instrum. Methods Phys. Res., (in press 2004).

[Scha98] H. Schatz *et al.*, Phys. Rep. **294**, 167 (1998).

[Sche97] J.N. Scheurer *et al.*, Nucl. Instrum. Methods Phys. Res. A **385**, 501 (1997).

[SchK94] K. Schmidt *et al.*, Z. Phys. A **350**, 99 (1994).

[SchKH00] K.-H. Schmidt, Eur. Phys. J. A **8**, 141 (2000).

[SchK00] K. Schmidt *et al.*, Eur. Phys. J. A **8**, 303 (2000).

[SchA00] A. Schmidt *et al.*, Phys. Rev. C **62**, 044319 (2000)

[Schn94] R. Schneider *et al.*, Z. Phys. A **348**, 221 (1994).

[Segr46] E. Segré, "Chart of Isotopes", Los Alamos Scientific Lab report, LADC - 36 (July 3, 1946)

[Sewe95] D. Seweryniak *et al.*, Nucl. Phys. **A589**, 175 (1995).

[Shib97] M. Shibata *et al.*, Phys. Rev. C **55**, 1715 (1997).

[Simo00] M.W. Simon *et al.*, Nucl. Instrum. Methods Phys. Res. A **452**, 205 (2000).

[Simp97] J. Simpson, Z. Phys. A **358**, 139 (1997).

[Sina92] J. Sinatkas *et al.*, J. Phys. G **18**, 1377 and 1401 (1992).

[Skep99] O. Skeppstedt *et al.*, Nucl. Instrum. Methods Phys. Res. A **421**, 531 (1999).

[Skou77] L.D. Skouras and C. Dedes, Phys. Rev. C **15**, 1873 (1977).

[Skou93] L.D. Skouras and P. Manakos, J. Phys. G **19**, 731 (1993).

[Skyr59] T.R.H. Skyrme, Nucl. Phys. **9**, 615 and 635 (1959).

[Slav92] B. Slavov, "Introduction in theoretical nuclear physics" (in Bulgarian), University of Sofia Press, 1992.

[Spoh94] K. Spohr *et al.*, Proc. Conf. on Phys. from large γ-ray detector arrays, Berkeley, Ca., August 2-6 1994, vol.2, LBL 35687, 140 (1994), and references therein.

[Spoh95] K. Spohr *et al.*, Acta Phys. Pol. B **26**, 297 (1995).

[Stel91] H. Stelzer, Nucl. Instrum. Methods Phys. Res. A **310**, 103 (1991).

[Stol01] A. Stolz, Ph.D. Thesis, TU München, (2001).

[Sümm00] K. Sümmerer and B. Blank, Phys. Rev. C **61**, 034607 (2000).

[Szer95] J. Szerypo *et al.*, Nucl. Phys. **A584**, 221 (1995).

[Szer97] J. Szerypo *et al.*, Z. Phys. A **359**, 117 (1997).

[Tara03] O.B. Tarasov and D. Bazin, Nucl. Instrum. Methods Phys. Res. B **204**, 174 (2003).

[Thei98] Ch. Theisen *et al.*, Conference Proceedings of the Second International Workshop on Nuclear Fission and Fission-Product Spectroscopy, AIP Conference Proceedings 447, 143 (1998).

[Tigh94] R. J. Tighe *et al.*, and J. Cerny, Phys. Rev. C **49**, R2871 (1994).

[Town85] I. S. Towner, Nucl. Phys. **A444**, 402 (1985).

[Vaut72] D. Vautherin and D.M. Brink, Phys. Rev. C **5**, 626 (1972).

[Voss95] B. Voss *et al.*, Nucl. Instrum. Methods Phys. Res. A **364**, 150 (1995).

[VXIs92] VXIbus System Specification Rev 1.4 April 21 1992 The VXIbus Consortium.

[Weis51] V.F. Weisskopf, Phys. Rev. **83**, 1073 (1951).

[Weis52] J. M. Blatt and V.F. Weisskopf , "Theoretical nuclear physics" (Wiley, New York, 1952); T. Ericson; And. Phys. **63**, 479 (1960).

[Weiz35] C. F. von Weizsäcker, Z. Phys. **96**, 431 (1935).

[Werf78] S. Y. Van der Werf, Nucl. Instrum. Methods **153**, 221 (1978).

[Whit77] R.R. Whitehead, A. Watt, B.J. Cole and I. Morrison, Adv. in Nucl. Phys. **9**, 123 (1977).

[Wilh96] M. Wilhelm *et al.*, Nucl. Instrum. Methods Phys. Res. A **381**, 462 (1996).

[Yari79] Y. Yariv and Z. Fraenkel, Phys. Rev. C **20**, 2227 (1979).

[YordPC] O. Yordanov, Private communication.

[Zwar85] D. Zwarts, Comp. Phys. Comm. **38**, 365 (1985).